UNIVERSITY OF SOUTHAMPTON

School of Electronics and Computer Science

Electrical Power Engineering Group

Modelling and Performance Simulation of a High Temperature Superconducting Synchronous Generator

by

Kar Seng Ship

A dissertation submitted for the degree of Doctor of Philosophy at the University of Southampton, United Kingdom

November 2005

UNIVERSITY OF SOUTHAMPTON

ABSTRACT

SCHOOL OF ELECTRONICS AND COMPUTER SCIENCE

Doctor of Philosophy

MODELLING AND PERFORMANCE SIMULATION OF A HIGH TEMPERATURE SUPERCONDUCTING SYNCHRONOUS GENERATOR

by Kar Seng Ship

This dissertation deals with electromagnetic field modelling and performance simulation of a synchronous generator with a high temperature superconducting rotor. The work presented in this thesis covers detailed modelling of magnetic field distributions and optimisation undertaken in parallel with the design and manufacturing. The design of the generator is a very complex process involving electromagnetic, mechanical and thermal aspects, thus thorough understanding of the technology is very important. Hence, the first part of this thesis gives an introduction to superconductivity including layout of the most advanced high temperature superconducting materials and the state-of-the-art in the most recent designs of electric power devices using superconductors. The superconducting tape's characteristics that are necessary for the generator design and modelling are described. The selection of the rotor core material is also discussed from the point of view of very low temperature environment. The OPERA finite-element software package is used to model various rotor designs. Three electromagnetic issues were identified as of particular importance in this design: shaping of the magnetic field in the region of the superconducting tapes to reduce the field perpendicular to the broad face of the tape, harmonic content in the voltage waveform and reduction of losses released in the cold region. The undesirable harmonics of the output voltage, which tend to circulate harmonic currents in the stator winding and the external circuit, are identified and minimised where possible, and the prediction results are compared to those obtained from measurement. Furthermore, finite-element analysis was employed to evaluate the critical parameters such as reactances and time constants required for future stability studies. A possible design and structure of the next generation synchronous generator with a HTS coreless rotor are briefly discussed based on the current design.

Contents

ACKNOWLEDGEMENTS

The years of research culminating with a dissertation involve many encounters with numerous specialists in different fields, researchers, students, administrative personnel and so forth, who all have had an impact on the evolution of the project. It is impossible to mention all and everyone here, so even if you are not personally mentioned here, I still remember the influence you have had on this work and my time at the University of Southampton. Even so, I would like to take the opportunity to show my gratitude for their kind assistance and support throughout the years. My acknowledgments must, naturally, start with expressing my profound thanks to my supervisor Professor Jan Sykulski for giving me the opportunity to be part of the team to design, build and test of a high temperature superconducting demonstrator synchronous generator. Needless to say without his guidance and confidence during this work it would not exist. I am grateful for having had the opportunity to work in such a well-balanced and friendly research group. I would like to thank the School of Electronics and Computer Science, University of Southampton and the Engineering and Physical Science Research Council, United Kingdom for the award of a research council grant and financial support. I would like to sincerely thank Dr. Kevin Goddard for the many stimulation discussions we have had and his expertise in modelling of electrical machine, which he has generously shared with me. I gratefully acknowledge the cooperation and advice, which I have received from Prof. Carlos Beduz, Dr. Maitham Al-Mosawi, Dr. Neil Stephen, Dr. Richard Stoll and especially Dr. YiFeng Yang and Bing Xu for taking the time to share their knowledge in superconductivity. On a more personal level, I am grateful to my parents for supporting me in this experience abroad, as they have always done during all my studies. I would also like to thank my lovely wife Nien Xi for her patience, support and affection, which she demonstrated in the last and most difficult months of this thesis. Last but not least, this dissertation is especially dedicated to my two wonderful children Ee Thern and Ee Lyse.

INTRODUCTION

One of the hallmarks of the twentieth century physics was the discovery of superconductivity, a phenomenon found out by Kamerlingh Onnes in 1911 at the University of Leiden. It had been known for years that the electric resistance of metals should disappear as the temperature approaches the absolute zero; the limiting values of the resistance at finite temperatures were not known at that time. In his pioneering experiments with liquid helium Onnes was able to obtain temperatures as low as 1K, and observed that instead of a smooth decrease of the resistance of mercury as the temperature was gradually reduced towards 0 K, it sharply disappeared below a certain temperature (4K), which is now referred to as the critical temperature. Onnes recognised that below 4K mercury passes into a new state with electric properties unlike any known before, and this new state was called the superconducting state. Later, many different superconductors have been discovered. Metallic elements and alloys, which exhibit superconducting properties below 30K have been named low temperature superconductors (LTS), in contrast to certain oxide compounds with critical temperature exceeding 30K, named high temperature superconductors (HTS). Above their critical temperature, the superconductors have electric resistance higher than the resistance of good metal conductors, such as copper. Most of them are resistive materials at room temperature. With the years of development of superconductivity, the critical temperature has been increasing and currently has exceeded 130 K for certain oxide superconductors. The higher the critical temperature, the easier is the construction and maintenance of cryogenic systems needed to cool down the superconductors in their applications.

The use of LTS materials for the implementation of powerful DC magnets had been a leading application of superconductors for years. The discovery of new HTS compounds in 1986 offered new possibilities for power applications at 77 K, the temperature of liquid nitrogen. This has lead to a variety of power devices employing HTS being prototyped, in particular rotating electric machines. The application of

superconductors to electric machine windings overcomes the major factor limiting both output capability and efficiency, namely the 'ohmic' losses. Losses in superconducting windings approach zero with DC and can be kept small even with AC by appropriate conductor screening design. The superconducting generator has great potential for large scale commercial application of superconductivity. This type of machine with a superconducting adjustable field rotor keep power loss to a minimum since the stator is phase-locked in synchronism with the rotating rotor field. Moreover, the high magnetic flux density which could be produced by the superconducting rotor field winding permits a great reduction in the amount of iron required in both the rotor and stator. The availability of high quality superconducting tapes with improved strength and critical currents makes the design even more attractive.

Interest in superconductivity at Southampton University has a long history, both in the Electrical Power Engineering Research Group and Institute of Cryogenics, including the work on a low temperature superconducting generator in the early eighties. Close collaboration between the two departments on power applications of HTS materials started in 1991 and progress has been significant. A completion of a feasibility study and design of a HTS grid transformer demonstrated that the unit had exceeded design expectations [1]. In 1999, Engineering and Physical Science Research Council (EPSRC), United Kingdom, approved the proposal to design and build a high temperature superconducting demonstration synchronous generator under research grant GR/N21253/01. The project was carried out with the unique collaboration of researchers with wide spectrum of expertise in electrical and mechanical engineering. The project had the following overall objectives:

- Design, build and test a demonstrator generator to assess the potential of HTS technology in electric power applications.
- Study fundamental problems associated with the use of HTS materials in such applications.
- Study and optimise heat transfer and refrigeration within a rotating cryostat.
- Conduct a comprehensive program of tests to assess the performance of HTS tapes under operating conditions.

- Develop computer simulation models for virtual prototyping.
- Produce flexible design guidelines for electric power devices using HTS tapes.

1.1 Objectives of the project

A careful study of field distributions in the generator was required before the final design could be agreed. HTS tapes are known to have strong anisotropic properties and it was essential that the tapes are positioned in such a way so as to avoid deterioration of their performance. Since the overall performance of the winding is decided by its 'worst' section, thus significant modelling effort was needed to achieve best solutions. Furthermore, the use of a superconducting field winding and hence operation in low temperature environment makes the machine more vulnerable to system instability. This is because any losses in the rotor will contribute to the load on the cooling system, thus increasing the cooling power required. It is therefore imperative to first conduct computational and simulation studies to evaluate the losses and identify critical performance issues.

Finite-element analysis has been widely used by many researchers worldwide as part of their design tools to simulate electrical machines. In the field of superconducting generator, the finite-element simulations were mainly applied to deal with general performance and transient stability studies [2-4]. These simulations ignored important factors such as harmonics and their associated losses in the cold region. In this thesis, detail studies of field distributions have been undertaken to identify the undesirable harmonics and to evaluate the losses. The design of this generator presents many challenges particularly the added complexity due to flux diverters. In the United Kingdom, Southampton University was the first research group to introduce and incorporate this unique feature into their HTS transformer [1]. The effectiveness of the flux diverters was proven and hence it was adopted in this machine. Simulation techniques employed in the HTS transformer were extended in this thesis by incorporating multiple flux diverter rings. In this project, I was assigned as part of these PhD studies to work full-time on field modelling of the HTS synchronous generator in

parallel with the design and manufacturing. In the context of the overall aims of the EPSRC project to which this PhD was attached, the particular objectives of this thesis were identified as follows:

- Study and explore the state-of-the-art in the electric power devices using superconductors and their characteristics.
- Assist the research team in the design of the superconducting generator particularly determination of the superconducting tape's characteristics.
- Establish relevant 2D and 3D models using available commercial software and discuss appropriateness of 2D modeling and provide guidelines on when 3D models may be necessary.
- Model and identify important parameters through various modes of operation.
- Undertake comprehensive studies of field distributions and loss calculations for various rotor designs.
- Identify important principles and characteristics of modeling devices containing superconducting tapes.
- Suggest and explore other configurations for future designs of superconducting generators.

1.2 Structure of the thesis

The essence of the thesis is field modelling and simulations studies of a synchronous generator with a HTS superconducting rotor. Chapter 2 gives an introduction to superconductivity and its applications. The fundamental features of superconductors, including layout of the most advanced high temperature superconducting materials, are discussed. Emphasis is put on the explanation of the different types of superconductors and their AC losses. Moreover, attempt is made to provide an overview of the state-of-the-art in the most advanced designs of electric power devices using superconductors and various challenges that must be overcome in order to realise commercialisation.

Chapter 3 discusses the underlying principles of a superconducting generator. It introduces the basic features of a generator and the benefits of employing

superconducting windings. The generator characteristics and constructional features are also discussed. Furthermore, this chapter highlights the major components of the Southampton's HTS generator design, in particular the superconducting field winding and rotor. The superconducting tape's characteristics that are necessary for the generator design and modelling are described. The selection of the rotor core material is also discussed from the point of view of very low temperature environment.

Chapter 4 deals with virtual prototyping of the 100 kVA synchronous generator with superconducting field windings. The OPERA finite-element software is used to model various rotor designs. Some general discussion of most widely used numerical methods, specifically a finite-element method, are presented. The undesirable harmonics of the output voltage, which tend to circulate harmonic currents in the stator winding and the external circuit, are identified and minimised where possible, and their results are compared to those obtained from measurement. The initial analysis was done using 2D finite-element models since this allowed a large number of designs to be considered.

Chapter 5 details the losses evaluations in the cold region of the generator and critical parameters required for future stability studies. Two different methods were used to estimate the no-load and load-dependant losses: full transient non-linear rotating machine model to model no-load losses and combined static and steady-state AC models to model full-load losses. These losses must be estimated carefully so as to make sure that adequate refrigeration power is provided to remove them from the system. Meanwhile, two methods using finite-element analysis were employed to evaluate the reactances and time constants: first, the sudden three-phase short-circuit, and second, frequency response.

Chapter 6 highlights the next generation synchronous generator with a HTS coreless rotor. A possible design and structure of the machine are briefly discussed based on the current design. Preliminary modelling studies have been undertaken and the results are presented. Finally, the thesis is completed with the conclusions (Chapter 7) followed by the list of references, and publications.

SUPERCONDUCTIVITY AND APPLICATIONS

Superconductivity is a phenomenon which occurs in certain materials and is characterised by the absence of electrical resistivity. The purpose of this chapter is to give an introduction to high temperature superconductivity by outlining the current state of the development of high temperature superconductors, as well as the basic properties of the materials. The occurrence of superconductivity in high temperature materials is not yet fully understood; as a matter of fact the classical superconducting theory known as BCS theory [5] to date does not completely explained the phenomena even though it satisfactorily describes the low temperature superconductors. This is probably caused by the fact that in these complex materials it is very hard to establish the mechanism uniquely, even through experimental methodology, as well as by the evolution of many competing models, which seem to address only particular aspects of the problem. Nevertheless, the fundamental characteristics of superconductors and their applications have been explored. Section 2.1 describes the fundamentals of superconductivity and the main features of Type-I and Type-II superconductors respectively, Section 2.2 explains different types of ceramic superconductor's characteristics and their development, and finally, Section 2.3 discusses the AC loss mechanisms in high temperature superconductor. These sections by no means cover all aspects of the physics of HTS materials, but are provided to underpin the discussion of the design of the superconducting machine. Finally Sections 2.4 and 2.5 are dedicated to applications of high temperature superconductors to electric power devices, including an overview of its technological advancements since they were first discovered, the design goals and technological.

2.1 Fundamentals of superconductivity

Superconductors are divided into two types depending on their characteristic behaviour in the presence of a magnetic field. Type-I superconductors are pure metals, whereas Type-II superconductors are comprised primarily of alloys or inter-metallic compounds. However, both have one common feature: below a critical temperature their resistance vanishes. It is important to understand the transport and magnetic behaviour of these novel materials in order to have a better understanding of the basic phenomena of superconductivity. Hence, in the following sections, an introduction to superconductivity and high temperature superconductors is provided. The fundamental features of Type-I and Type-II superconductors, including an overview of the most advanced high temperature superconducting materials are discussed. Finally, different types of losses under AC operating conditions are discussed.

2.1.1 Basic features of superconductors

2.1.1.1 Type-I superconductors

Metals, such as titanium, aluminium, tin, mercury, lead, and others, become superconducting when their electric resistance completely disappears after they are cooled below their critical temperature. These metals were the first superconductors to be discovered and have been later named Type-I superconductors or low temperature superconductors (LTS). They require extremely cold temperatures to slow down molecular vibrations sufficiently to facilitate unimpeded electron flow in accordance with what is known as BCS theory (BCS are the initials of the authors of that theory: Bardeen, Cooper and Schrieffer). The theory explains the microscopic origins of superconductivity at temperatures close to absolute zero. The basic idea behind the theory was that electrons in the elements would pair up together and help each pass through the material avoiding obstacles. In a typical Type-I superconductor, attractive forces exist between electrons due to Coulomb attraction between the electron and the crystal lattice. An electron in the lattice will cause a slight increase in positive charges around it. This increase in positive charge will, in turn, attract another electron. These two electrons are known as a Cooper pair. If the energy required to bind these electrons

together is less than the energy from the thermal vibrations of the lattice attempting to break them apart, the pair will remain bound. This is the reason why superconductivity requires low temperatures so that the thermal vibration of the lattice is kept small enough to allow the forming of Cooper pairs. Hence, the Cooper pair is more stable than a single electron within the lattice as it experiences less resistance.

It was discovered that superconductivity is destroyed when the metal becomes normal again, or in the presence of certain level of magnetic field, which is referred to as the critical field H_c. The critical temperatures T_c, magnetic fields H_c and magnetic flux densities B_c of several Type-I superconductors are given in Table 2.1 [6]. As shown in the table, the critical magnetic field in metal superconductors is very low. While instructive for understanding superconductivity, the Type-I superconductors have been of limited practical importance in application such as high energy physics and medical magnetic resonance imaging because the critical magnetic fields are so small. Moreover, the total cost of refrigeration to cool these materials down to 1-7 K and maintain their operating temperatures is formidable [7]. This cost includes capital and operating components; capital is required to purchase thermal insulation and cooling equipment, and operating costs to pay for the coolant makeup and, in some cases, for energy required to remove the heat that penetrates the thermal insulation.

Table 2.1 T_c, H_c, and B_c of Type-I superconductor

Metal	T_c (K)	H_c (A/m)	B_c (Tesla)
Titanium (Ti)	0.4	0.42×10^{4}	5.60×10^{-3}
Aluminium (Al)	1.2	0.79×10^{4}	10.5×10^{-3}
Tin (Sn)	3.7	2.40×10^{4}	30.5×10^{-3}
Mercury (Hg)	4.2	3.30×10^{4}	41.1×10^{-3}
Lead (Pb)	7.2	6.40×10^{4}	80.3×10^{-3}

2.1.1.2 Perfect diamagnetism

The discovery that a metal in the superconducting state never allows a magnetic flux density to exist in its interior by Walter Meissner and Robert Ochsenfeld in 1933

showed that it exhibits perfect diamagnetism and the equality $B = 0$ always holds [8]. This property, which cannot be explained by an equivalence of superconductors with perfect conductors, has been named Meissner effect. The magnetic behaviour of a superconductor, in contrast to a perfect conductor, is illustrated in Fig. 2.1. The expulsion of an applied field is a result of the existence of induced currents in a superconductor, which generate magnetic field, opposite in direction and equal in magnitude to the external field, so that the total field inside the superconductor is zero. The cancellation of flux lines within the superconductor may be viewed as if the external field lines were 'forced' to circumvent the specimen and not allowed to enter inside.

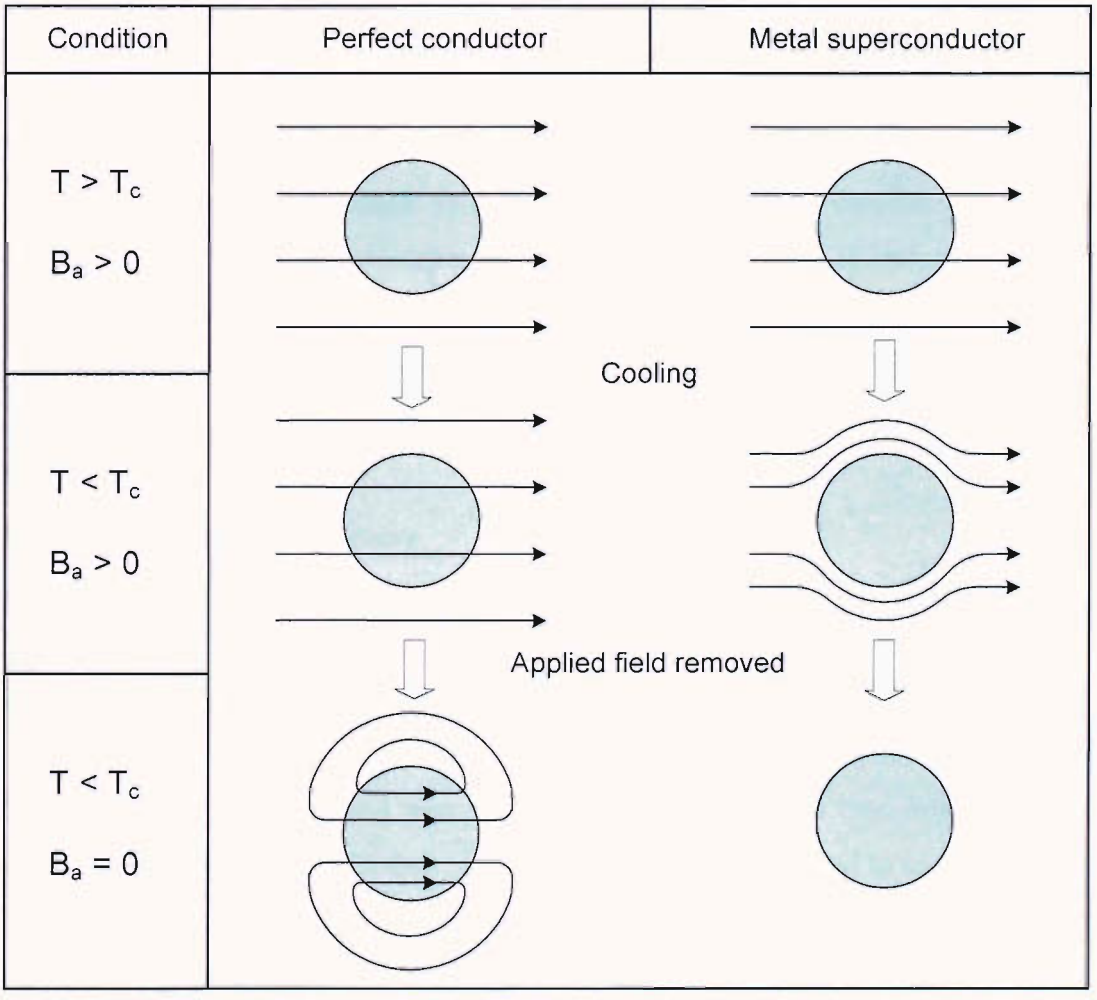

Figure 2.1 The magnetic behaviour of a superconductor in contrast to a perfect conductor

2.1.1.3 AC Resistivity

Zero resistance in a superconducting metal means that there is no voltage drop along the metal when a current is passed through, and by consequence no power is dissipated. This is, however, strictly true only for a DC current of constant value. A superconductor below its critical temperature is permeated by two electron fluids: one of normal electrons and one of superelectrons. Superelectrons which form Cooper pairs and carry electricity without resistance and the rest behaving like normal electrons, which scatter and when passing through the metal lattice experience resistance. For a constant direct current, all of the current is carried by the superelectrons. For a constant current to exist, the velocity of all the electrons must be the same along the current path, the electrons do not accelerate, and no electric field exists. If an electric field existed then the electrons would be accelerated continuously and the current would increase to an infinitely large value. If the current in the superconductor is changing, or AC, an electric field must be present in the superconductor to accelerate the electrons. This electric field is caused by electrons moving perpendicular to the flow of the rest of the current. These electrons then collide with the other electrons and this creates resistance. Therefore, AC current in a superconductor creates resistance. In addition, due to the presence of electric field, some current will be carried by the normal electrons, so that in overall the AC current will cause some power dissipation in a superconducting metal [9].

2.1.2 Type-II superconductors

2.1.2.1 Magnetisation of Type-II superconductors

Type-I superconductors are composed entirely of metallic chemical elements, but Type-II superconductors may be metal alloys or even some pure metals, such as Niobium (Nb) and Vanadium (V), and also different oxide compounds (see Section 2.2.2). All metals and metal alloys have their T_c below 30 K and are referred to as low temperature superconductors, while the oxide superconductors have their T_c above 30 K and are referred to as high temperature superconductors (HTS). Type-II superconductors are characterised by two critical fields; lower critical magnetic field, H_{c1} and upper critical magnetic field, H_{c2}. Typical values of the critical field for several Type-II

superconductors are given in Table 2.2 [6]. At magnetic fields weaker than the lower critical field H_{c1} are completely excluded from the bulk of the material by superconducting screening currents flowing in a very thin layer at the surface. Magnetic fields between H_{c1} and the upper critical field H_{c2} penetrate the material in the form of flux lines. Both critical fields depend on the temperature and they are zero at the critical temperature as shown in Fig. 2.2.

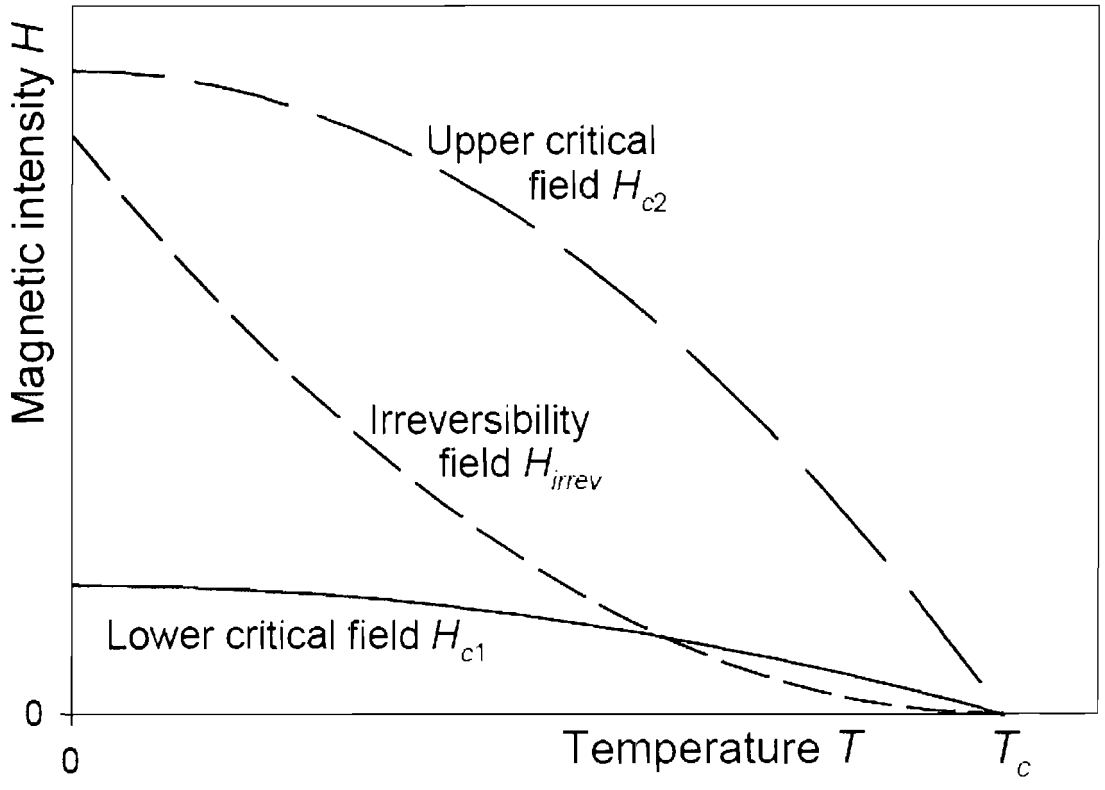

Figure 2.2 Phase diagram with critical magnetic fields of a type-II superconducting material versus temperature

In an idealised Type-II superconductor, the flux density, B, field intensity, H, and magnetisation, M are uniquely related to one another and the magnetisation curve is reversible. Their relationship can be illustrated by Fig. 2.3. The state of perfect diamagnetism $B = \mu_0 (H + M)$, exists only below H_{c1}, afterwards the flux starts to penetrate, and above H_{c2} there is no magnetisation at all and the material returns to its

normal state. As the magnetic field is decreased below H_{c2}, the reverse magnetisation path will exactly retrace the forward one. However, no real material exhibits the exact retracing of the idealised curve. Structural imperfections or chemical impurities act as barriers for flux movement into the crystal; this is referred to as flux pinning [10]. As a matter of fact, it is the practical goal of material engineers to introduce as many pinning sites as possible in order to allow high currents to flow under high magnetic fields.

Table 2.2 T_c, H_c, and B_c of Type-II superconductor

Compound	T_c (K)	H_{c2} (A/m)	B_{c2} (Tesla)
Nb-Ti (alloy)	10	0.9×10^{7}	12
Nb_3Sn	18	1.6×10^{7}	22
Nb_3Ge	23	2.2×10^{7}	30
Nb_3Al	19	2.3×10^{7}	32
$PbMo_6S_8$	14	3.3×10^{7}	45

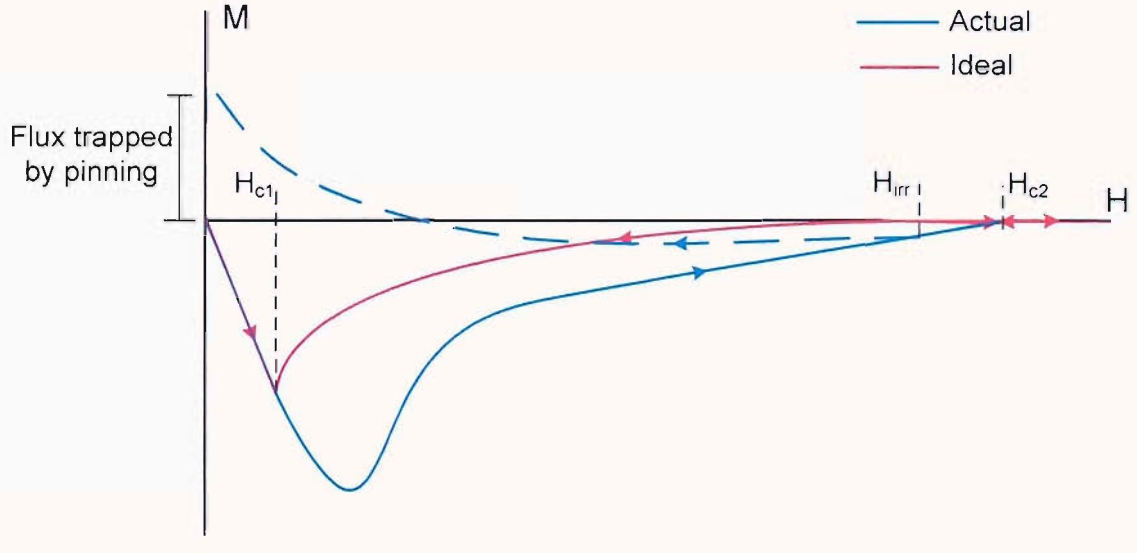

Figure 2.3 Magnetisation of Type-II superconductor.

A real Type-II superconductor has a more complicated magnetisation path, which is depicted in Fig. 2.3. Noticeable difference is the absence of sudden change in magnetisation M as H passes through H_{c1}. Only the slight deviation from linearity conveys that the diamagnetic state is no longer perfect, and that flux has started to

penetrate into the material. The increase of H leads to more extensive flux penetration, and at H_{c2} the state of full penetration is achieved, $B = \mu_0 H$ and the material becomes normal. In the superconducting state, some of the flux is trapped within the material. After reaching H_{c2}, when H is reduced, flux lines are free to move at first, and so the H-M curve retraces its path until a point H_{irr}, the irreversibility field, when flux pinning becomes stronger, B declines slower than H, and M deviates from the forward curve. As H is further decreased, B remains high and since $B = \mu_0 (H + M)$, M rises to a positive value. At the end of the reverse cycle, when $H = 0$, the value of B remains finite due to the flux trapped by the superconductor.

2.1.2.2 Mixed state

Apart from the normal and superconducting states, Type-II superconductors exhibit a peculiar property, which is called the mixed state. This state allows the existence of normal regions in the material. In a normal Type-I material, magnetic fields can either be expelled completely when it is in its superconducting phase, or it can be penetrated by a magnetic field when it is in is normal phase. Mixed state is sometimes called a vortex state because vortices of superconducting currents surround filaments or cores of normal material as shown in Fig. 2.4.

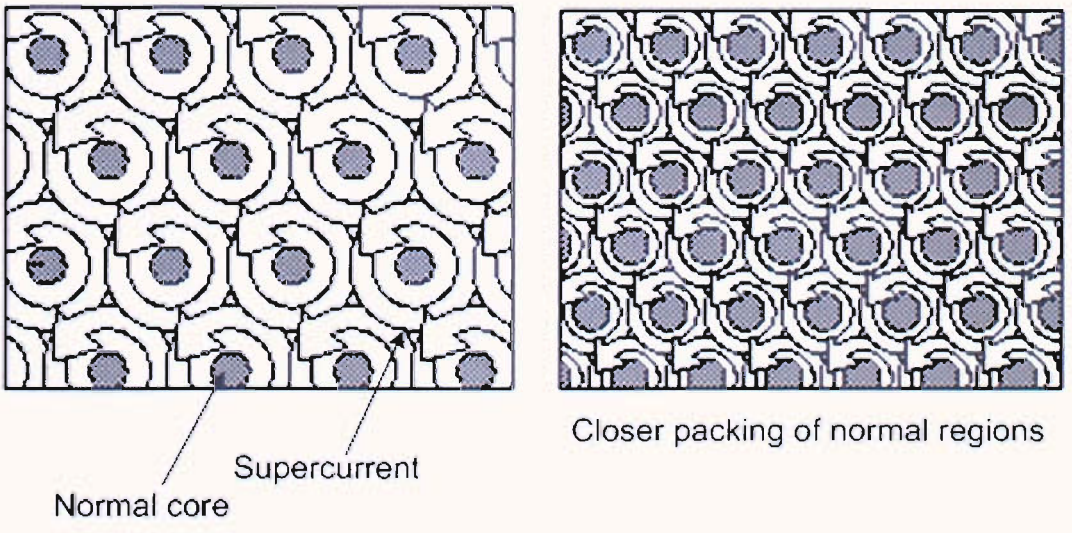

Figure 2.4 The mixed state, showing normal cores and encircling supercurrent vortices.

As the temperature of the material increases (starting from absolute zero) or critical magnetic field is approached, the normal cores become bigger and eventually overlap, thus reverting the substance back to a normal conducting state. In the mixed state, Meissner effect is no longer present and magnetic flux may partially penetrate the superconductor; the superconductivity however, is not lost. A great advantage of Type-II superconductors is the large magnetic fields which they can support without losing their superconducting properties, compared to Type-I superconductors for which the values of H_c are very low.

2.2 High temperature superconductors and their development

The high temperature superconductors represent a new class of materials which bear extraordinary superconducting and magnetic properties and great potential for wide ranging technological applications. Until 1986, the highest known critical temperature of a superconductor was 23.2 K for Nb_3Ge. Low working temperatures require sophisticated and expensive cooling technology, which is a major drawback for large-scale use of superconductors. Devices based on low temperature superconductors are usually cooled with liquid helium, which boils at a temperature of 4.2 K. In 1986, Bednorz and Müller measured a critical temperature of about 30 K in La_2CuO_4 [11]. This material was the first of a new class of ceramic 'high temperature superconductors'. Ceramic materials were soon found with critical temperatures higher than 77 K, which is the boiling point of liquid nitrogen. At the moment the highest known critical temperature is 139 K for (Hg, Pb) $Ba_2Ca_2Cu_3O_x$ [12]. However, this compound has not received the development effort that some others have and is generally considered too difficult or expensive to produce for applications. The most commonly used high temperature superconducting materials are: $YBa_2Cu_3O_x$ (Y-123), $Bi_2Sr_2CaCu_2O_x$ (Bi-2212) and $Bi_2Sr_2Ca_2Cu_3O_x$ (Bi-2223).

2.2.1 Common features of ceramic superconductors

The first superconductor with T_c more than 77 K is YBCO, which together with the bismuth oxides Bi-2212 and Bi-2223 mentioned in previous section, are at present the

most advanced HTS materials. High temperature superconductors are chemical compounds, consisting of repeating patterns of atoms of different elements, called unit cells. The unit cell of one HTS superconductor – $Bi_2Sr_2Ca_2Cu_3O_x$ and $Bi_2Sr_2Ca_1Cu_2O_x$ – is depicted in Fig. 2.5 [8]. Trillions of unit cells form a very small crystal, known as a grain. Millions of grains are needed to make a macroscopic sample.

The crystal structure of all ceramic high-temperature superconductors consists of highly conducting copper oxide layers sandwiched between non-conducting layers of other elements. Due to the layered structure of the unit cells, high temperature superconductors have intrinsic anisotropy along the *c*- and *a*,*b*-planes of their crystals, and as a result of the rolling during the manufacturing process. Figure 2.5 shows a single unit cell of two Bismuth compounds. The *a*- and *b*-directions of the crystal are defined along the copper oxide layers and the superconducting current transfer is localised in these layers. Therefore, the critical current density is higher in the *ab*-plane than in *c*-direction, however no significant difference is observed between the *a*- and *b*-directions [13]. It should be noted that all critical current densities and magnetic fields listed earlier in Table 2.1 are oriented in the *ab*-plane of the ceramic.

A very important characteristic of BSCCO is the strong anisotropy of the critical current density for applied magnetic field perpendicular to the broad side of the tape; J_c decreases quickly, while for applied parallel magnetic field, the decrease of J_c is much more moderate. Experimental investigations into the current density in Bi-2223 tapes in fields with different orientation have been reported [14-16] and the anisotropy has been attributed also to the different pinning forces in parallel and perpendicular fields.

HTS are brittle ceramic materials, most of which are oxides and their resistivity at room temperature is about hundred times higher than that of copper. Furthermore, the critical current density of each of the ceramic superconductor increases as its temperature declines. Each of the three ceramic high temperature superconductors can be described to engineering accuracy by the same kind of phenomenological E versus J curve (electric field versus current density). The only difference is in the values of the relevant

parameters, each being particular to whatever material is under consideration. Together, the phenomenological E versus J curve, the principles of electricity and magnetism lead to expect hysteresis, the irreversible dissipation of electrical energy, in a cyclic process, of which AC is the most prominent example. This hysteresis is the principal contributor to AC losses and will be explain briefly in Section 2.3.1.

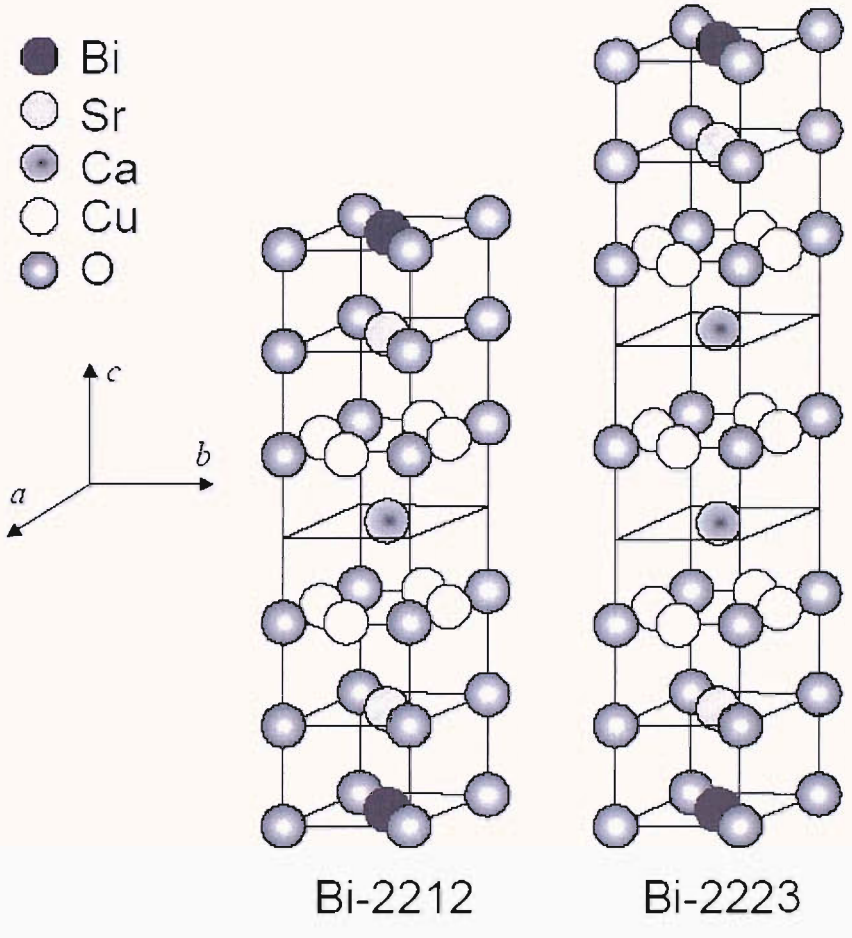

Figure 2.5 Unit cells of two different Bi-compounds

Unlike copper or aluminium, ceramic superconductors cannot stand by themselves; they must be embodied within a matrix or laid down upon a substrate. To date, the only matrix materials known to have suitable properties are the noble metals, of which silver is the least expensive. Unfortunately, even silver is not cheap, and it is also an excellent conductor. The conductivity of silver would raise no problem if the current were DC.

However, when AC is conveyed, the silver is exposed to time dependent magnetic fields, and silver's excellent conductivity allows non-negligible currents to be induced. These eddy currents dissipate electrical energy, something the use of superconductors is meant to avoid, and generate heat, which must be removed to maintain the operating temperature of the superconductor.

2.2.2 Types of ceramic superconductors

2.2.1.1 BSCCO

Bismuth strontium calcium copper oxide, also known as BSCCO, is used to make conductors that represent the basis for all present large scale applications of HTS. They are called conductors of first generation (1G). BSCCO has a well established manufacturing technology, and commercial conductors are available in long lengths. Transport current applications are among the main targets for BSCCO conductors. They are produced by the Oxide-Powder-In-Tube (OPIT) process, a simple sketch of which is shown in Fig. 2.6 [17]. At a glance, the manufacturing includes the following steps [18]. A Bi-2212 powder (of precursor grains) is put in a silver tube, mechanically deformed and heat treated in oxygen atmosphere until a round multifilamentary wire is obtained. The wire is rolled into a flat tape in order to texture the grains and to enable bending of the brittle composite conductor over smaller radius. Further thermo-mechanical cycles form the right superconducting phase, heal cracks, increase the compaction and improve connectivity between individual grains.

The current in BSCCO conductors has to pass through the grain boundaries, which obstruct current except when at low angle. Therefore, strong texture is necessary and the better the grains are aligned, the higher the critical current density of the conductor is. In order to obtain texture and alignment of the grains in the oxide powder, which are initially randomly oriented, rolling is required in the manufacturing process and the superconductors are made in the form of thin tapes; usually having width of 2-4 mm and thickness 0.2-0.4 mm. As mentioned earlier, HTS compounds are very brittle materials, thus in order to improve the mechanical characteristics of the tapes the superconducting

core is placed in a tube, made of silver, which is selected for its good mechanical and oxygen diffusion properties. Moreover, silver matrix does not react chemically with the filament material during heat treatment process.

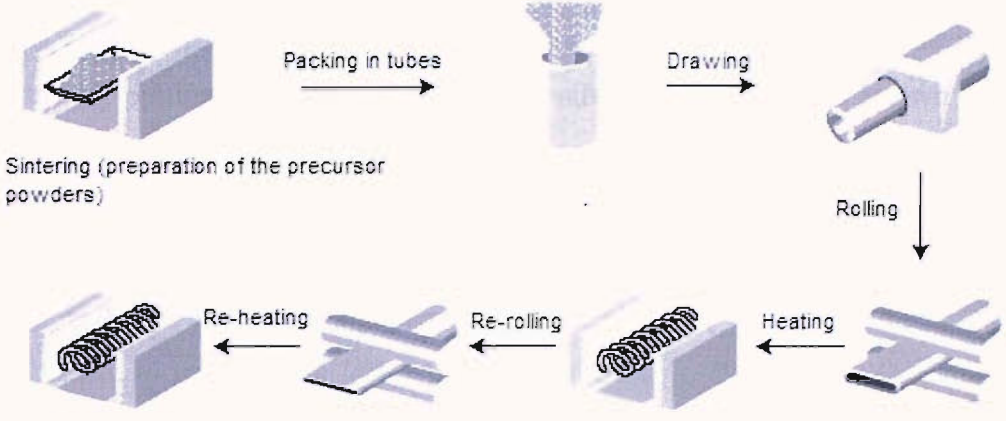

Figure 2.6 Schematic presentation of the OPIT process

One of the two Bismuth compounds known as Bi-2223 has the highest transition temperature approximately 110 K. Up to date, Bi-2223 has been used in many prototypes especially in power equipment that were cooled by liquid nitrogen. Some researchers have considered using Bi-2223 at such temperatures because its performance in magnetic fields improves substantially at lower temperatures (e.g. at 65 K and 45 K) without incurring a greatly increased cooling penalty. Many companies like Intermagnetics General Corporation and American Superconductor Corporation (AMSC) in USA, Sumitomo Electric Industries in Japan, Trithor and Supercables in Europe are involved in the manufacturing of practical superconductors of sufficient quality and quantity. The superconducting field winding for the Southampton 100 kVA superconducting synchronous generator was purchased from AMSC with rated nominal current of 115 A. A decision was made early to operate the tape at 77 K using liquid nitrogen to improve cooling efficiency and reduce running costs.

The other Bismuth HTS compound known as Bi-2212 has the lowest transition temperature, approximately 80 K. Hence, its practical application would entail operating

temperatures below the boiling point of liquid nitrogen (77 K). Many researchers have considered using Bi-2212 at liquid helium temperatures because its performance in high magnetic fields, at those temperatures, surpasses that of Nb_3Sn. Bi-2212 is appealing because it is less expensive to fabricate a conductor from it than from the other materials. Moreover, it can be made to have less anisotropic response to magnetic field than a conductor made from Bi-2223. Like Bi-2223, Bi-2212 is made into conductor either by putting it into tubes of silver or silver alloy, a method known as OPIT, with subsequent bundling and drawing; or by coating silver or silver alloy tapes with Bi-2212. Despite today's price, BSCCO superconductors will continue to be offered by competing firms, in the hope that one day the price will fall significantly to become comparable to conventional material.

2.2.1.2 YBCO

Currently, the development of a viable and low cost processing route based on $YBa_2Cu_3O_7$, called YBCO-123 is of great interest and forms a central research area for many years to come. The material known as YBCO for short, is categorised as second-generation (2G) superconductor wire. The advantage of the 2G superconductor is the possibility of achieving commercially viable in-field electrical performance at higher temperatures than 1G wire. The reason for this lies in the irreversibility line, which is the limit of superconductor critical current density in the magnetic field or temperature plane. At any given magnetic field, the irreversibility line of YBCO lies at much higher temperature than that of Bi-2223, fundamentally because of the different coupling between adjacent sets of copper oxide planes in the atomic structure of these materials. However, the most significant 2G advantage of all turned out to be the possibility of lowering wire cost below that of 1G HTS wire. The price-performance ratio of 1G HTS wire is continuing to drop rapidly towards an eventual £28 per kAm level as the production is scaled up and yields are optimised [19]. While this is adequate for many commercial applications, the range of economic applications broadens substantially if the price-to-performance ratio can drop below that of copper, which is £8-14 per kAm at the full operating level of most large electrical equipment. However, 2G wire has the

possibility of dropping even below the copper level, a factor of 2-5 lower than 1G wire [20].

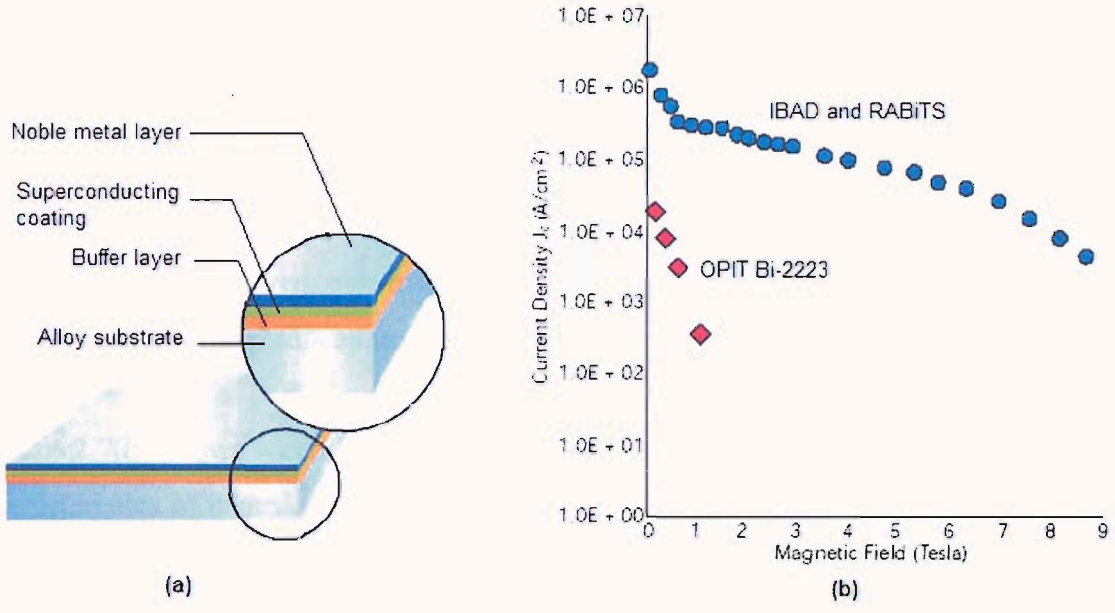

Figure 2.7 Second generation YBCO superconductors (a) YBCO coated conductor composite, (b) IBAD, RABiTS and OPIT performance characteristics

In 1991, Fujikura in Japan announced a novel kind of HTS wire in which a thin layer of HTS material was deposited onto a flexible tape shaped substrate, as shown schematically Fig. 2.7(a) [20]. The method Fujikura used to align the grains on the surface of a flexible tape was called IBAD, or ion beam assisted deposition. The coated conductors shown in figure above consist of multiple layers deposited onto a nickel alloy substrate. In general, coated conductors are fabricated by depositing a superconducting material onto a long, flexible base material. A critical requirement of the base material is that it must be textured in a preferred orientation in order to promote biaxial growth (growth in one specified orientation) of the buffer layers and superconducting film [21]. In 1995, Los Alamos National Laboratory, United States has successfully optimised the process and achieved a superconducting critical current density of 10 kA/mm^2 at the 77 K temperature range. This means that with the current density, a one micron thick layer of YBCO could carry 100 A of electrical current at 77 K in a 1 cm wide strip [22]. However, all the conductors are produced in laboratory

samples and limited only in short lengths of 1m at most. The main obstacles to the manufacture of commercial lengths of YBCO wire has been the phenomenon of weak links: grain boundaries formed by the misalignment of neighbouring YBCO grains are known to form obstacles to current flow.

Currently, there are many competing processes have been developed for fabricating second generation high temperature superconducting wires. The RABiTS known as the rolling assisted textured substrate process like IBAD process, creates an aligned crystalline texture and this approach relies on the expitaxial deposition of YBCO onto a textured template of one or more oxide buffer layers and a normal metal substrate [23]. Figure 2.7(b) shows recent tests on laboratory samples and demonstrates performance characteristics of coated conductor processing methods using IBAD and RABiTS to be nearly 50 times better than the state of the art Bismuth OPIT wires [24]. Manufacturers around the world are in the process of taking the technology to the pilot scale to produce commercially viable 100 m lengths.

2.3 AC loss mechanism

Superconductors have zero resistance and no power is dissipated only when DC current below the critical value is passed through. As briefly explained in Section 2.1.1.3, any applied AC current or changing magnetic field would inevitably lead to losses as heat is being dissipated in the superconductor. Superconductors which are developed for application in high power devices such as transformers, power transmission cables, motors and generators have to meet several requirements in order to compete with the presently used normal conductors. A high critical current and a low price are required. The price of superconductors is normally expressed as cost per meter length, per ampere of critical current. The AC loss should be low enough to justify the extra investment in the superconductor and the cooling equipment. The decision to apply superconductors is ultimately based on financial considerations: the cost of energy, the superconductor price (including extra production steps intended to decrease the AC loss), the cost of the refrigerator, maintenance and reliability.

The AC loss in a superconductor is usually much lower than the resistive loss in a normal conductor under the same circumstances. Nevertheless, minimisation of the AC loss is technically important because the energy is dissipated as heat in a low temperature environment. The heat has to be removed by a refrigerator that consumes a multiple of the dissipated energy. Therefore it is important to look into the different type of AC losses in the superconductors. AC losses are generated by three mechanism: hysterisis in the superconductor, ohmic loss in the metal matrix when current flows from one superconducting filament to another known as coupling current loss, and ohmic loss in metal sheath enveloping the filaments, that is generated by induced eddy currents, which flow even when there is no transport current in the superconducting filaments [25].

2.3.1 Hysteresis loss

Hysterisis losses are result of magnetic flux moving in and out of a superconductor. When this occurs, an electric field is generated that does work on any flowing currents. They are called hysteresis losses because the flux that entered the superconductor does not leave precisely in the same manner. The electrical energy loss per cycle is proportional to the area of the hysterisis loop, provided that no transport currents are flowing. Such hysteresis losses are eventually dissipated as heat. Hysteresis loss is the main type of AC loss in a Type-II superconductor. As an external magnetic field is applied, flux starts partially penetrating into the bulk of the superconductor, and currents are induced at the surface, much like the skin effect in a copper conductor. There are, however, two differences in this analogy. Firstly, due to the initial state of infinite conductivity, the superconductor exhibits a skin effect even at zero frequency, and secondly, the induced current density has a critical value J_c, which is a decreasing function of the magnetic field at a given temperature, in contrast to the normal skin effect, where the induced current density is proportional to the field amplitude for a fixed frequency.

Figure 2.8 shows the depth of flux penetration into the superconductor (a and b) up to a point where it is completely penetrated (c) where B_a is the applied external field. The

penetration starts from the edges of the superconductor, while the central area is current and flux free. Now, if the field starts to reverse, the flux will not recede in the same way since it is pinned by defects in the material. As a consequence, when the applied field is decreased (d), and the surface electric field changes its direction, a new region with reversed current density is formed at the surface, and starts to propagate inwards as the applied field is further reduced. It is precisely this irreversibility and the flux pinning that cause the hysteresis loss.

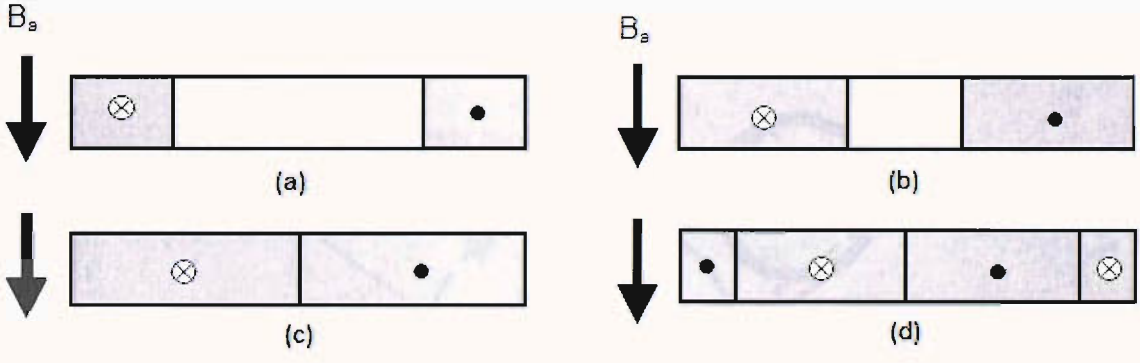

Figure 2.8 Zones of magnetic flux and current penetration into the cross section of Type-II superconductor. The opposite directions of the induced currents are denoted by ⊗ and •.

2.3.2 Eddy current loss

For reasons already explained, HTS are manufactured from fine filaments embedded in normal metal matrix, made of silver. Eddy current loss, which occurs in the silver sheath, is known to contribute negligibly in the low frequency range, and is shown to have an increasing contribution as the frequency goes beyond several hundred hertz. When a sinusoidal AC current is applied to a metal wire, the resulting changing self field has its magnetic flux lines in the form of concentric oval around the conductor in a plane perpendicular to the direction of the current. As a consequence, undesirable voltage is induced in this region of space where changing magnetic field exists.

Eddy current loss is the loss occurring as a result of induced currents in the normal metal matrix by the applied external magnetic field or by the self field of the applied transport current. This loss deserves special attention for HTS applications, since the resistivity of the normal matrix is orders of magnitude higher than the resistivity of the superconducting core, and the undesired flow of eddy currents leads to heat dissipation due the friction and motion of electrons in the metal lattice of the sheath [26]. When a sinusoidal AC current is applied to a metal wire, the resulting changing self field has its magnetic flux lines in the form of concentric ovals around the conductor in a plane perpendicular to the direction of the current.

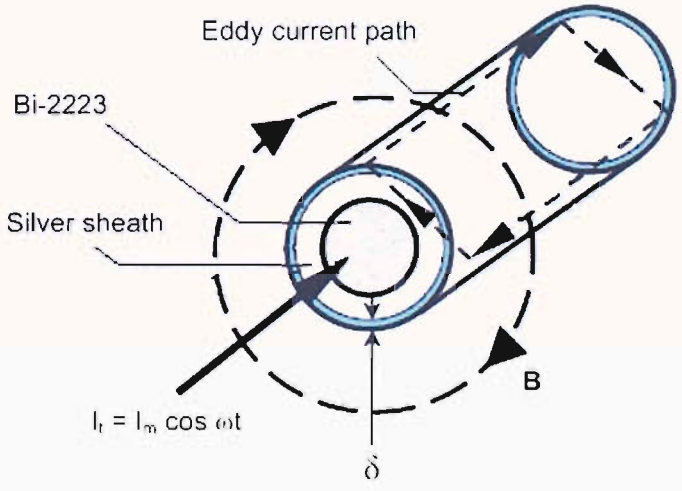

Figure 2.9 Generation of eddy currents in a cylindrical superconductor by the self-field of applied transport current.

Figure 2.9 shows a simplified sketch of a Bi-2223 monocore cylindrical wire, as well as the directions of the applied transport current, I_t and the resulting self field, B. Faraday's law states that a voltage is created or induced in a region of space when there is a changing magnetic field:

$$V = -\frac{d\Phi}{dt} \tag{2.1}$$

where $\Phi = \Phi_m \cos \omega t$ is the magnetic flux around the wire and Φ_m is the maximum flux. The induced voltage also varies sinusoidally with time; following Ohm's law for a driving voltage, V and a finite value of the wire's silver sheath impedance, Z_{Ag}, a current will flow, $I_e = V_e / Z_{Ag}$. These induced currents are known as eddy currents because of their circulatory paths. Eddy currents are closed loops circulating in planes perpendicular to the magnetic flux. The eddy current flow, however, is limited to the area of the inducing magnetic field. The depth of their penetration decreases with the transport current frequency, ω, and is a function of the electrical conductivity, σ, and the relative magnetic permeability of the material, μ_r. This dependence has been termed 'skin effect'. The penetration, or skin depth, is calculated as:

$$\delta = \sqrt{\frac{2}{\omega \sigma \mu_0 \mu_r}} \tag{2.2}$$

2.3.3 Coupling current loss

In a normal conductor an external alternating magnetic field induces eddy currents. A quite a different sort of eddy current is induced in a superconductor consisting of separate filaments embedded in a normal material. The filaments are embedded in a silver (silver alloy) matrix, which is chosen for its good mechanical properties and permeability during the oxidation annealing process. The presence of applied magnetic field induces layers of screening currents in the superconductor, trying to shield the interior from the external field. Inside the filaments the currents flow practically without resistance. In low external fields, the filaments are not coupled such as shown in Fig. 2.10(a). However, when the applied field is strong enough, the coupling between the filaments is complete and the screening currents will cross the silver matrix to form their return paths (see Fig. 2.10(b)).

Coupling between the filaments is highly undesirable for two reasons. First, the magnetisation losses in the superconductor are proportional to the field penetration profile (the shaded triangular area in Fig. 2.10). This area in multifilamentary tapes will

be much larger in the coupled than in the uncoupled case for fields above the full penetration. Secondly, the flow of coupling currents across the metal matrix results in heat dissipation, referred to as coupling current loss.

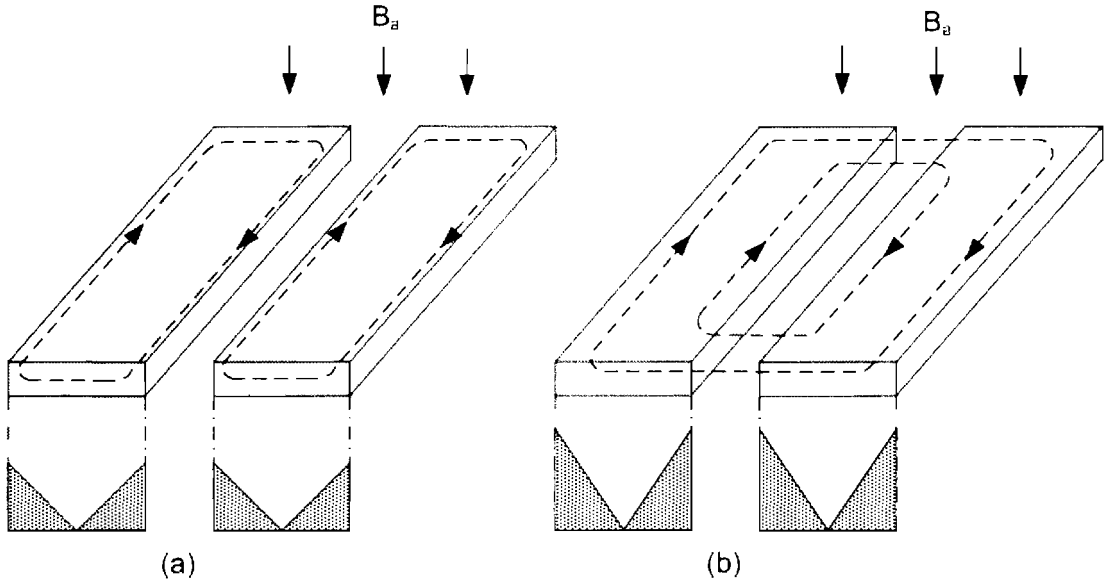

Figure 2.10 (a) Filaments free of coupling effect, and (b) Filaments completely coupled

2.4 Power applications using high temperature superconductors

Although discovered in 1911, the first generation of low temperature superconductors only reached the commercial market in the 1970s; most notably for medical magnetic resonance imaging systems and for use in electromagnets for commercial laboratories and particle accelerators. However, their stringent cooling requirements and high costs inhibited further commercial development for power devices. The discovery of high temperature materials in 1986 reignited interest in superconducting power applications, largely because their higher operating temperature translates into lower cooling costs. The general acceptance of superconducting power equipment by the electric utilities and other end users will ultimately be based on the respective system performance, efficiency, reliability and maintenance, operational lifetime, and installed cost compared

to conventional technologies. Progress has been made steadily in recent years in overcoming technological and manufacturing challenges.

Superconducting electric devices, especially large scale devices for power industry, depend critically on wires with high critical current densities at temperatures where cryogenic losses are tolerable. Compared with the small scale applications, a large scale application generally means that much larger currents and lengths of superconductor are required in a working environment where the magnetic field may be several Teslas. The applications that are actively being pursued are magnets, power transmission cables, fault current limiters, transformers, generators, motors, and magnetic energy storage. Table 2.3 compares various electric power applications with regards to the HTS wire or tape performance requirements for prototyping and eventual commercialisation, as defined by the industry. At present time this restricts the choice to two high temperature cuprate superconductors, $(Bi,Pb)_2Sr_2Ca_2Cu_3O_x$ and $YBa_2Cu_3O_x$ and possibly to magnesium diboride (MgB_2), recently discovered to superconduct at 39K.

Table 2.3 High temperature superconducting applications based on industry's wire performance requirements [27].

	Industry driven device requirement and goals							
	J_c (A/cm^2)	Field (T)	Temp (K)	I_c (A)	Wire length (m)	Strain (%)	Bend radius (m)	Cost ($/kA.m)
Motor (1000 HP)	10^5	2-4	25-77	100-500	1000	0.2-0.3	0.05	10
Generator (100 MVA)	5×10^4	4-5	20-50	500-1000	500-1000	0.2	0.1	10
Fault current limiter	10^4-10^5	0.3-3	40-77	10^3-10^4	1000	0.2	0.1	10-30
SMES (1MWh)	10^5	5-10	20-77	10^4	1000	0.2	1	2-5
Transmission cable	10^4-10^5	Below 0.2	65-77	25-30*	100	0.4	2*	10-100
Transformer	10^4-10^5	0.1	20-77	200-1400	1000	0.2	0.2	10

*Current for individual wire and the bend radius is the cable requirement

The present high cost of HTS conductors is not likely, however, to limit attempts to construct and demonstrate the various applications, which are born out by many

successful tests of electrical power devices. The commercially available composite wire referred to as 'first generation wire' has the production capacity of 100km per year and is expected to increase to 10000 km per year [28]. This is due to broad acceptance of HTS wire solutions and the implementation of more automated processes in advanced manufacturing plants which will produce higher throughput. Furthermore, due to the discovery of much lower cost and improved properties second generation coated conductor technology using yttrium-based superconductor materials, the cost of HTS wires may attain £5 per kAm [28]. From this arose a vision of a new superconducting age where copper or aluminium had been, superconductors now may be considered a good alternative. Superconducting generators would produce electricity, superconducting cables would transmit it, superconducting current limiters would monitor potential faults, and superconducting magnetic energy storage units would manage the power quality. An ideal vision of the superconducting power system is as depicted in Figure 2.11. In the following sections, a general overview and status of some of the most important applications of HTS in power systems are described.

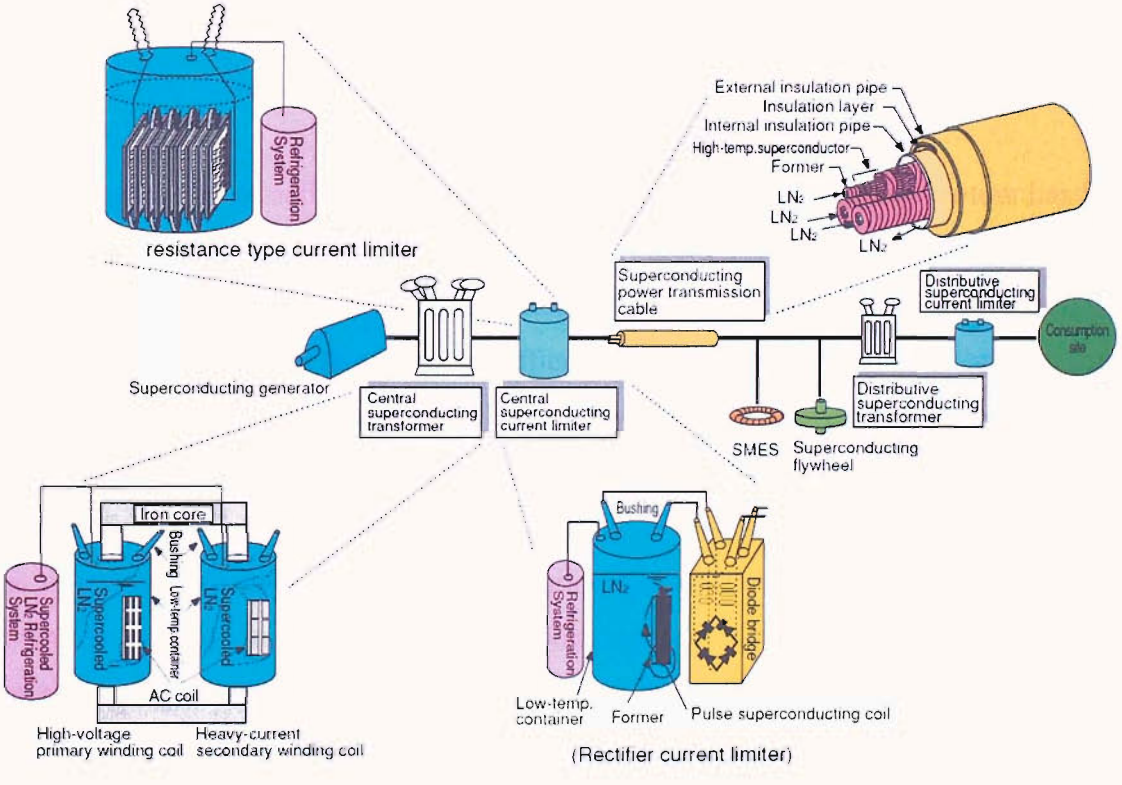

Figure 2.11 Superconductivity in the electric power system of the future [29]

2.4.1 Generators and motors

Magnetic fields in conventional motors and generators are created by large coils of copper or aluminium wire. Since HTS wires have much higher current capacities, it is possible to generate much more powerful magnetic fields in a given volume of space, thus smaller motors and generators can be built. In superconducting motors and generators, usually the field windings are made with HTS conductor material and can be cooled with inexpensive, off-the-shelf cryocoolers available from a number of manufacturers throughout the world.

It is known that industrial electric motors consume most of the electricity used in a typical manufacturing operation; increased efficiency should yield significant savings in power costs. Industrial electric motors consume 70% of the electricity used in a typical manufacturing operation, so increased efficiency yields immediate savings in power costs [30]. Each one percent in efficiency improvement provided by HTS motors would result in huge savings. The most promising applications of HTS motor will be in transportation applications particularly for naval and commercial ship electric propulsion, where critical size and weight savings will provide a key benefit by increasing ship design flexibility [31, 32].

Up to date, the most active and extensive research of superconducting motors has been the United States. American Superconductor Corporation (AMSC) has built and tested a 5000 HP, 1800 rpm superconducting motor for industrial market. The HTS motor cuts losses in half compared to an energy efficient AC induction motor and has an active volume that is 55% of conventional [33]. They have also developed a design for a 5 MW HTS model motor for ship propulsion; this motor demonstrates technologies to be employed in a full size 25 MW, 120 rpm low speed HTS motor [34]. Figure 2.12 shows the overview diagram of the motor. The model motor will be scheduled for rigorous testing to evaluate its capability using a dynamometer controlled by a real time digital simulator. The results will be used as guidelines for the 36.5 MW motor under the £40 million navy contract. Elsewhere in Europe, Siemens has built a synchronous machine consisting of an HTS rotor and an air-cored stator [35]. The machine was designed for a

rated power of 380 kW, but test results show that it achieved a maximum continuous power of 450 kW and a short term maximum power of 590 kW at 1500 rpm. In all cases, output power was limited by stator cooling.

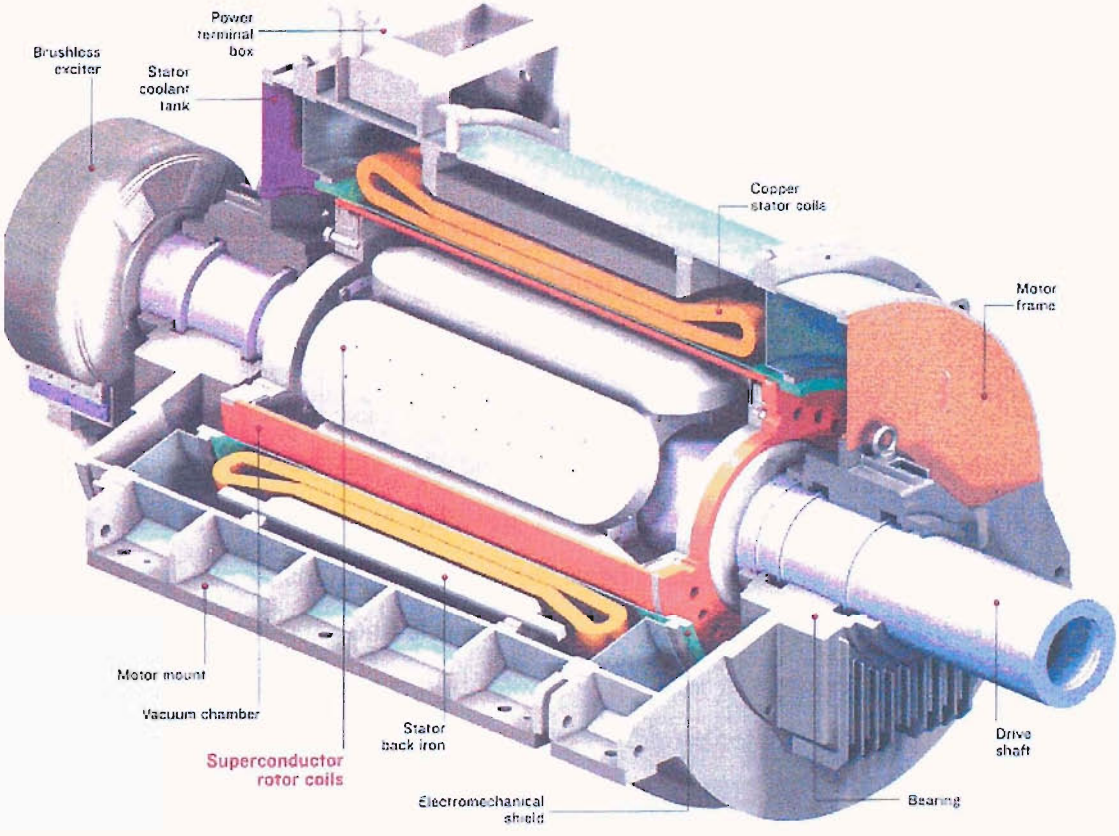

Figure 2.12 Cutaway view of the 5 MW superconducting motor built for US Navy [36]

Another major opportunity for the use of HTS in electrical machines is in generators. Like motors, superconducting generators can be designed to have lower losses and maximised efficiency; because of their smaller size, they can have lower synchronous reactance, which is helpful for voltage regulation and stability. Generators are at the high end of the megawatt ratings of rotating machinery. Hence, they are also one of the most favourable opportunities for HTS application, and design work in these areas is actively underway. Recently, General Electric has received a large funding from the Department of Energy, United States to design and develop a 100 MVA superconducting generator [37]. The proposed program will include the production and

testing of a 1.5 MVA proof-of-concept model for the rotor, cryorefrigeration and HTS subsystems. Those results will be scaled to a 100 MVA prototype generator that will be fully tested under load. In Japan one of the longest running and most extensive projects known as Super-GM (Engineering Research Association for Superconductive Generation Equipment and Materials) has been ongoing since 1988 [38-40]. The goal for Super-GM was the design, construction, and test verification of three types of 70 MW class superconducting generator model machines for establishing technologies to design and manufacture a 200 MW class pilot machine suitable for commercialisation. The project is in its second phase which aims to improve output density and enhance the generator capacity base on the results obtained from previous tests [41].

2.4.2 Transformers

Transformers represent one of the oldest and most mature elements in a power transmission and distribution network. A key advantage of HTS transformers is the capability to work continuously in overload conditions without any lifetime loss because of the ultra cold operating range of 20 K to 77 K, even if this is done at the expense of increased used of liquid nitrogen. Another advantage is the reduction in size and weight, which can go down to 30-50% of the values for conventional transformers [42]. Moreover, in the HTS transformers the only substance present in large volume is non-flammable and environmentally benign liquid nitrogen.

During operation, a transformer heats up and this heat must be dissipated. In conventional transformers, this is achieved by immersing the coils in oil, which also serves to insulate them electrically. The hot oil conducts the heat away from the coils and prevents the transformer from overheating. In a HTS transformer, some heating also occurs and the cryogenic fluid conducts this heat away from the coils. Usually in a HTS transformer, only the coils operate at cryogenic temperature whereas the core operates at a temperature somewhat above ambient. This approach avoids the penalty of removing heat generated by core losses at cryogenic temperature.

The first major transformer prototype was a 630 kVA built by ABB and operated to power a building in Geneva for a year, beginning 1997 [4]. It is a 3-phase transformer with an output of 630 kVA and was designed to convert power from 18.7 kV to 420 V. Currently, there are several ongoing projects for HTS transformers. Siemens is building a 1 MVA transformer in Germany and has started a program for development of onboard transformers for electric rail vehicles [44]. Meanwhile, in 1999, a small 10kVA HTS transformer demonstrator, built and tested at Southampton University demonstrated that the unit had exceeded design expectations and behaved consistently well throughout the duration of the tests without any deterioration of performance [1]. The development of HTS transformers continues. A project, lead by Waukesha Electric Systems in the United States, is currently looking at a 5/10 MVA transformer, whose operational tests were scheduled for 2003, with plans for scaling up to 30/60 MVA units [45].

2.4.3 Fault current limiters

Fault current limiters (FCL) using high temperature superconductors offer a solution to controlling fault current levels on utility distribution and transmission networks. These fault current limiters, unlike reactors or high impedance transformers, will limit fault currents without adding impedance to the circuit during normal operation. Superconductors offer a way to break through system design constraints by presenting impedance to the electrical system that varies depending on operating conditions. Superconducting FCL normally operate with very low impedance, hence they are invisible components in the electrical system. In the event of a fault, the limiter inserts impedance into the circuit and limits the fault current [46].

Development of superconducting fault current limiters is actively being pursued by several utilities and electrical manufacturers around the world, and commercial equipment is likely to be available soon. So far the biggest HTS demonstrator is a 1.2 MW, 3-phase FCL made by ABB, which was tested for one year in a Swiss power plant without major problems [47]. ABB also recently announced the development of a 6.4 MVA fault current limiter which will be one of the most powerful in the world [48]. In

United States Department of Energy has awarded a £6.7 million contract to Superpower (subsidiary of Intermagnetics General Corp) to built a fault current limiter. With a voltage of 138 kV this is expected to be the first FCL worldwide for the transmission level, culminating with the installation of the HTS FCL in a utility substation by 2006 [49]. In United Kingdom, a new project is lead by Rolls-Royce to create a new kind of superconducting self resetting solid state fuse also known as 'superconducting fault current limiter' and this project is supported by Department of Trade and Industry (DTI) under the LINK programme.

2.4.4 Transmission cables

In HTS power transmission cables, conventional conductor wire of copper or aluminium is replaced by HTS wire, enabling the cable to carry greater amounts of current with lower resistive losses and reduction of size up to 50% [50]. Moreover, the motivation for developing HTS power transmission cables comes primarily from the need to increase the power handling capabilities of existing underground circuits. Successful application of HTS conductors to transmission cables would allow the use of underground HTS cables for the replacement of overhead lines. HTS cables not only offer more power per circuit, they also provide an environmentally attractive solution, because a leak in an underground HTS system would cause a benign release of nitrogen, whereas a leak in existing oil filled high voltage cables could result in devastating soil contamination. Where oil filled cables are used underwater, such leaks could produce even greater environmental damage. HTS cables use one of two designs: cold dielectric (coaxial and concentric) or warm dielectric [51]. The designs offer distinct advantages that make one type of cable preferable over the other for particular applications.

Figure 2.13 shows the warm dielectric cable, which carries only one phase of current and is relatively simple in design [52]. At its core is a duct through which the cryogenic medium flows. The duct is surrounded by the HTS wire, which is insulated with a dielectric sleeve and over the dielectric is a protective sheath. The whole assembly fits into a pipe or duct. The main advantage of the warm dielectric cable is that its impedance matches that of a conventional cable of similar diameter. With the same

impedance as the cable it replaces, the warm dielectric cable will not affect the flow of power through other cables. Hence, such a warm dielectric cable can easily substitute for a conventional cable in a retrofit. The simpler design of the warm dielectric cable compared with the cold dielectric cable also translates into a lower cost. In Detroit, three warm dielectric HTS cables built by Pirelli using HTS material from AMSC, each carrying 2,400 A at 24 kV, are used to replace nine traditional copper lines in Detroit Edison's Frisbie substation [53].

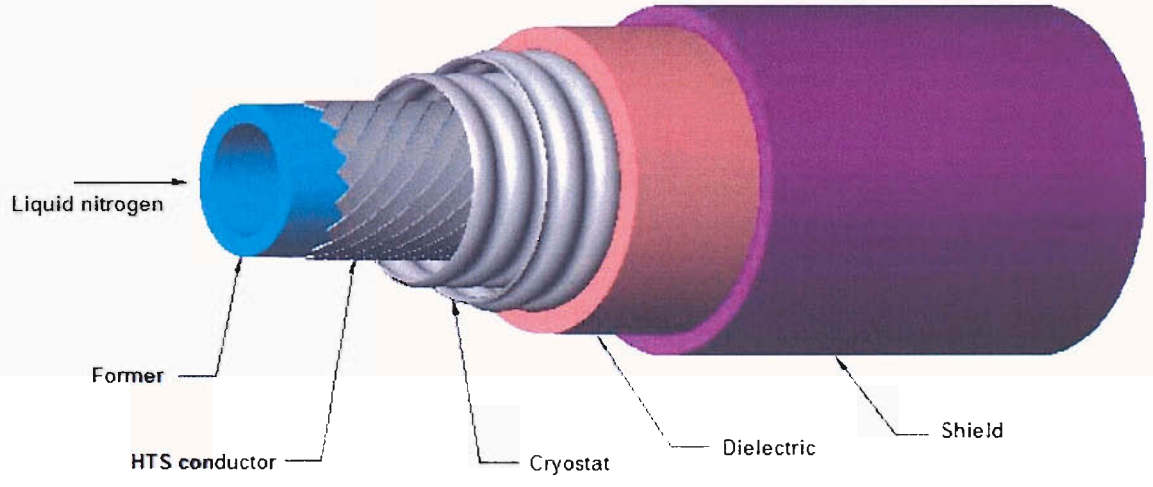

Figure 2.13 Warm dielectric HTS cable

The cold dielectric cable can be configured in different ways, depending on how many layers are concentric and depending on where the cryogen flows. The design consists of a central cryogen duct surrounded by a support and the HTS wire as shown in Fig. 2.14 [77]. A dielectric separates the inner conductor that carries the current from an outer HTS sleeve that acts as a return and shields the inner conductor from external magnetic fields. Because the three phases are adequately shielded from one another, they can fit together in a common cryostat where they are bathed in a cryogen bath. The lifetime operational costs are lower than those of a warm dielectric design, but the initial investment cost is higher because more HTS tapes are needed for the return conductor. Southwire has built three 30 m, single-phase HTS cables rated 12.4 kV, 1250 A based

on cold dielectric coaxial conductor design. They have been operated for more than three years and the cables have provided good reliability and service [52].

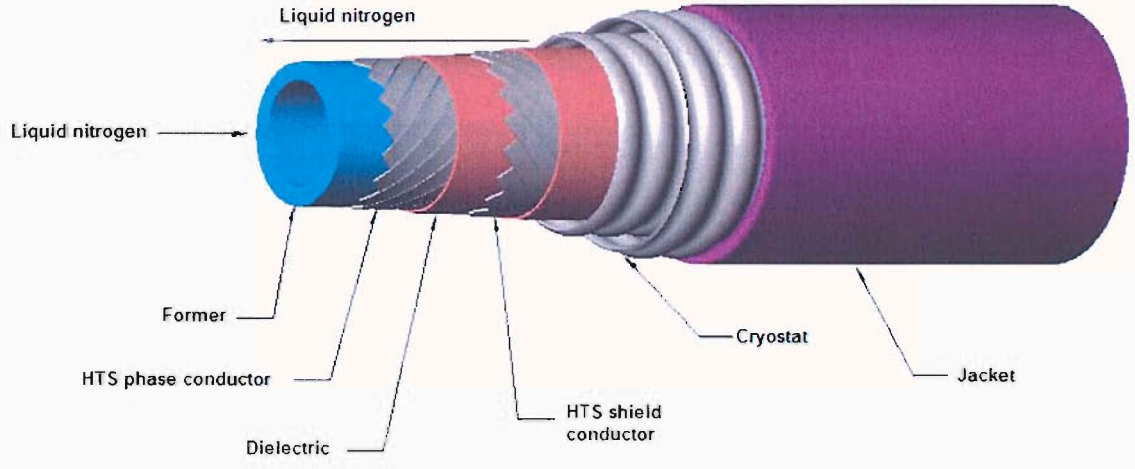

Figure 2.14 Cold dielectric HTS cable

The major organisations that are actively involved in research and development of power transmission cables using high temperature superconductors are: Economic Policy Research Institute (EPRI), International General Corporation (IGC), Oakridge National Laboratory, Department of Energy (DOE), American Electric Power (AEP), Ultera, Pirelli and Southwire Corporation in the United States; Siemens, Pirelli, Ente Nazionale per l'Energia Elettrica (ENEL) and Edison in Europe; and Sumitomo Electric Corporation, and Tokyo Electric Company in Japan [54]. Most of the major corporations manufactures their own HTS tapes, and mostly all experimental and prototype HTS cables have been manufactured with multifilamentary tape containing the Bi-2223 compound. Currently, the highest current HTS cable project is the Bixby Substation 13.2 kV, 3000 A base on Triaxial design [55]. A new Triaxial conductor design places all three phase conductors concentric around a common central core. Hence, the cross sectional area is only slightly larger than that of a single phase in a traditional HTS cable design. This concept reduces the quantity of HTS wire needed, and the cold surface area, thereby reducing cooling requirements. Table 2.4 summarises some of the ongoing and already completed projects of HTS power cable [56].

Table 2.4 HTS cable demonstrations and tests projects

Participants	Voltage (kV)	Current (kA)	Cable length (m)
EPRI Pirelli, DOE	115	2	50
DOE, IGC, Southwire	12	1.25	5
Tokyo Electric Company, Sumitomo	66	1	30
Electricité de France, Pirelli	225	3	50
NKT Cables, Nordic Superconductor Tech , Danmarks Tekniske University	60	2	30
ENEL SpA, Pirelli, Edison SpA	132	3	30
EPRI, Pirelli, DOE, Detroit Edison	24	2.4	120
Southwire, DOE, Oakridge National Lab	12.4	1.25	30
Ultera, AEP	13.2	3	200*

*Target length

2.4.5 Magnetic energy storage devices

Superconducting energy storage systems have significant advantages over conventional power quality equipment, such as uninterruptible power supplies, batteries and diesel generators. Some of the advantages are reduced environmental impact, low maintenance and operation costs, small size and weight, increased safety and reliability. In general, there are two technologies that are currently under development: one based on flywheels and the other on magnetic fields. Flywheel energy storage devices are based on rotating discs that float on superconducting magnets and store energy in their spinning motion. Passive superconducting bearings integrated into the disc module are used for frictionless levitation. Once charged, these discs will spin almost indefinitely, without losing any of their energy due to complete lack of friction. Figure 2.15 shows the outline diagram of the flywheel system with integrated superconducting bearing. Superconducting magnetic bearings are a promising extension of magnetic bearing technologies. Stable levitation can be obtained without any electronic feedback control system due to their inherent stability. Other benefits of this design are increased load capacities, compact dimensions and the ability to suspend machine parts at ambient temperatures. By using permanent magnets for the field excitation system, superconducting magnetic bearing are total passive systems [57].

Another type of energy storage is known as superconducting magnetic energy storage (SMES); it is a device for storing and instantaneously discharging large quantities of power. It stores energy in the magnetic field created by the flow of DC in a coil of superconducting material that has been cryogenically cooled. The SMES recharges within minutes and can repeat the charge or discharge sequence thousands of times without any degradation of the magnet. The main application areas of superconducting magnetic energy storage (SMES) are focused on issues related to power quality and custom power. Power quality applications refer to the solutions where the energy storage capacity is used to mitigate the effect of momentary loss of power or possible voltage drops. Custom power refers to storage applications where a small amount of load levelling is used to smooth out power requirements.

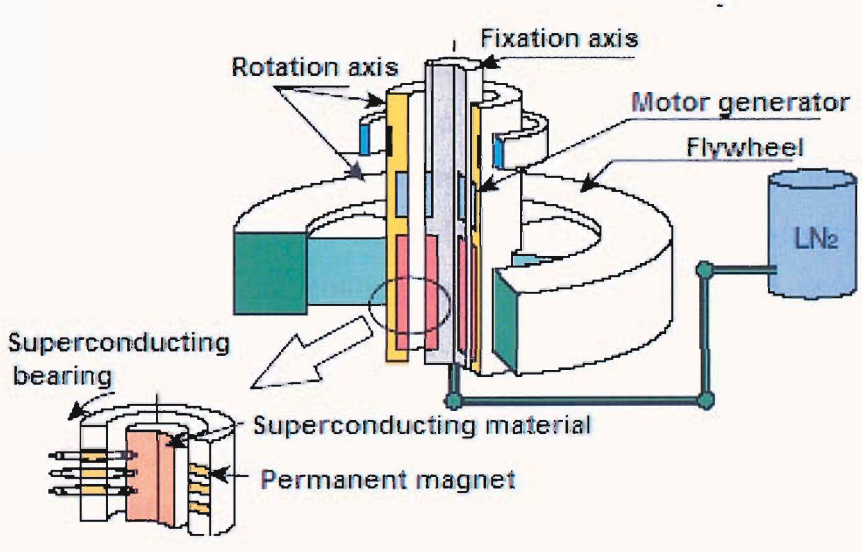

Figure 2.15 Flywheel system and details of superconducting magnetic bearing assembly

In Germany, an interesting large scale high temperature SMES project has been designed and is being built by ACCEL Instruments in cooperation with the German companies AEG SVS GmbH, and EUS GmbH, and the utility company E.ON Bayern AG [58]. It is designed to operate at 77 K using 20 km of Bi-2223 tape and capable to deliver 150 kJ of energy. The SMES will be integrated in a 20 kVA uninterruptible power supply system coupled to the electrical grid for enhancing the power quality of a

selected grid user. Meanwhile, the latest 10 kWh flywheel system prototype incorporating HTS bearings is being developed by Boeing and Argonne National Laboratory [59, 60]. The HTS bearing designed for the 10 kWh system employs YBCO tiles and operates at 77 K which enables the flywheel to rotate at 20000 rpm.

2.5 Challenges for full scale industrial applications

Many challenges to commercialising high temperature wire for electric power applications involve materials issues. The main obstacle is that all of the high temperature compounds under consideration are brittle in bulk form. This brittleness makes it difficult to manufacture them into wire, which must be wound in a variety of shapes without loss of the wire's critical current density. In polycrystalline form, most high temperature compounds demonstrate 'weak links' at grain boundaries, which significantly limit current carrying capacity. Increasing the critical current density of long length wires is the key to commercial electric power applications. Another difficulty is that as current flows through a high temperature material, it generates a magnetic field, which forms vortices of current inside the material that must be pinned. The ultimate limiting factor is cost; materials for high temperature wire are expensive, as are the manufacturing and cooling costs. For the successful development of applications using high temperature wire, the cost of the wire along with total equipment costs and performance needs to be competitive with existing technologies.

2.5.1 Development of superconductivity market

There are a few different studies available, which assess the potential of the market for superconducting devices, for example the reports of the Consortium of European Companies Determined to use Superconductivity, Conectus [61] and Oak Ridge National Laboratory [62]. The estimates for the worldwide market for superconductor applications, recently made by Conectus, are shown in Fig. 2.16. These figures are rather conservative in comparison to the other reports, made mainly by United States institutions. As can be seen, almost all of the present commercial superconducting products still use LTS materials, which have well established applications, mainly for

magnet technology ranging from small magnets for laboratory purposes to high power magnets used in particle physics. The largest share of the LTS market is taken by magnets for advanced medical diagnosis like magnetic resonance imaging equipment.

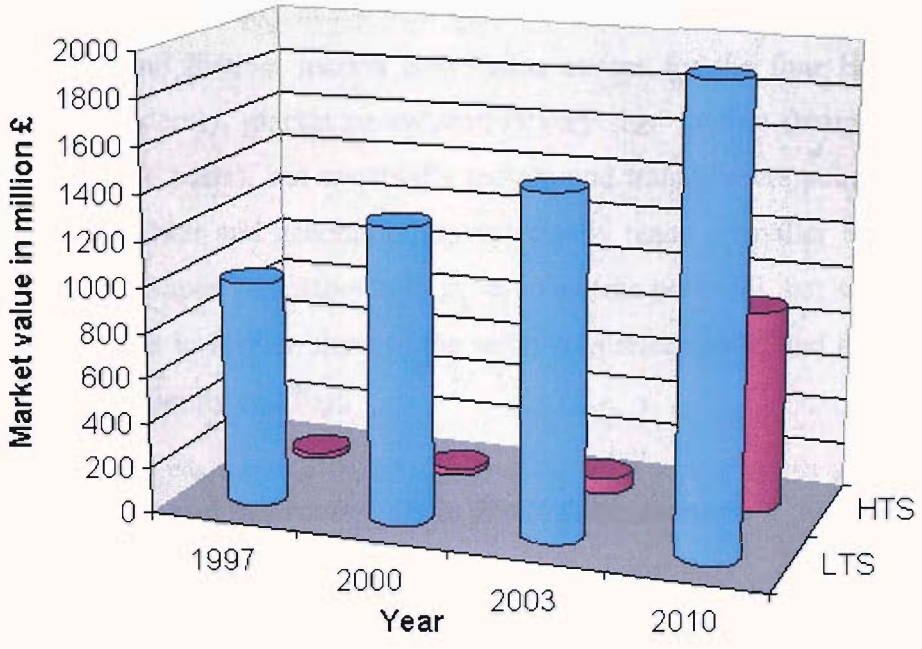

Figure 2.16 Worldwide markets of superconductor applications.

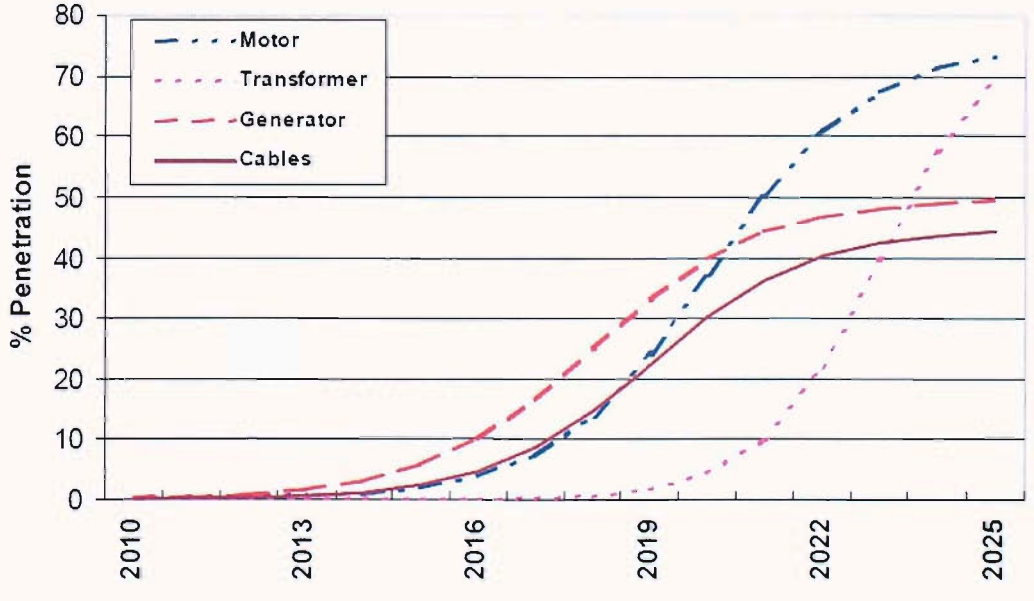

Figure 2.17 Market penetration of HTS power devices

A boom of the utilisation of HTS in different areas, such as electric power systems, industrial processing, transportation, medical and magnet technology, communication and information systems, and electronics, is expected in the second half of this decade, so that the worldwide market of HTS would reach an estimated £1 billion by 2010 and would increase exponentially in the next decade, reaching £23 billion by 2020. Figure 2.17 shows the four distinct market penetration curves for the four HTS devices in United States. Evidently, market penetration is very slow at first (mainly due to wire costs and cryogenic costs), but eventually motors and transformers penetrate to nearly the same levels; cables and generators asymptotically reach a smaller fraction of their available markets. Superconductors hold great economic potential, but sustained efforts are required in order to further increase the technical performance, and in order to bring down process complexity and cost.

2.5.2 Advancement and improvements in BSCCO conductors

2.5.2.1 Cost reduction

The economic viability of Bi-2223 conductors is a very important factor taken into consideration by the end users. Currently, the manufacturing cost of silver sheath Bi-2223 tapes is £80-250 per kAm. With large scale tape manufacturing and an increase of critical current, this cost can be reduced to £20-£30 per kAm. Around 50% of the manufacturing cost is attributable to the sliver (silver alloy) matrix, so by replacing, say, 50% of the silver with a cheaper metal or alloy, the cost could be reduced further. For acceptable device application cost, the manufacturing cost of a Bi-2223 conductor must be reduced by a factor of 10-15, so that the sale price amounts possibly to £10-15 per kAm, in order to compete with the current prices of copper wire, which are around £10-20 per kAm [63]. Furthermore, for full utilisation of the potential of Bi-2223, various improvements must be achieved in the next few years along with the development of reliable and inexpensive cryogenic systems.

2.5.2.2 Critical currents

The term critical current is defined as follows: Given the critical current I_c, the critical current density J_c is obtained after dividing I_c by the cross section of the superconductor, while the engineering critical current density J_e is equal to I_c divided by the cross section of the entire conductor. For any application, high I_c and J_e values in long length conductors are required. The best Bi-2223 tapes available in lengths of a few hundred meters are manufactured by American Superconductor with I_c = 100-135 A, J_c = 300-400 A/mm^2 and J_e = 120-150 A/mm^2. Short length tapes have been made also by AMSC with J_c = 800 A/mm^2 with special geometry using thin filaments and thick matrix. The best one km tape was made by Nordic Superconductor Technologies (NST) with J_c = 230 A/mm^2. The potential of Bi-2223 has been demonstrated by high J_c values on short length tapes and by the J_c values of thin Bi-2223 films being a factor of 10-100 higher. Unfortunately, cracks and other macroscopic defects appear in the manufacturing process of long-length tapes and limit their performance. Furthermore, for the need of AC reduction, multifilamentary tapes (almost exclusively manufactured nowadays) must be twisted, which results in additional decrease of J_c. For the successful implementation of large scale applications with Bi-2223 conductors, the competitive J_c values at 77 K must be in the range 500-800 A/mm^2 and I_c must be 200-300 A [64].

2.5.2.3 Mechanical strength

Bi-2223 as a ceramic material is hard and brittle. It may well withstand high pressure but has low strength in bending, twisting and tension. Improvements are required in the manufacturing process so as to keep the strain on the tape as low as possible. A considerable decrease in the I_c of the tapes results when bending with radius below the critical one is applied. A low critical bending radius, which is now around 25-30 mm for tapes manufactured by NST and 35-50 mm for tapes manufactured by AMSC may be useful considering, for example, that retrofitting in the existing underground cable ducts may lead to sharp curvatures in some places. The maximum values of the strain and stress Bi-2223 conductors can support may be increased up to a factor of two by special mechanical reinforcement. The superconducting tape used in the field winding of the

Southampton's 100kVA HTS synchronous generator project was supplied by AMSC and it is reinforced with a layer of stainless steel material. Further details of the tape including properties will be discussed in the next chapter.

2.5.2.4 AC losses

The aspect of AC loss reduction is another key issue for improving the function to cost ratio of Bi-2223 conductors. The removal of every single watt of cold power dissipated in superconducting applications may cost too high to the utilities. It is, therefore, essential to obtain as low AC losses as possible, especially in magnetic field applications, in which the magnetisation losses are much higher than transport current losses. It is difficult to quantify the desired AC reduction in Bi-2223 conductors. There is no much room for AC reduction in transport current applications, where a decrease of 30-40% would be welcome, while in magnetic field applications there is a need of greater AC loss reduction [65].

2.5.3 Cryogenic technology

Historically, a major impediment to the commercialisation of LTS technology has been the cooling of the superconductors. In most cases, the cooling technology greatly influences user perception of the superconductor product, in particular its reliability and ease of use. Except for certain high value added applications, potential users deplore the requirement to transfer liquid cryogen periodically. HTS suffer from the same requirement of low maintenance for commercial acceptability. The eventual widespread introduction of HTS into power applications will require reliable closed cycle refrigeration systems. Both two stage Gifford-McMahon (GM) and pulse tube cryocoolers are reliable, with many hours of maintenance free operation. The reliability of the GM machines is due primarily to the use of commercial air conditioning compressors. The compressor can be remote from the cold head by several meters of flexible pressure lines. At liquid nitrogen temperatures, GM machines are usually used for 10W to 200W cooling requirements. Pulse tube refrigerators are a newer technology and have the advantage of no moving parts in the cold head, leading to reduced

vibrations. Therefore, no expensive high precision seals are required and the cold head can be operated without any service inspection. They are commonly available for 10W cooling capacities, and their size is increasing as the technology improves. Improving the understanding and performance of pulse tube cryocoolers is one of the most active fields of research today in cryogenic technology. Several such coolers have been developed to achieve high reliability and low weight. One of which is designed by TRW Incorporated; 1.5 W of cooling at 115 K, requires 38.2 W of input power, and weighs only 2.3 kg, not including the control electronics [66]. This is an example of the potential of cryocoolers – particularly pulse tubes – that will make it easier to incorporate cryocoolers in a variety of future superconducting power applications.

SUPERCONDUCTING GENERATOR

Superconducting electrical devices, particularly rotating machines have been actively studied since early seventies to meet the rapid growth of electrical demand. The application of superconductors in generator (or motor) windings overcomes the major factor limiting both output capability and efficiency, namely, the ohmic losses. Moreover, better performances in terms of volume and mass power densities bring the possibility of building superconducting generators with higher ratings than may be achieved with conventional technology. However, earlier prototypes suffered the costs and technical complications of low temperature cooling using liquid helium. Notwithstanding, the longest and biggest surviving government sponsored project 70 MW-class superconducting generator known as Super-GM operates in the 'low temperature' regime. Super-GM emphasis on the major advantages of SC generators was related to performance in power systems specifically with respect to steady state and transient stability, improved reactive power capability, and improved ability to tolerate negative sequence fields [67]. There are many others superconducting generator projects that are actively pursued by different organisations throughout the world. The generators are constructed following various design or configurations, but ultimately aim to achieve the same goal: a more powerful, efficient, compact and stable machine compared to its conventional counterpart. Southampton's 100 kVA superconducting synchronous generator was built to demonstrate the feasibility of 'true' high temperature operation at 77 K. In this chapter, the overall generator construction is discussed. Section 3.1 introduces the basic features of generator and the benefits of employing superconductors. The superconducting generator characteristics and constructional features are also discussed. Section 3.2 highlights the major components of the Southampton's design, in particular the superconducting field winding and rotor.

3.1 Introduction

The market for generators encompasses many shapes and sizes, from small, portable equipment in the 1 kW range, up to large, stationary sized equipment used in base load nuclear plants, in the GW range. However, the adoption of superconductors in generators will become beneficial mainly in large scale devices due to the complexity and cost of the refrigeration equipment, and the challenging nature of thermal insulation systems. Therefore, better understanding of the generator is imperative in order to demonstrate the capability of superconducting technology. In the next section, the basic operation principles of the generator will be highlighted. The benefits and common constructional features of superconducting generators are also discussed.

3.1.1 Principle of operation and constructional features

Electric generators are devices that convert mechanical energy into an electrical energy. This process, known as electromechanical energy conversion, involves magnetic fields that act as an intermediate medium. The fundamental law for all rotating electric machines is associated with Faraday's law, which describes the electromagnetic energy conversion related to mechanical movement. In brief, if a coil (or winding) is linked to a varying magnetic field, then an electromotive force (EMF), or voltage is induced across the coil. Thus, generators have two essential parts: one creates a magnetic field and the other where the EMFs are induced. The magnetic field is typically generated by electromagnets, whose windings are referred to as field windings or field circuits. The coils where the EMFs are induced are called armature windings or armature circuits. One of these two components is stationary, and the other is a rotational part driven by an external torque. Conceptually, it is immaterial which of the two components is to rotate because, in either case, the armature circuits always experience a varying magnetic field. However, practical considerations lead to the common design that for AC generators, the field windings are mounted on the rotor and the armature windings on the stator. In contrast, for DC generators, the field windings are on the stator and armature on the rotor.

AC generators are considered either brush or brushless, based on the method used to transfer DC exciting current to the generator field. In addition, AC generators are classified as salient pole or non-salient pole (cylindrical). Figure 3.1 shows a typical salient pole and cylindrical synchronous machine constructions. An AC generator needs a separate DC source to feed the magnetic field. The required DC is provided by an external source called an exciter. Usually, the exciter is a small DC generator that is driven by the generator rotor. The exciter may be mounted on the rotor shaft or rotated by belt-drive. In some cases the generating systems use a static, solid-state exciter to provide DC. A voltage regulator controls the induced voltage by regulating the strength of the EM field established by the exciter. Frequency is controlled by the speed at which the prime mover rotates the rotor. In addition, AC generators are classified as single-phase or polyphase. A single-phase generator generates AC power at a specific utilisation voltage and they are usually used in smaller systems. Polyphase generators produce two or more alternating voltages usually two, three, or six phases. Two-phase power is used in only a few localities and six-phase is primarily used for operation of rotary converters or large rectifiers. Three-phase alternators are the most widely used for power production.

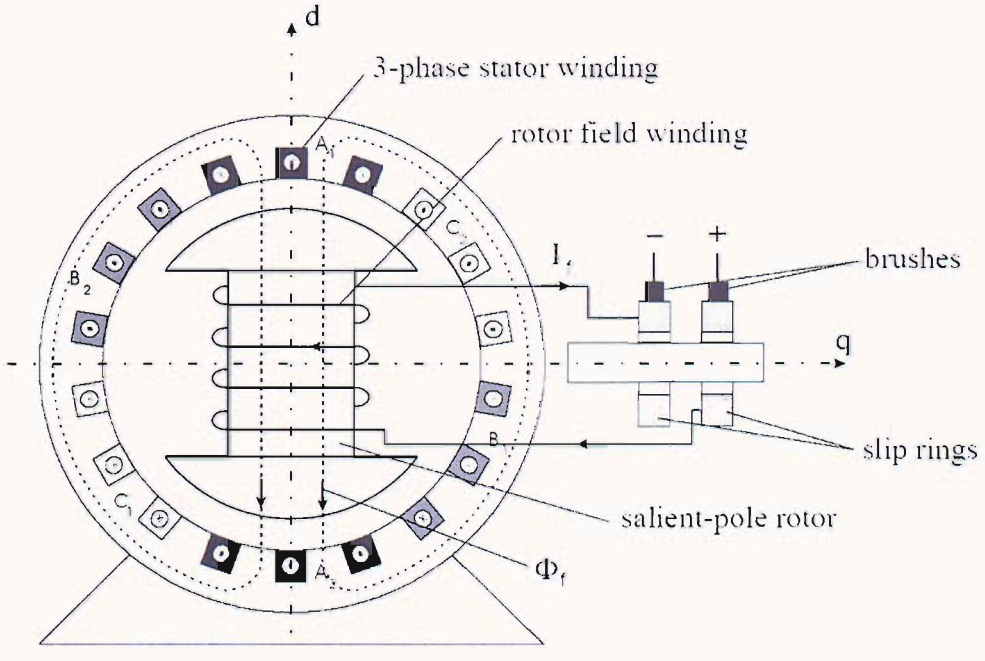

(a)

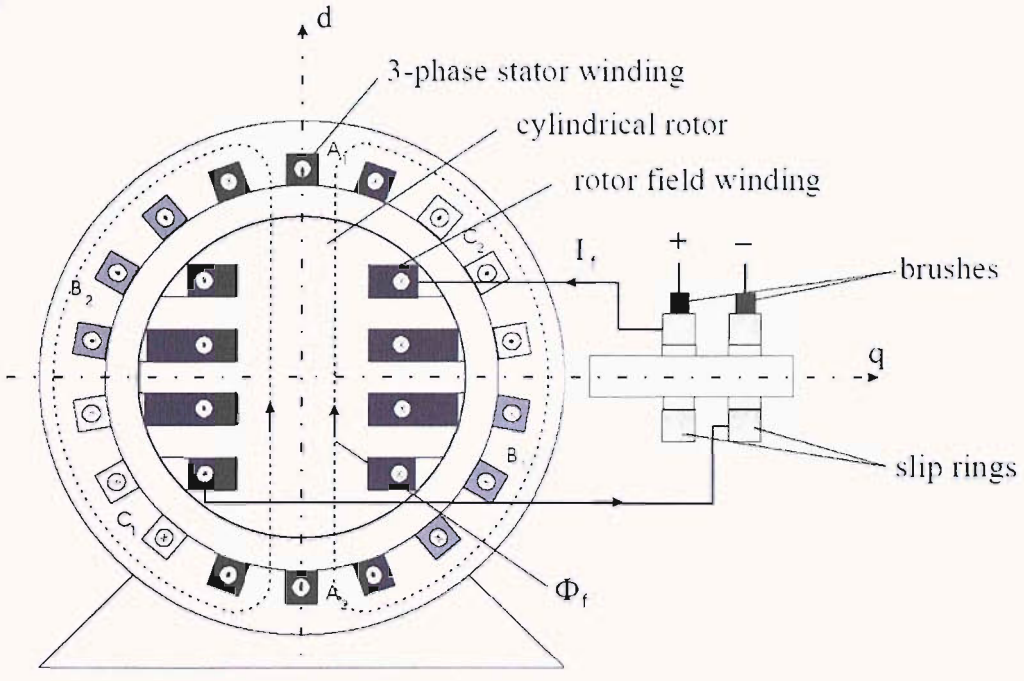

(b)

Figure 3.1 Construction scheme of synchronous machine with: (a) salient pole rotor, and (b) cylindrical rotor

It is well known that AC generators that operate at a speed that is exactly proportional to the frequency of the output voltage are synchronous generators. Currently, this type of generator is widely used in most electric power. Synchronous generators rotate at a constant speed, called synchronous speed; this speed is dictated by the operating frequency of the system and the machine structure. In a synchronous generator, the rotor consists of a winding wrapped around a steel body. A DC current is made to flow in the field winding, and this results in a magnetic field. When the rotor is made to rotate at a constant speed, the three stationary windings experience a periodically varying magnetic field. Thus, EMF is induced across these windings. This EMF is AC and periodic; each period corresponds to one revolution of the rotor. Thus, for a 2-pole operating at 50Hz electricity, the rotor has to rotate at 3000 rpm; this is the synchronous speed of the given machine. Because the windings are displaced equally in space from each other by 120 degrees, the EMF waveform is displaced in time by 1/3 of a period. The machine is therefore capable of generating three-phase electricity. When the stator

windings are connected to an external electrical system to form a closed circuit, the steady-state currents in these windings are also periodic. These currents create magnetic fields of their own. Each of these fields is pulsating with time because the associated current is AC; however, the combination of the three fields is a revolving field. This revolving field arises from the space displacements of the windings and the phase differences of their currents. In summary, for a loaded synchronous generator operating in a steady state, there are two fields rotating at the same speed: one is due to the rotor winding and the other due to the stator windings. Hence, the armature circuits are in fact exposed to two rotating fields, one of which, the armature field, is caused by and in fact tends to counter the effect of the other, the rotor field. The result is that the induced EMF in the armature can be reduced when compared with an unloaded machine (open-circuited stator windings). This phenomenon is referred to as armature reaction. The EMF induced in a stator winding completes one period for every pair of north and south poles sweeping by; thus, each revolution of the rotor corresponds to two periods of the stator EMFs [68].

3.1.2 Why superconducting?

Superconducting generators for utility applications have been studied throughout the world since 1970s to evaluate the technical and economic potential of generators using superconducting windings. These programs have ranged from demonstration of technical feasibility with small generators up to more powerful machines as large as few hundred megawatts. This is because a superconducting generator has the greatest potential for large scale commercial application of superconductivity. Such a machine should be able to convert mechanical energy to electric energy more efficiently and with greater economy of weight and volume than any other method. There are at least four methods by which superconducting generators can substantially improve electric power systems [69].

- They could greatly reduce both the capital and operating costs.
- They could increase grid stability.

- They could be used for volt-ampere-reactive (VAR) generation.
- They are smaller and lighter

Voltage is induced and power is produced as the magnetic field lines of a rotating rotor periodically cut the stator windings. A conventional generator with iron teeth has a magnetic field of around 1T at its surface. This may be understood from the fact that the conductor slot width is approximately equal to the tooth width, since iron saturates at about 2T [70]. Therefore, a conventional generator operates between the limits of field saturation at the rotor and at the stator. However, superconducting rotor fields could be up to approximately 5T, greatly exceeding the saturation field of iron. This might eliminate the use of iron in the stator and also reduces insulation requirements, thus giving more flexible usage of space and materials.

Although the actual cost of an AC generator is relatively insignificant compared with the cost of a power plant, it may be considered to be pivotal element of the plant. Conventional generators are approximately 99% efficient, an increase of 0.5% to 99.5% efficiency, made possible by superconducting generators, is equivalent to a much more impressive 50% reduction in losses. Since superconducting generators are significantly smaller than conventional generators, there are substantial savings in construction, financing and operating costs. Table 3.1 make a comparison between conventional and possible superconducting 1200 MVA generators. The reason that superconducting generators are significantly smaller than conventional ones of the same power output is because the power density of a generator is approximately proportional to the square of the magnetic excitation field.

The potential for increased AC system stability afforded by a superconducting generator is also of great importance. When a system is perturbed electrically or mechanically, the resulting transient is oscillatory. If the oscillations damp out to the original or a new steady state operating condition, the system is stable, otherwise it is unstable. In general, the generators' stability improves with lower reactances. The per unit synchronous reactance of a superconducting generator is about one quarter that of a conventional

generator of similar rating; this results in an increased steady state stability limit of the superconducting machine by as much as a factor of four when the transmission line reactance is relative small. The full description and calculations of the HTS synchronous generator reactances are discussed in Chapter 5.

Table 3.1 Comparison of conventional and possible superconducting 1200 MVA generator characteristics [71]

Properties	Superconducting Generator	Conventional Generator
Phase-to-phase voltage (kV)	26-500	26
Line current (kA)	27-14	27
Active length (m)	2 5-3 5	6-7
Total length (m)	10-12	17-20
Stator outer diameter (m)	2 6	2.7
Rotor diameter (m)	1	1
Rotor length (m)	4	8-10
Field exciter power (kW)	6	5000
Generator weight (kg)	160000-300000	600000-700000
Total losses (MW)	5-7	10-15
Field strength (T)	5 T	2 T

A superconducting generator can also be operated as synchronous condenser to adjust the reactance of a line, known VAR generation. Static VAR generators introduce undesirable harmonics into the system unless there is sufficient filtering. A superconducting synchronous condenser, also better known as dynamic superconducting condenser, would only introduce negligible harmonics. The dynamic superconducting condenser's voltage regulation systems detect and instantaneously compensate for voltage disturbances by injecting leading or lagging reactive power, measured in VARs, precisely where it is needed on the grid. This is because as power demands increase in any AC system, the need for reactive power generally increases. When the transmission grid is forced to deliver large amounts of reactive power over long distances, it can limit the amount of real power that can be generated and delivered across a transmission grid. Therefore, it is advantageous to produce the necessary reactive power close to the loads.

As mentioned earlier, a superconducting generator will also typically be smaller and lighter, about one third the overall volume of its conventional equivalent [72]. Superconducting generators could increase generating capacity without using additional space in power plants where expansion is difficult particularly on ships or locomotives. Moreover, the use of superconductors to achieve higher current densities allows an overall reduction in cross section and field winding volume compared to ordinary copper wound rotors. The reduced winding volume thus leads to a reduction in the size and weight of the entire machine. Further reduction in size and weigh is also possible with the use a 'coreless' design, eliminating much of the structural and magnetic steel of a conventional equivalent. Construction, shipping, and installation are all simplified and less costly as a result of the smaller dimensions and lighter weight.

3.1.3 Characteristics and design variations of a superconducting generator

Generator designers follow two distinctly different approaches to the design of an HTS generator. One approach is to retain the conventional stator core and frame with its magnetic structures and adds an HTS rotor that contains an iron core. This approach completely eliminates any risk associated with the design of the stator and provides a magnetic structure in the rotor to enhance torque transmission. It offers immediate efficiency benefits, compatibility with the turbine drive train, and the ability to retrofit HTS rotors into existing generators. Furthermore, additional and fairly expensive stator development is not needed, thus the primary goal to demonstrate the technical feasibility of an HTS rotor can be achieved more easily. An insertion of a HTS rotor into a conventional stator also allows a modest upgrade in the capabilities of an existing machine. General Electric (GE) advanced 1.8 MVA HTS synchronous generator design was based on this concept [73]. It relies on conventional generator design elements whenever possible to reduce design, development, and operational risks, which to accomplish rapid market acceptance. The design retains a conventional stator, both in dimensions and technology. A similar constructional concept was adopted in Southampton's HTS synchronous generator.

The other alternative is known as a coreless or 'air-core' design, eliminating much of the structural and magnetic steel thus obtaining a generator that can be smaller and lighter than an equivalent conventional generator. In applications where size or weight reduction is an advantage (although not in utility power plants), such as ships or trains, superconducting generators could increase generating capacity without using additional space. Construction, shipping, and installation may be simplified and perhaps less costly as a result of the smaller dimensions and lighter weight. However, air core HTS generators do pose significant reliability risks in regard to transmission of torque within the generator and the potential for amplification of fault torques during operation [74]. This air-core concept is also applicable to stator winding. The HTS conductors permit higher air-gap fields in the stator winding which would saturate the iron of a conventional stator. The use of a high performance air-core stator winding may lead to a most compact design, smaller compared to conventional machines. Such concepts have been already developed and successfully tested by Alstom and American Superconductor in their 5MW ship propulsion motor [75]. The stator design employed dielectric fluid cooled Litz-wire coils supported by non-magnetic and non-conducting teeth.

The principal component target for superconducting generator has always been the rotor since stator AC losses have been deemed too severe to sustain. Hence, it is common in superconducting generators that an electromagnetic shield surrounds the rotor to shield the HTS coils from asynchronous magnetic fields and torque pulsations, and also to provide the rotor vacuum enclosure. Furthermore, in order to minimise the requirement for cooling of the superconducting field winding, heat leak to the cold space should be kept as low as possible. Convective heat transfer between the warm structure of the generator and the cold rotor is mostly eliminated by maintaining a high vacuum insulating space around the rotor and the radiation heat leak is reduced substantially by the use of radiation shields. The rotor is isolated from the warm portion of the drive end by a mechanical connector called torque tubes that – as the name suggests – transmit the drive torque to the rotor.

3.2 Southampton's 100 kVA HTS synchronous generator

Rapid advances in the development of HTS wires over the past 15 years have resulted in superconducting electromagnets that can operate at substantially higher temperatures than those made of LTS materials, and which as a consequence can utilise relatively simpler, less costly, and more efficient refrigeration systems. These factors make HTS wire technically suitable and economically feasible for use in the development and commercialisation of power applications, especially generator at power ratings much lower than could be considered with LTS wire. Moreover, higher operating temperature, availability of long length of HTS wire and simpler cooling system have made this technology suitable and economically feasible for use in the development and commercialisation of generator applications. Based on the encouraging factors mentioned above, and most importantly the experience and success of building the previous HTS demonstrator transformer, Engineering and Physical Sciences Research Council (EPSRC), United Kingdom have granted financial support to work on a HTS synchronous generator demonstrator under the project number GR/N21253/01 in 2000.

The machine, which was designed, built and tested at Southampton University, is a three-phase two-pole 100kVA 3000rpm synchronous generator which can operate in a temperature range 73-77 K and was tested at approximately 77.4 K. In order to build this machine there were four major parts that needed to be considered; rotor core, HTS field winding, stator, and refrigeration system. Figure 3.2 shows the major components of the final design of the HTS synchronous generator. The generator uses an existing stator from a conventional induction machine and specially designed rotor with superconducting field winding. In the final design, the HTS field winding is made of ten identical single-layer coils connected in series. Each coil has 40 turns of silver sheathed BSCCO tape. The required low temperatures are provided using purpose built closed circuit liquid cryogen cooling system with pipe-network feeding liquid cryogen to the rotor body of the generator. The rotor of the generator is made of 9% Ni steel. The selection of the rotor core material is very important due to very low temperature

environment. The detailed designs of the major components are discussed in the following sections.

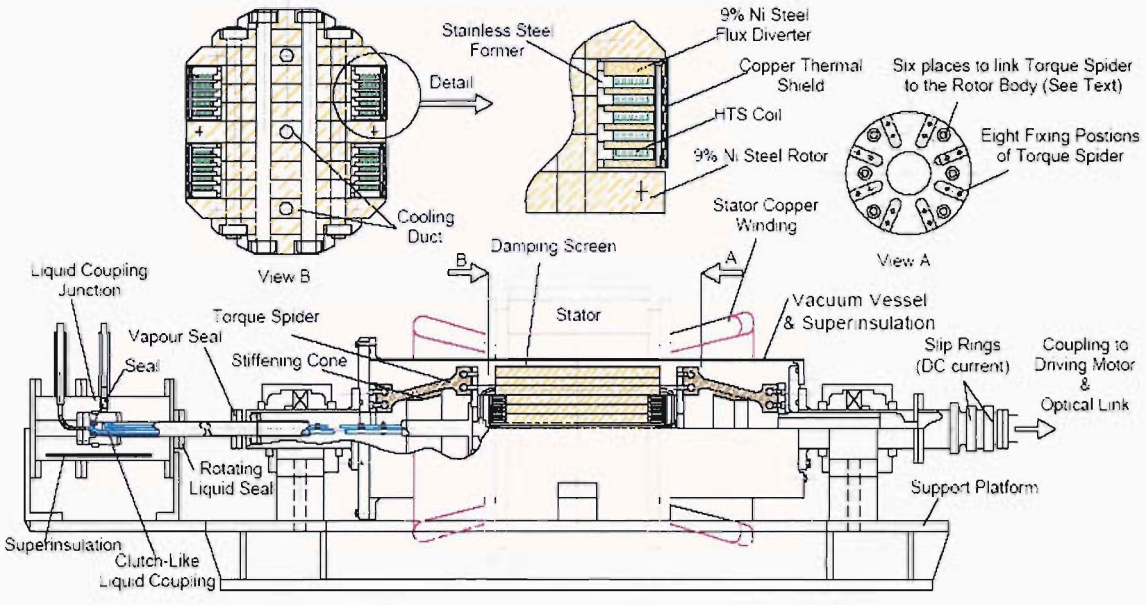

Figure 3.2 The overview of the Southampton HTS generator

3.2.1 Rotor

3.2.1.1 Design consideration

In the early designs, the rotor core was of the round rotor type, but with all the slot sides parallel to the quadrature axis so that all the superconducting coils would be flat. In such a rotor, each pair of coils would have a different width and may have a different number of turns. While it appeared that the above design could deliver satisfactory performance, it would be difficult to build and there was a risk of damaging the core during assembly. It was therefore decided that a hybrid design (a salient and round combination) should be used. This design greatly simplifies the construction of the HTS coils, since the coils can be wound separately and tested before fitted to the core. Moreover, by making all the coils identical, it was possible to produce spare coils to insure against the failure of any one coil.

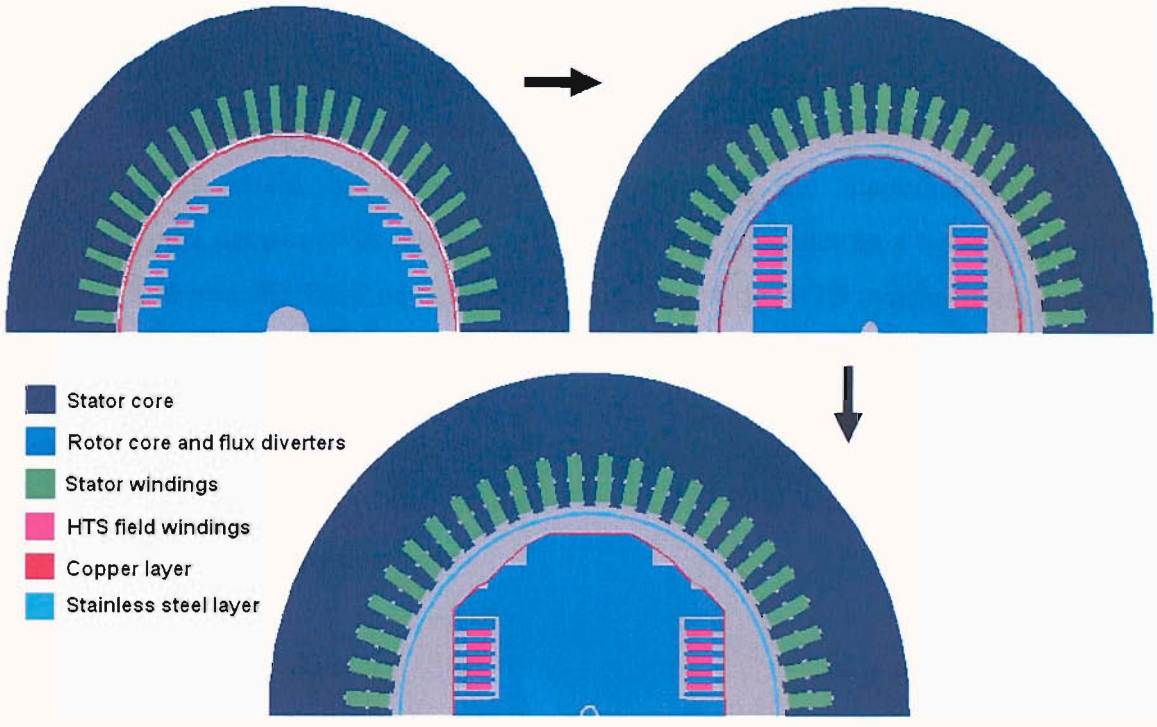

Figure 3.3 Superconducting rotor design

It is well known that salient pole structures are generally mushroom-shaped and may contain considerable 'pole shaping' along the peripheral edges of the poles in order to achieve flux distribution along the air gap to be more sinusoidal distribution. This design structure was considered in conjunction with the use of Invar material (in particular Invar with 36% Ni and 64% Fe composition). However, due to circumstances which will be explained later (see 3.2.1.2) the rotor needed to be redesigned to accommodate a different material. Figure 3.3 shows the major design changes from preliminary to final design. Other minor changes to the shape of the pole face are not shown in the diagram, but more detailed design considerations using finite-element modelling will be presented later in Chapter 4.

The choice of a two-pole machine imposed on this design was dictated by the simplicity of the design, but also due to budget restrictions, so that an existing stator which was originally installed in an induction motor could be used. A four-pole rotor was also considered as an option because the rotating speed would be halved and this design

configuration is also achievable using the existing stator by rearranging winding connections. However, a four-pole machine would require longer winding and might need a higher magnetising current. Furthermore, the available winding space in a four-pole machine would be reduced thus complicating the manufacturing process. Ultimately, the decision was made to design the HTS generator as a two-pole machine. Figure 3.4 shows the finished rotor core assembly of the HTS synchronous generator without the superconducting coils.

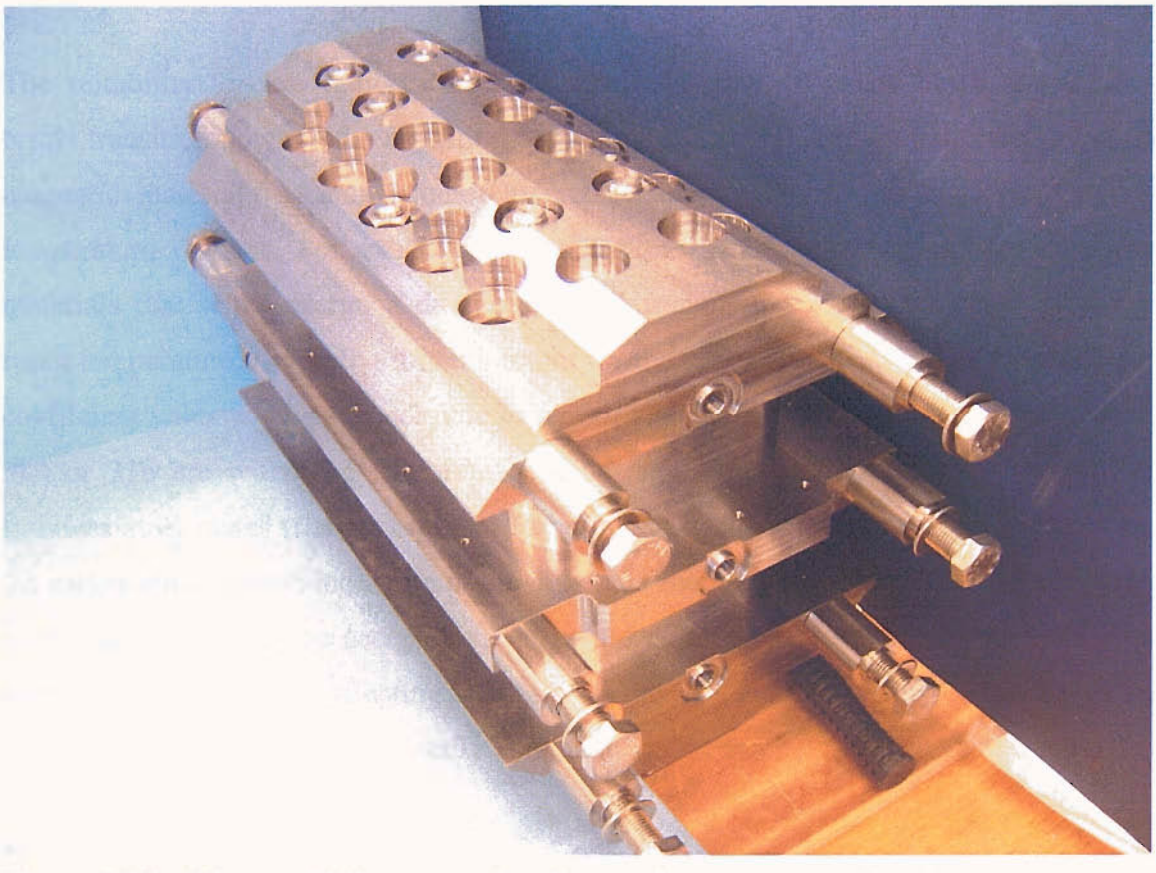

Figure 3.4 Partly assembled superconducting synchronous generator rotor core

3.2.1.2 Material selection

The design of the rotor of this HTS generator assumed using a magnetic metallic core. The design of the superconducting rotor using a magnetic core has two principal advantages; first, it greatly reduces the magnetising current, which allows the rotor to be constructed using much less superconducting tape, and secondly, it allows the flux

density in the superconductor to be reduced and its direction to be controlled. It therefore becomes possible to use liquid nitrogen cooling at 77 K instead of more expensive, complex and less efficient gaseous helium or neon cooling (at temperatures below 30 K) which would be required in a coreless design. Furthermore, this could demonstrate the use of 'true' high temperature cooling using liquid nitrogen. The selection of the magnetic material of the rotor was based on the following criteria; suitability for low temperature application, including the magnetic properties of the materials, availability and cost.

The suitability for low temperature applications refer to no existence of the ductile-brittle transition down to the operating temperature. It is well known that most common magnetic materials used at room temperature application are not suitable for low temperature devices. For example, pure iron and FeSi (silicon steel) are common materials that will undergo a ductile-to-brittle transition at some temperature below room temperature. Secondly, it is important for the chosen material to have the thermal coefficient value as close as possible to that of stainless steel (values for stainless steel 304 or 316 are within 12-16 μm/mK). This requirement is due to the intermediate stainless steel plates (flanges) needed to be joined to the magnetic rotor. Furthermore, the saturation magnetic induction of the materials should not be less than 1.5T, although a smaller value might be acceptable, but would require major design changes. Finally, another important factor affecting the design is the cost and availability of the materials. Ideally the materials should be easily obtainable on the market at a reasonable cost.

Based on factors mentioned above, it was found that most grades of Invar are suitable for use down to 1.8 K. These are also known as Iron-Nickel alloys, and are identified by the percentage of nickel. Various Iron-Nickel alloys were investigated and initially, Invar36 (Fe/36wt%Ni) was considered for the rotor core. However, the low thermal expansion coefficient of Invar presented great difficulty, since it must be connected to non-magnetic structural materials (stainless steel and fibreglass). Moreover, at the time of design Invar was not available locally, thus making the cost of the material to exceed the allocated budget. Hence, other Iron-Nickel alloys were considered in particular

Invar48 and Invar50, because they possess saturation flux density of 1.6 T (higher at 77 K) and thermal coefficients of contraction better than those of Invar36. However, these materials are not easily obtainable commercially for the required quantity at reasonable cost, and its coefficient of thermal expansion is still significantly less than that for any suitable non-magnetic material. Fortunately, generous Kawasaki Steel provided sufficient quantity of 9% Nickel steel (Fe/9wt%Ni) at no cost which eventually was used as the rotor core. Based on the manufacturer's data sheet, this material possesses mechanical properties similar to that of Invar and approaching those of stainless steel, especially its thermal coefficient of contraction, which was very encouraging. In order to confirm the suitability of the material magnetically, the magnetisation (or BH) curve was measured. The curves are also needed to perform finite element analysis calculations later. The BH curve was determined using samples in the shape of toroid (ring) core as shown in Fig. 3.5. The dimensions of the core are as follows: D_1 = 65.01 mm, D_2 = 45.01 mm, h = 11.94 mm. The core was wound with primary winding, N_1, and secondary winding, N_2, with a total of 24 and 920 turns, respectively. The resulting current distribution was assumed to be smooth so that the fine structure of the field, caused by the finite size of the wires, was disregarded. The slight pitch of the coil and the associated small current component circulating inside the toroid space were also ignored. If the mean radius of the magnetic path of the toroid were a, then the magnetic path length would be $2\pi a$, and the total MMF produced would be $N_1 I$. Hence, from Ampere's Law, the magnetic field inside the toroid can be determined by

$$H = \frac{N_1 I}{2\pi a} \tag{4.1}$$

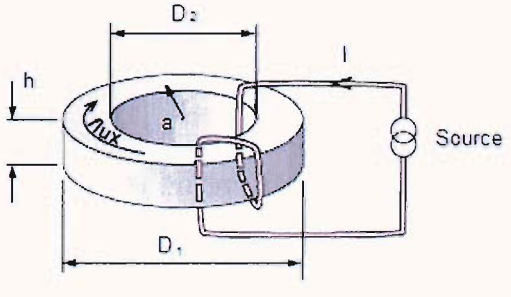

Figure 3.5 Magnetisable toroid core and the dimensions

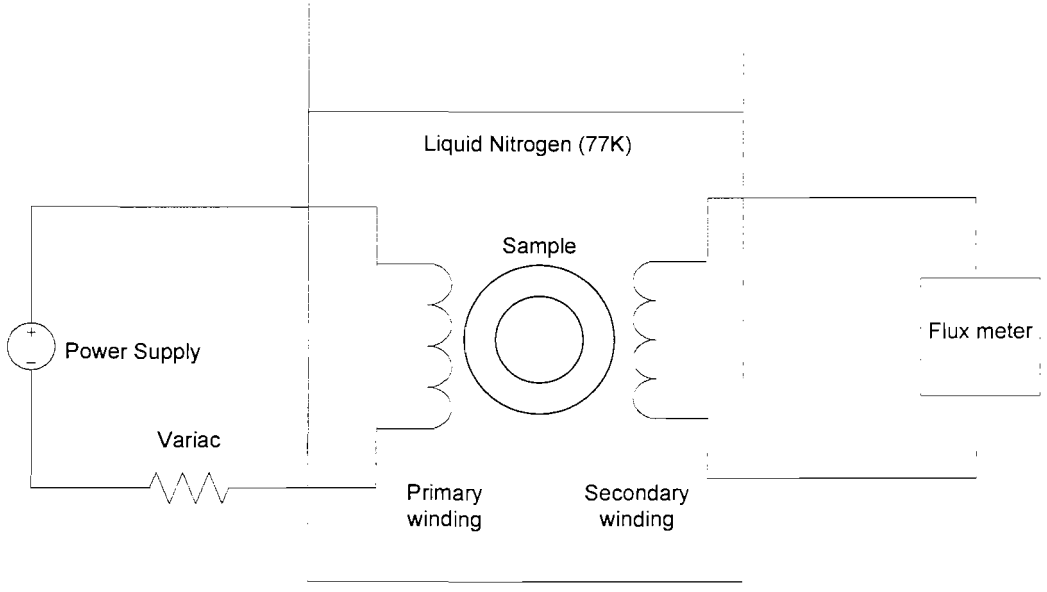

Figure 3.6 Experimental setup for measuring magnetisation curve

The samples were measured at about 77 K by immersing in the container of liquid nitrogen and the currents were varied up to about 18 A. Figure 3.6 shows the experimental setup for measuring the BH curve. According to Faraday's law of induction, the measurement of the terminal voltage of an additional coil, having N_2 turns wound on the core, gives information on B. The total flux was measured using the fluxmeter connected to the secondary winding. Subsequently, the flux density, B, was obtained by dividing the total flux by the effective area of the core. A common problem with this circuit is a drift due to voltage and current offsets. Hence, measurements were done using both positive and negative supplied currents. The results obtained were then averaged to plot the magnetisation curve. Figure 3.7 shows the BH curve for 9% Nickel steel together with a curve for Invar for comparison. As the magnetic field is increased from zero (current through the primary coils), the magnetic flux density increases to a point where saturation level is reach.

The saturation flux density for 9% Nickel steel was found to satisfy the requirement specified earlier. Moreover, the value was higher compare to Invar, thus reducing further the ampere-turns needed. Therefore, 9% Nickel steel was chosen as the material

for the rotor core. Since the raw material of 9% Nickel steel is produced in plates, the rotor had to be redesigned.

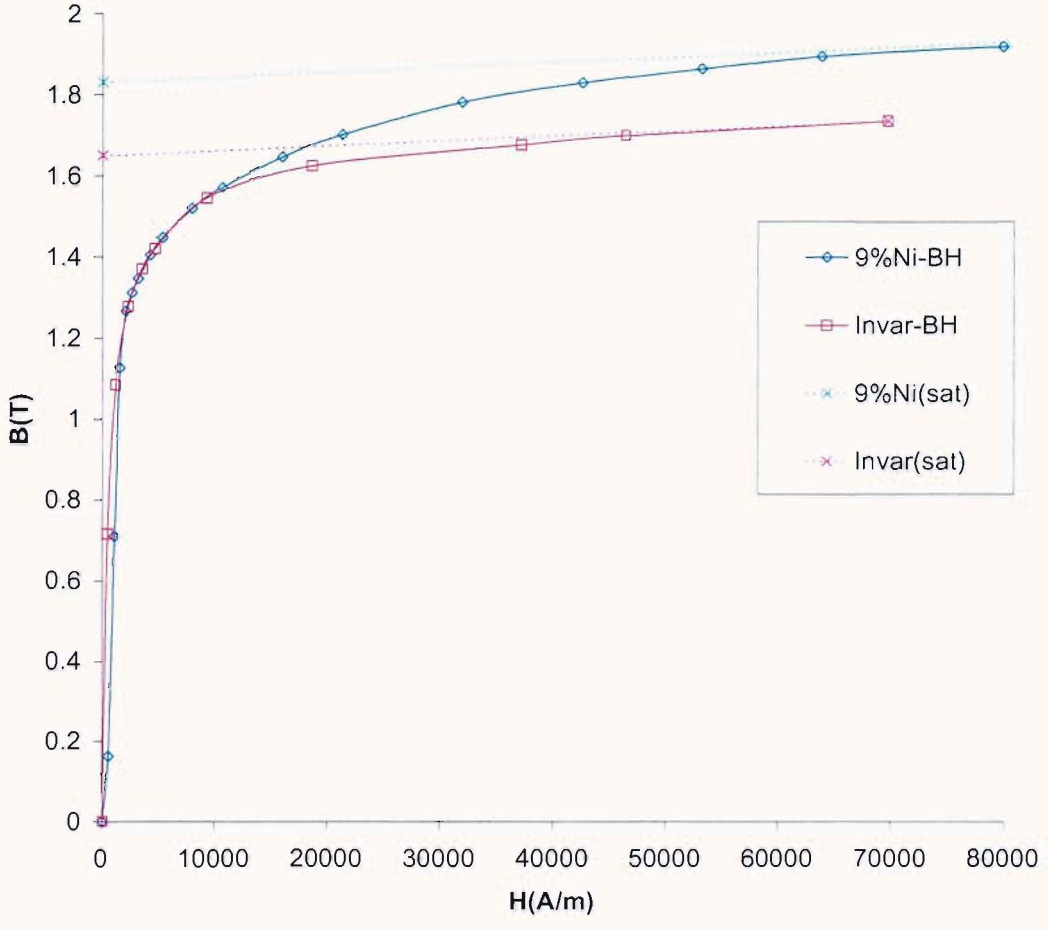

Figure 3.7 The B-H curves for Invar and 9% Nickel steel

3.2.1.3 Flux diverters

In the final design, flux diverters made of 9% Nickel steel were placed between the coils to reduce the normal field in the coils by diverting flux around the coils. As explained in Chapter 2, if the superconducting tapes are exposed to external fields which are directed perpendicular to the broad face of the tape they experience reduction in critical current due to the anisotropic nature of the material. Finite element analyses were carried out to confirm the effect of the flux diverters. It can be seen in Figure 4.8 of Chapter 4 that the flux diverter rings virtually eliminate the normal field components in the coils.

3.2.1.4 Screening

The radiation screen (copper layer) shown on Figure 3.3, which is made of 0.9 mm copper layer, functions as a shield to avoid the superconducting field winding being exposed to the time varying AC fields produced by the armature. It also helps to avoid excessive eddy-current loss in the rotor pole faces. Moreover, the radiation screen, together with the vacuum space, act as a thermal shield by reducing the heat travelling into the cold region. This shield is mounted on the same rotating structure as the field winding and normally travels synchronously with the fundamental flux wave. Therefore, it isolates the field coils from external disturbances that can potentially cause the superconductors to quench and thus disable the machine. The losses due to this screen were modelled in Chapter 5 to estimate the amount of cooling power required.

In the early design with Invar rotor core, the losses in the copper screen were estimated to be around 6.3 W, which would contribute a significant proportion of the load on the cryogenic cooling system. Therefore, in order further to reduce the losses dissipated inside the cryostat, one or all of the harmonic fields must be excluded by the use of a warm screen instead. The losses dissipated in a warm screen would be substantially higher than those saved in the cold screen, but would not be added to the load on the cooling system. Although substantially higher losses may be permitted in a warm screen, the proximity of this screen to the teeth of the stator core leads to very large increases in the losses caused by the stator teeth cutting through the rotating field of the rotor. It is therefore impractical to exclude all the harmonic fields from the cold parts of the rotor.

3.2.2 Superconducting field winding

3.2.2.1 Specifications

The multifilamentary silver-sheathed Bi-2223 high strength reinforced tapes received from American Superconductor consist of 85 filaments with no twist. The dimensions of the tape are: thickness approximately 0.3 mm, width 4.1 mm, and the nominal critical current is 115 A. The tape robustness has been increased by introducing a thin layer of

stainless steel reinforcement to both sides of the HTS tape. The added reinforcement gave close to about 400 MPa tensile stress and 0.5% tensile strain at 77 K according to the manufacturer's specifications [76]. Figures 3.8 and 3.9 show the cross section of the tape in detail [77].

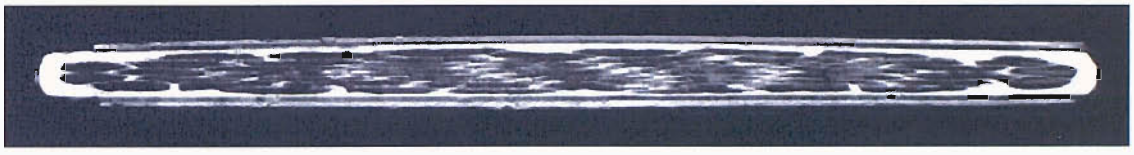

Figure 3.8 Cross section of an insulated Ag sheath Bi-2223 tape: 1mm

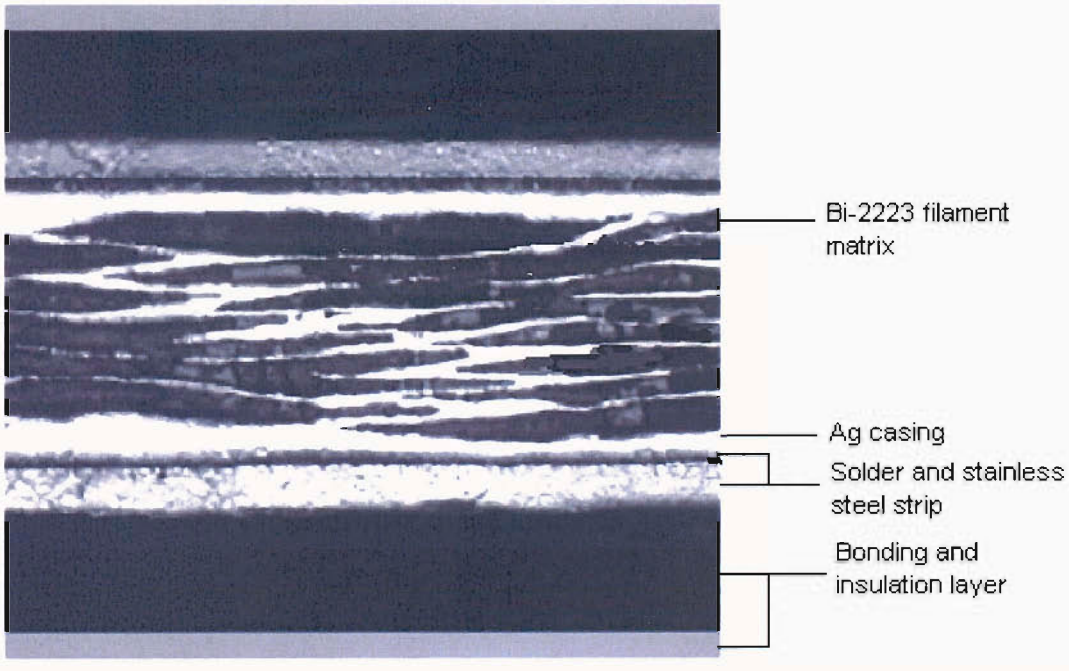

Figure 3.9 Close up view of the insulated Ag sheath Bi-2223 tape: 100μm

In the latest design, the HTS rotor windings were made of ten identical single-layer vacuum impregnated pancake coils as shown in Fig. 3.10. They are connected in series to minimise the required field current. Each coil has 40 turns of silver-sheathed BSCCO tape wound on a stainless steel former and interleaved by a fibreglass sheet. Fibre glass sheet is widely used as an insulation material between the turns. This layer acts as

electrical insulation as well as compensates thermal contraction of the epoxy resin which is used to hold the multi-turns windings. The radial and axial inner diameters of the coils are 168 mm and 344 mm respectively with a 30 mm bend radius at the corners. Each turn is assumed to occupy a 4.5×0.5 mm space, and is placed 0.5 mm away from the outer flux diverter ring. The total space allowed for each coil is 6.5 mm. To maintain tension during the winding process, tapered fibreglass slips were attached to the long sides of the race track stainless steel former to provide some curvature. The connections between the coils are made from copper strips, which are kept as short as possible to ensure that they have low resistance. The ends of the winding are connected to the central current leads by two wide copper strips, which are indirectly cooled via liquid cooled copper layers. This cooling is necessary since the heat conducted along the current leads would otherwise cause a significant temperature rise in the end coils of the winding, which would reduce the critical current of the whole winding.

Finite-element analyses have predicted (see Chapter 4) that using the field current of 63 A would produce an air-gap flux density of about 0.66 T, while producing a normal field of only 0.038 T in the superconductor. This field current requires the winding to operate at about 77 K. Operating at lower temperatures would allow a higher field current, which would increase the stator flux linkage, permitting a higher output power. The HTS coils had been successfully manufactured and tested over several thermal cycles. The coils behaved consistently well throughout the duration of the tests without any deterioration of performance.

Several test and experiments were jointly conducted by the Institute of Cyrogenics and Electrical Power Engineering Group, University of Southampton, in order to evaluate the performance and suitability of the tapes for the project. Electrical, magnetic and mechanical characteristics of the superconducting tapes are important for design of this machine. The tape was characterised with the following properties:

- Electrical contact resistivity of the stainless steel layer with respect to the tape.
- Critical current density and I-V characteristics.

- The magnetic field dependence of the critical current.
- The field angle dependence of critical current at 77.4 K.
- The strain tolerance of the tape.

Figure 3.10 The HTS field windings in racetrack form

3.2.2.2 Electrical contact resistivity

The purpose of evaluating the electrical contact resistivity between the layers (stainless steel, silver and superconducting core) is to determine the heat generated when currents are transported. This is particularly important in applications where a high current is applied because any measurable contact resistance could results in contact heating. This would expose the vulnerable superconducting core to the undesirable heat thus degrading its superconductivity. Furthermore, any non-uniformity in the contact can result in hot spot formation that could lead to localised thermal quenching and destruction of the contact due to much increased power dissipation [78].

The electrical resistance of the tape was measured using two short length tape samples which were soldered together (overlapped by 10 mm) on the broad side of the tape. Transport currents were fed through the tapes via copper plates and a series of voltages are recorded at the voltage taps. Figure 3.11 shows the measured results as current varies up to 100 A. It can be seen that the resistance across the contact is constant at liquid nitrogen temperature. The electrical contact resistivity per centimetre square of the contact area was found to be $0.18\,\mu\Omega cm^2$, compare to those of pure stainless steel is $0.20\,\mu\Omega cm^2$. Since resistivity was found be of no significant difference, the flow of high current would not produce significant heat that could cause breakdown at the current feeding junction.

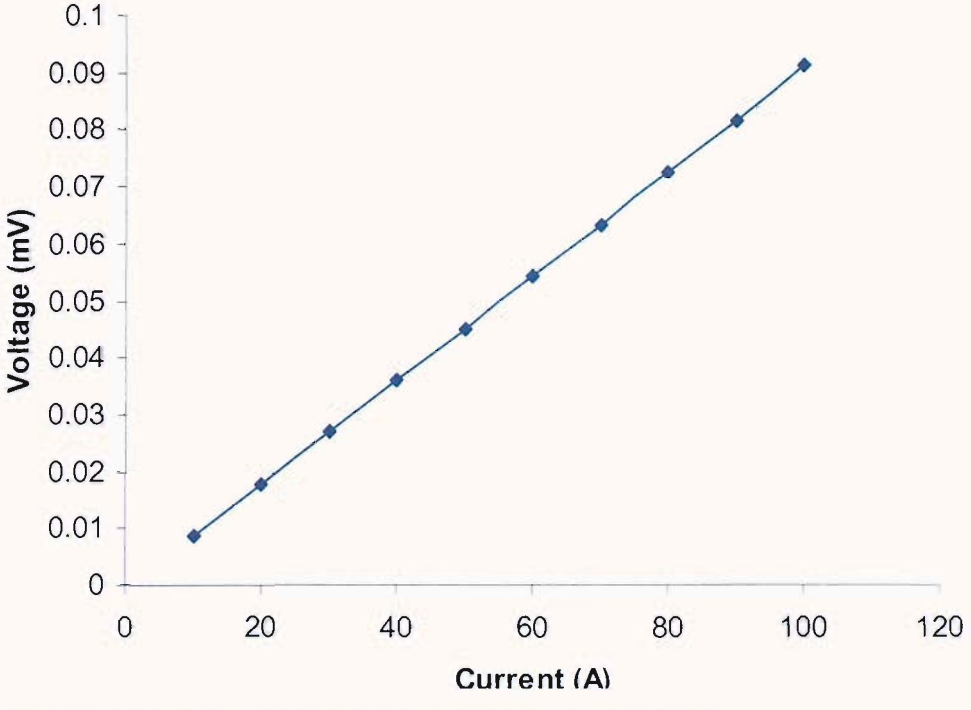

Figure 3.11 Measured voltages by varying current at 77 K

3.2.2.3 Critical current and *I-V* characteristics

The transport current was applied and the voltage was measured between voltage taps using a four-probe resistive method. This is a technique for measuring the resistance of low resistance material. Unlike two probe resistance measurements where the voltage

drop is measured by the same probe that does the current excitation, the four probe technique separates the voltage drop measurement probes from the current excitation probes. This separates the probe resistance from the actual sample resistance measurement. The sample was placed into a purpose built rig containing liquid nitrogen. The critical current in the self field, at the operating temperature was determined using a 1 μVcm^{-1} criterion [79]. The results of the measurements are shown in Fig. 3.12. As shown clearly on the graph, the critical current falls in the range of 125 A - 135 A at 77 K.

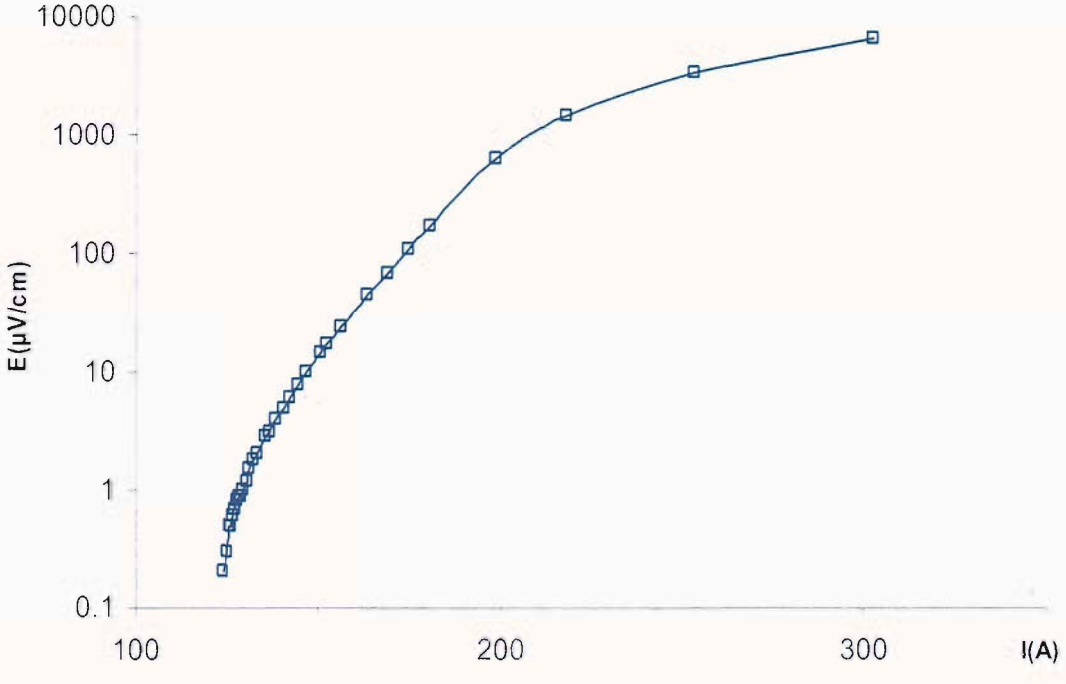

Figure 3.12 *I-V* characteristics of the tape in self-field at 77K.

The critical current density was calculated based on the measured critical current and it was found to be 9.2 kAcm^{-2}. In the range 1-100 μVcm^{-1}, the *n*-value for the American Superconductor reinforced superconducting tape is 15.5 at 77 K. The *n*-value is the exponent $V \alpha I^n$ of the current-voltage characteristic at the transition from the normal to the superconducting state, measured at the industry standard value of 1 μVcm^{-1}. It describes the relationship of the voltage drop across the wire to the applied current. The

HTS tapes have different critical currents, I_c and n-value in different areas due to inhomogeneity. Generally, the area with high n-value is considered to have better superconducting properties than that of low n-value [79]. This is because with a steep transition the tape can carry a current very close to I_c thus generating a very low voltage.

3.2.2.4 Magnetic field dependence on the critical current

Three various samples of the multifilamentary Bi-2223 high strength reinforced tapes supplied by American Superconductor were measured at fields up to 0.5 T at different field orientation. The samples were taken from different sections of the supplied 200 m tape and the samples A, B and C represent sections used. Figure 3.15 shows the measured field dependence on the critical current at 77.4 K in fields up to 0.5 T for parallel ($B_{//}$ or axial) and perpendicular ($B_{\perp}$ or radial) fields. The parallel (ab-plane) and perpendicular (c-direction) is referring to the orientation of the tape with respect to the magnetic field as shown in Fig. 3.13. Due to the effect of anisotropy, the critical current reduces drastically when the tape is exposed to radial fields, whereas the fields parallel to the plane of the tape have least effect.

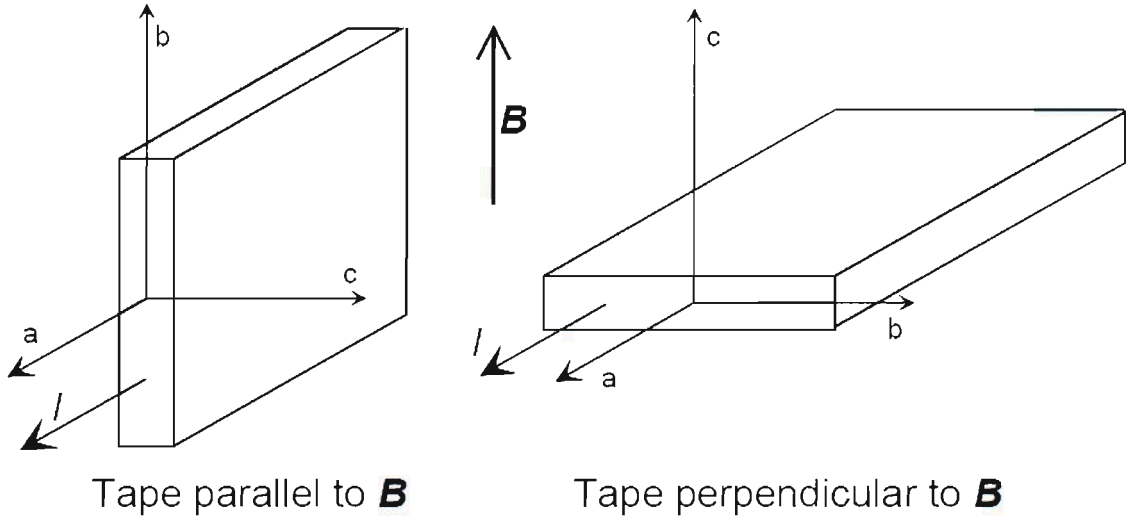

Figure 3.13 Tape orientations with respect to the applied field

All high-T_c materials have a layered crystal structure, with alternating copper oxide (CuO) planes and planes of different material as shown earlier in Chapter 2 of Fig. 2.5.

The superconducting properties are much better within the CuO planes (*ab*-planes of the crystal) than normal to the CuO planes (*c*-direction). Therefore the critical current density inside the grains is higher in the *ab*-plane than in *c*-direction. Figure 3.14 shows the magnetic field angle dependence of the critical current at different field values from 0 T to 0.5 T with field angles of 0° to 90° with respect to the broad side of the tape at 77.4 K. Therefore, to avoid the radial component of flux density in the superconductor, separate ferromagnetic rings known as flux diverters are sandwiched between superconducting coils. Considering the worst case by using the value of the peak normal field (0.038 T) which was obtained from finite-element modelling, the maximum achievable critical current would be in the range of 67 A to 83 A as shown in Fig. 3.15 (dotted lines). Hence, this concludes that the tape used would be in the target specification of the design.

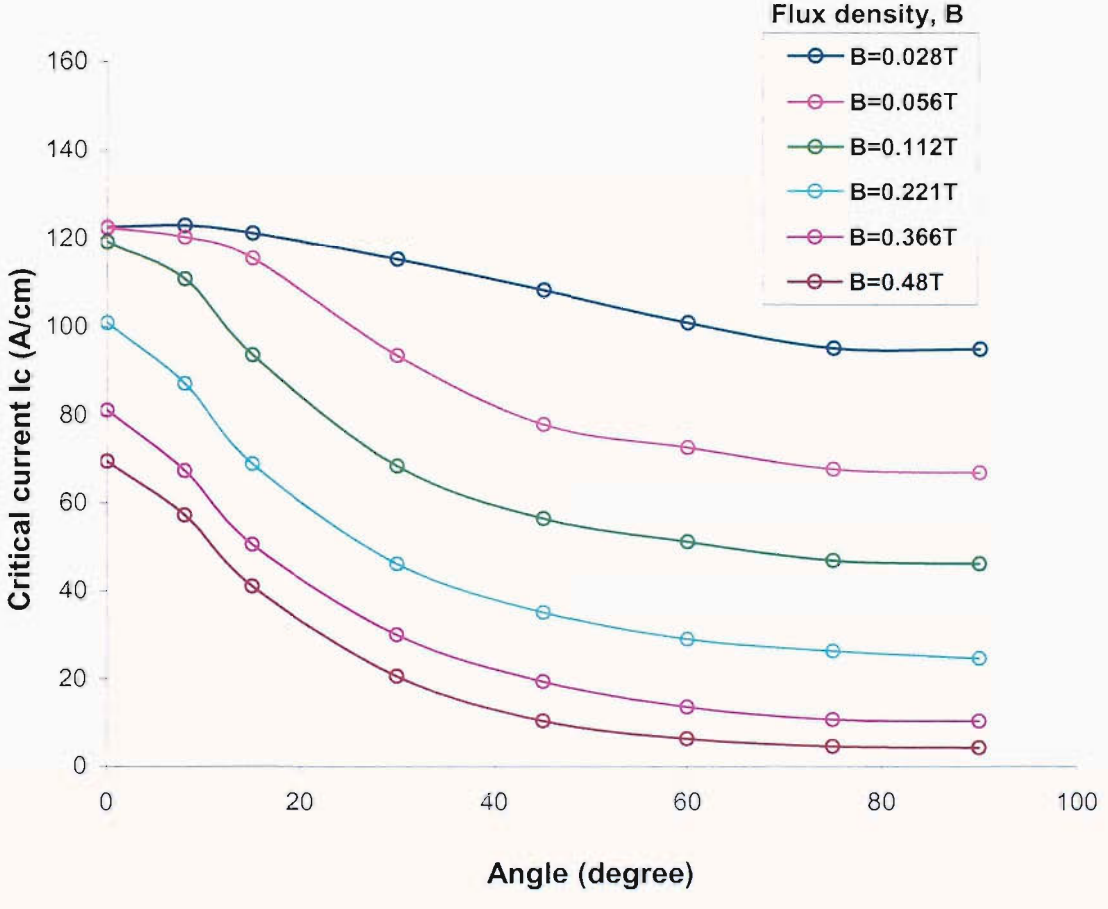

Figure 3.14 Magnetic field angle dependence of the critical current.

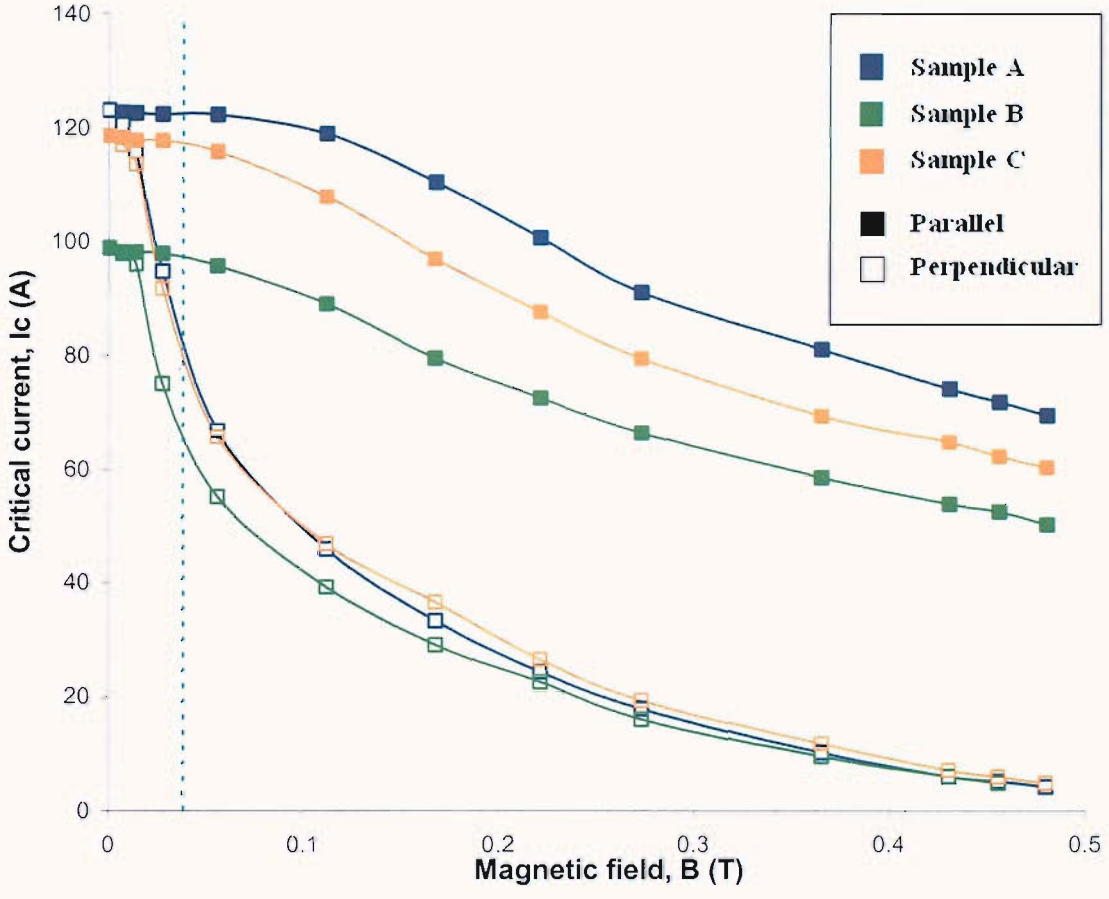

Figure 3.15 Magnetic field dependence of the superconducting tape at 77.4 K

3.2.2.5 Strain tolerance

It has been well established that a superconducting tape has a certain value of strain limit before it affects the transport critical current by reducing its value [80]. The strain effect happens during the fabrication of the device and due to thermal cycling (operation in large magnetic fields). Moreover, during the assembly of the superconducting tapes to form racetrack field coils, the tapes will undergo tensile and bending strains. Hence, the effect of these strains on the critical current of the tape needs to be investigated.

Figure 3.16 shows the critical current and bending strain characteristics of a 50 mm long sample of Bi-2223 reinforced tape. The measurements were done using a purpose built bending apparatus that was designed for the previous HTS demonstrator project [1]. It can be seen that there is no decrease in the critical current up to a strain value of 0.2% –

0.3% (with bending radius of 40 mm - 60 mm), and approximately 12% drop in the critical current with strain value of 0.74% (with bending radius of 28.5 mm). In the latest design, the bending radius of the field winding is 30 mm, thus there is a reduction of 0.5% in the value of the critical current reduction; which is still over 100 A. Therefore, a good safety margin in the bending strain will ensure the superconducting field winding to operate with enough critical current density even in large magnetic fields.

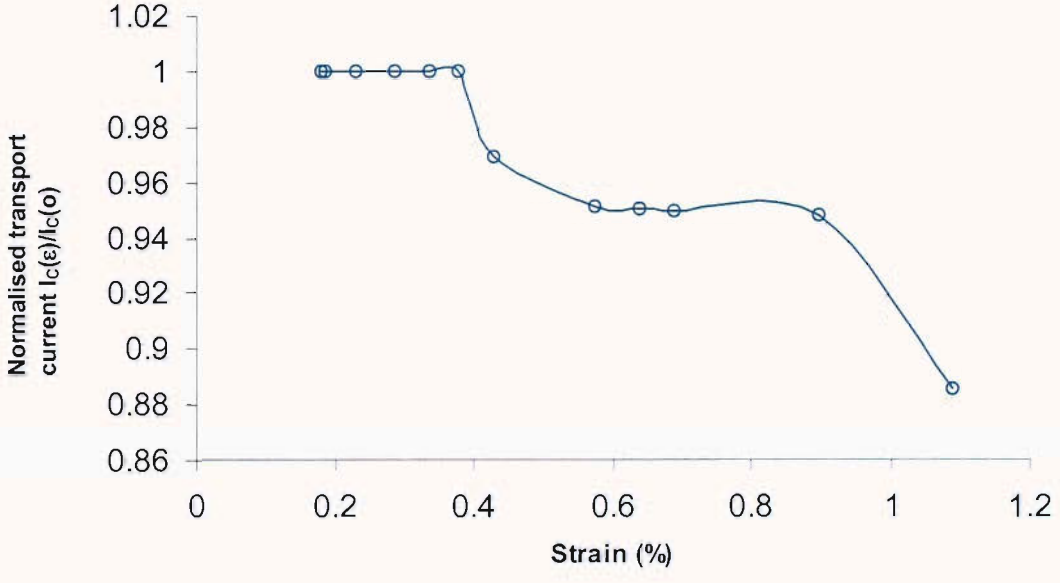

Figure 3.16 Bending strain characteristics of the Bi-2223 high strength reinforced tape

3.2.3 Stator

3.2.3.1 Existing stator

The generator uses an existing stator from a conventional 100 kVA, 3-phase 2-pole induction machine, which has a 330mm bore diameter and 325 mm iron length. There are a total of 48 slots with a 2-layer winding connected in parallel with a 3-turn per coil arrangement. The stator winding is composed of conductors in slots distributed around the periphery of the air gap, connected together at the ends, and grouped to form separate phase windings. The windings were short-pitched (14/24 pitch coils) with the

aim to reduce the length of the coil-end connections and the magnitude of harmonics in the waveform of the generated EMF.

Table 3.2: Specifications of the stator

Stator details	Value
Rated output, kVA	100
Power rating, W	100
Rated current, A	193
Rated voltage, V	415
Bore, m	0.33
Diameter, m	0.54
Iron core length, m	0.325
Overall length, m	0.795
Number of turns in each coil	3
Number of poles	2
Number of slots	48
Slot size, mm	40 x 10.5 with 3 x 2 mm groove in sides and bottom
Winding connection	Star, parallel circuits
Coils pitch	14/24
Working temperature	25 –50°C
Cooling method	Air

Figure 3.17 shows the full winding configuration of the stator. The stator was constructed of magnetic laminations assembled in the axial direction and separated by thin films of electrically insulating materials. The laminations are held together to form a rigid body by means of pressure bonding, with insulating material as the bonding agent. The stator stack was further strengthened by the stator housing at its outer periphery and secured to the housing by means of radial bolts. The full specification of the stator is shown in Table 3.2. A substantial campaign of finite element analysis has been undertaken to minimise the problems caused by air-gap flux harmonics, due to the restrictions imposed by the choice of existing stator. These problems are of two types: losses in the rotor that must be removed by the cryogenic cooling system, and stator

voltage harmonics that can drive currents in the external circuit. The former will be discussed in detail in Chapter 4 and the later in Chapter 5.

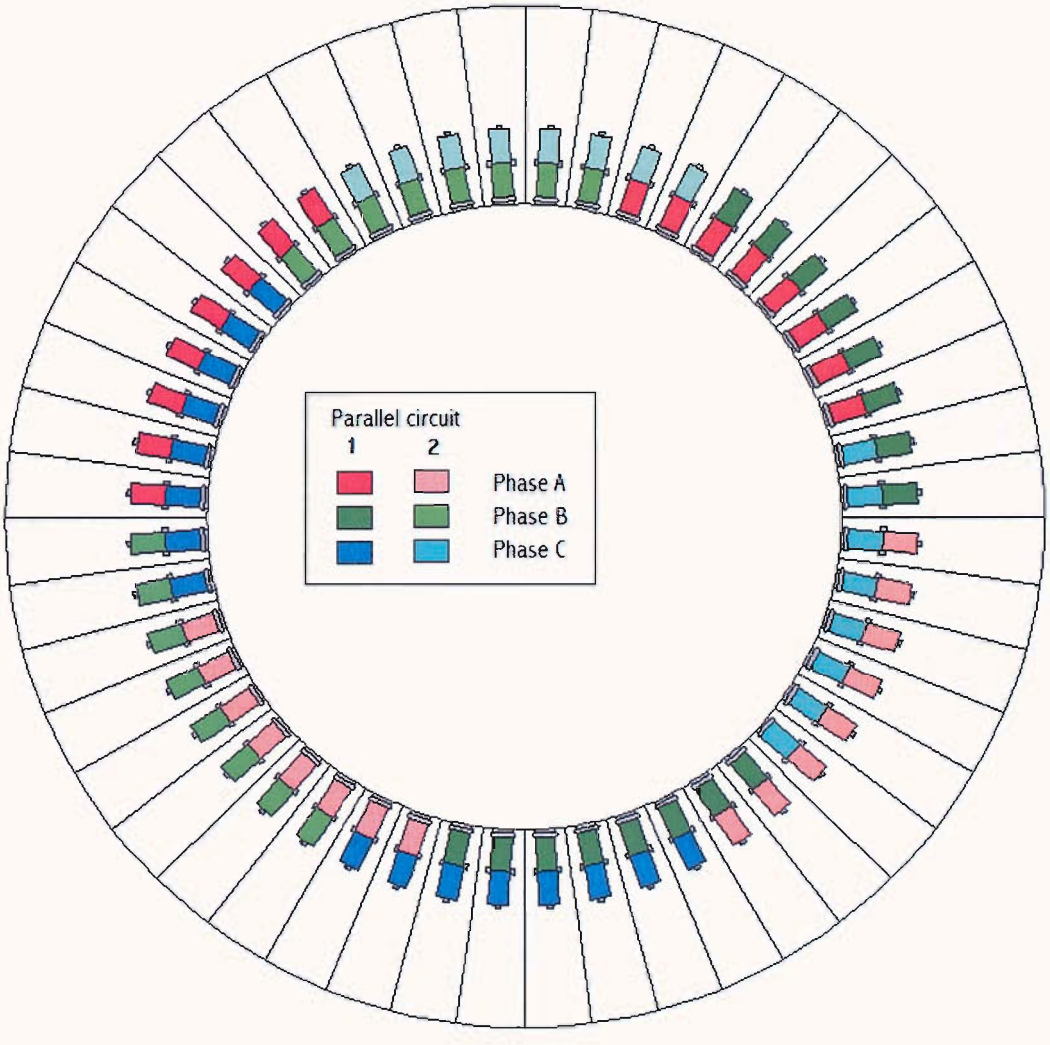

Figure 3.17 The winding configuration of the stator

3.2.3.2 Stator redesign

If there were flexibility to design a new stator with the same rating to accommodate the superconducting rotor, the performance of the machine could be improved. The improvement could be significant in reducing undesirable harmonics which eventually give a better output voltage waveform. Therefore, the open circuit waveform of a generator might be closer to a sine wave to assure satisfactory operation of the

connected load. The simplest and most cost effective method would be to adjust the coil pitch of the stator winding.

Table 3.3 Odd order harmonic voltage contributions for different stator coil pitch.

Order of harmonic \ Coil pitch	10/24	11/24	12/24	13/24	14/24	15/24	16/24	17/24	18/24	19/24
1	100	100	100	100	100	100	100	100	100	100
3	1.55	1.29	1.02	0.76	0.49	0.24	0.00	0.22	0.42	0.60
5	0.03	0.09	0.14	0.17	0.17	0.16	0.14	0.10	0.06	0.01
7	1.74	1.53	1.07	0.46	0.18	0.71	1.07	1.19	1.07	0.74
9	0.70	0.33	1.11	1.45	1.29	0.74	0.00	0.69	1.11	1.15
11	0.67	0.78	0.51	0.04	0.39	0.60	0.51	0.18	0.21	0.49
13	0.12	0.01	0.09	0.13	0.07	0.02	0.09	0.10	0.04	0.04
15	0.10	0.25	0.17	0.04	0.19	0.17	0.00	0.15	0.17	0.03
17	0.11	0.03	0.07	0.09	0.01	0.07	0.07	0.01	0.07	0.06
19	0.00	0.02	0.02	0.01	0.02	0.00	0.02	0.01	0.01	0.02
rms harmonic voltage, %	2.53	2.19	1.93	1.71	1.47	1.24	1.20	1.42	1.62	1.57

Due to the armature winding being located in a discrete finite number of stator slots, the MMF wave of armature reaction contains all odd order harmonics, their amplitudes varying more or less inversely with their order. To obtain the best voltage waveform, each individual odd harmonic order needs to be known. This can be done using 2D finite element analysis with their harmonics components extracted using Fourier series. Table 3.3 shows the individual harmonic voltage contributions in percentage up to 19^{th} order and the total rms voltage for coil pitch from 10/24 up to 19/24. Referring to the table, coil pitch of 16/24 gives the lowest total harmonic voltage, thus is the preferable choice of coil pitch for this machine.

4.2.4 Torque tube design

At both ends of the rotor, six stainless steel bolts and bushes clamp the rotor body to carefully placed 9% Ni steel plates. This non-magnetic mechanical link is used to break

the magnetic circuit. The room temperature stainless steel stub shafts are linked to the two 9%Ni steel plates using a novel design of a fibreglass 'torque spider' to provide the mechanical support required and to reduce the heat intake into the generator cold space. Moreover, the torque tubes should be strong enough in torsion to carry operating and fault torques in the machine and rigid to prevent the rotor from excessive vibration during operation. Therefore, a fibreglass epoxy composite was chosen as the torque tube construction material to reduce heat leak through conduction. The torque spider consists of eight fibreglass legs, which are strengthened by a 'stiffening cone' as seen in Fig. 3.18. The entire assembly (rotor, HTS winding, torque spider and flanges) is wrapped by layers of superinsulation and encapsulated by the outer vacuum cryostat.

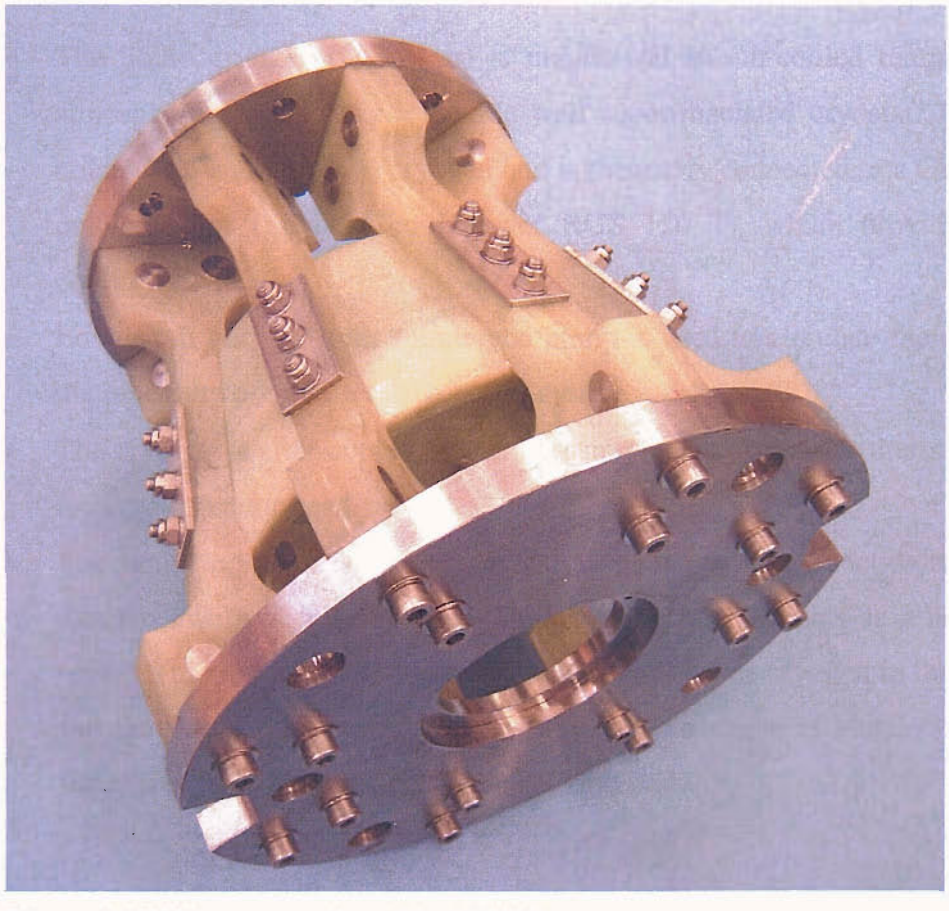

Figure 3.18 The torque tube with stiffening cone

3.2.5 Cooling system

The required low temperatures are provided using purpose built closed circuit liquid cryogen cooling system with pipe-network feeding liquid cryogen to the rotor body of the generator. The warmed fluid exiting the rotor is cooled by means of a heat exchanger and a cryogenerator with cooling power of the order of 100 W at 60 K. To enhance the critical current as much as possible, the cryogen may be sub-cooled near to the freezing point. If the liquid nitrogen is used, the minimum usable temperature is approximately 65 K. The heat load into the entire generator has been estimated to be around 60W. The refrigeration system can be divided into four components: cryostat, cryogenic pump, heat exchanger, and liquid coupling junction [81]:

- The liquid cryogen (N_2 or air) is maintained at sub-cooled temperature and one atmosphere pressure inside double wall super-insulated cryostat. The inner vessel holds up to eight litres of cryogen and is thermally connected to a Gifford McMahon cryogenerator (Leybold cool power RGS 120 T), which provides the required cooling power.
- Long shaft purpose built submerged pump is used to circulate the cryogen through the pipe-network of the refrigeration system.
- The cryogen is after-cooled further by using a heat exchanger thermally anchored to the cryogenerator head.
- The liquid cryogen is carried to and from a coupling junction via two flexible vacuum insulated transfer lines. The coupling junction acts as a liquid sealed link between the rotating pipe-network, which supplies the cryogen to the generator rotor and the stationery transfer lines. The junction consists of clutch-like feeding port, vacuum capsule and two cryogenic rotating seals.

HTS ROTOR DESIGN

The rotor of the Southampton's superconducting synchronous generator contains a magnetic metallic core. The presence of the core greatly reduces the magnetising current and also allows the flux density in the superconductor to be reduced and its direction to be controlled. It therefore becomes possible to use liquid nitrogen cooling at 77 K instead of more expensive and less efficient gaseous helium or neon cooling. The entire rotor structure has to be fitted into the existing stator with the bore diameter of 330 mm. Mechanical constraints dictate that the air-gap has to be around 20 mm which is needed for thermal insulation, thus the core must be able to fit within a 145 mm radius limit. Due to the choice of salient pole structure and the use of an existing stator, the air gap flux density waveform needs to be studied carefully. OPERA 2D and 3D [82] finite-element (FE) software was used to model and evaluate various rotor designs. The structure of the software will be described briefly in Section 4.1.4. Some general discussion of most widely used numerical methods, and specifically finite-element method is also presented in the following sections. A substantial programme of FE investigations has been undertaken to model the generator's harmonic fields and to identify specific areas for improvement. It should be noted that the majority of the designs are greatly influenced by mechanical requirements and, a lesser extent, by time constraint. The modelling analyses were carried out to confirm the machines design to be realistic and within the acceptable operating conditions.

4.1 Introduction

Advancements in computer technologies and techniques have revolutionised the way in which electromagnetic problems are analysed. The modelling of electromagnetic processes on a computer enables the designer to understand how devices work and hopefully lead to better products as underlined by the philosophy of computer-aided design (CAD). Many branches of industry have already incorporated CAD in electromagnetics into their everyday design practise. Currently, commercial finite-element codes [83, 84] are readily available that have graphical user interfaces and can determine the optimum placement of node points for a given geometry automatically. Moreover, with the use of powerful, low cost computers, the modelling is very fast and it is easy to compute the distributions of electromagnetic fields generated by complicated electromagnetic devices, such as electrical machines, in 2D as well as in 3D geometries. Figure 4.1 shows an idealisation of the design process in which a designer iterates towards a satisfactory solution by the heuristic approach [85] integrated into a CAD system. The designer plays an important role to input sufficient details of design parameters and mathematical models to ensure the success of the whole process. Hence, if the model is not adequate or wrongly interpreted, no matter how accurate the computations are conducted, the results may be of no relevance.

In general, a typical CAD system can be classified into three phases: pre-processor, solver and postprocessor. All three processes need to access a common database where the results and data files are stored. The discretisation process takes place inside the solver, which can generate a mesh adaptively to achieve a specified accuracy. The post-processor, as well as the pre-processor, are at the engineering interfaces and are the key element in the loop of the heuristic design procedure as shown in the figure. The essence of each of the processes will be briefly described in the Section 4.1.4 to facilitate better understanding of their function and importance in a CAD system.

The mathematical formulation of numerical methods involved are beyond the scope of this thesis, thus in the following section only a general overview of the most frequently

applied numerical techniques in electromagnetics is provided with particular emphasis upon the finite-element method. The components of a practical software environment for electromagnetics CAD are also discussed in Section 4.1.3.

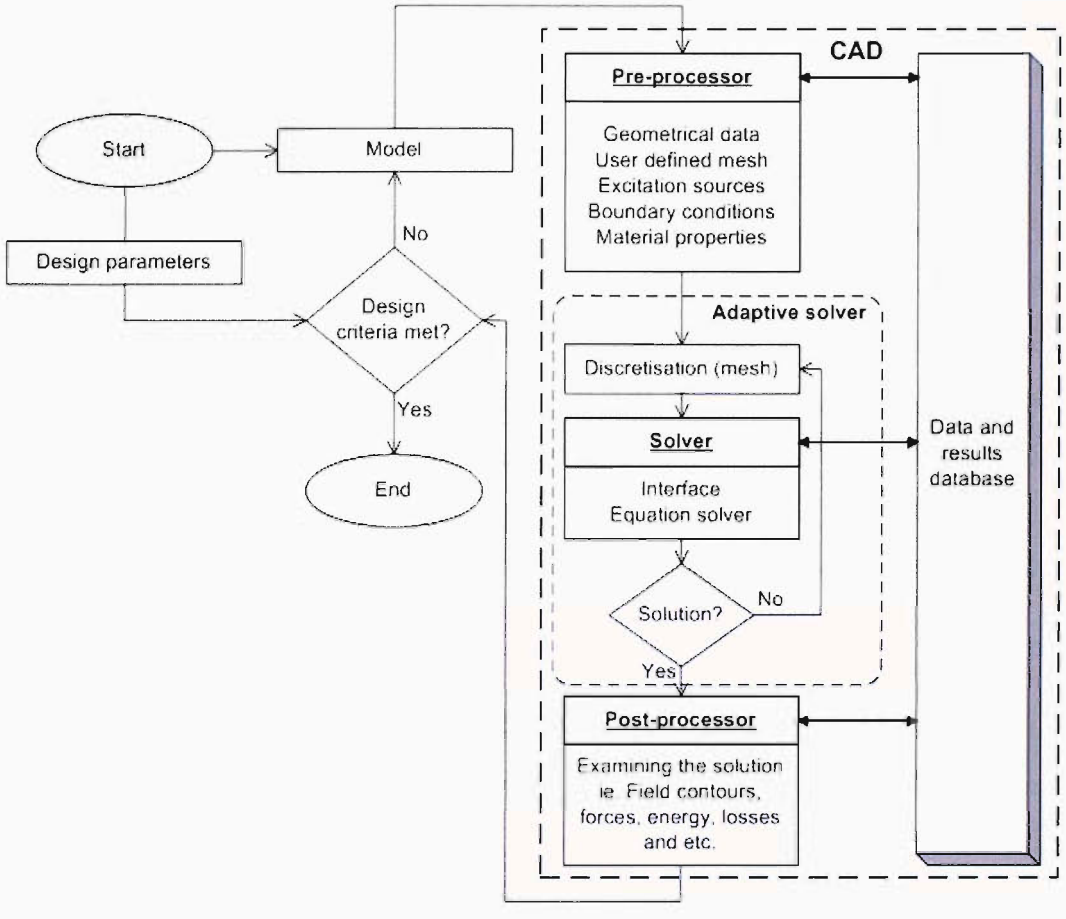

Figure 4.1 Flow diagrams for heuristic design and components of CAD system.

4.1.1 Computational methods in electromagnetics

It is well known that most electromagnetic problems ultimately involve solving partial differential equations subject to boundary constraints, and very few practical problems can be solved without the aid of a computer. Numerical techniques generally require more computation than analytical techniques, but they are very powerful and rapidly advancing electromagnetic analysis tools. Numerical techniques analyse the entire geometry provided as an input without making a priori assumptions about which field

interactions are most significant. A number of different numerical techniques for solving electromagnetic problems are available. The numerical methods for solving such problems can be classed with other methods of solving partial differential equations, such as the finite difference method (FDM) [86], finite-element method (FEM), boundary element method (BEM) [87] and method of moments (MOM) [88]. Each numerical technique is well suited for the analysis of a particular type of problem.

4.1.2 The finite-element method

Finite-elements made their earliest appearance in 1950's, when they were introduced by Turner et al [89]. The method was based on a variable inside an element and it is expressed in terms of interpolated nodal variables. In electrical engineering, the first work using FEM was done by Winslow [90]. It was then Silvester who, together with his colleagues, developed the method to new heights in electrical engineering and brought it to the notice of the electrical engineering community [91]. Much of the initial work in electromagnetic finite-elements began with analysis of synchronous machines [92].

From the early seventies the FEM has been progressively developed into an analysis technique which is used consistently in design of electrical equipment either as part of a design procedure or to support design. In spite of its short period of implementation in the field of electromagnetics, FEM has been successfully applied to the analysis of various problems including electrostatic and magnetostatic fields, eddy-current problems, high-frequency problems, electromagnetic scattering and wave propagation phenomena. Currently, the FEM is a widely established procedure for analysis, optimisation and design of electromagnetic devices; a large portion of modern CAD modules are partially or entirely based on this method.

A major advantage that the FEM technique has over other EM modelling methods stems from the fact that the electric and geometric properties of each element can be defined independently. This permits the problem to be set up with large number of small elements in regions of complex geometry, and fewer, larger elements in relatively open

regions. Therefore, it is possible to model configurations that have complicated geometries and many arbitrarily shaped regions in a relatively efficient manner especially in rotating electrical machines. There are many books specifically dedicated to finite-element analysis of electrical machines [93-95] and literally thousands of papers have demonstrated good consistency of the numerical results with empirical data.

The basic concept of the finite-element method is to divide the domain under investigation, either being two-dimensional (2D) or three-dimensional (3D), into finite number of simple sub-domains – elements (triangles in 2D or tetrahedra in 3D domain) and then to approximate the unknown variable in each sub-domain by low order piecewise functions – usually polynomials. The nodes are linked to form elements of the selected shape. The values of the unknown variable at each node of such an established network of elements, usually called finite-element mesh, are the main aim of the finite-element analysis. These values at each point inside the domain of analysis can be computed by using the node values of each primitive, and the previously established piecewise approximation functions. Alternative formulations, using edges or facets instead of nodes, have recently become available and offer improved accuracy and faster solutions.

4.1.4 Elements of a CAD system

4.1.4.1 Pre-processing and mesh generation

The function of a pre-processor is to allow user to define of the geometry, input the material data and define the sources as well as boundary conditions. In addition most commercial programs offer useful extra features for pre-processing, such as tools to enable repeated structures to be defined effectively, generating and checking meshes, libraries of shapes, magnetisation curves and material properties. Usually the geometry of a device is presented to the pre- and post-processor as a set of polygonal areas or regions on a 2D plane. One region can be a 'background' region which covers the whole problem space. The others are non-overlapping polygons which specify the other materials in the problem. In magnetic devices, a region can represent one of the

following: free-space, a conductor with a prescribed or induced current density, and permeable material with a linear or non-linear material characteristic.

Within each region, finite-element mesh generation is automatic, using as input data the coordinates of the vertices and the curvatures and subdivisions of the sides. There are two classes of regions shapes: quadrilaterals and general polygons. The mesh within quadrilaterals is generated by transformation to a unit square and regular subdivision. The mesh is therefore predictable and mesh generation times are short. Furthermore, in most commercial packages it is possible to generate elements with large aspect ratios necessary for small air gaps. As for the mesh within polygons, it can be generated using an algorithm based on Delaunay triangulation [96]. Internal nodes are added if necessary to achieve element sizes which vary smoothly across the regions and element shapes which are as near to equilateral as possible. Polygons allow large areas of space, especially near a 'far-field' boundary, to be meshed with a minimal number of regions.

4.1.4.2 Solver

The heart of any electromagnetics software system is the solution processor or solver. This processor is equipped with all the necessary algorithms to discretise the governing field equations, generate the matrix coefficients and solve the simultaneous linear or non-linear algebraic equations. These operations are the least visible to the user and usually do not involve the user, although the user is still normally responsible for initiating the process. Some programs provide approximate techniques for automatically estimating mesh discretisation error for certain types of analyses. This process of automatically evaluating mesh discretisation error and refining the mesh, called adaptive meshing [97], continues through a series of solutions until the measured error drops below some user defined value (or until a user defined limit on the number of solutions is reached). Using this measure of mesh discretisation error, the program can then determine if a particular mesh is fine enough. If it is not, the program will automatically refine the mesh so that the measured error will decrease.

4.1.4.3 Post-processor

The function of the post-processor is to enable the conversion of numerical results of a problem solution to useful and meaningful engineering quantities. The solutions consist of the nodal (or edge, or facet) values of potential, and element values of current or charge density, permeability or permittivity and many others. Any simple field quantity such as potential, field intensity, flux density, and current density can be displayed at points, along lines or as contour plots over regions. Hence, the post-processor provides the most important initial step for engineer to establish the likely validity of the overall form of the solution by examining graphically its principal features in the light of geometry, boundary conditions and sources of excitation. Conceptually, a post-processor is a computer tool capable of manipulating the field solutions in much the same way as a hand calculator manipulates numbers.

Another aspect of post-processing is to help the user to compare results for a number of closely related problems, each having slightly different geometry, material properties and source strengths. This leads directly back to the input pre-processor where design changes are defined, and thus heuristic procedure begins all over again. At this point the question of optimisation arises; thus it is the designer's role to provide creativity and to devise an effective algorithm in order to obtain the optimised solution in time.

4.2 Detailed design considerations and modelling

The use of an existing stator lowers the costs but restricts the flexibility to control the voltage waveforms; thus careful positioning and shaping of the flux diverters and HTS field winding become very important. Furthermore, due to the anisotropic properties of the superconducting tape, it is necessary to control the magnetic field normal to the broad face of the tape. In addition, the machine will be subjected to the effect of harmonics in MMF, voltage and current as a result of spatial harmonics and possibly of those from electrical harmonic sources. Spatial harmonics are basically due to two phenomena: first, electrical windings in the rotor and stator are not perfectly distributed about the air-gap circumference, but are grouped in discrete bundles known as phase

belts, and secondly, the magnetic surfaces of both the rotor and stator are non-uniform and may consist of alternate magnetic and non-magnetic regions due to salient pole structure. The requirements mentioned above are very different from the usual design criteria for a conventional generator. In the following sections, various rotor designs that have been considered since early stages of the project are reported. A series of finite-element simulations were performed to evaluate the behaviour of the field distribution.

4.2.1 Preliminary rotor construction

The early designs of the rotor were of the cylindrical type, but with all the slot sides parallel. This modification to the normal non-salient rotor design was used so that the superconducting coils would all be flat. The first thought to have a cylindrical rotor design was due to the fact that the distributed windings exhibit a better voltage waveform when compared to a salient type rotor, and are also more suitable for high speed operation. This design not only gives a better voltage waveform, but also offer some savings of superconducting tapes. Figures 4.2 and 4.3 show the earliest cylindrical rotor designs and results obtained from 2D finite-element analysis. Both the total resultant root-mean-square (*rms*) harmonic voltage and field distribution normal to the broad face of the tape were found to have met the original requirements.

While it appeared that the above design could deliver satisfactory performance, it would be difficult to build due to the different inner diameters of each HTS coil. It was therefore decided that a salient pole design should be investigated and was later adopted. This greatly reduced the risk of the project failure, since the coils could be wound separately and fitted to the core later. Moreover, by making all the coils identical, it was possible to produce spare coils to insure against the failure of any one coil.

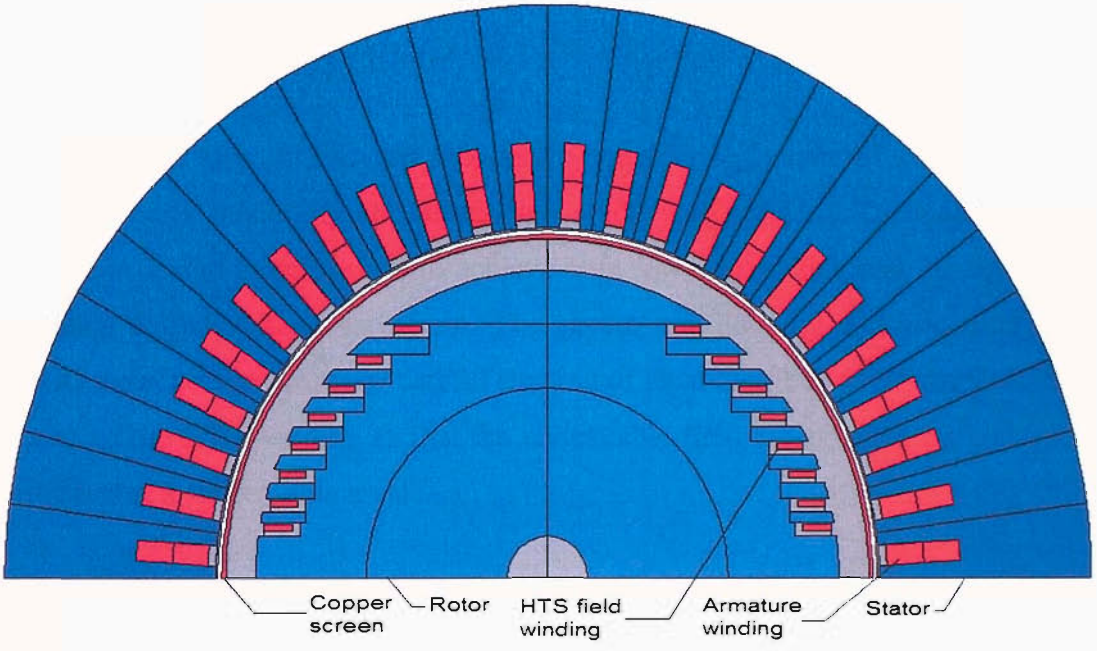

Figure 4.2 Preliminary design of the round rotor.

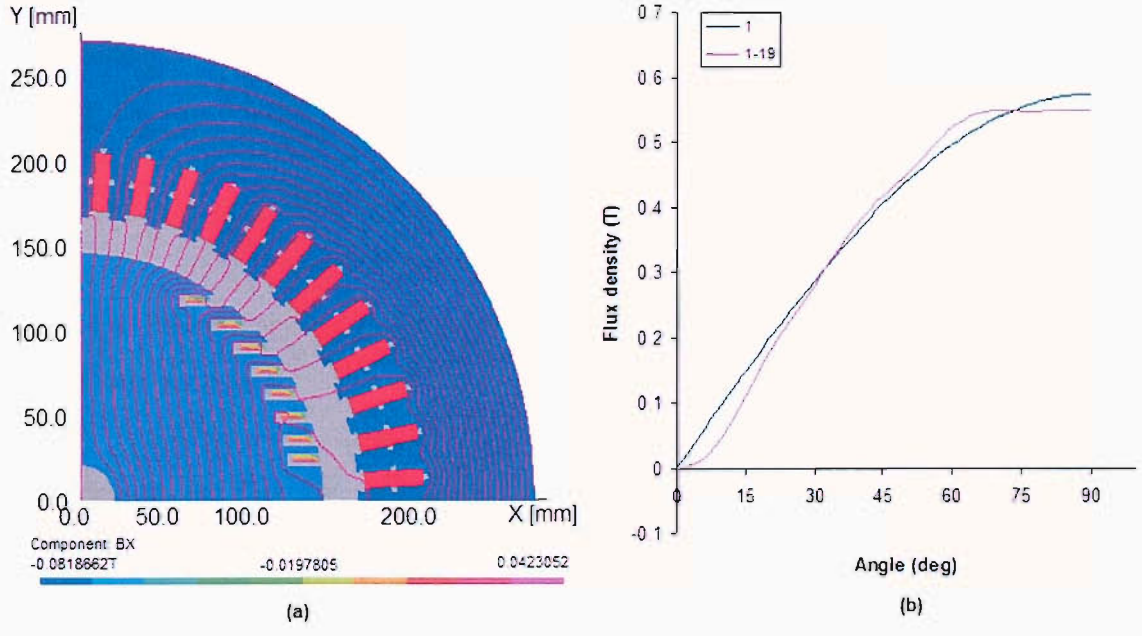

Figure 4.3 The results of the preliminary design: (a) Flux lines and normal field distribution in the coils, and (b) Air-gap flux density waveform from 1-19th harmonic

4.2.2 Hybrid salient pole rotor

4.2.2.1 Invar core

In a salient pole rotor, the air-gap flux density waveform is expected to be much worse, thus a thorough modelling and simulation study was required. Development of the salient pole design therefore had to achieve both low normal fields in the coils, and an acceptable output voltage waveform. The severe non-linearity and anisotropy of the BSCCO tapes necessitates very careful shaping of local distribution of magnetic field in the area of the HTS winding so that the undesirable field components are reduced and maintained at an acceptable level.

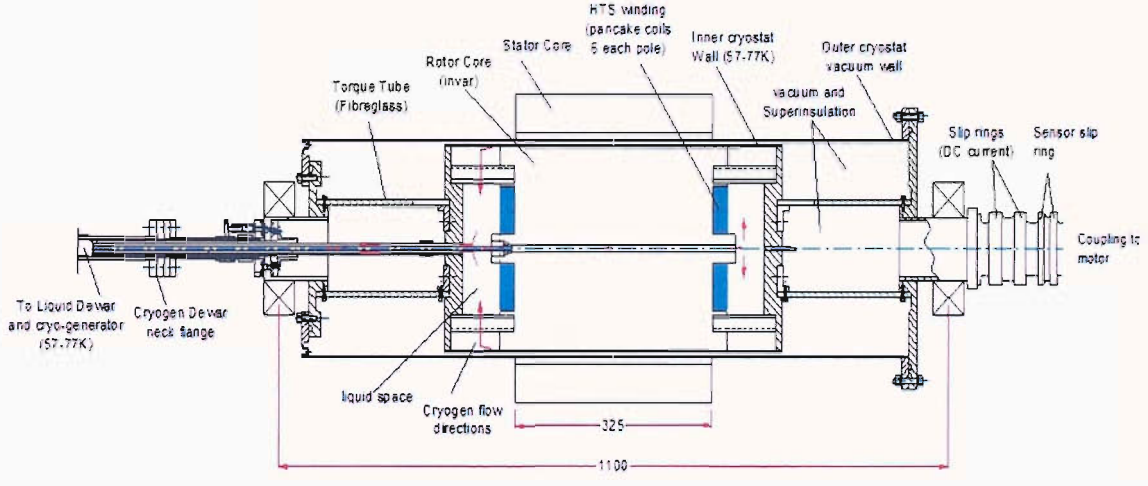

Figure 4.4 Preliminary design of the hybrid salient pole rotor of a 100kVA HTS synchronous generator

In this design, the flux diverters and rotor core of the generator are made of Invar and equipped with a high temperature superconducting field winding made of Ag-clad Bi-2223 tapes. Figure 4.4 shows the overview of the HTS generator. The superconducting winding consists of twelve 50 turns identical flat coils. In order to model the generator, it was desirable to reduce the region considered as far as possible by making use of symmetry. In this case the stator had an integer number of slots per pole per phase, thus only one half pole pitch of the generator needed to be considered for no-load

calculations. Hence, the symmetry of the machine was exploited by considering a quarter of the area; regions are bounded by the rotor polar axis, the inter-polar axis and the back of the stator core; the rotor polar axis and back of the stator core were taken as flux lines with A=0 and the rotor inter-polar axis had a zero normal derivative. Non-linear analysis was performed throughout since saturation of the magnetic flux diverters was thought to be important. The BH curve of Invar36 from Figure 3.6 was used for the analysis.

The initial shape of the salient pole rotor together with its flux diverters is as shown in Fig. 4.5. The mesh is generated automatically based on the defined input data of the coordinates and subdivisions of the sides of the regions. The elementary rule for a good FE mesh is that more points should be placed where the field variation is expected to be high. Figure 4.6 shows the mesh generated (total 14194 elements) using mixed quadrilateral and polygon shape elements.

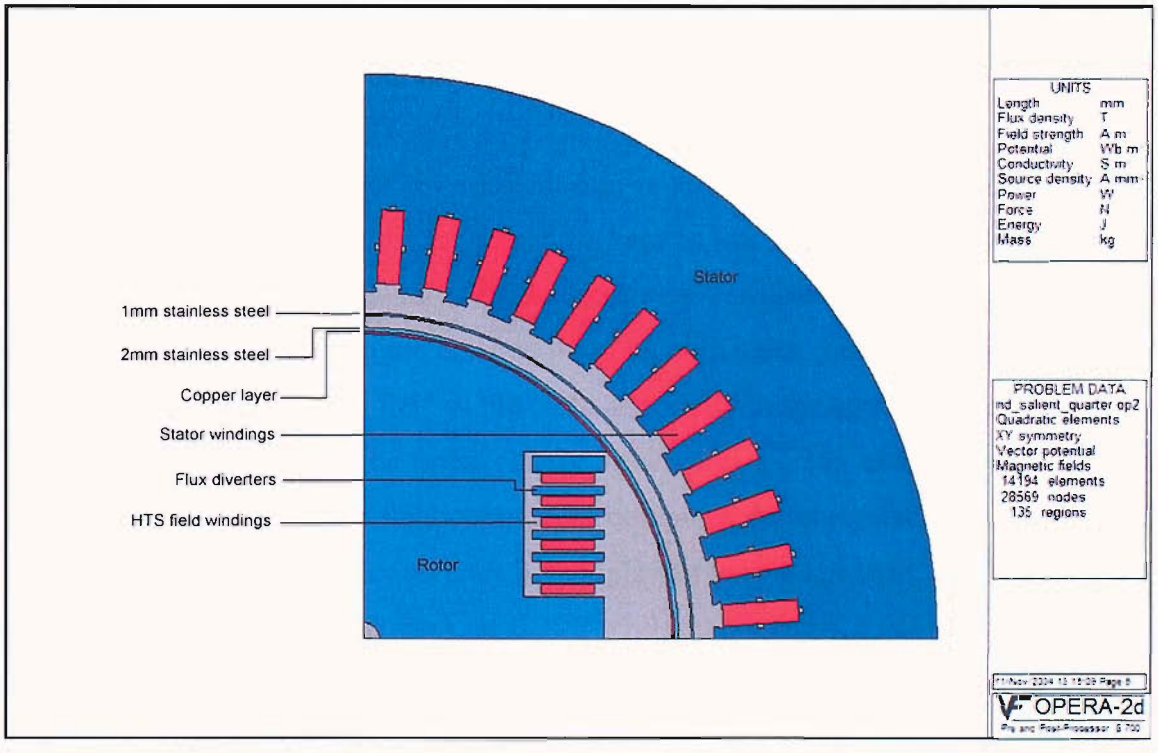

Figure 4.5 2D model of the salient pole rotor

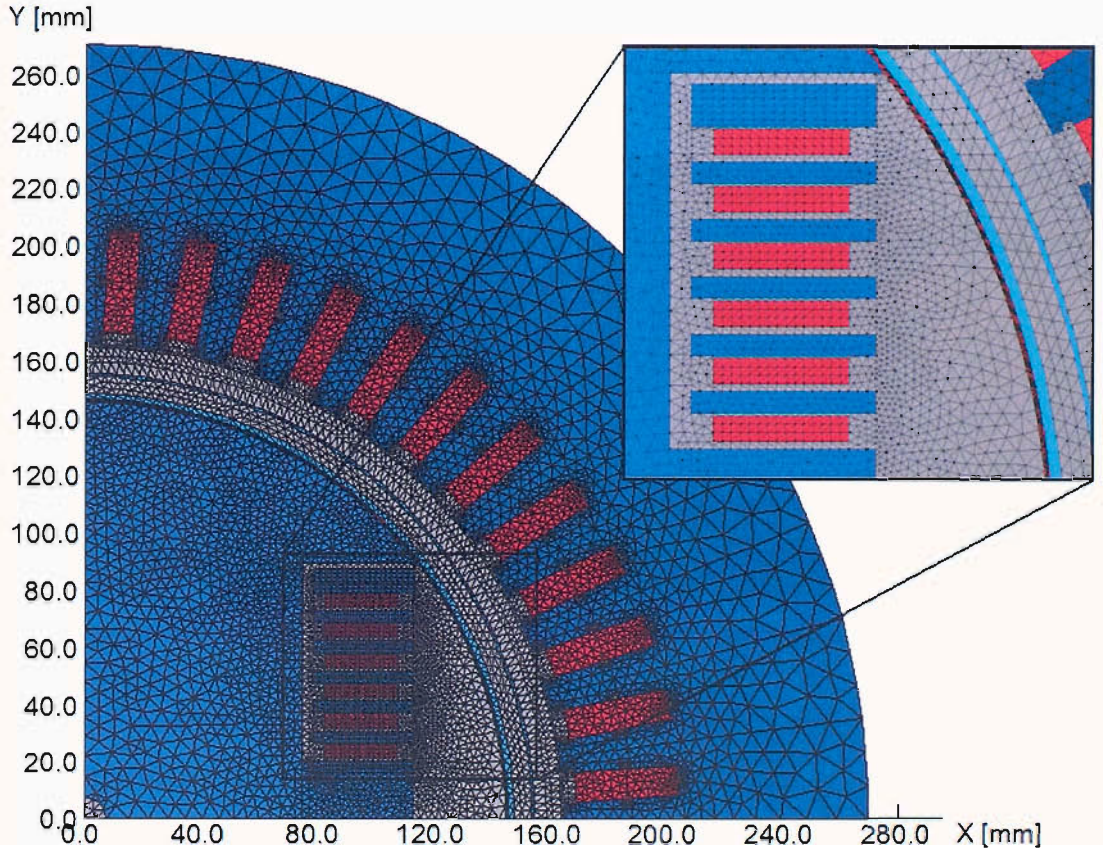

Figure 4.6 The mesh generated for the 2D analysis

The target air-gap density of the rotor design is around 0.6T, while the flux density normal to the broad face of the tape must be kept as low as possible. Therefore, based on the previous experience with HTS demonstrator transformer [1], the flux diverters were made to be longer than the coils by 4mm on both sides. This significantly reduces the undesirable high normal field in the coils, especially in the corner region. The effect of the flux diverters can be seen clearly in Figure 4.7 (a) and (b), which show distribution of the magnetic field component normal to the broad face of the tape ($\boldsymbol{B}_x$). The effect of placing one flux diverter in the relevant area is apparent. In Figure 4.7 (a), the normal field in the coils peak at 0.28T while in Figure 4.7 (b), the flux diverter located on top of the uppermost coil reduces it to 0.17T. As explained earlier in Chapter 4, the normal field higher than 0.1T would significantly reduce the critical current and could cause the coils to loose superconducting properties. By positioning all the flux

diverters directly on top of the coils, further reduction of the undesirable magnetic field normal to the broad face of the tape is achieved as shown in Fig. 4.8.

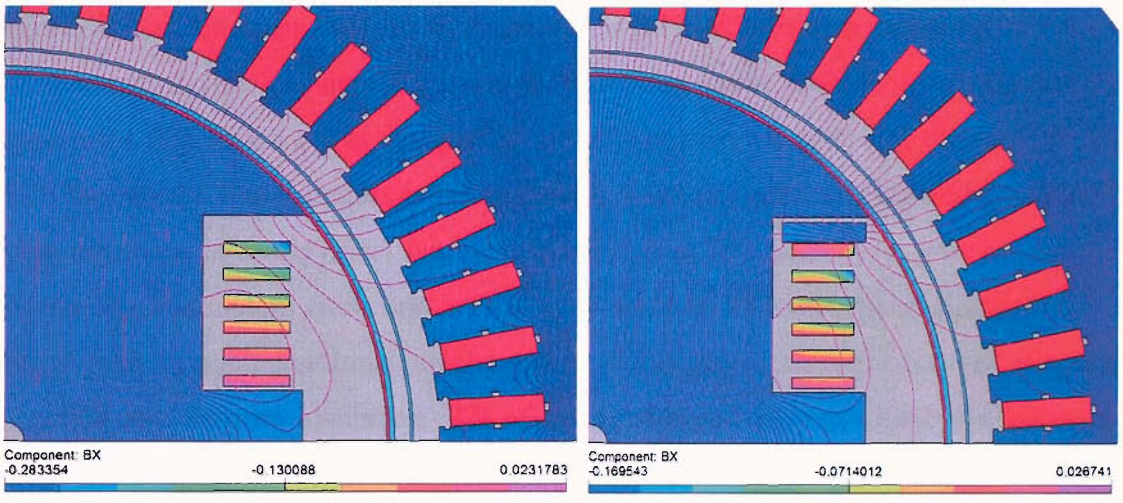

(a) (b)

Figure 4.7 The distribution of the normal field in the HTS coils and flux lines in the rotor: (a) Without flux diverter, and (b) With one flux diverter

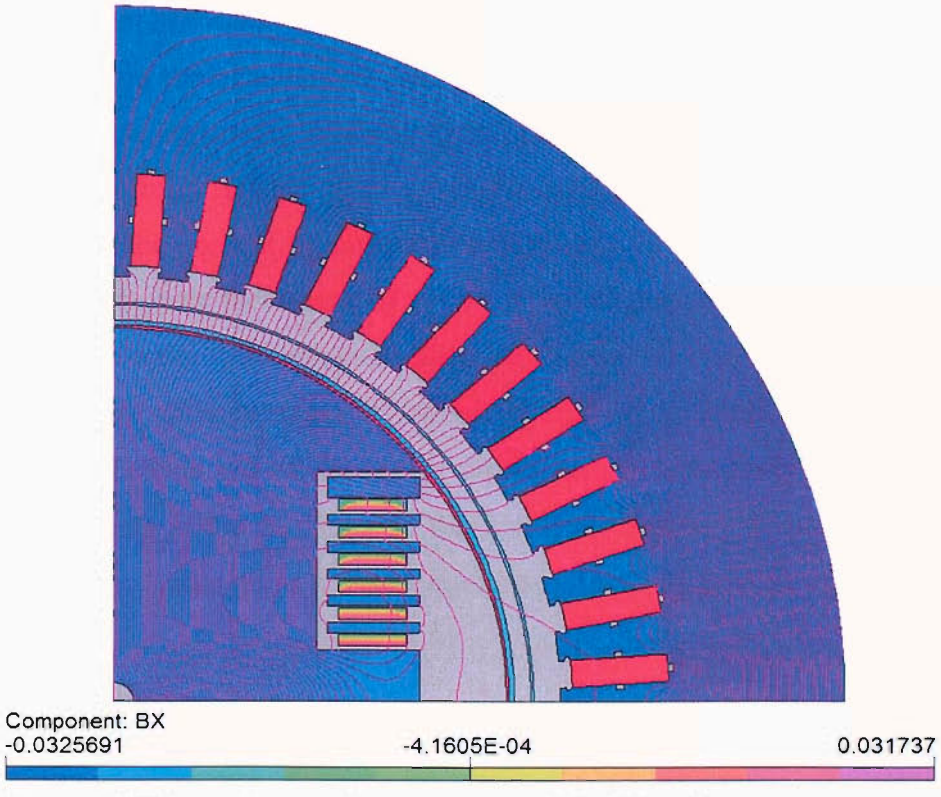

Figure 4.8 The position and arrangement of the flux diverters

With this design, an air-gap flux density of about 0.79T can be achieved when operating at 77K with a DC current of 54A, which produces a maximum normal field component of 0.033T in the winding (as shown in Fig. 4.8). From the flux lines plotted in the figure, it can be seen that these rings are highly effective in reducing the normal component of flux density in the superconducting coils. Due to iron saturation the uppermost flux diverter was designed to be thicker than the rest. The distance from the HTS tape to the flux diverters is 0.5mm and 1.5mm respectively (top and bottom). The gaps are there to avoid short circuit contact and at the same time provide space for connecting conductors from one HTS coil to another. The air-gap was designed to be larger than in a conventional machine due to the space required for the supporting structure and thermal insulation. All of the HTS racetrack coils have the same inner diameter, number of turns, and thickness. These constraints significantly reduce the amount of work involved during the manufacturing process, thus making the design less prone to failure.

The above modelling analyses successfully optimised the undesirable magnetic field component normal to the broad face of the tape to an acceptable level. However, when considering superconducting machines with large air gaps, their synchronous reactance is low; consequently, small voltage harmonics can drive significant currents in the external circuit. Hence, shaping of the pole face of the rotor is necessary to aim at reducing the content of undesirable harmonics in the voltage waveform. In order to analyse the pole face shape of the rotor, the magnitudes of the sine components of odd harmonic order were extracted using Fourier series. These data can be used to construct the voltage waveforms and the resultant *rms* value. When the Fourier series are fitted, the coefficients (β) of the series expansion are calculated. Only changes in the sine components of the flux density harmonics are considered, since the geometry has odd symmetry. These terms are calculated by performing the following integrals:

$$\beta_n = \frac{4}{\pi} \int_0^{\pi/2} B_r \sin(4n\theta)\, d\theta \tag{4.1}$$

where

$$B_r = B_x \cos(\theta) + B_y \sin(\theta), \tag{4.2}$$

where n is the harmonic order, θ is the angle from the point on the circle to the local x axis, $\boldsymbol{B}_r$ is the radial flux density, and $\boldsymbol{B}_x$ and $\boldsymbol{B}_y$ are the x and y component of flux density. It should be noted, as mentioned before, that due to symmetry the air-gap flux-density waveform contains no even harmonics.

In order to obtain the actual harmonic contributions, the winding factor must be included in the evaluations. The winding factor reflects the reduction in voltage due to short pitching and distributed phase belts. The winding factor is defined as

$$K_{w_n} = K_{p_n} K_{d_n} \tag{4.3}$$

where K_p is the pitch factor

$$K_{p_n} = \sin\left(\frac{n\pi\beta}{s}\right) \tag{4.4}$$

and K_d is the distribution factor

$$K_d = \frac{\sin\left(\frac{n\alpha S_{pm}}{2}\right)}{S_{pm}\left(\sin\frac{n\alpha}{2}\right)} \tag{4.5}$$

where n is the harmonic order, β is the coil pitch, s is the pole pitch, S_{pm} is the number of slots per phase per pole, and α is the slot pitch. The pitch factor is determined by the spatial location of the coil sides with respect to the magnetic axes of the north and south poles. The distribution factor is the ratios of flux linked by a given winding to the flux that would have been linked by that winding if it were fully pitched [101].

The total resultant *rms* harmonic voltage, also known as distortion factor, F_D, of a wave is obtained by dividing the *rms* harmonic content (the square root of the sum of the squares of the *rms* amplitudes of all frequency components except the fundamental), by the *rms* value of the wave including the fundamental, and it is usually represented in percentage form as

$$F_D = \frac{\sqrt{\sum E_n^2}}{E_{rms}} \tag{4.6}$$

where $\sum E_n^2$ is the sum of squares of all components of the voltage except the fundamental and E_{rms} is the rms value of the voltage [106]. In most cases, the amplitudes of the harmonics decrease as the order of the harmonic increases so that determination of the amplitudes of the first few harmonics is all that is needed to obtain a satisfactory value of the distortion factor. However, if the waveform indicates the presence of significant high frequency ripples, the harmonics of relatively high frequencies may have significant amplitudes, and thus should be included in the evaluation.

The salient pole rotor design of the previous section was found to produce total resultant *rms* harmonic voltage or F_D of 3.672%. As mentioned earlier, the air-gap flux density waveform, especially due to the 5th space harmonic for the hybrid salient pole structure, is much worse when compared to a cylindrical rotor (see Fig. 4.9). Table 4.1 shows the harmonic component values extracted directly from the program. This confirms earlier assumption that the air-gap flux-density waveform contains no even harmonics and only sine components. Table 4.2 shows the actual values of individual harmonics up to the 19th taking into account the winding factor and the harmonic contribution. The waveforms of the harmonic components were plotted as shown in Figure 4.10 and it was found that the 5th space harmonic contributes significantly. The higher order fields are reduced by the distribution of the phase conductors throughout each phase belt. The 5th harmonic of the stator MMF is causing substantial losses in the cold region (as this

will be explained in details in Chapter 5 and [98]) and undesirable harmonic voltage in the external circuits.

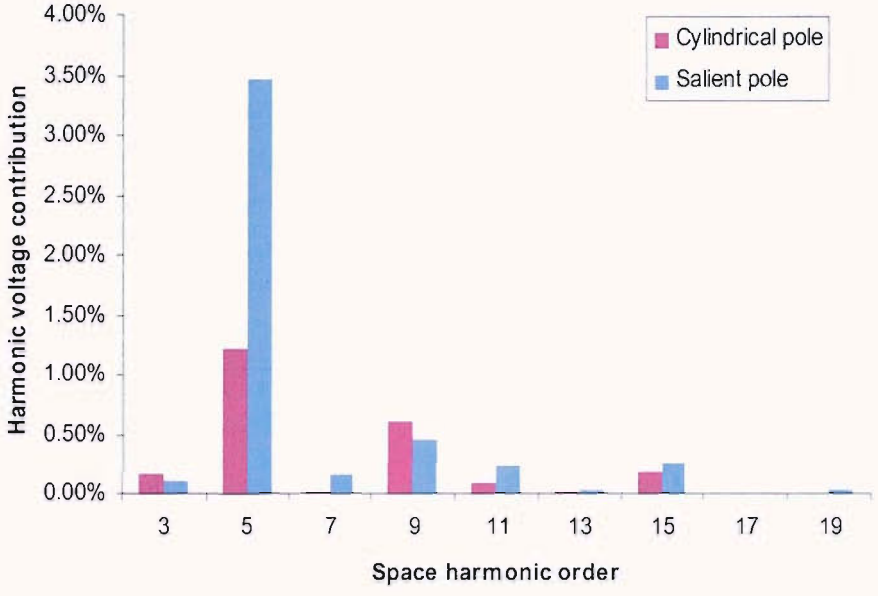

Figure 4.9 The harmonic component for cylindrical and hybrid salient pole rotor

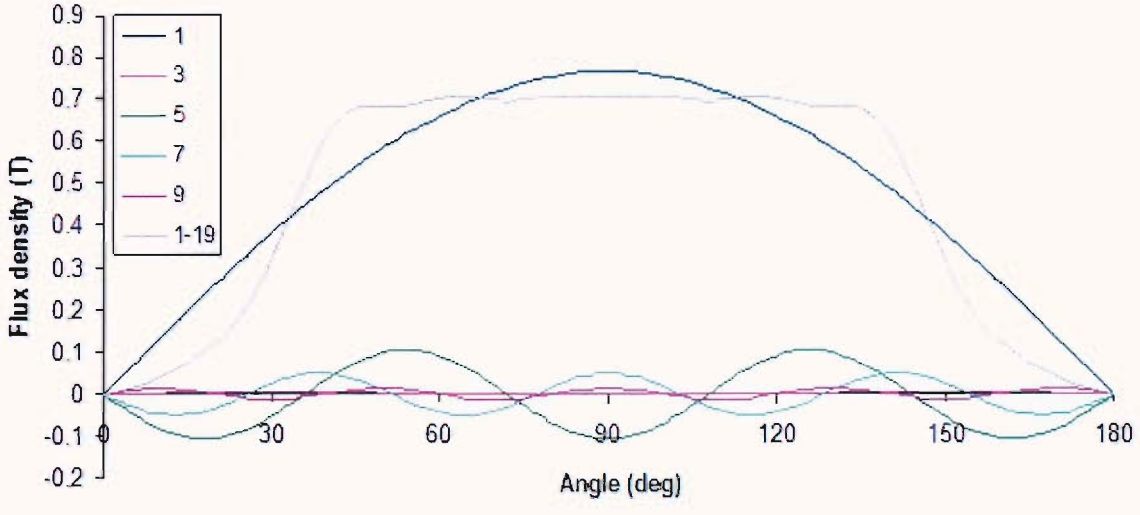

Figure 4.10 Voltage waveform of the salient pole rotor

Table 4.1 Harmonic components of air-gap flux density

Harmonic order no.	Sine term	Cosine term	Harmonic order no	Sine term	Cosine term	Harmonic order no	Sine term	Cosine term
1	-7.657E-01	-9.330E-07	18	-2.767E-17	9.330E-07	34	1.295E-16	9.330E-07
2	1.009E-17	9.330E-07	19	-3.475E-03	-9.330E-07	35	3.882E-04	-9.330E-07
3	-2.764E-03	-9.330E-07	20	8.964E-17	9.330E-07	36	-4.147E-17	9.330E-07
4	-9.400E-17	9.330E-07	21	-3.969E-03	-9.330E-07	37	1.302E-03	-9.330E-07
5	1.047E-01	-9.330E-07	22	-2.483E-16	9.330E-07	38	2.337E-17	9.330E-07
6	-3.890E-17	9.330E-07	23	8.177E-05	-9.330E-07	39	3.703E-04	-9.330E-07
7	4.951E-02	-9.330E-07	24	-8.563E-17	9.330E-07	40	4.212E-16	9.330E-07
8	2.587E-18	9.330E-07	25	2.399E-03	-9.330E-07	41	-2.209E-03	-9.330E-07
9	-1.290E-02	-9.330E-07	26	2.520E-16	9.330E-07	42	2.073E-17	9.330E-07
10	-2.805E-17	9.330E-07	27	7.898E-04	-9.330E-07	43	-5.011E-03	-9.330E-07
11	-2.338E-02	-9.330E-07	28	4.256E-17	9.330E-07	44	-4.899E-17	9.330E-07
12	-4.165E-17	9.330E-07	29	-9.587E-04	-9.330E-07	45	-4.855E-04	-9.330E-07
13	-4.496E-03	-9.330E-07	30	-2.748E-17	9.330E-07	46	-1.189E-16	9.330E-07
14	-1.256E-16	9.330E-07	31	-8.861E-04	-9.330E-07	47	3.206E-02	-9.330E-07
15	1.094E-02	-9.330E-07	32	5.098E-18	9.330E-07	48	4.813E-17	9.330E-07
16	-4.427E-18	9.330E-07	33	-1.238E-04	-9.330E-07			
17	5.628E-03	-9.330E-07						

Table 4.2 Harmonic components of air-gap flux density of the salient pole rotor (Total *rms* harmonic voltage 3.532%).

Space Harmonic Order	Sine Harmonic Magnitude	Winding Factor	Actual Harmonic	% Harmonic Voltage Contribution
1	0.765714	0.758138	0.580517	100
3	0.002764	0.245196	0.000678	0.12
5	-0.104740	0.192774	0.020191	3.48
7	-0.049508	0.018445	0.000913	0.16
9	0.012903	0.207867	0.002682	0.46
11	0.023384	0.057705	0.001349	0.23
13	0.004496	0.050606	0.000228	0.04
15	-0.010940	0.138893	0.001519	0.26
17	-0.005628	0.009096	0.000051	0.01
19	0.003475	0.065438	0.000227	0.04

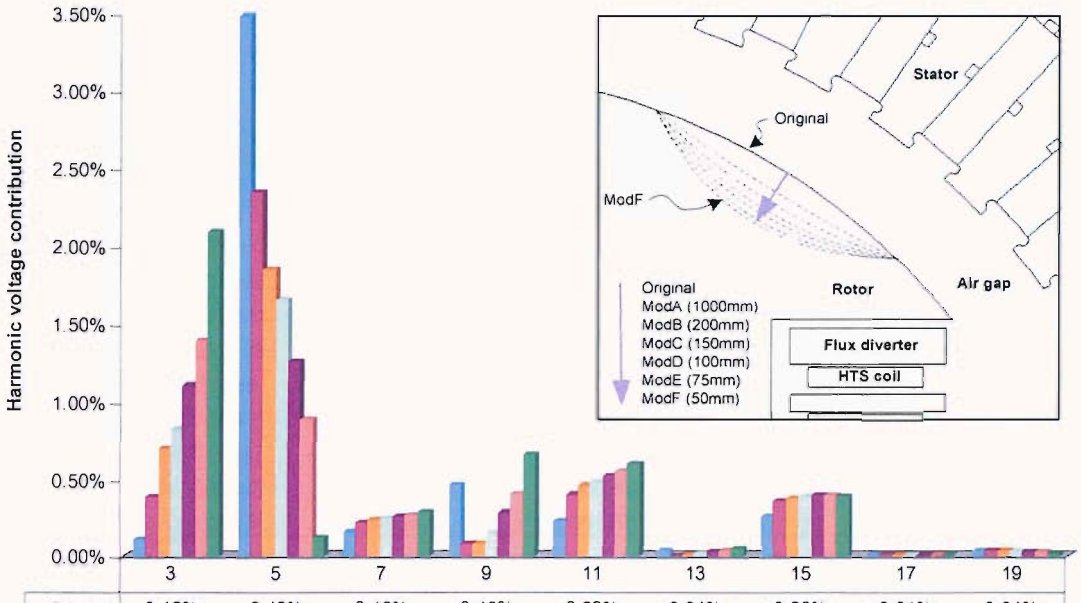

	3	5	7	9	11	13	15	17	19
Original	0.12%	3.48%	0.16%	0.46%	0.23%	0.04%	0.26%	0.01%	0.04%
ModA	0.38%	2.35%	0.22%	0.08%	0.40%	0.00%	0.35%	0.01%	0.04%
ModB	0.69%	1.85%	0.24%	0.08%	0.46%	0.01%	0.38%	0.00%	0.03%
ModC	0.82%	1.65%	0.25%	0.15%	0.48%	0.02%	0.38%	0.00%	0.03%
ModD	1.10%	1.26%	0.26%	0.28%	0.51%	0.03%	0.39%	0.00%	0.03%
ModE	1.40%	0.89%	0.27%	0.41%	0.55%	0.03%	0.39%	0.00%	0.03%
ModF	2.09%	0.12%	0.28%	0.65%	0.60%	0.05%	0.38%	0.00%	0.02%

Figure 4.11 The harmonic voltage contribution up to 19th order for different 'scallop' radius curvature

In order to minimise the undesirable harmonics, a series of models were built with different 'scallop' radius intersecting the 145 mm radius at 20° and 45° from the centre of the pole face. The specified region was selected in order to reduce the gap density where the 5th harmonic contribution is positive. The radius curvature of the 'scallop' was varied from 1000 mm (ModA) up to the maximum allowable radius of 50mm (ModF). Figure 4.11 (inset) illustrates the region where the radius was varied and the results of the analysis. As can be seen clearly from the above diagram, the 5th space harmonic was reduced significantly compare to the original design. The total resultant *rms* harmonic voltage was also reduced to 1.84% with the 'scallop' radius curvature (ModD) of 100 mm and the voltage waveform is shown in Fig. 4.12. Ideally, the undesirable harmonics could be further suppressed by extending the intersecting radius to 60°, but this would interfere with the mechanical constraints.

Table 4.3 Harmonic components of air-gap flux density of the modified salient pole rotor with 'scallops' (Total *rms* harmonic voltage 1.835%).

Space Harmonic Order	Sine Harmonic Magnitude	Winding Factor	Actual Harmonic	% Harmonic Voltage Contribution
1	0.749026	0.758138	0.567865	100
3	-0.025480	0.245196	0.006247	1.10
5	-0.037188	0.192774	0.007169	1.26
7	-0.079565	0.018445	0.001468	0.26
9	-0.007703	0.207867	0.001601	0.28
11	0.050638	0.057705	0.002922	0.51
13	-0.002805	0.050606	0.000142	0.03
15	-0.015937	0.138893	0.002214	0.39
17	-0.002183	0.009096	0.000020	0.00
19	0.002605	0.065438	0.000170	0.03

The modification successfully reduced the undesirable fifth harmonic as shown in Table 4.3 when compared to those values shown in Table 4.2, and more importantly the overall *rms* harmonic voltage was also reduced. The method used is simple, yet effective, by targeting the source of the problem directly. Moreover, the above modifications have demonstrated how the harmonic content of the voltage waveform could be reduced below acceptable maximum levels and at the same time maintaining the magnetic field normal to the broad face of the HTS tape to the minimum as shown in Fig. 4.13.

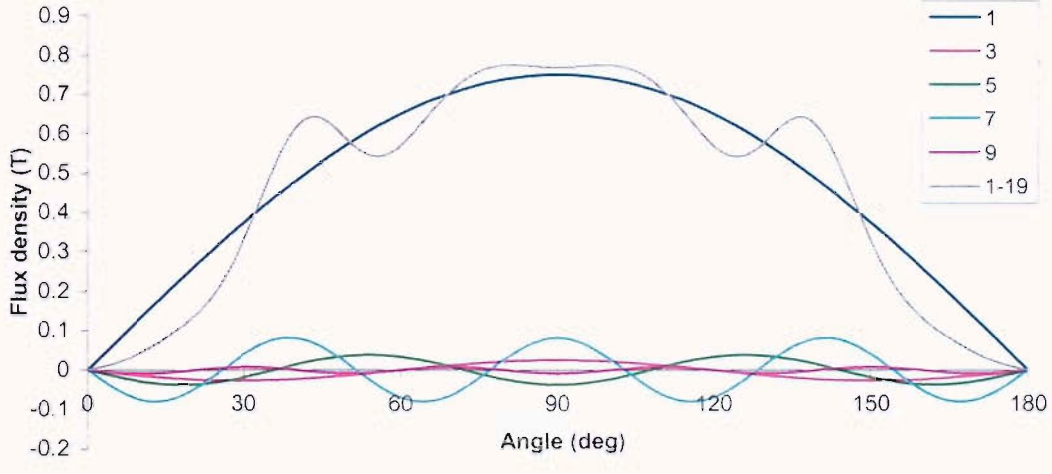

Figure 4.12 The air-gap field up to 19th order

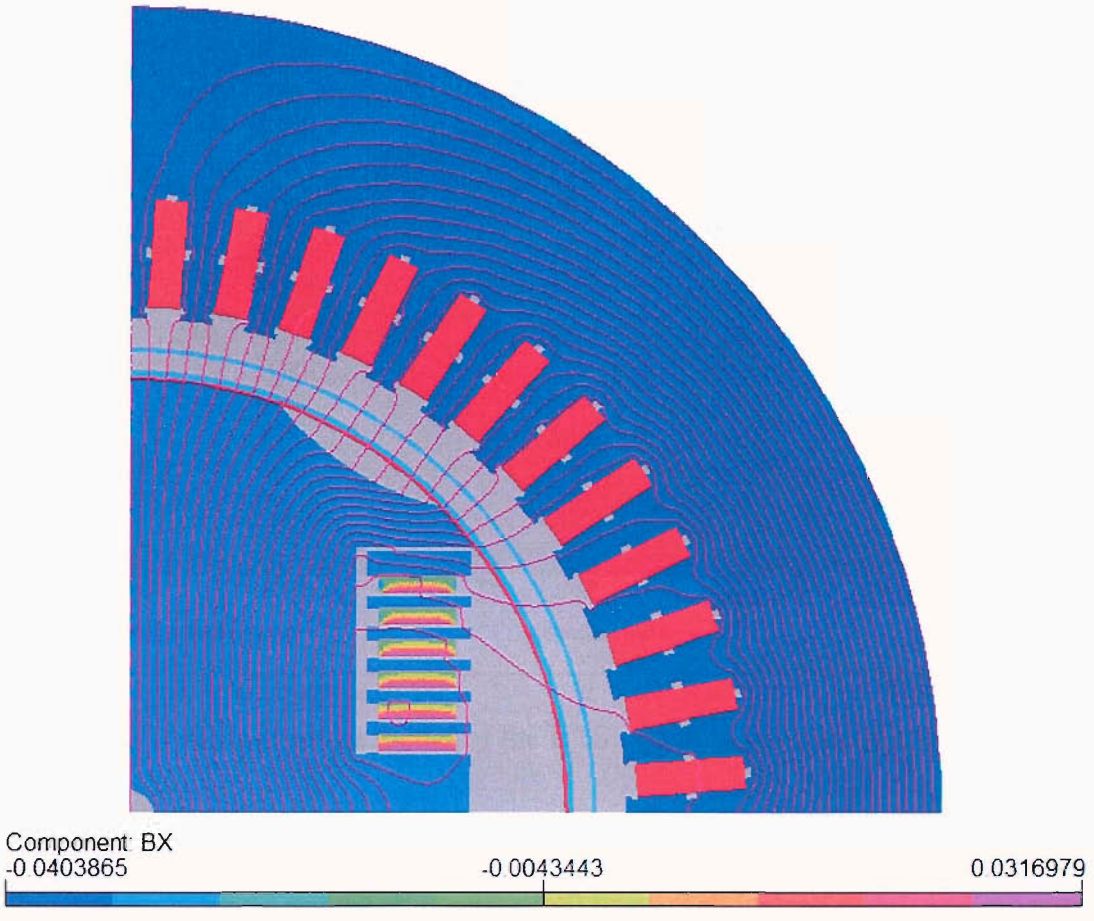

Figure 4.13 Flux lines and normal field distribution in the coils of the modified salient pole

4.2.2.2 9% Nickel steel core

In previous designs the rotor was made of Invar36, but this was later rejected, as large difference in thermal expansion coefficients would make it difficult to connect to stainless steel shaft. Moreover, the difficulties in obtaining the material of specified dimensions and of required quantity would greatly increase the project costs and introduce delays. Therefore, after thorough investigation, it was decided to use 9% Nickel steel to replace Invar36. Since the 9% Nickel steel is usually produced in plates of up to 30 mm, the rotor needed to be redesigned to accommodate the new material. Figure 4.14 shows the 2D model generated for finite-element analysis and changes made in the new design.

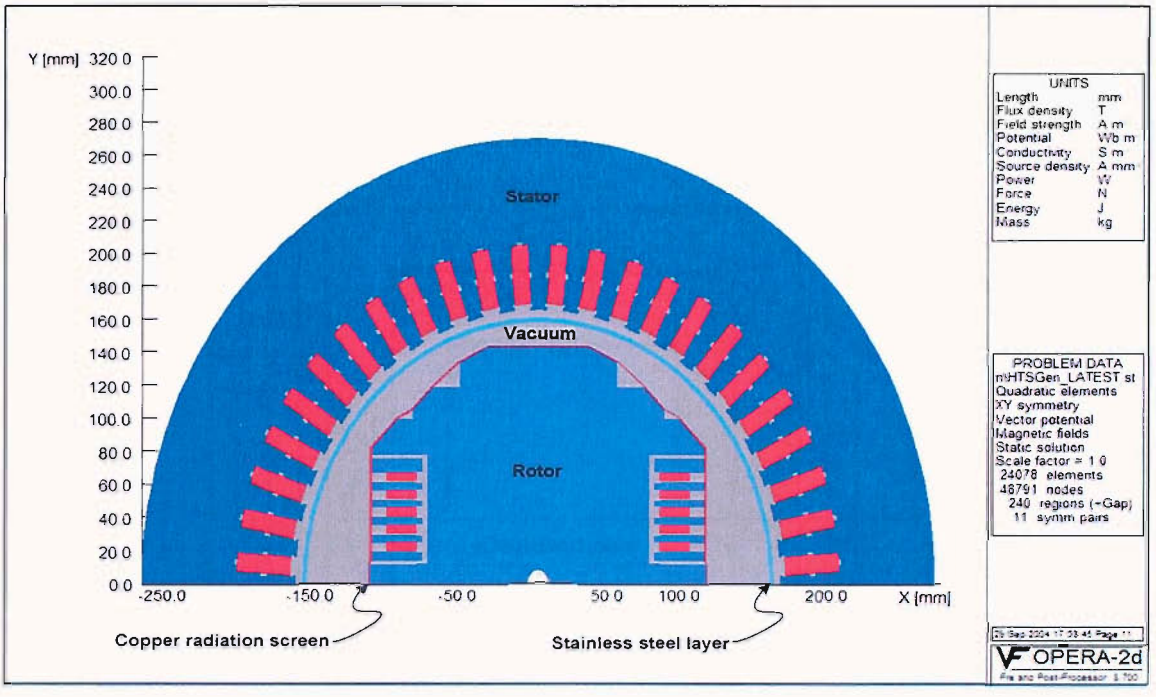

Figure 4.14 2D finite-element model of the HTS synchronous generator with 9% Nickel steel rotor

In this design, the field windings consist of 40 turns each instead of 50, and the number of coils was reduced to 10. These reductions were possible as the air-gap flux density obtained in the previous design was above the target value. This modification was necessary to provide more flexibility for placing the flux diverters and to allow space for support structure. The stainless steel layer, which was located directly on top of the copper screen in the previous design to hold the liquid nitrogen, was removed. The cold copper screen is placed directly around the rotor core. In the final design the required low temperature (77 K) would be radiated from the tubes which are carrying the circulating liquid nitrogen which are attached to the outer wall of the copper screen. Figure 4.15 shows the dimensions of half of the rotor core using the new 9% Nickel steel material. The hybrid salient pole rotor core is formed from a stack of 9% Nickel steel plates, which are tied together using through bolts. Each plate has a thickness of 22 mm except the centre plate which is 24 mm. The shape of the rotor pole face was obtained by fitting the three uppermost plates within the 145 mm radius.

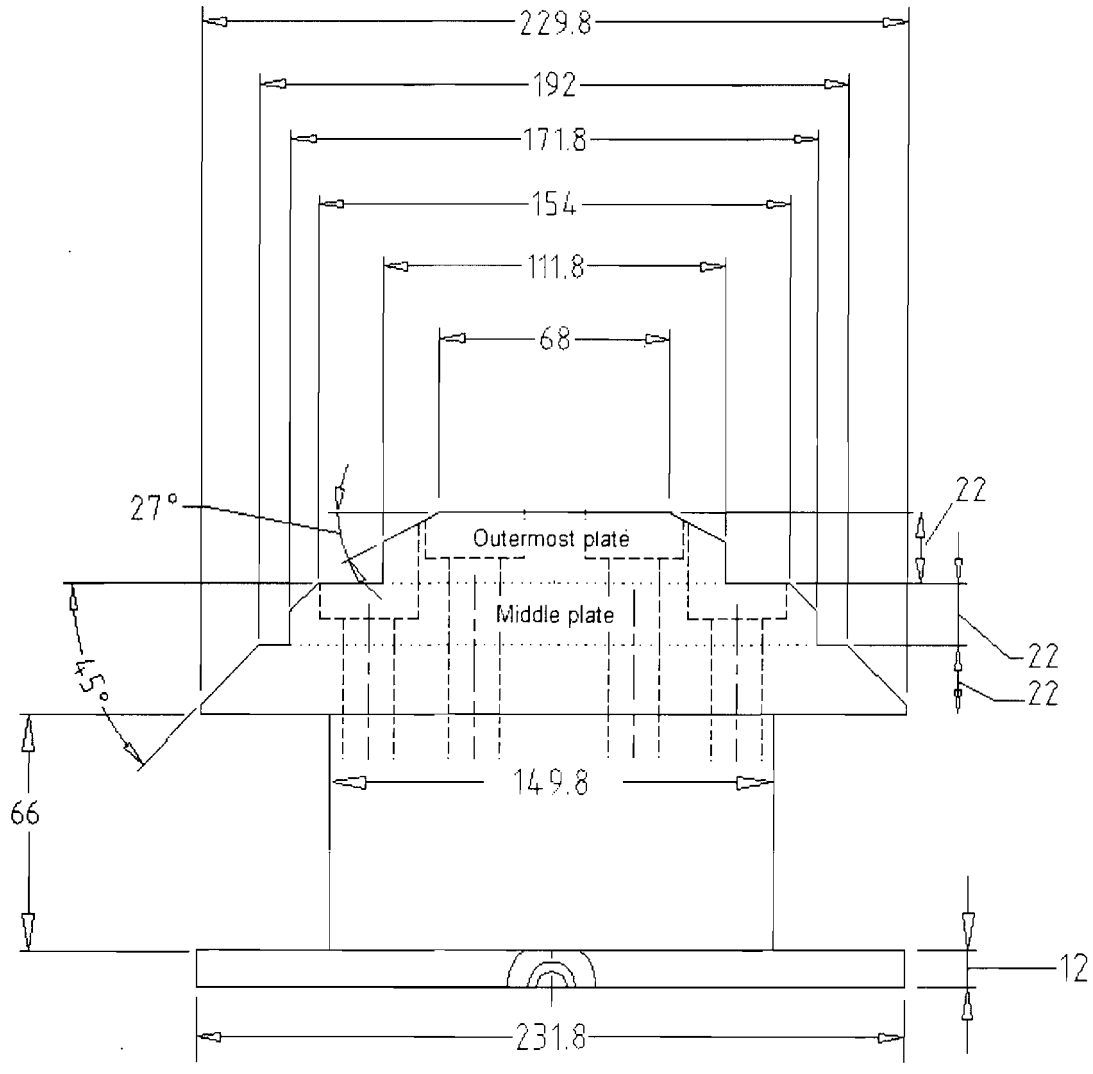

Figure 4.15 Dimensions of the latest rotor core

In order to analyse the magnetic field distribution of the machine, the static analysis option of OPERA program was used. This analysis module allows the inclusion of nonlinear material permeability such as the 9% Ni steel and the stator iron core. The field winding of the generator was excited with 64 A and the armature winding not loaded. Like in the previous rotor design, there is not much room for major modification as this has the effect on the overall design that may cause conflict with other critical mechanical requirements, which makes work more complicated. Hence, based on the constraints mentioned earlier, the slopes of 27°, 45° and 45° (from top to bottom plate),

as shown in Fig. 4.14, were introduced as a simple modification to determine the effect on overall voltage waveform.

The air-gap flux density of the new model was analysed and the total distortion factor was found to be 1.58%. Each individual harmonic component was evaluated and they are shown in Table 4.4. The results proved to be very encouraging; the distortion factor for this design has even better than the old design with Invar36 rotor. However, at a later design stage, it was realised that more space was needed in the outermost plate for the through bolts and also for connecting the stainless steel tubes. Hence, the outermost and the plate directly below it were modified to 24 mm and 19 mm thickness, respectively. The rotor would retain the same dimensions since the previous modelling results proved to be satisfactory, and at the same avoid any unnecessary complication. This is because part of the rotor components had already been drafted in detail and ready for machining. Therefore, this rotor design was approves for the generator project.

Table 4.4 Harmonic components of air-gap flux density of the modified hybrid salient pole rotor using 9% Nickel steel (Total rms harmonic voltage 1.58%).

Space Harmonic Order	Sine Harmonic Magnitude	Winding Factor	Actual Harmonic	% Harmonic Voltage Contribution
1	0.680197	0.758138	0.515683	100%
3	-0.015914	0.245196	0.003902	0.76%
5	-0.020723	0.192774	0.003995	0.77%
7	-0.036677	0.018445	0.000677	0.13%
9	-0.025937	0.207867	0.005392	1.05%
11	0.023856	0.057705	0.001377	0.27%
13	-0.005824	0.050606	0.000295	0.06%
15	0.013487	0.138893	0.001873	0.36%
17	-0.011672	0.009096	0.000106	0.02%
19	-0.002775	0.065438	0.000182	0.04%

The latest rotor design, and the potential variation together with the normal field distribution in the coils, were plotted as shown in Fig. 4.16. Plotting of flux lines or equipotentials provides useful way of checking the solution; it enables boundary condition errors to be spotted quickly, and areas where potential gradients change rapidly can be examined. Table 4.5 shows each individual harmonic component of air-

gap flux density and the gap field waveforms are shown in Fig. 4.17. Both the total rms harmonic voltage of 1.36% and the air-gap flux density of 0.66 T were found to be within the targeted value. The distribution of the relative permeability and magnitude of magnetic flux density in the generator were also analysed and they are shown in Figure 4.18 and 4.19 respectively. As expected, the stator is slightly saturated due to the applied MMF in the superconducting field windings. Although there were significant changes made to machine, the modified design still managed to maintain the required low normal field in the coils (see Fig. 4.16). Further evaluations and optimisation using 3D models were performed later to compare the results generated using 2D analysis and to confirm the effectiveness of the changes to the design in reducing the undesirable harmonics.

Table 4.5 Harmonic components of air-gap flux density and phase voltage of the latest hybrid salient pole rotor using 9% Nickel steel (Total rms harmonic voltage 1.36%).

Space Harmonic Order	Sine Harmonic Magnitude	Winding Factor	Actual Harmonic	% Harmonic Voltage Contribution
1	0.663765	0.758138	0.503225	100%
3	-0.003602	0.245196	0.000883	0.18%
5	-0.018884	0.192774	0.003640	0.72%
7	-0.042403	0.018445	0.000782	0.16%
9	-0.025105	0.207867	0.005218	1.04%
11	0.026205	0.057705	0.001512	0.30%
13	-0.006566	0.050606	0.000332	0.07%
15	0.011286	0.138893	0.001568	0.31%
17	-0.008739	0.009096	0.000079	0.02%
19	-0.004068	0.065438	0.000266	0.05%

Further improvement can be achieved by targeting appropriate area of the rotor pole face. It can be easily identified based on Fig. 4.17, that further improvement is attainable by optimising the areas the around 30° and 75° regions. However, changes are only feasible in the 75° region, since the other area would require major modification of the flux diverters which could affect the entire design. Hence, the outermost plate was reduced in length as shown in Fig. 4.20(a) by 3 mm while maintaining the same slope angle as in the previous model. Figure 4.20(b) shows the results of the modified rotor and the distortion factor was found to have improved to 1.024%. It shows clearly that

almost all the harmonics were eliminated; although the 7th space harmonic is significant, it was reduced by the distribution of the phase conductors throughout each phase belt (inclusion of winding factor).

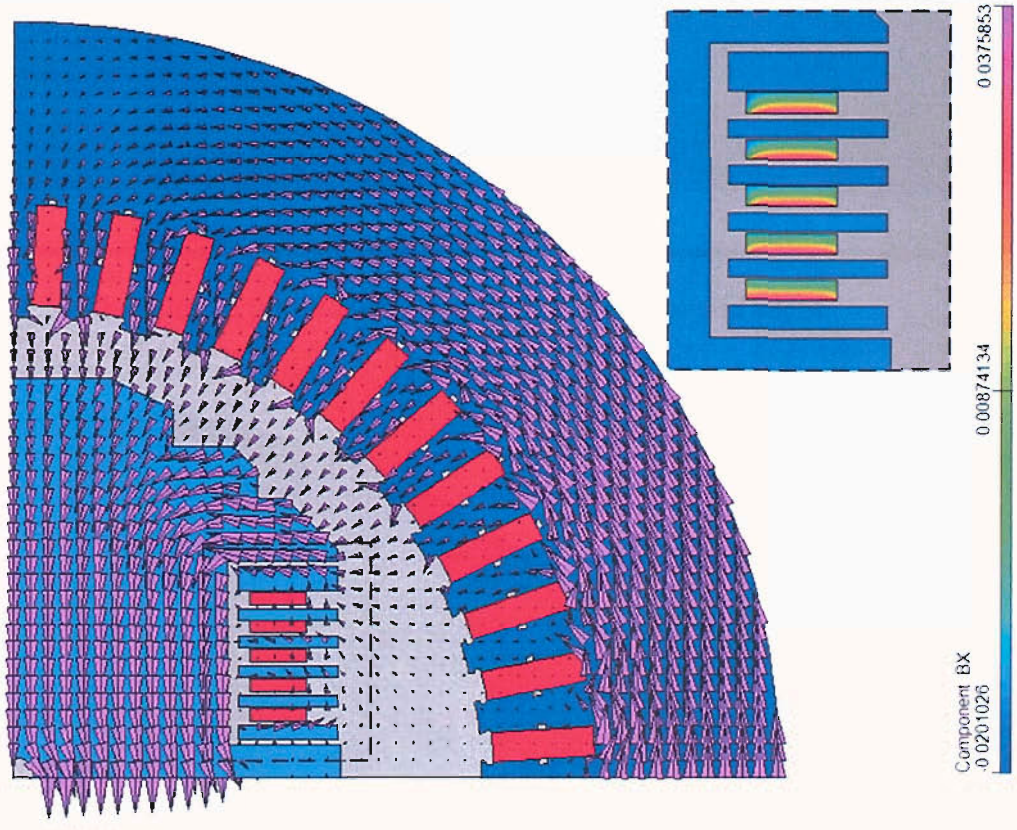

Figure 4.16 The vector potential and normal field distribution in the HTS coils

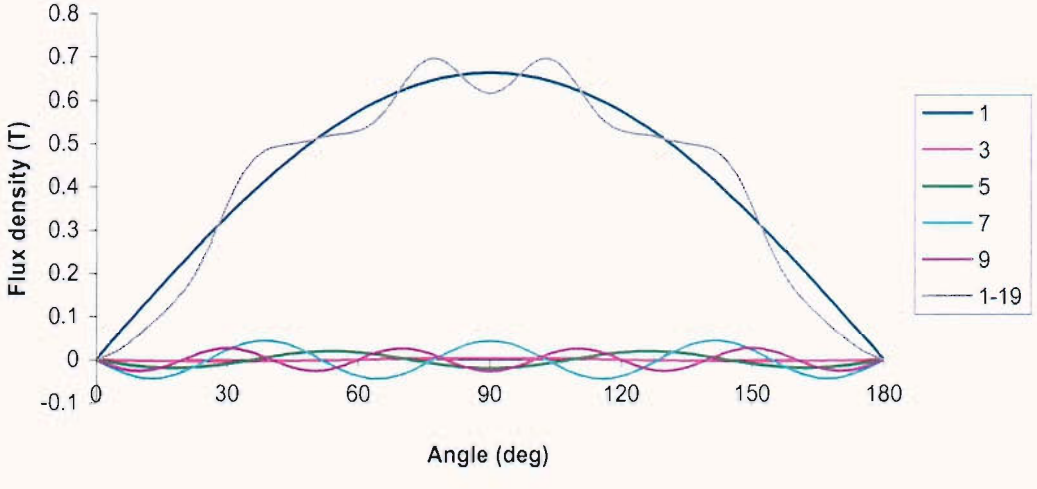

Figure 4.17 Air-gap flux density waveform of the latest rotor

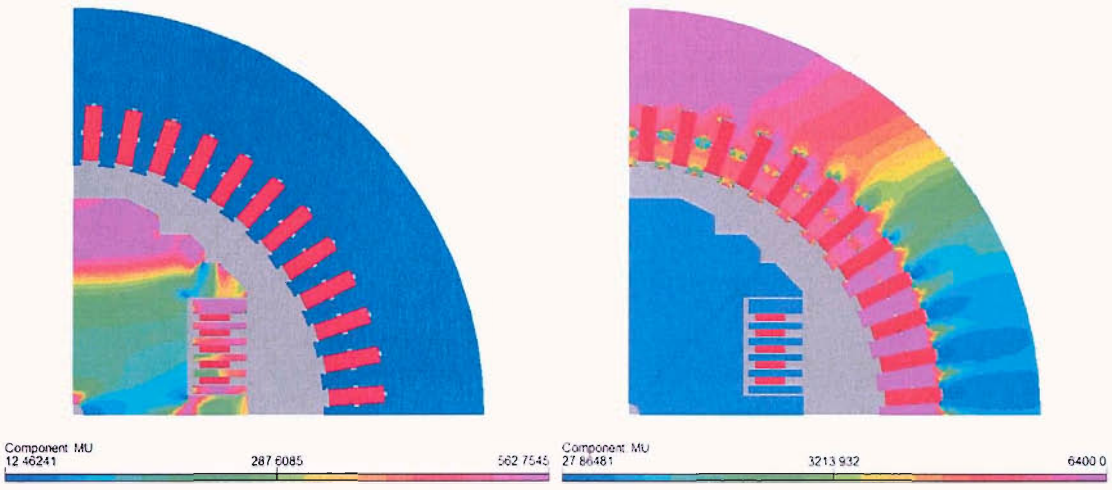

Figure 4.18 The relative permeability distribution the rotor and stator

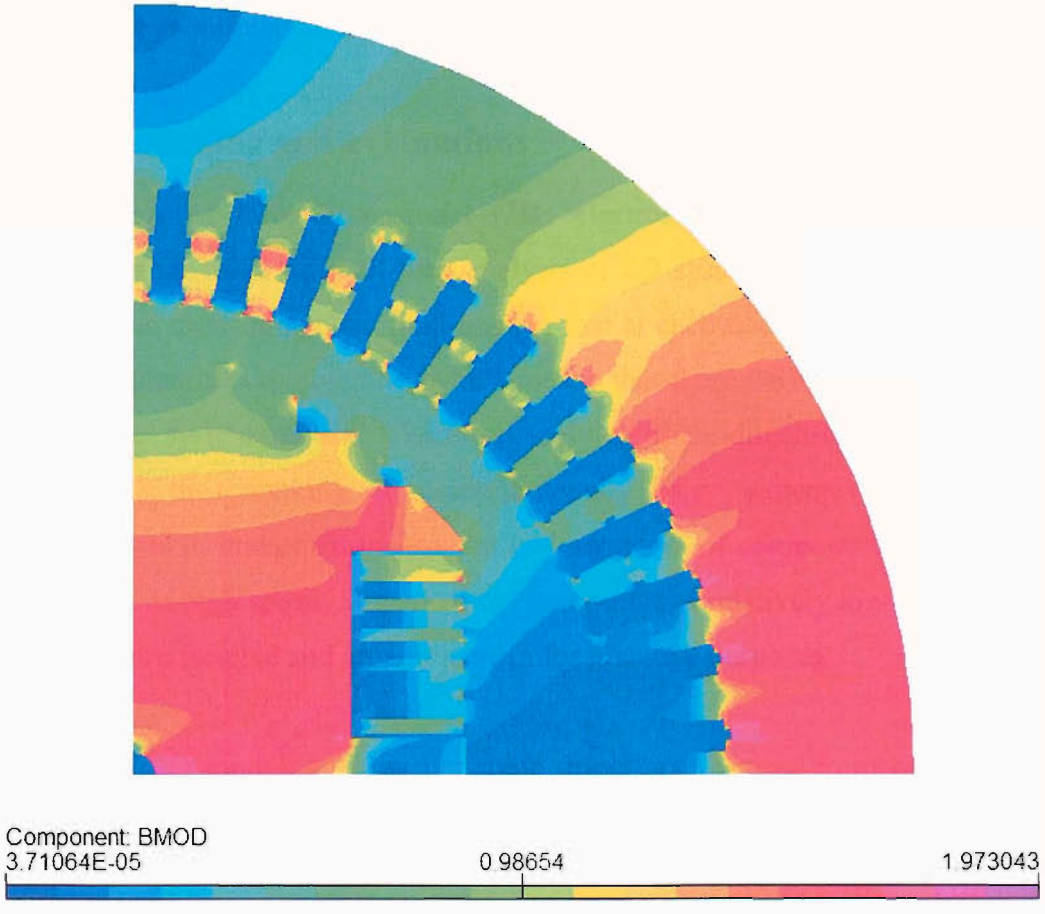

Figure 4.19 Magnitude of magnetic flux density contour plot

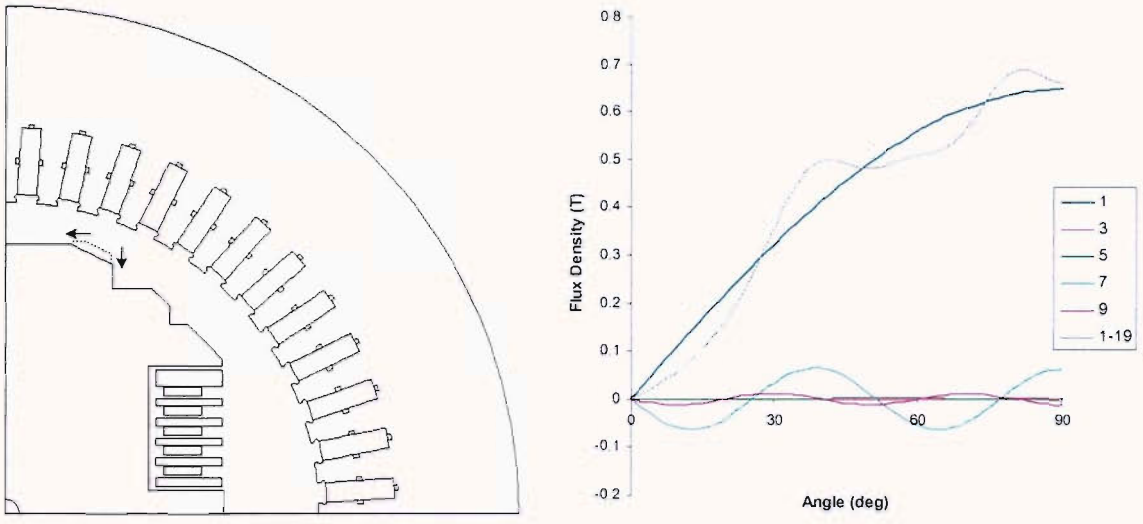

Figure 4.20 Further modification to reduce the undesirable harmonics: (a) FE model showing the modification, and (b) The air-gap flux density waveform up to 19th order

4.3 3D modelling and evaluations

The analysis of three-dimensional (3D) electromagnetic fields, whether static or dynamic, is far more difficult than analysis of 2D systems. In a 3D model, the vector nature of the electromagnetic field implies that at each node there will be at least three unknown quantities to compute, which means that there will be a threefold increase in size of the system matrix. Therefore, solving three-dimensional problems is time consuming, thus making it computationally very expensive. However, recent developments in numerical techniques and advances of computer technology, with the availability of high speed, large memory computers at relatively low price, make 3D FE analysis more feasible and attractive even for practical purposes.

The use of 2D modelling prevents some important features from being investigated, hence 3D FE models have been used in the later stages of the design process. Using 3D models the behaviour of the voltage waveform could be predicted more accurately. Furthermore, 3D models are capable of incorporating the presence of through bolts into the design. Results from a 3D model were therefore compared with those from the final 2D model, and used to guide further changes to the design. The differences between the

predictions of the 2D and 3D models were evaluated, and the flux distortion caused by the bolts and their holes was estimated. Finally, the 3D model was modified to confirm the effectiveness of the changes to the design in reducing the undesirable harmonics. In addition, the final results were compared to those obtained from measurements.

4.3.1 Model construction

The FE models of the superconducting generator were constructed using primitive volumes, swept surfaces and Boolean operations. The initial 3D model analysed was without any through bolts. This allows direct comparison with the results of the models. A 3D model was constructed based on results of earlier models as shown in Figure 4.16. Since no load is involved only one-eighth of the whole machine is used for modelling. In order to avoid any mistake during model construction, it was easier and more efficient to build the entire generator model initially as shown in Fig. 4.21. In addition, the one-eighth model was created using a background volume, which also defined the outer boundary of the model. The background volume, as shown in Fig. 4.22(b), extends up to 500 mm radially and 400 mm axially, and encloses the entire model.

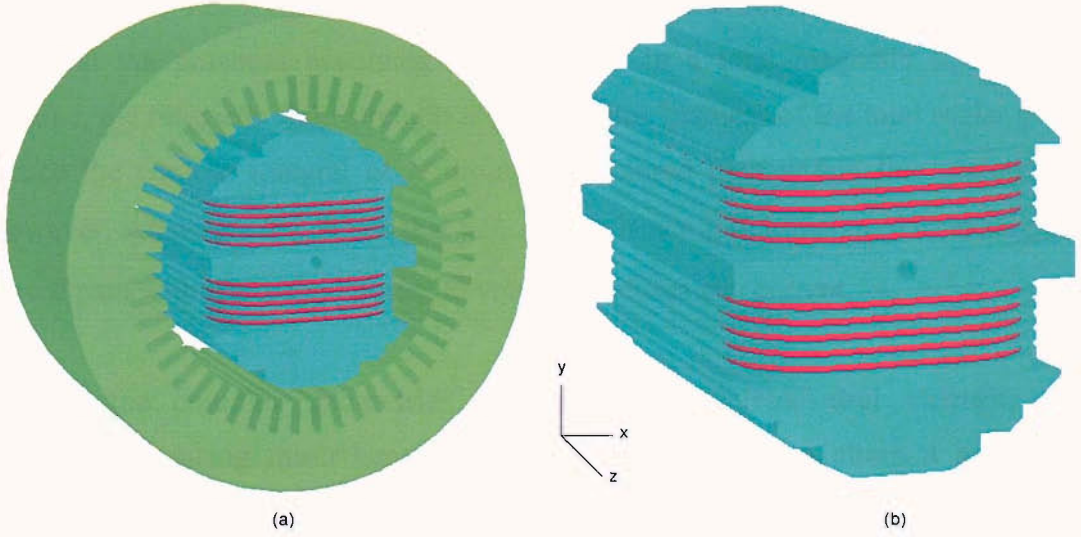

Figure 4.21 3D FE model of the HTS generator: (a) Rotor and stator, and (b) Rotor core with HTS field winding

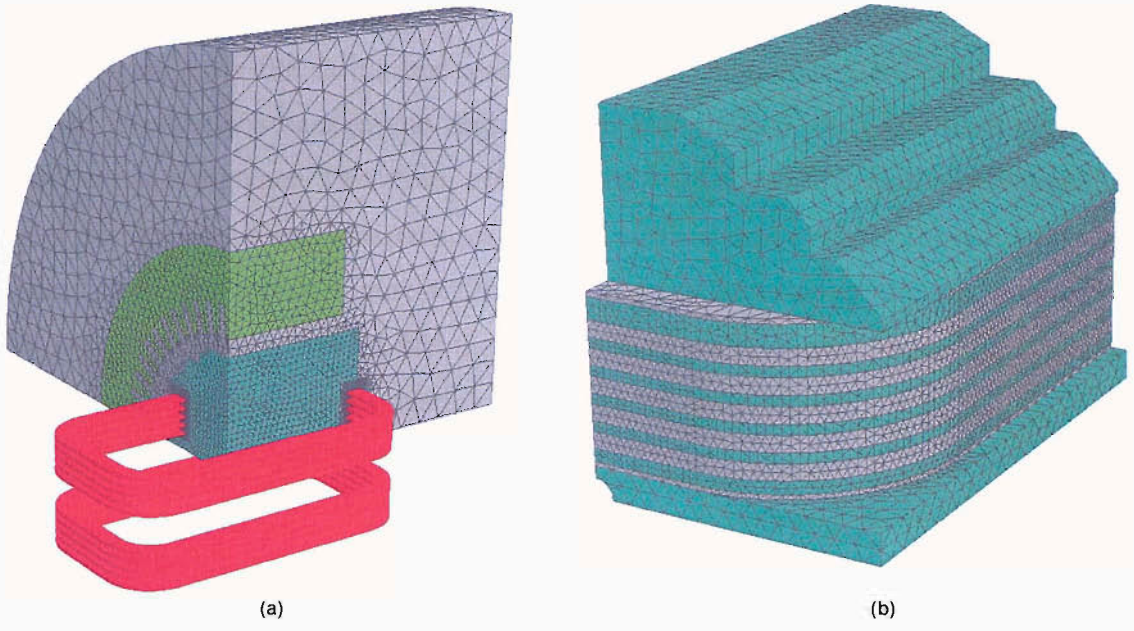

Figure 4.22 The 3D models of the HTS generator for FE analysis: (a) The model used for FE analysis together with the mesh generated, and (b) Mesh generated in the rotor

The definition of air regions in 3D electromagnetic field analysis is very important when current carrying conductors are considered. Each of the superconducting coils is surrounded by an air volume of reduced potential type as shown in Fig. 4.22 (b). This is to avoid the potential becoming multi-valued. In a total magnetic scalar potential volume, the magnetic field strength is given by the gradient of the total scalar potential. Hence the contour integral of H around any closed path within this region is zero. However, Ampere's law states that $\int H \cdot dl = I$, hence it is imperative to ensure that no closed path within any total potential volume encloses any current.

Due to the complex geometries of the generator, tetrahedral elements created automatically using mesh generator were used. In order to attain a high level of accuracy, only quadratic elements were defined. Furthermore, the discretisations near the coil region and flux diverters were refined. Although it is possible to reduce the number of elements considerably using brick (hexahedral) elements to achieve the same accuracy, it is extremely time consuming to build. The mesh generation is divided into

two stages: surfaces of volumes (cell) are discretised into triangles, and then using the surface mesh, each cell is meshed automatically into tetrahedra. A common meshing problem is when the background region is too complicated, thus the mesh generator cannot connect together. Therefore, extra regions were added to effectively connect the model surfaces together. This ensures a better surface mesh, which the volume mesh generator can then utilise. Figure 4.22(a) and (b) show the extent of the models together with the volume mesh created and the mesh around the HTS coils, respectively. There are a total of 380455 elements making 516281 nodes in the model.

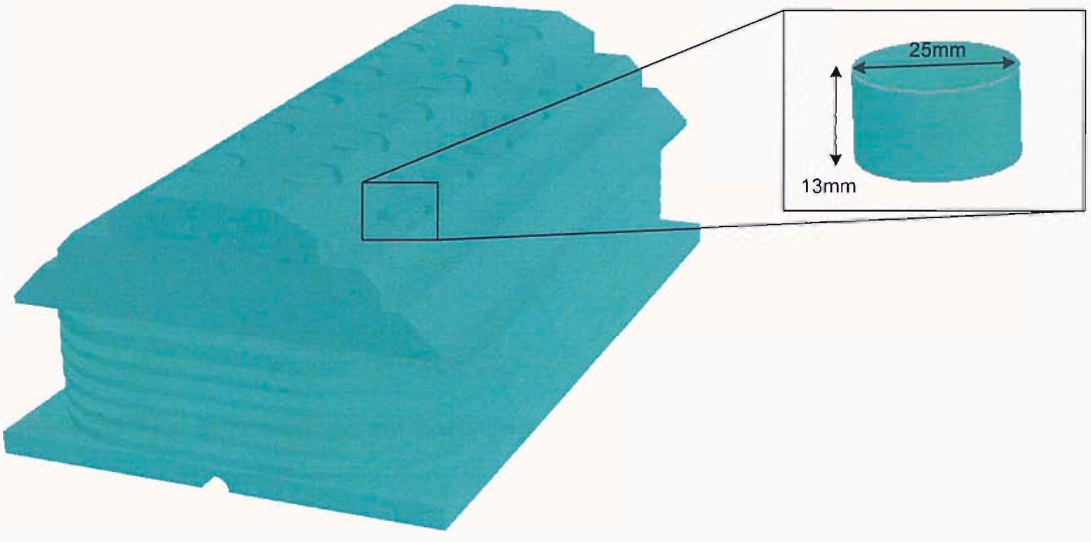

Figure 4.23 The rotor incorporating the round through bolts

More 3D models were built to include the effect of the through bolts. Two rows of 6 bolts clamp the outermost pair of plates in place, while two further rows of 5 bolts press directly on the second pair of plates. It is important to take into account the effect of the bolts to make sure that it will not cause significant deterioration in performance particularly related to voltage waveform. Initially for ease of construction and in order to gain some idea on the effect they have on the overall air-gap flux density waveform, the bolts were approximated to be of round shape. The bolts were deliberately built to the same level as the plate, so that they will not severely affect the air-gap density. However, mechanical constraints dictate that the base of the bolt holes to the plate directly below them has to have at least 9mm. This modification is a necessary safety

margin to avoid any fracture or crack in the plates. Therefore, the height of the outer pair of through bolts was increased by 2mm. Figure 4.23 shows the model incorporating the round through bolts. The bolts were later constructed based on the actual bolts as shown in Fig. 4.24. This was to ensure that the model geometries were as close as possible to the actual machine being built, to give more accurate results.

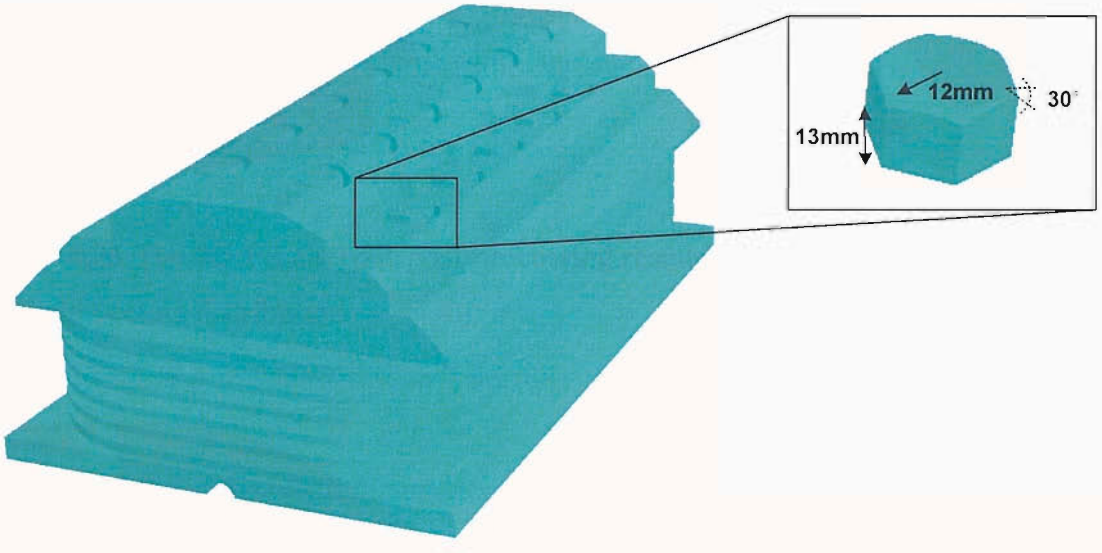

Figure 4.24 The rotor with actual bolts and their dimensions

4.3.2 Field modelling and evaluations

A module known as TOSCA, which is part of Opera 3D finite-element software was used to analyse the models. The permeability of the magnetic materials was defined using a non-linear characteristic BH curves as shown in Fig. 3.7 of Chapter 3. Since the stator is laminated, a packing factor of 0.95 was defined in the *xy*-plane of the model. Initially, a 3D model equivalent to 2D model (based on Fig. 4.21) was built without the through bolts. A typical field distribution under no-load conditions is shown in Fig. 4.25(a) and (b). Generator models incorporating the through bolts were also constructed and analysed. Figure 4.26(a) shows field distributions together with the mesh generated in the model with round bolts (see Fig. 4.23). Fig. 4.26(b) shows the field vectors in the rotor of the model using bolts with the actual dimensions.

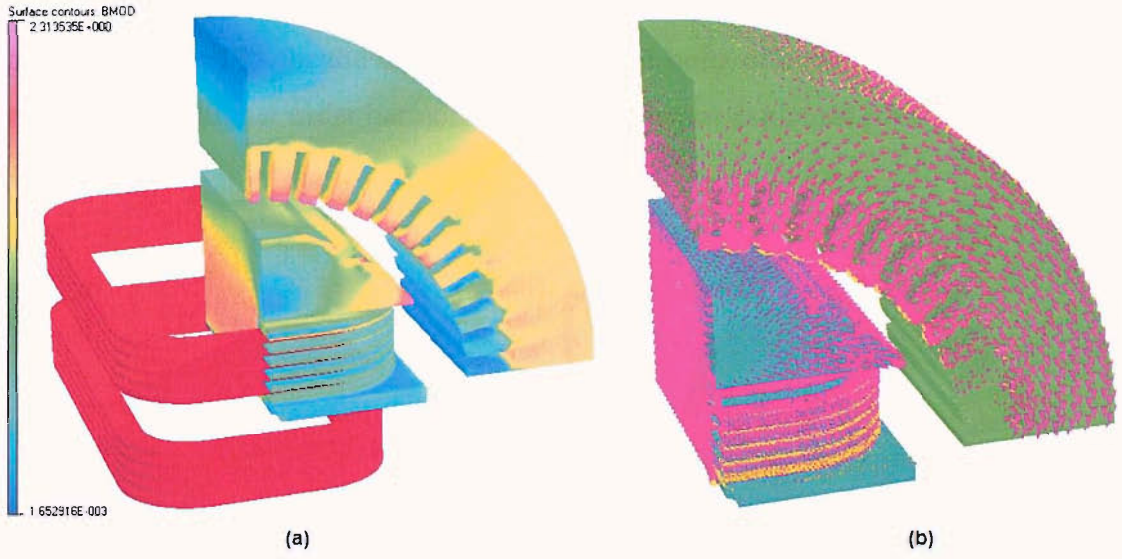

Figure 4.25 The 3D FE analysis post-processing results: (a) Flux density contours, and (b) Field vectors distribution

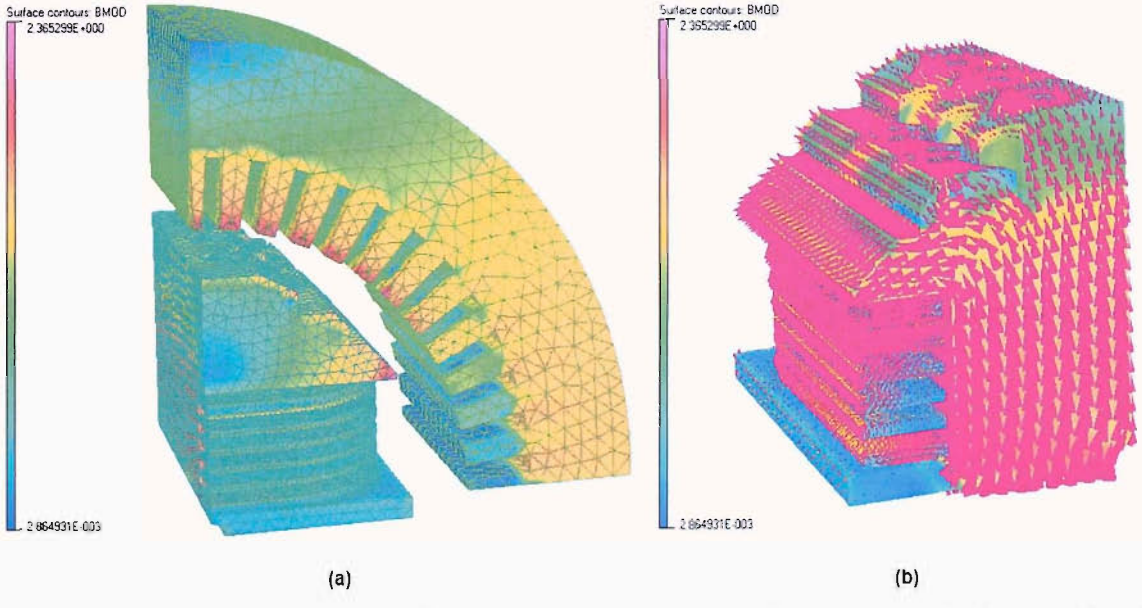

Figure 4.26 3D model incorporating through bolts in round shape: (a) Mesh created and the field distribution and, (b) Field vectors distribution in the rotor

In a 3D model, the field component was analysed to extract the harmonics of the air gap flux density using Fourier series (using Equation 4.2). The radial field over a patch of 90° arc and 200 mm length at 160 mm radius for the model with actual bolts is shown in

Figure 4.27. Table 4.6 shows the individual harmonic components of air gap flux density up to the 19th for the modified model with bolts of actual dimensions. Like in the 2D analysis, higher order harmonics are negligible as explained previously.

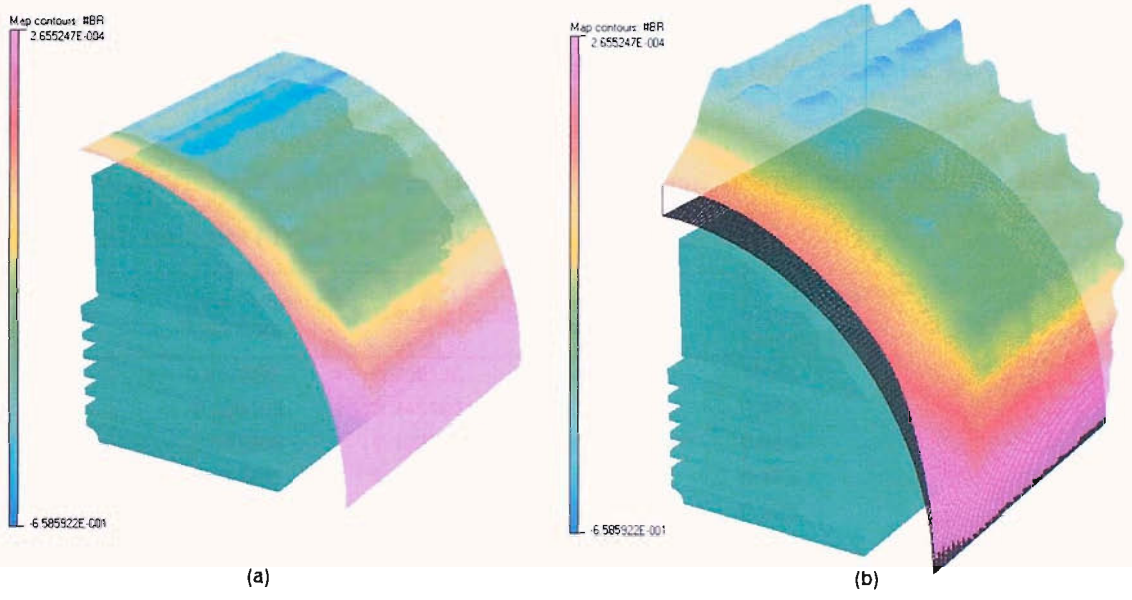

(a) (b)

Figure 4.27 The gap flux density distribution: (a) Over a patch, and (b) Histogram view of the patch

Table 4.6: Harmonic components of air-gap flux density and phase voltage of the 3D model with actual bolts (Total *rms* harmonic voltage 1.367%).

Space Harmonic Order	Sine Harmonic Magnitude	Winding Factor	Actual Harmonic	% Harmonic Voltage Contribution
1	0.618092	0.758138	0.468599	100%
3	-0.009499	0.245196	0.002329	0.50%
5	-0.020388	0.192774	0.003930	0.84%
7	-0.044165	0.018445	0.000815	0.17%
9	-0.018449	0.207867	0.003835	0.82%
11	0.022809	0.057705	0.001316	0.28%
13	-0.006209	0.050606	0.000314	0.07%
15	0.012248	0.138893	0.001701	0.36%
17	-0.010646	0.009096	0.000097	0.02%
19	-0.003858	0.065438	0.000252	0.05%

The overall harmonic contribution for the model with no bolts was found to be 1.43% which was higher than that predicted by 2D and the 3D model with the through bolts. Table 4.7 shows the individual harmonic components of air-gap flux density. This is the consequence of including the through bolts and their holes in the model. The peak flux density for the 3D model is lower due to saturation of the pole neck by leakage flux at the ends of the rotor, which is also an unaccounted effect in the 2D model. When compared to 2D model, the gap density was reduced from 0.66 T to 0.62 T.

Table 4.7: Harmonic components of air-gap flux density and phase voltage of the 3D model with no bolts (Total *rms* harmonic voltage 1.434%).

Space Harmonic Order	Sine Harmonic Magnitude	Winding Factor	Actual Harmonic	% Harmonic Voltage Contribution
1	0.617366	0.758138	0.468048	100%
3	-0.009193	0.245196	0.002254	0.48%
5	-0.021305	0.192774	0.004107	0.88%
7	-0.042793	0.018445	0.000789	0.17%
9	-0.020665	0.207867	0.004296	0.92%
11	0.024607	0.057705	0.001420	0.30%
13	-0.005130	0.050606	0.000260	0.06%
15	0.009737	0.138893	0.001352	0.29%
17	-0.007854	0.009096	0.000071	0.02%
19	-0.005560	0.065438	0.000364	0.08%

Consequently, the total *rms* harmonic voltage in the 3D model increases from 1.36% to 1.43%. Meanwhile, the total *rms* harmonic voltage for the model with real bolts is 1.37%, similar to the model with round bolts. This confirms that the approximation introduced earlier on the shape of the bolt in the FE analysis is valid. Furthermore, the inclusion of the bolts has indirectly suppressed its total *rms* harmonic voltage from 1.43% to 1.37% which is almost equivalent to those predicted in 2D. Figure 4.28 compares the percentage contribution of individual harmonic components for the 2D model (Fig. 4.21), 3D model with no bolts and real bolts.

In the generator, the rotor is connected to a flange (also made of 9% nickel steel) through stainless steel tubes at both ends to provide the required mechanical support. Therefore, it is very important to make sure that these flanges do not severely affect the

gap field. Since this can only be model accurately using 3D, a model based on the actual position and dimensions of the flange was built. Figure 4.29 shows the 3D model constructed for the analysis together with the flux density distribution. Fixture holes were not included in the flange as they were found to have a negligible effect. The contour maps of the z-component of the magnetic flux density was plotted in between the flange and the rotor core at z = 230 mm. Figure 4.30 shows the plot, and as expected, the flux density of the z-component is higher in the model with the flange. This is due to the flux leakage from the rotor core to the ferromagnetic flange. The harmonic components for both the models were extracted and analysed. Fortunately, this had very little effect on the overall air-gap flux density as the total *rms* harmonic voltage distortion increased only slightly to 1.4%.

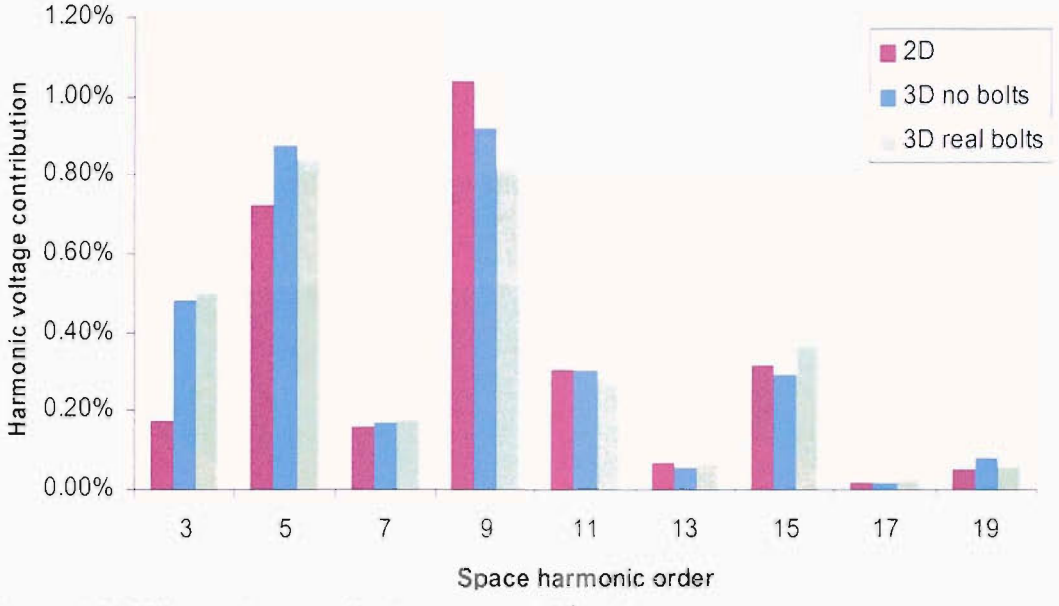

Figure 4.28 Harmonic contributions up to 19th order

Figure 4.29 3D model with the flange and its magnitude of flux density distributions

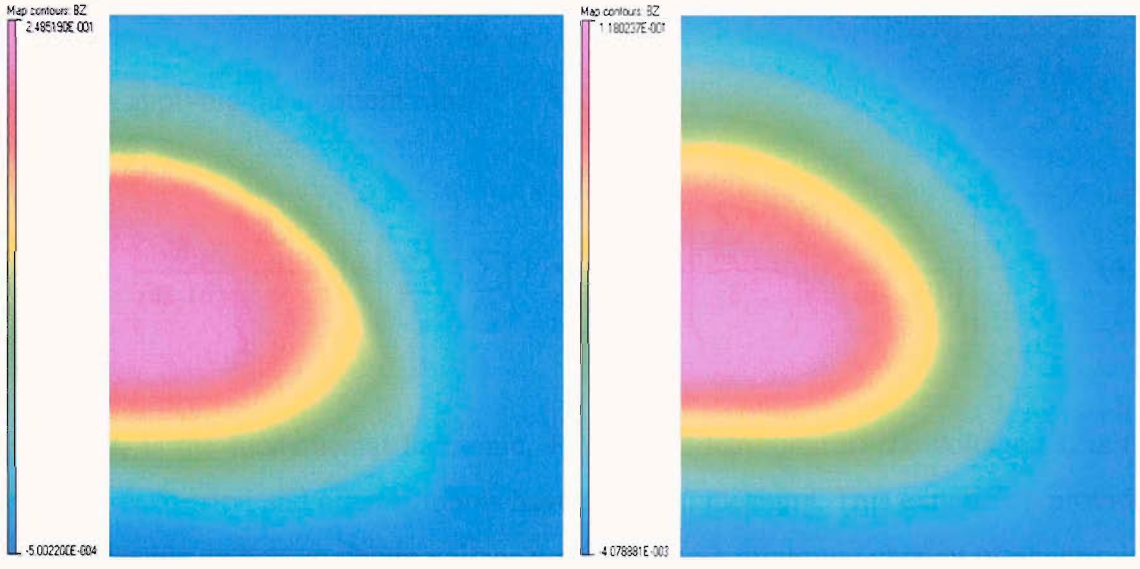

(a) (b)

Figure 4.30 Contour map of z-component magnetic flux density: (a)With flange, and (b)Without flange

4.3.3 Field optimisation

In the previous design, the 2D non-linear finite-element models have successfully analysed and the harmonic content of the air-gap flux density estimated. However, due to the presence of the through bolts the analysis really requires a 3D model to accurately predict the voltage waveform. The 3D modelling analysis – which has been evaluated – confirmed that the main concern is the 5th and 9th harmonic voltages which will drive the largest harmonic currents through the external circuit, causing additional I^2R losses. In order to minimise the undesirable harmonic voltages it would be desirable to have some indication of the effect of changing the local flux density on the total harmonic content of the voltage waveform. Moreover, since there are at least two harmonics that are dominant, it would be difficult to determine the area for optimisation. Hence, a simple formula was devised to provide guidance in improving the voltage waveform. This formula of partial derivative was devised to target the specific area for voltage waveform improvement. These partial derivatives may be calculated by first using,

$$\frac{\partial V_i^2}{\partial \mathbf{B}_r(\theta)} = 2V_i \frac{\partial V_i}{\partial \mathbf{B}_r(\theta)} \tag{4.7}$$

and then applying the quotient rule:

$$\frac{\partial}{\partial \mathbf{B}_r(\theta)}\left(\frac{\sum V_i^2}{V_1^2}\right) = \left(\frac{2}{V_1^2}\right)\left[\sum_{i>1}\left(V_i \frac{\partial V_i}{\partial \mathbf{B}_r(\theta)}\right) - \left(\frac{\sum V_i^2}{V_1^2}\right)\left(V_1 \frac{\partial V_1}{\partial \mathbf{B}_r(\theta)}\right)\right] \tag{4.8}$$

where V_1 is the fundamental harmonic, V_i is the i^{th} harmonic of the voltage, B_r is the radial flux density, and other symbols have the usual meaning. This expression provides a useful guide on how to obtain voltage waveform with minimum content of undesirable harmonics. This partial derivative for the 3D model incorporating the actual through bolts (modelled earlier, see Fig. 4.24) has been evaluated using the above equation for angles between 0° and 90° and is plotted in Fig. 4.31. The graph labelled Line Voltage

includes only harmonics of order $6n\pm1$, while that labelled Phase Voltage includes all odd harmonics.

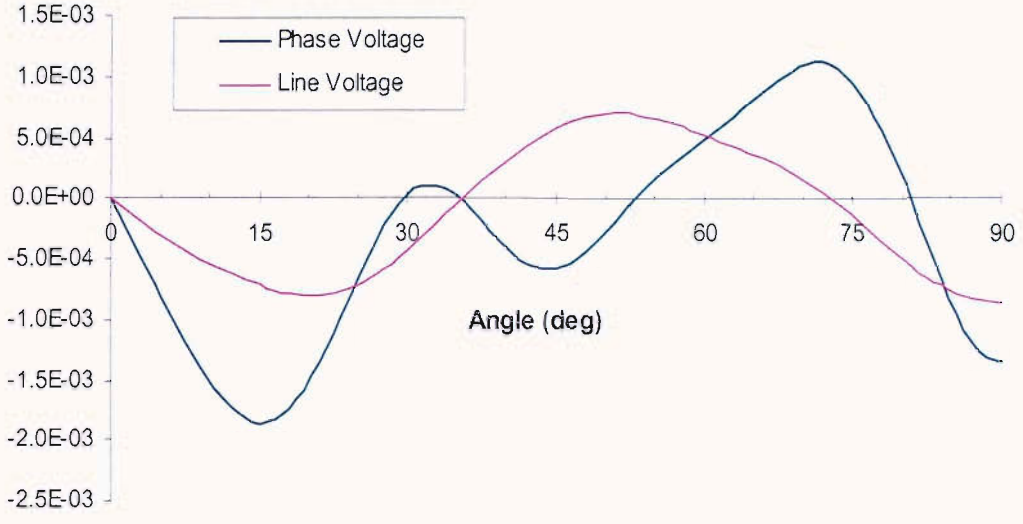

Figure 4.31 Weighted errors in the air-gap flux density for 3D model incorporating bolts with actual dimensions

According to Fig. 4.31, the total harmonic content of both phase voltage and line voltage can be reduced by reducing the air-gap flux density at any angular position between 53° and 73°. The pole face of the outermost plate and the one directly below it fall in the region. Unlike in the old design, with equal 9%Ni plate thickness, only the height of the through bolts on the outermost plate are permitted for adjustment since the bolts on the plate directly below are restricted due to thinner dimension. Hence, the two rows of bolts on the outermost plate were reduced in an attempt to improve the voltage waveform, but mechanical constraints only gave slight improvement. The bolts were sunk 2 mm into the core and caused the total *rms* harmonic voltage to reduce to 1.35%. Figure 4.32 shows the air-gap density waveform of the modified rotor and Table 4.8 lists the individual harmonic components up to 19^{th} order. Measurements based on this model were also carried out to find the output voltage and waveform [99]. The high temperature superconducting rotor was driven by a 3 kW inverter-fed motor via a belt drive. The resulting voltage harmonics are listed in Table 4.9. The total *rms* harmonic

voltage distortion was found to be 1.39%, which is in excellent agreement with the FE results.

Table 4.8: Harmonic components of air-gap flux density and phase voltage of the 3D model with the bolts on the outermost plate sunk by 2 mm into the core.

Space Harmonic Order	Sine Harmonic Magnitude	Winding Factor	Actual Harmonic	% Harmonic Voltage Contribution
1	0.614658	0.758138	0.465995	100%
3	-0.005724	0.245196	0.001404	0.30%
5	-0.022260	0.192774	0.004291	0.92%
7	-0.043408	0.018445	0.000801	0.17%
9	-0.018652	0.207867	0.003877	0.83%
11	0.021954	0.057705	0.001267	0.27%
13	-0.004074	0.050606	0.000206	0.04%
15	0.009724	0.138893	0.001351	0.29%
17	-0.007209	0.009096	0.000066	0.01%
19	-0.006446	0.065438	0.000422	0.09%

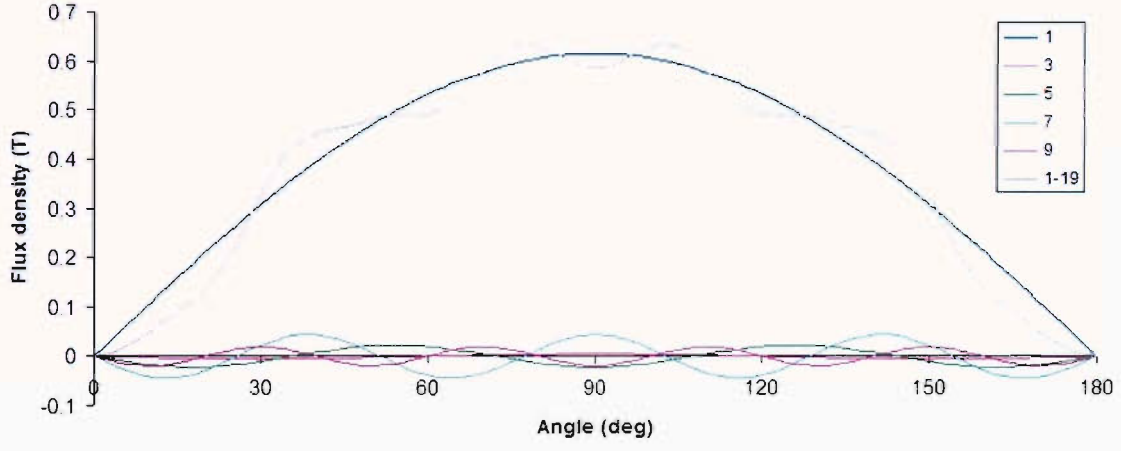

Figure 4.32 The air-gap density for the modified 3D model

The above weighted errors analysis also confirms the effectiveness of the adjustment made earlier in Fig. 4.20. A 3D model similar to that of Fig. 4.20 was built to validate that the waveform was improved. In that model, the face of the slopes on the outermost plate was reduced by 3mm equally along the x- and y-axis. The modification successfully reduced the undesirable harmonics, especially the 9^{th} harmonic to 0.52% and the total *rms* harmonic voltage distortion to 1.14%. Figure 4.33 shows the weighted

errors after the modification (new phase and line voltage), which clearly indicates that, for the range of angles analysed, the harmonic content especially for the phase voltage were improved significantly. Cutting the slopes further in the same direction would improve the waveform, but the improvement would be small. This is due to the effect of the protruding bolts.

Table 4.9: Measured harmonic voltage contribution

Space harmonic order	Harmonic voltage (Volts)	Percentage harmonic contribution
1	56.46149	100
3	0.206494	0.36
5	0.496861	0.88
7	0.145230	0.26
9	0.565247	1.00
11	0.133328	0.24
13	0.026906	0.05
15	0.135284	0.24
17	0.009484	0.02
19	0.027485	0.05

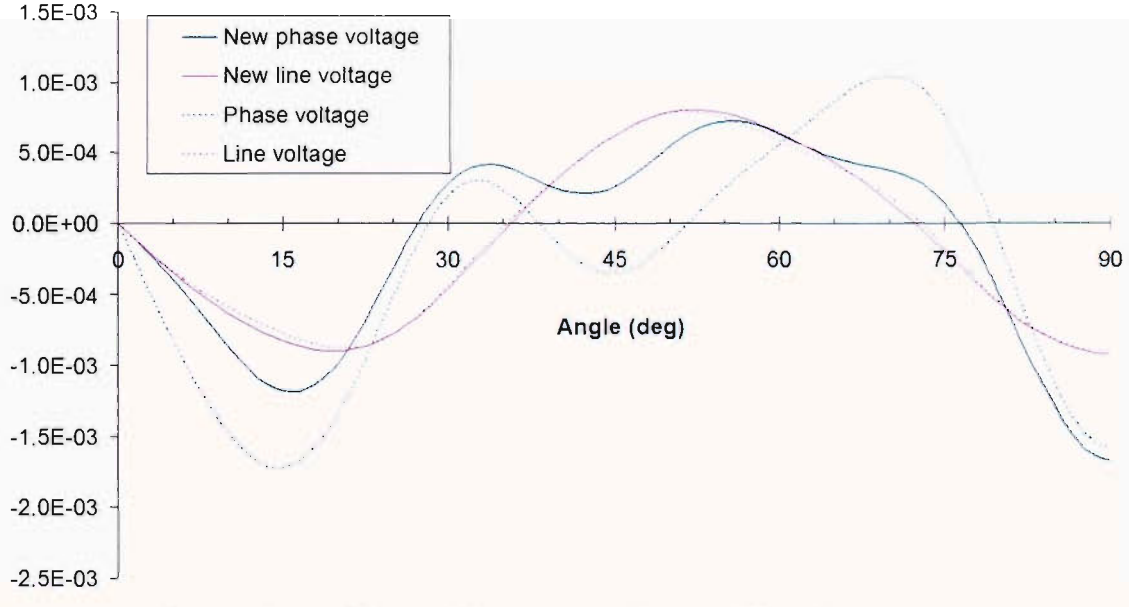

Figure 4.33 Comparison of the weighted errors after modification

Based on the waveforms in Fig. 4.33, the undesirable harmonics can still be further reduced by targeting around the 55° region. It was noted that the middle plate of the rotor hat lies in such a position. Hence, the face of the slopes on the middle plate was

reduced in the direction as shown in Fig. 4.34(a) by 3 mm. The modification successfully reduced the total *rms* harmonic voltage distortion further to 1%. Figure 4.34(b) shows that the changes made have greatest effect on reducing the undesirable 5^{th} harmonic component.

The 2D and 3D models show consistent results, but the 2D analysis underestimates the harmonic content of flux and voltage waveforms due to the effect of through bolts. Although the overall accuracy of 2D modelling is satisfactory, on this occasion a full 3D treatment was necessary which unfortunately added to the complexity of the simulation technique. To mitigate this problem, a formula was specifically devised to provide essential information to reduce the total harmonic content. Changes to the rotor design were proposed and the 3D model was modified to confirm that the waveform was improved.

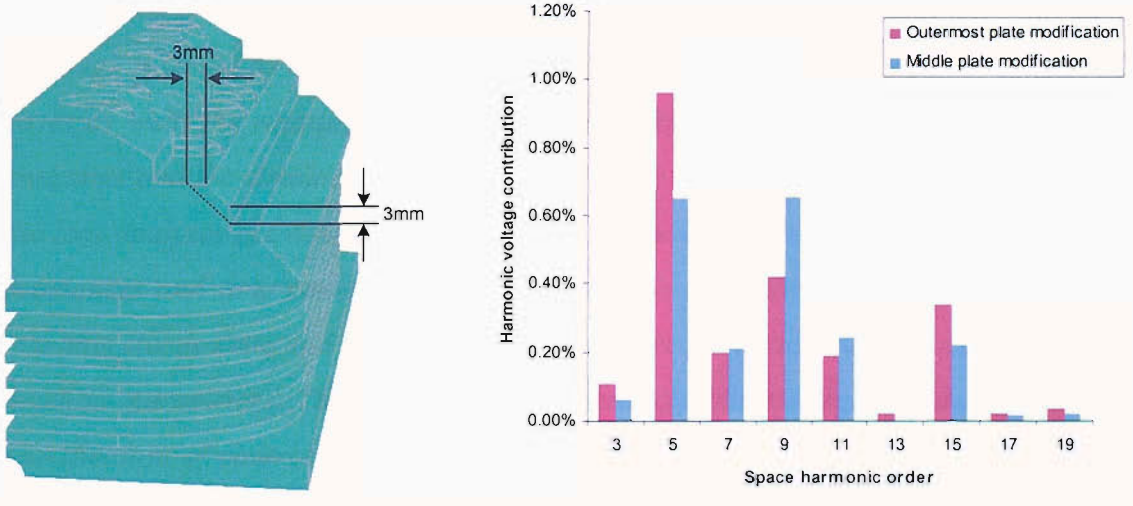

Figure 4.34 Further modification to improve the voltage waveform: (a) Region targeted for optimisation, and (b) Individual harmonic contribution before and after modification

EVALUATIONS OF LOSSES AND REACTANCES

The operation of a HTS synchronous generator at low temperature (65 K-78 K) makes it vulnerable to temperature perturbation due to losses in the cold region. Therefore, it is most important to carry out studies on the losses in the cold layer. These losses must be removed by the liquid nitrogen and therefore burden the refrigeration system. Losses that may affect the cold region can be divided into no-load and full-load losses. No-load tooth ripple losses are due to the distortion of the fundamental flux density wave by the stator slotting. Full-load losses are losses that include the effects of the MMF harmonics of the stator winding. Two different methods were used to estimate the no-load and load-dependant losses; full transient non-linear rotating machine model to model no-load losses and static and steady-state AC models to model full-load losses. Although it would be desirable to use the rotating machine transient solver for full-load cases as well, the rotating machine solver was found to be too slow due to long time constants and the simulation was still far from the steady-state condition. The details of the loss analyses are described in Section 5.1. Meanwhile in Section 5.2, the machine's reactances and time constants are evaluated. The accurate prediction of synchronous machine steady state and transient performances requires accurate determination of the machine parameters. This will provide essential stability margins and hence suitable specification of control system and protective devices can be decided upon before the machine is built. Hence, it is important to estimate the generator reactances and time constants. Two methods using finite-element analysis were employed to evaluate the reactances and time constants; first, the sudden three-phase short-circuit, and second, frequency response curve.

5.1 Losses modelling

For a balanced three-phase winding, most harmonic voltages cancel, only fields of order $6n\pm1$ remain to be considered [100]. Moreover, the design of the existing stator of the machine is such that the winding produces almost negligible 7^{th} harmonic fields, while the higher order fields are reduced by the distribution of the phase conductors throughout each phase belt. Consequently, the primary concern is the effect of the 5^{th} harmonic of the stator MMF. The field produced by this MMF harmonic appears on the rotor at 300 Hz (6^{th} time harmonic), and if not controlled would produce substantial losses in the rotor. The losses of other higher harmonics were also evaluated to confirm that their effect is negligible. These losses would heat the rotor and contribute to the load on the cooling system, thus increasing the cooling power required. Such losses may be greatly reduced by introducing a thin layer of copper placed over the rotor surface to provide a low resistance path for the eddy currents. These losses must be estimated carefully so as to make sure that refrigeration power is sufficient to remove them from the system.

Two methods of modelling were used: the first utilises a full transient non-linear rotating machine model, whereas the second method relies on the much less computationally expensive combined static and steady-state AC models. Initially, it was hoped that a rotating machine model could be used to estimate the eddy current losses at full load too. However, the solver is too slow and the machine takes a long time to reach the steady state condition. This is due to the low resistance of the cold copper layer increasing the decay time constants, which are long in relation to the period of the steady state eddy current waveform. Rotating machine analysis was therefore used to model only the no-load case, in which it appears that the slower components of the initial transient are much smaller and may be neglected. A series of steady state AC models was then used to determine the load dependant losses. In the following sections, the losses in the cold copper screen of the two machine models based on the earlier design with Invar rotor, and latest design with 9% nickel steel rotor are evaluated.

5.1.1 No-load tooth ripple losses

A 2D full transient non-linear rotating machine model was used to evaluate the no-load losses. The rotating machine solver is a transient eddy current solver, extended to incorporate the effects of rigid body (rotating) motion. The stationary and rotating parts of the model must be separated by a 'gap region'. The gap region has no internal nodes, and should therefore be thin. For better results a layer of air elements should bound the gap region on both its rotor and stator surfaces. Since the generator has rotational symmetry about an axis, only a single pole pitch needs to be modelled. The boundary condition of the stator outer region was taken as a flux line $\boldsymbol{A} = 0$, corresponding to zero leakage outside the core; the quadrature axis had a periodic boundary condition with $\boldsymbol{A}$ at 180°= $-\boldsymbol{A}$ at 0°. In order to capture the induced current correctly, the copper screen was finely discretised. Figure 5.1 shows the 2D model of the generator with rotor made of Invar used for the rotating machine finite-element analysis.

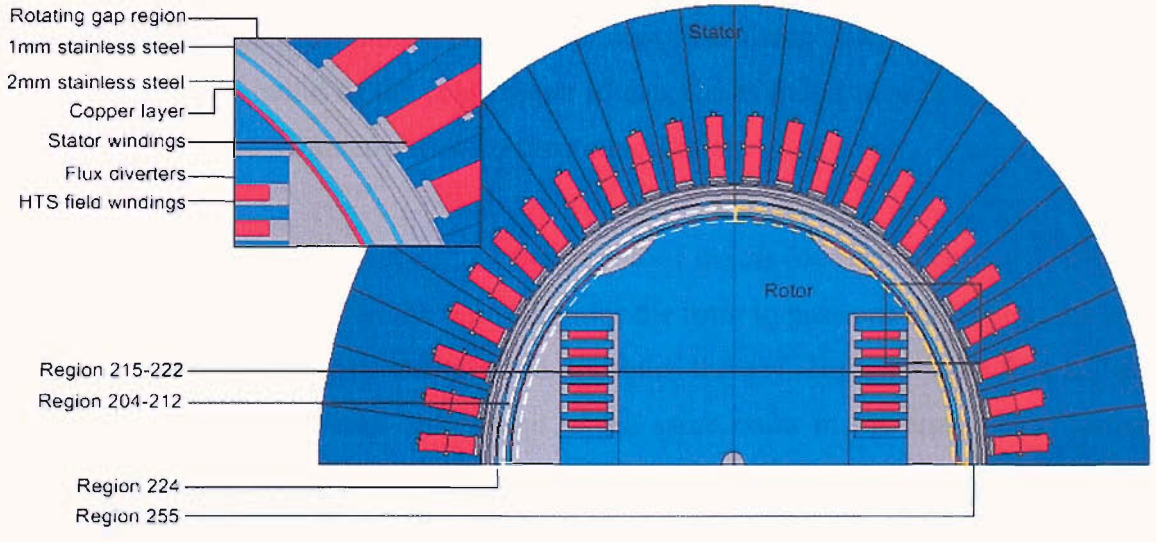

Figure 5.1 2D finite-element model for loss analysis

Within the rotating frame of reference defined by the D and Q axes of the rotor, both changes in reluctance caused by passing stator slots and changes in the stator MMF caused by unbalanced loads, or by harmonics of the stator MMF, drive changes in the rotor flux. Consequently, this would induce changes in the field current to maintain

constant flux linkage [101]. However, the cold copper screen prevents such external sources from driving any significant fluctuations in the field current. It is therefore permissible to solve for a fixed value of field current, which avoids the need to define an equivalent supply voltage and resistance for the superconducting winding.

The analysis options were set to use a fixed DC field current and a fixed angular velocity of 3000 rpm. Non-linear analysis was used as defined by the BH characteristics of the magnetic materials to include the effect of saturation. A small fixed time step was used to ensure that the number of non-linear iterations required for each time step is small. Since a long initial transient was expected, some output was required to monitor the progress of the solution. This was obtained by setting a few early output times, and by the use of a log file. The data used to estimate the steady-state no-load loss was obtained from the final 11 output times, which cover the period taken for the rotor to rotate past one stator slot. Two types of data were extracted from the solution files for these 11 output times: the integral of the loss density over the area of all the cold conducting regions of the model, and the odd space harmonic components of the current density at the mid radius of the cold copper screen; the even harmonic components were not extracted, since symmetry leads to their cancellation.

Symmetry considerations dictate that the period of the no-load eddy-current waveform on the rotor must be equal to the time taken for the rotor to pass one stator slot; the eddy currents occur at 48^{th} time harmonic and multiples thereof. Therefore, the first and last of the 11 output times used correspond to the same point in the steady-state current waveform, which would suggest that one of them is redundant. The additional output time was used primarily to confirm that there are no significant changes in the current densities over one cycle. The data for the losses per unit length were obtained by extracting the integrals of J^2/σ over the cross sectional area of the cold conductors at each output times. In this 2D model, the cold regions consist of the 2 mm thin stainless steel layer and the 1mm copper screen. They are made up of two groups of region as shown in Table 5.1. As expected, the eddy-current loss on the rotor at 172.5° and 180° are similar due to reason mentioned above.

Table 5.1: No-load eddy-current loss in the cold region

	Power per unit length (W/mm)		
Rotor angle (°)	Region 205-212	Region 215-222	Total
172.50	6.9447E-04	6.8603E-04	1.3805E-03
173.25	7.5386E-04	7.3962E-04	1.4935E-03
174.00	8.0446E-04	8.1608E-04	1.6205E-03
174.75	6.8599E-04	6.6846E-04	1.3545E-03
175.50	7.0020E-04	6.9169E-04	1.3919E-03
176.25	6.9473E-04	6.8813E-04	1.3829E-03
177.00	7.5558E-04	7.3956E-04	1.4951E-03
177.75	8.4143E-04	8.1577E-04	1.6572E-03
178.50	6.8797E-04	6.6636E-04	1.3543E-03
179.25	7.0233E-04	6.8944E-04	1.3918E-03
180.00	6.9427E-04	6.8604E-04	1.3803E-03

The data for these output times was then averaged to leave 10 sets of data equally spaced over one cycle of the steady state waveform. Doubling this average value, since only half of the machine is included in the model, and multiplying by the length of the stator core (325 mm) gives a steady-state no-load loss. The estimate obtained by this calculation was 0.944 W. However, this loss includes some components due to the presence of transient eddy currents, which should not be included in the evaluation of the steady-state loss.

A reasonable estimate of the losses due to the transient eddy currents can be obtained by analysing the space harmonic components of the current density in the cold screen. Once the data from the finite-element model is transformed into the rotor frame of reference, the periodic nature of the eddy currents becomes clear. Figure 5.2 illustrates the behaviour of the 47^{th} and 49^{th} space harmonics of the current density in the rotor screen as the rotor turns through one stator slot pitch. The line graphs show the data fitted by the 48^{th} time harmonic. It can be seen that the 48^{th} time harmonic is predominant.

Since the remaining transient eddy currents change little over the last period of the steady state eddy-currents, the time average of the eddy currents is representative of the transient eddy currents. The *rms* magnitude of the DC component of the current is given by

$$J_{rms} = \sqrt{\sum_{Odd\ i} a_i^2 + b_i^2}\ , \tag{5.1}$$

where a_i and b_i are the DC sine and cosine components of the i^{th} space harmonic of J. The transient loss is then given by

$$P_{Tr} = \frac{2\pi R L t J_{rms}^2}{\sigma} \tag{5.2}$$

where R, t *and* σ are the mean radius, thickness and conductivity of the cold screen, and L is the length of the stator core. Thus P_{Tr} is 0.0103 W, which was considered to be negligible. However, this loss is subtracted from the first estimate above, to give the final estimate of the no-load steady-state eddy-current loss in the rotor of 0.934 W. The loss in the warm stainless steel layer (region 224 and 255) has also been evaluated. Table 5.2 shows the power per unit length for each rotor angle analysed. The total losses in the warm region were found to be 44.5 W. This value is considerably higher than those in the cold regions due to the proximity of the stator, but these losses do not contribute to the refrigeration system.

Table 5.2: No-load loss in the warm layer

	Power per unit length (W/mm)		
Rotor angle (°)	Region 224	Region 255	Total
172.50	0.02682	0.02685	0.05367
173.25	0.02765	0.02841	0.05606
174.00	0.06102	0.06206	0.12308
174.75	0.02747	0.02717	0.05464
175.50	0.02785	0.02709	0.05494
176.25	0.02682	0.02684	0.05366
177.00	0.02758	0.02844	0.05602
177.75	0.06101	0.06204	0.12305
178.50	0.02741	0.02723	0.05464
179.25	0.02778	0.02723	0.05501
180.00	0.02682	0.02685	0.05367

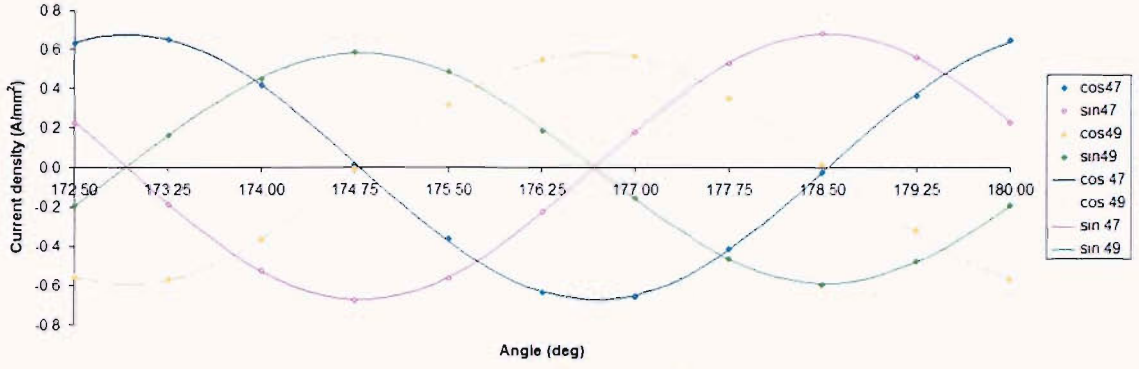

Figure 5.2 The variation of the dominant 47th and 49th space harmonic components.

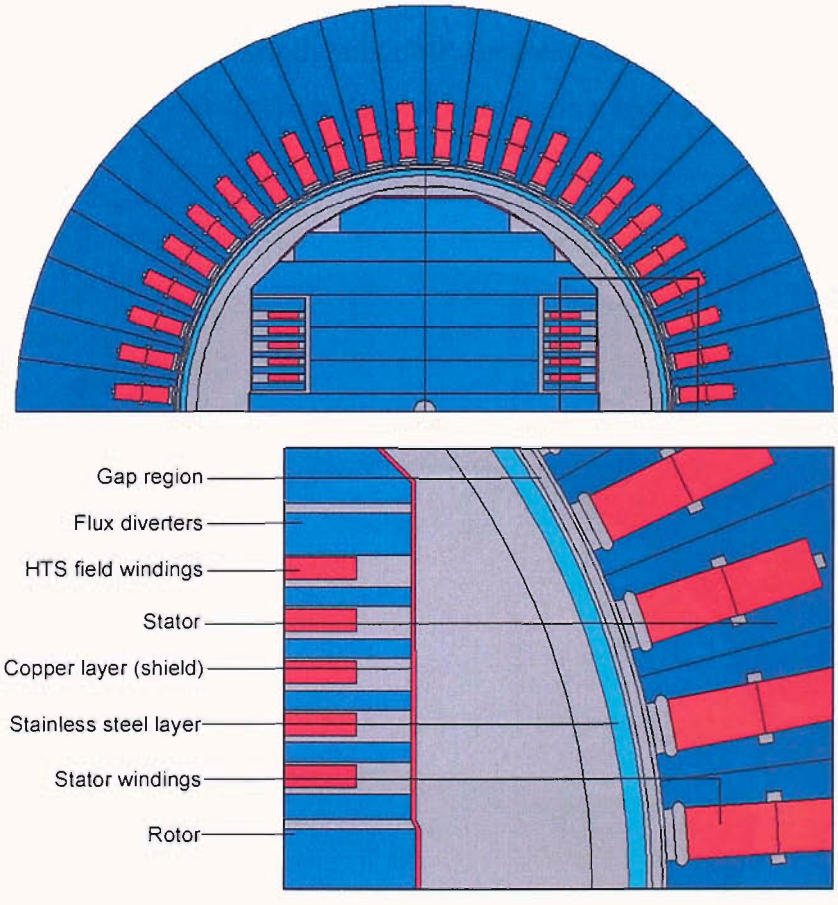

Figure 5.3 2D model of the latest design for no-load loss simulation

The simulation above was also performed on the latest rotor design with 9% nickel steel core. Figure 5.3 shows the model used for this analysis. This model is similar to the one shown earlier in Section 4.2.2.2 of Chapter 4, but with the copper and stainless steel

layer included in the model. The copper screen in this model was designed to wrap around the rotor core as shown in the diagram, thus eliminating the need of the stainless steel reinforcement layer.

Figure 5.4 shows the displaced position of the original rotor pole at 172.5° (at time 9.583 msec) and its flux lines. It can be clearly seen that the periodicity boundary conditions have been enforced radially in the air-gap to ensure that contours leaving the stator side at the gap reappear at the rotor side. The no-load loss in the rotor was evaluated using the same procedure as described previously. The effect of the transient eddy current was ignored and the total no-load losses were found to be 0.227 W. The reduction compared to the previous model is apparent due to the fact that the copper screen was placed further away from the stator teeth, thus reducing the effect caused by tooth ripple fields.

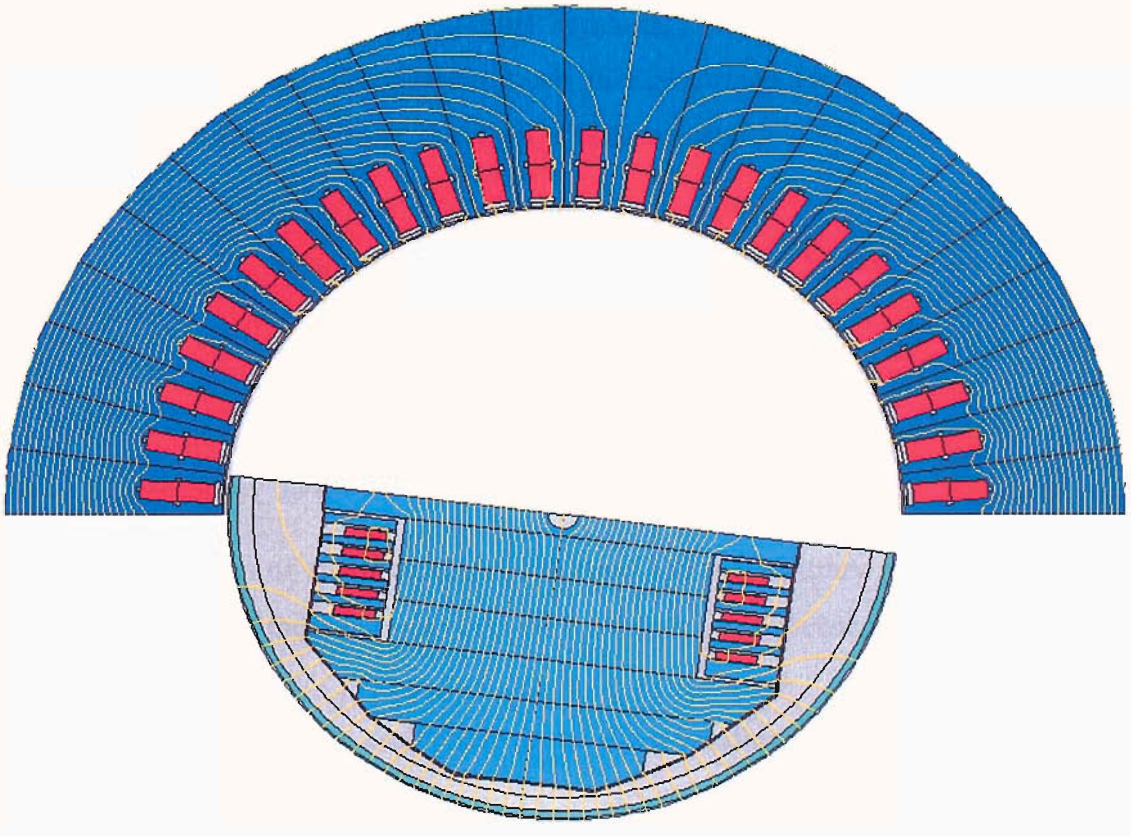

Figure 5.4 Flux lines at 172.5°

5.5.2 Full-load losses

The Steady-state AC Analysis program solves eddy current problems where the driving currents or voltages are varying sinusoidally in time. The permeabilities may be functions of the flux density, but are constant throughout the cycle. If the AC field is small in relation to a superimposed DC field, the incremental permeability data from a non-linear static model of the DC field can be used in the AC model. This type of model is particularly appropriate for a synchronous machine since, in the rotor frame of reference, the field is predominantly DC. In principle, since the model exists in the rotor frame of reference, the stator slots should be moving. However, the AC analysis program does not model motion. Instead, only the stator currents are moved.

As mentioned earlier, the 5^{th} space harmonic of the stator MMF drives a 6^{th} time harmonic field in the rotor, which causes the majority of the load dependant losses. A series of equations must therefore be established to determine the DC component and the magnitude and phase of the 6^{th} time harmonic component of the current in each stator coil of the model. Calculations were also performed for the 12^{th} and 18^{th} time harmonics, and it was confirmed that their effects are small.

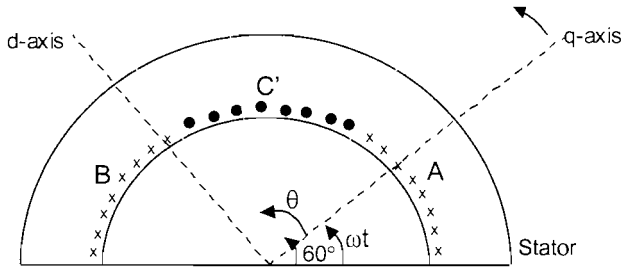

Figure 5.5 Variation of stator currents with time and the arbitrary angle θ, illustrating the transformation of these currents into the rotor frame of reference.

The instantaneous current in each phase of the stator winding is given by

$$I_A = I_0 \cos(\omega t + 60°) \tag{5.3}$$

$$I_B = I_0 \cos(\omega t - 60°) \tag{5.4}$$

$$I_{C'} = I_0 \cos(\omega t) \tag{5.5}$$

where I_0 denotes the peak current. Referring to Figure 5.5, it is apparent that transforming into the rotor frame of reference allows Equations 5.3 to 5.5 to be replaced by

$$I = I_0 \cos(\omega t + \phi), \tag{5.6}$$

where the angle ϕ is given by

$$\phi = 60° - 60° * \text{int}[(\theta + \omega t)/60°] \tag{5.7}$$

The angle θ is measured in the rotor frame of reference from the point of zero average current in the stator conductors. With a two-layer winding, there will be two values of θ for each slot, which will differ due to the short pitching of the stator coils. Use of AC analysis requires the currents to be Fourier transformed into the form

$$I(\theta,\omega t) = \sum_{n}^{\infty} [\alpha_n(\theta) \sin(n\omega t) + \beta_n(\theta) \cos(n\omega t)], \tag{5.8}$$

where n is the time harmonic order. Notice that equations 5.6 and 5.7 imply that

$$I(\theta,\omega t + 60°) = I(\theta,\omega t) \tag{5.9}$$

Hence only time orders which are multiples of six may be present. Only orders 6, 12 and 18 are therefore considered. Higher order terms were assumed negligible. Moreover, their inclusion would imply the existence of high spatial frequency components, which could not be represented by the current sampled at each stator slot position. In general, the coefficients of a Fourier series are given by

$$\alpha_n = \frac{1}{\pi} \int_0^{2\pi} f(u) \sin(nu)\, du \tag{5.10}$$

and $$\beta_n = \frac{1}{\pi}\int_0^{2\pi} f(u)\cos(nu)\,du \tag{5.11}$$

where u is equivalent to ωt in equation 5.8. From equation 5.9, it is clear that the above integrals may be evaluated by integrating over any 60° range. Substituting equation 5.6 and 5.7 into equation 5.10 and 5.11, and choosing the integration range to avoid the discontinuities in equation 5.7, we obtain:

$$\alpha_n = \frac{6}{\pi} I_0 \int_{\theta-\frac{\pi}{6}}^{\theta+\frac{\pi}{6}} \sin(u)\cos(n\,u)\,du \tag{5.12}$$

$$\beta_n = \frac{6}{\pi} I_0 \int_{\theta-\frac{\pi}{6}}^{\theta+\frac{\pi}{6}} \sin(u)\sin(n\,u)\,du \tag{5.13}$$

Separate AC models were built for the 6th, 12th and 18th time harmonics; equations 5.12 and 5.13 were used to calculate the phase and magnitude of the AC current density for each stator conductor position, and these values were imposed as source current densities.

The AC analysis solves formulations described by the Helmholtz equation of the form

$$\nabla \times \left(\frac{1}{\mu} \nabla \times A \right) = J_s - \sigma \frac{\partial A}{\partial t} \tag{5.14}$$

in which $\boldsymbol{J}_s$ is the current density of prescribed sources and σ ($\partial \boldsymbol{A}$ / ∂t) are the induced currents [102]. In 2D, only the z components of $\boldsymbol{A}$ and $\boldsymbol{J}_s$ exist. Since the currents and the potential are varying sinusoidally, they can be expressed as the real parts of the complex functions $Ae^{j\omega t}$ and $Je^{j\omega t}$ which can be solved using complex arithmetic. Thus, equation 5.14 becomes

$$-\nabla \cdot \frac{1}{\mu} \nabla A + j\omega\sigma A = J_s \tag{5.15}$$

The losses per unit length for the 6th, 12th and 18th time harmonics are obtained by extracting the integrals of J^2/σ over the cross sectional area of the cold conductors, and by multiplying by the core length and by a factor of two to allow for the half of the machine not included in the model. The total full-load losses from each individual time harmonic component of the generator with Invar rotor and 9% nickel steel rotor are as shown in the Table 5.3 and 5.4 respectively.

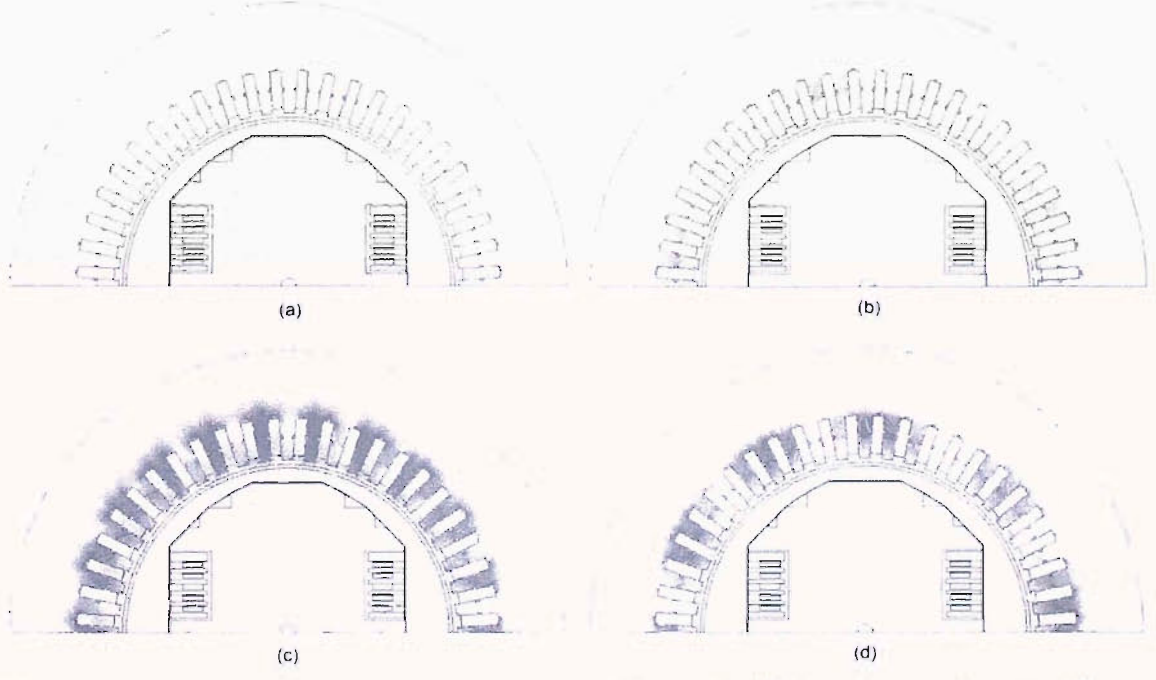

Figure 5.6 Contours of vector potential: (a) DC field, (b) 6th time harmonic, (c) 12th time harmonic, and (d) 18th time harmonic

Table 5.3: Full-load losses for the generator with Invar rotor.

Time harmonic order	Power per unit length (W/mm)	Full-load losses (W)
6th	8.19E-03	5.32
12th	6.63 E-05	0.04
18th	2.74E-05	0.02

Table 5.4: Full-load losses for the generator with 9% nickel steel rotor.

Time harmonic order	Power per unit length (W/mm)	Full-load losses (W)
6^{th}	3.35E-03	2.18
12^{th}	3.12E-05	0.02
18^{th}	1.92E-05	0.01

Figure 5.6 (a) shows the DC field and (b), (c), and (d) show the 6^{th}, 12^{th}, and 18^{th} superimposed AC fields respectively for the generator with 9% nickel steel rotor. They were obtained using non-linear static model and AC model with new current densities defined in each stator slot and incremental permeability data taken from the static model. It can be seen that when the machine is under load, the direct axis is no longer a line of symmetry nor is it a flux line. The rotor is not magnetically symmetric due to saturation, which is different on the leading and trailing edges of the pole. The largest eddy current loss component is that due to 6^{th} time harmonic eddy currents. These eddy currents are caused by the 5^{th}, and to a lesser extent the 7^{th}, space harmonics of the stator winding MMF. It can be concluded that the no-load losses, which are caused by the stator slots modulating the synchronous field, are significantly smaller than the full-load 6^{th} harmonic loss. Losses due to the 11^{th} and higher order harmonics of the stator MMF were found to be negligible.

5.2 Sudden three-phase short-circuit analysis

The characteristic values of transient and subtransient reactances of synchronous machines have been used for many years, and for many purposes. Initially such reactances and time constants were calculated to give both machines designers, and users, of synchronous machines a first hand knowledge of short-circuit current magnitudes and their rate of change of decay. Such magnitudes are important in establishing switchgear fault ratings. This knowledge also enables mechanical stresses to be calculated between armature windings resulting from excessive currents that occur during electrical disturbances at or near the synchronous machine terminals. Moreover, protective schemes could be devised so that relays could be correctly calibrated to trip armature or field circuit breakers, and thus remove the faulted machine from the power system. In addition to calculating these characteristics short-circuit reactance values, the

time taken for the fault currents to decay or pass through various states after a fault was of interest. Basically, there are two periods during which the rates of current decay: the initial and shorter period was named the time subtransient, and the subsequent and much longer period was called the transient.

The generator was subjected to a three-phase balanced short-circuit at the terminals under no-load condition. Important parameters, such as direct axis reactances and time constants, were derived from the predicted waveforms. Since it was unclear what value of resistance should be used for the field circuit, few models were produced. In the first approach, a constant value of field current was imposed by removing the field circuit from the model. In the second model, the actual resistance of silver was used to represent the resistance of the field circuit. Finally, the use of a substantial negative field voltage to reduce the large fault currents in the field circuit was investigated.

5.2.1 Constant field current excitation

In the past most designers relied on the use of complicated equivalent circuit machine models whose parameters are difficult to obtain with good accuracy during the design stage. The finite-element method provides better facilities to model complicated geometry of electrical machines, including saturation effects in iron, thus leading to better understanding of the short-circuit phenomenon [103]. The short-circuit analysis is of particular importance when considering devices operating in very low temperature environment. In this case the field winding of the HTS synchronous generator is made of silver clad BSCCO tapes which operate in a temperature range 73-77 K. During fault condition, large transport currents are expected to be induced in these windings; these cause large loss densities which may lead to thermal runaway and could damage the winding.

In general, there are several paths in the complete magnetic circuit of a synchronous generator that give rise to leakage reactance components of a synchronous generator. Leakage reactance components result from fluxes that exist in the various air paths. The leakage reactances result from magnetic flux components that do not enter into air gap

flux. Leakage flux generally exists in all nonmagnetic regions adjacent to armature conductors, as illustrated in Fig. 5.7. In the 2D models, the stator slot and air gap leakage are included in the stator flux linkages, however no account is taken of the stator end winding linkage and an estimate of this must be added to the finite-element derived linkages to obtain the total stator flux linkages. The end winding leakage reactance together with the winding resistance was obtained from manufacturer's data sheet; they are considered a fixed quantity and are used as input to the calculation.

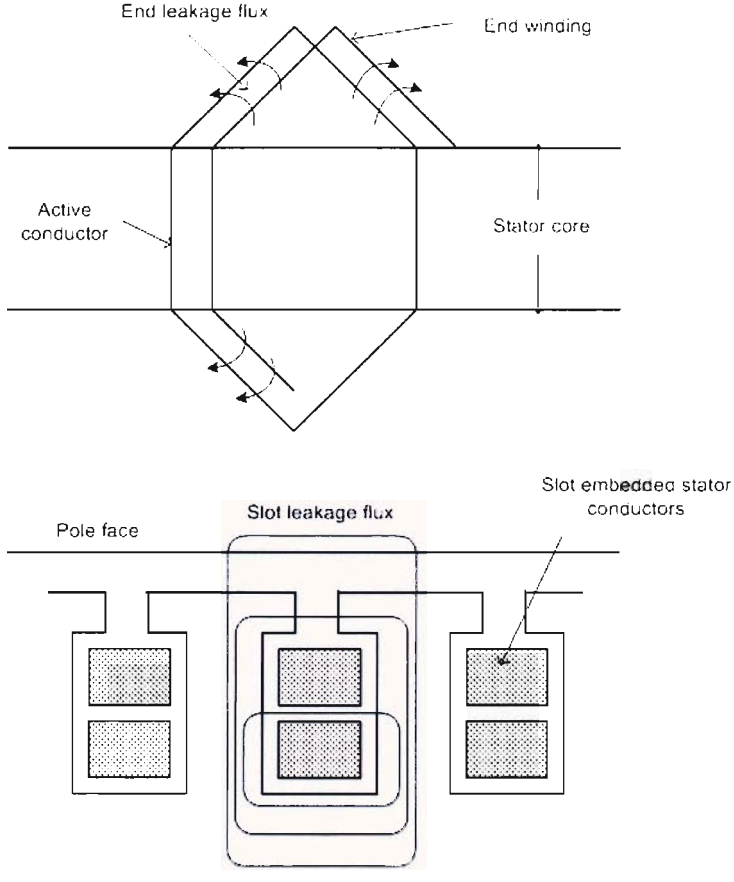

Figure 5.7: Leakage reactance components.

During a three-phase short circuit, the flux linking the stator immediately before the transient is trapped in the short-circuited windings and decays with the armature time constant, producing unidirectional currents in addition to the balanced three-phase currents. The transient can only be simulated properly by allowing relative movement

between stator and rotor. External circuits are linked to the 2D model to simulate the connections between the coils.

The rotor is set to rotate at a fixed speed of 3000 rpm and the time-step was chosen to hide the effects of tooth ripple, which in this case are believed not to be significant. As described earlier in the loss analysis, the long decay time constant due to low resistance of the copper layer make it impractical to use small time step. Therefore, a fixed time step of 0.417 ms was used which is equivalent to a period for the rotor to pass one stator slot. Non-linear analysis was used throughout because the saturation of the rotor core was thought to be important. For simplicity, the coils are considered as being constructed from filamentary wires such that skin and proximity effects in the turns are ignored. Therefore, the current density in each turn of the coil is assumed to be uniform.

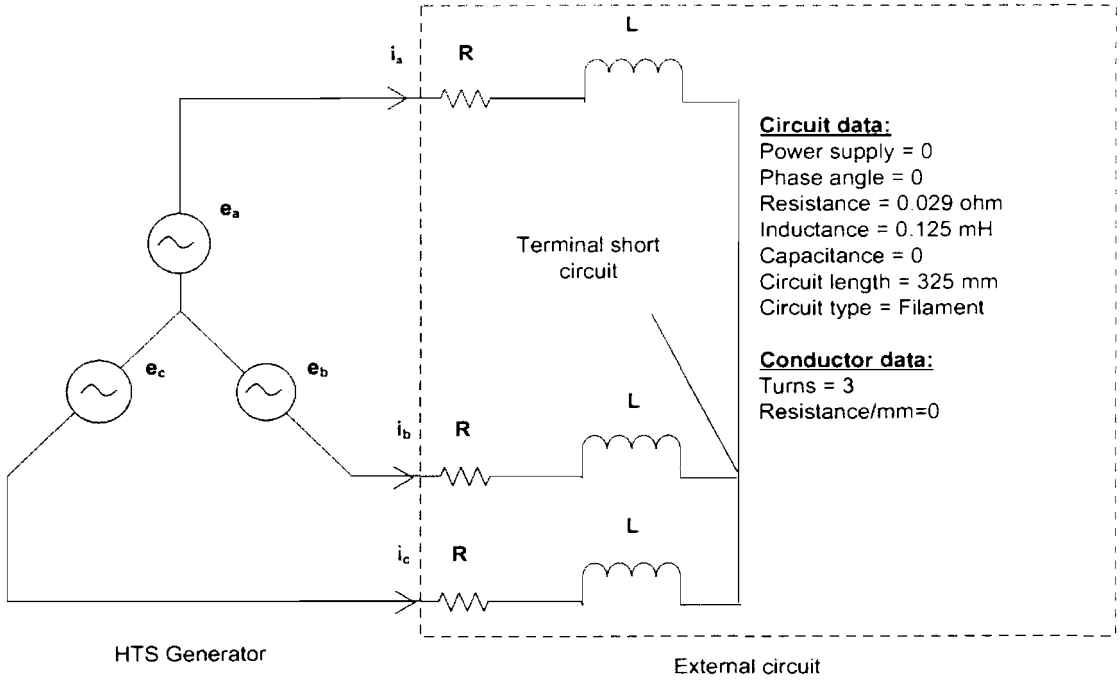

Figure 5.8 The circuit arrangement for finite-element modelling.

Figure 5.8 shows the external circuit arrangement for the model used for short-circuit analysis without considering the field circuit. The simulation was set to run for a period of 2.5 cycles (0.05 sec). Generally, in short circuit analysis, the first few cycles are of

most interest, since the largest currents occur during this period; thus it will normally not be necessary to continue the simulation until the steady state condition is reached. This would be sufficient to provide a good initial indication about the fault. Further modelling evaluations were carried later with field circuit included and appropriate resistance to obtain the reactance parameters.

The model similar to the one used earlier as shown in Fig. 5.3 was derived. The symmetry of the machine is exploited to halve the area that needs to be modelled; regions are bounded by the rotor inter-polar axis and the back of the stator core: the latter was taken as flux line with $\boldsymbol{A} = 0$ and the former had a periodicity boundary condition with $\boldsymbol{A}$ at $180^\circ = -\boldsymbol{A}$ at 0°. The model was discretised into 24496 elements in order to obtain a solution with minimal error. The analysis allows such models to be built by introducing an air-gap region between the rotor and the stator. As the generator has a large air gap, it is reasonable to assume that results are not greatly affected by permeance changes that occur as the rotor moves past the stator teeth and that therefore a single mesh can be used for all instants in the time-stepping process. However, the mesh in the air gap region is removed and re-built after the rotor regions are rotated to their new position for the next time-step. Figure 5.9 shows the mesh generated after the rotor rotates by one time step.

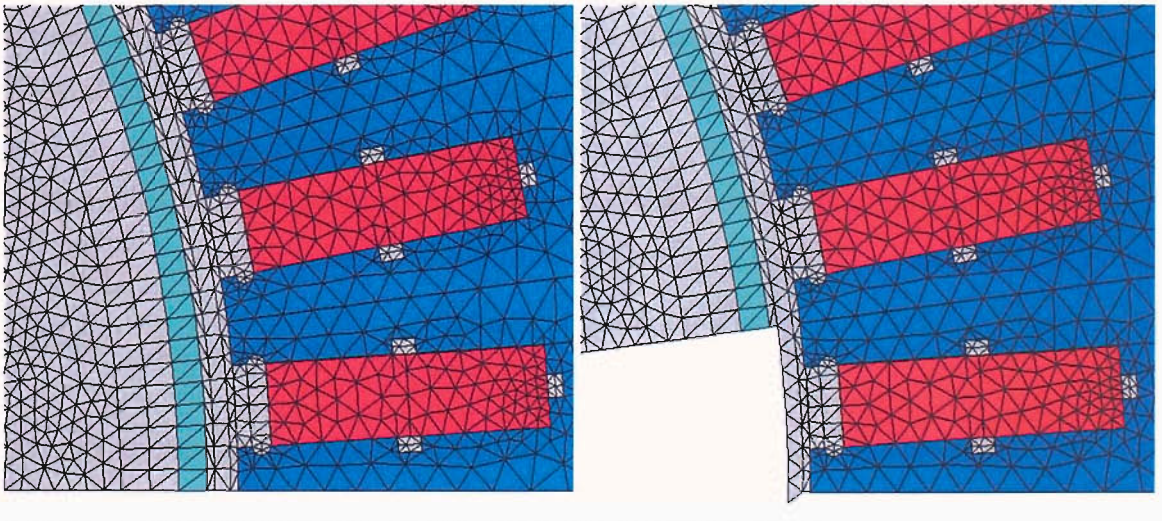

Figure 5.9 The gap region mesh before and after one time step.

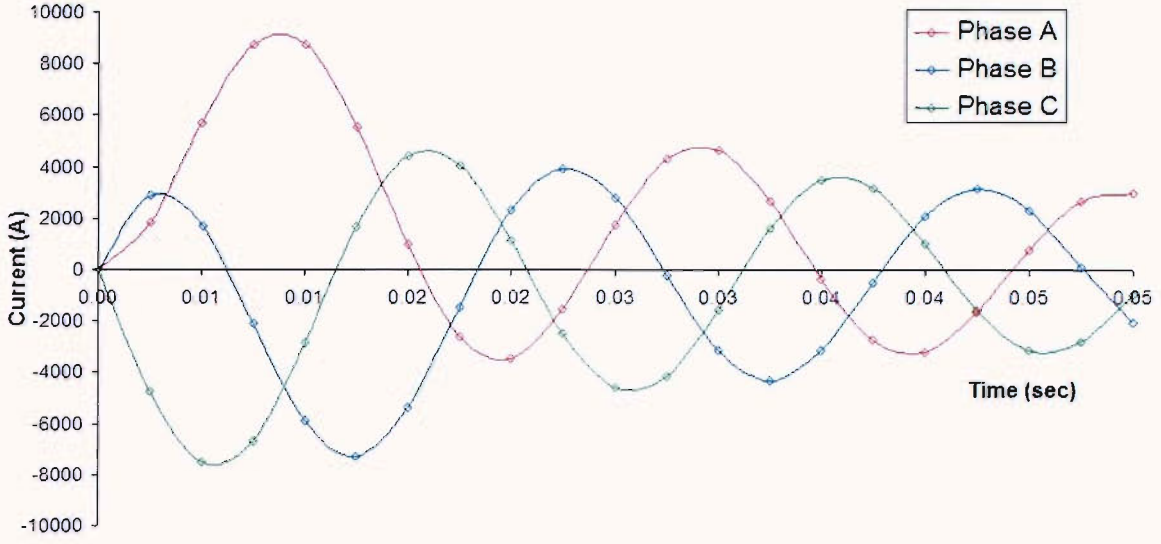

Figure 5.10 Currents as a function of time for HTS superconducting generator short-circuited while running at no-load.

The currents in each phase are recorded from each output time-step and the curves are fitted accordingly as shown in Fig. 5.10. The magnitudes of these currents subsequently decay exponentially towards their steady-state values as the trapped flux decays. However, it is apparent that the solution has not reached its steady state. These currents cause substantial losses in the stator winding. Figure 5.11 shows that the I^2R loss in the stator winding peaks at approximately 1.7 MW and then gradually decreases to its steady value. The large currents also produce a large torque (see Figure 5.12), which rapidly reduces the speed of the rotor. The torques were evaluated by performing integral along the air-gap half-way between the stator and the rotor, and taking into account the length of the core. These values were in turn used to obtain the angular momentum of the rotor for each time step using trapezoidal rule of integration,

$$\int L\,dt \approx \left[\left(T_n + T_{n+1}\right)/2\right] \times \Delta t \tag{5.16}$$

where L is the angular momentum of the rotor, T is the torque at time step n and Δt is the time step interval. Given the density of the 9% nickel steel rotor core, which is approximately 8000 kg/m^3, the rotor moment of inertia can be found. Consequently, the

machine speed decreases rapidly by 19.45% after 50 ms of fault simulation as shown in Figure 5.13. Finally, assuming the temperature before fault is 73 K, the temperature for each time step was evaluated using the copper loss density, ρJ^2 (ρ is the resistivity of copper), divided by the density and specific heat capacity of copper which is 8960 kg/m^3 and 370 J/kg/K, respectively [104]. Moreover, the high transient loss in the stator winding causes the temperature to rise to about 103 K as shown in Figure 5.14.

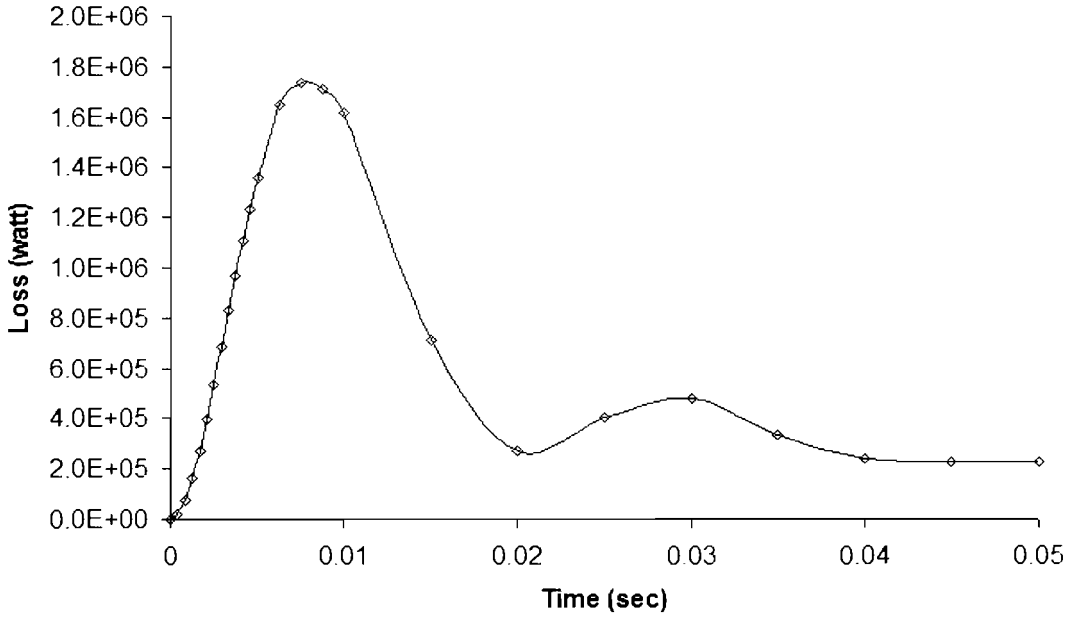

Figure 5.11 The I^2R losses during faults.

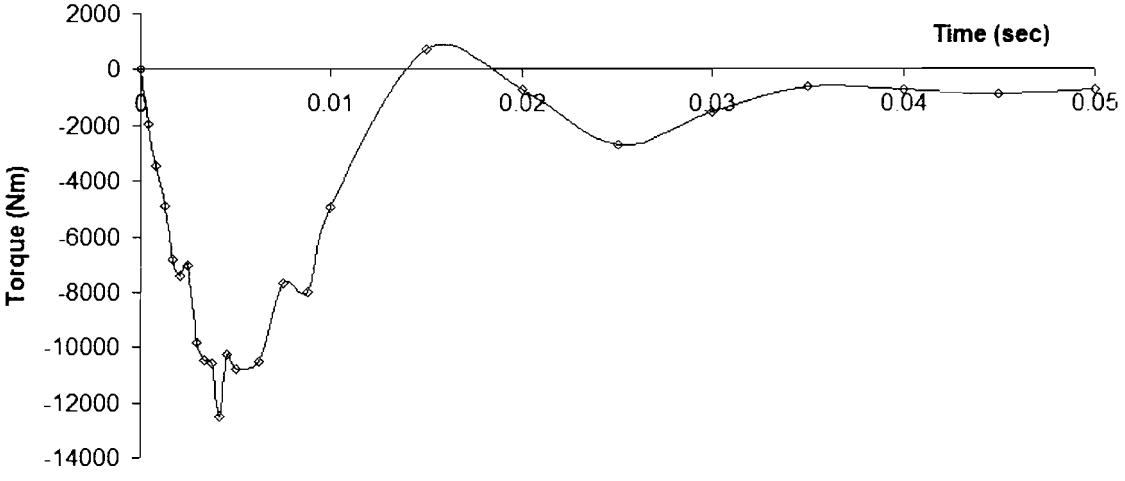

Figure 5.12 Torque during balanced 3-phase short circuit.

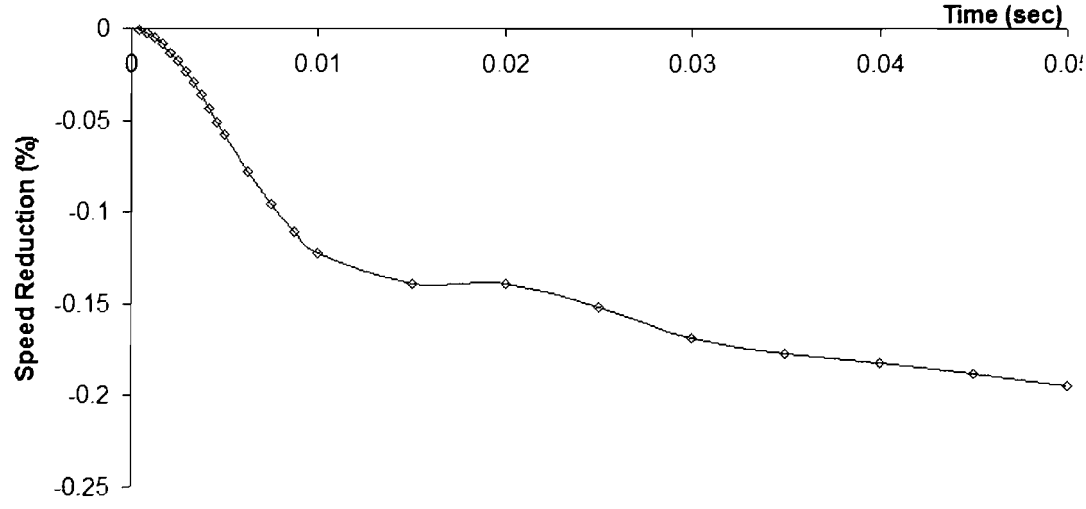

Figure 5.13 Rotor speed reduction during faults.

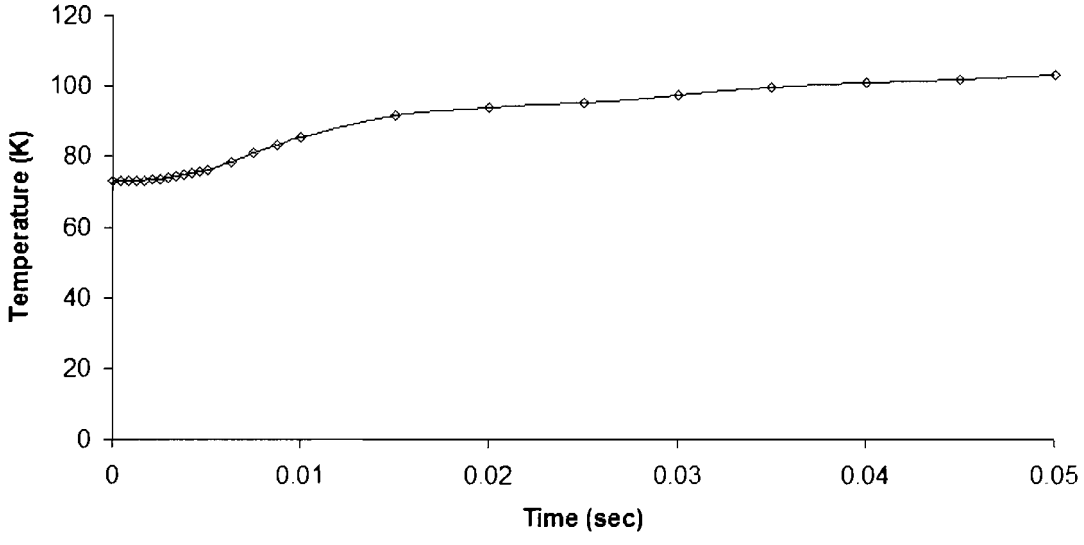

Figure 5.14 Temperature rise due to fault

5.2.2 Model with field circuit

A synchronous machine with its armature winding short circuited has other closed circuits which need to be taken into consideration. In order to simulate the effect it has on the field windings during fault, a finite-element model as shown in Fig. 5.15 was used. The field circuit, which is the high temperature superconducting field winding, is defined to have resistance equal to silver, 0.3×10^{-8} Ωm [105]. Based on the actual dimension of the superconducting tape used, the total resistance of the field circuit for

one pole was found to be 0.539 Ω. The similar modelling approach as in the previous section was used. The difference in the model of previous section is that the eddy currents in the field circuit are not allowed in the model. This is due to the fact that the constant field current applied does not affect the transient term.

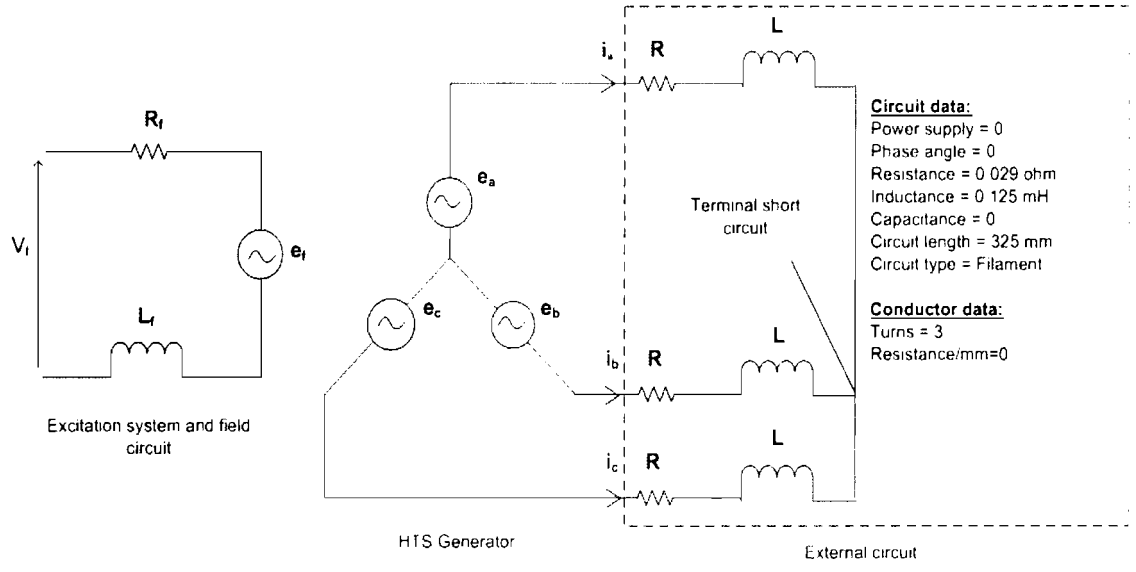

Figure 5.15 External circuit including field circuit connected to the FE model

Figure 5.16 shows the short-circuit currents for the HTS synchronous generator. The traces of the armature currents are not symmetrical about the zero current axis, and exhibit the DC components (red lines on Fig. 5.16) responsible for offset waves. The DC current components arise because, at the instant of short-circuit, the flux linking the stator windings differs from the value required to drive the sustained current. The DC components drive this additional flux, and are driven by the decay of the flux. The algebraic sum of the DC components is zero and they all decrease to zero exponentially with the same armature time constant, T_a. The initial value of these components depends upon the point in the cycle at which the short circuit occurs. The maximum possible initial value of the DC component is equal to the initial value of the envelope of the AC component. This value can occur in only one armature phase at a time. The transient and sub-transient currents arise from similar mechanism due to the flux trapped in the field winding and damper winding (radiation screen) respectively.

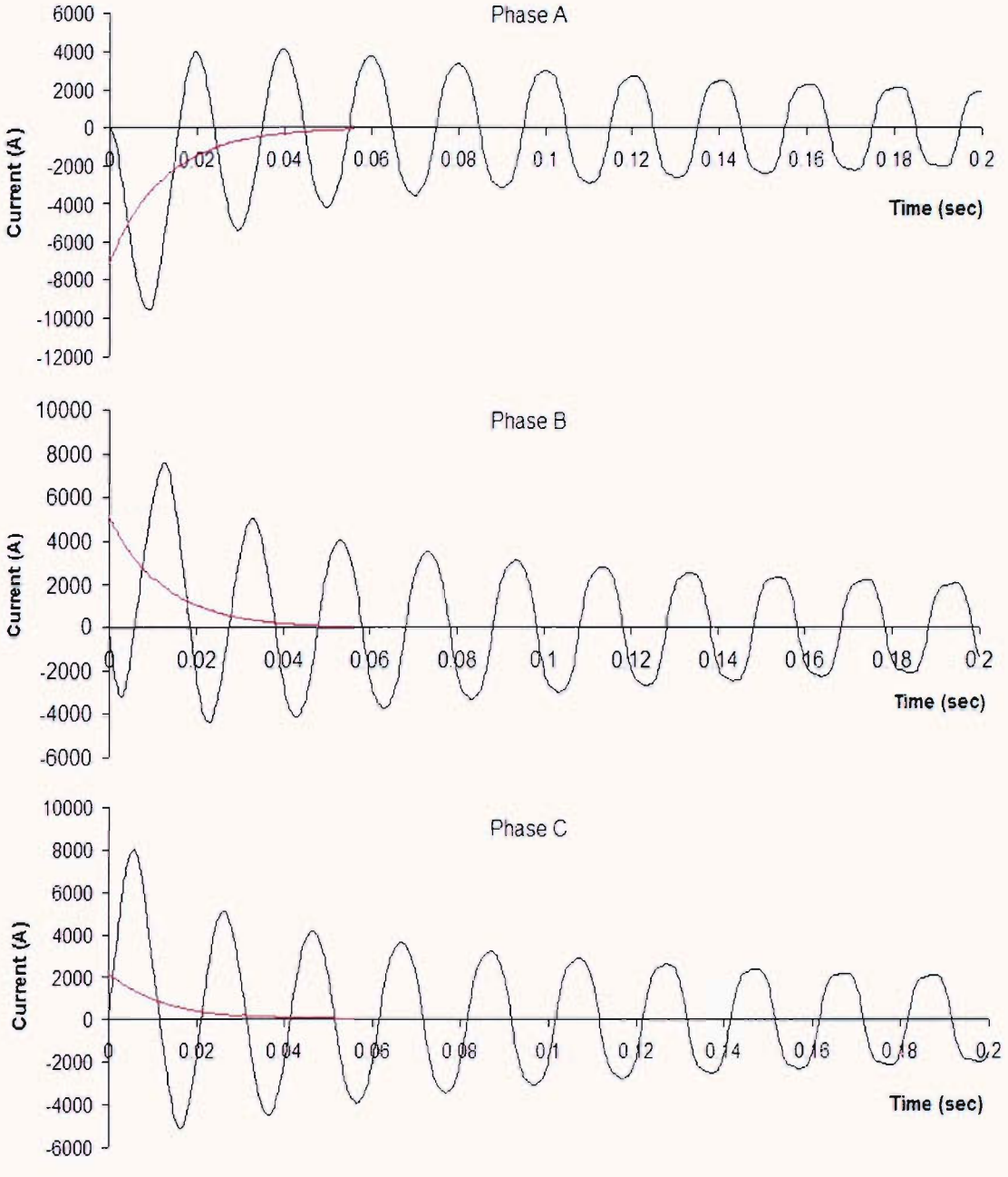

Figure 5.16 AC and DC components of armature currents as a function of time for HTS synchronous generator short-circuited while running at no-load (red lines indicate DC component)

The envelope of the AC component is high at the instant of short-circuit and decays ultimately to the sustained value I_s. If I_s is subtracted from the AC wave, the remainder

is found to consist of two exponential components: transient component I' with long time constant, T_d', and subtransient component I'' with short time constant, T_d''. In addition to these AC currents, the waveforms of the stator currents each include a decaying DC component. In general, each short-circuit armature current waveform consists of a unidirectional or DC component and three AC components, and is given by an expression of the form,

$$I_{SC} = I_{DC}e^{(-t/T_a)} + I_S\cos(\omega t + \phi_0) + I'e^{(-t/T_d')}\cos(\omega t + \phi_1) + I''e^{(-t/T_d'')}\cos(\omega t + \phi_2) \qquad (5.17)$$

The measurement of synchronous reactance, x_d is given as the ratio of open-circuit armature voltage to sustained short-circuit armature current, $x_d = E/Is$, where E is the open-circuit voltage and I_s is the sustained short-circuit armature current. The value of E was obtained from the open circuit voltage of an unsaturated machine, or the voltage read from the air-gap line of a saturated machine. The open-circuit characteristic was determined using finite-element calculations. Since a curve of field current against voltage is required, the field current was specified by varying its value up to 100 A, and the fundamental flux wave was evaluated to obtain the induced line-to-line stator voltage. Figure 5.17 shows the open-circuit characteristic curve of the HTS synchronous generator. If it were not for the magnetic saturation of the iron, the curve would be linear as represented by air gap line in Fig. 5.17. Similarly, the transient reactance, $x_d' = E/(I_s + I')$ and subtransient reactance, $x_d'' = E/(I_s + I' + I'')$ were evaluated by fitting the values into the short-circuit armature current curve using equation 5.17. Their values are shown in Table 5.5.

Table 5.5 The direct axis reactances and time constants

Reactance (p. u.)		Time constant (sec)	
x_d	0.232	T_d'	0.136
x_d'	0.055	T_d''	0.012
x_d''	0.038	T_a	0.012

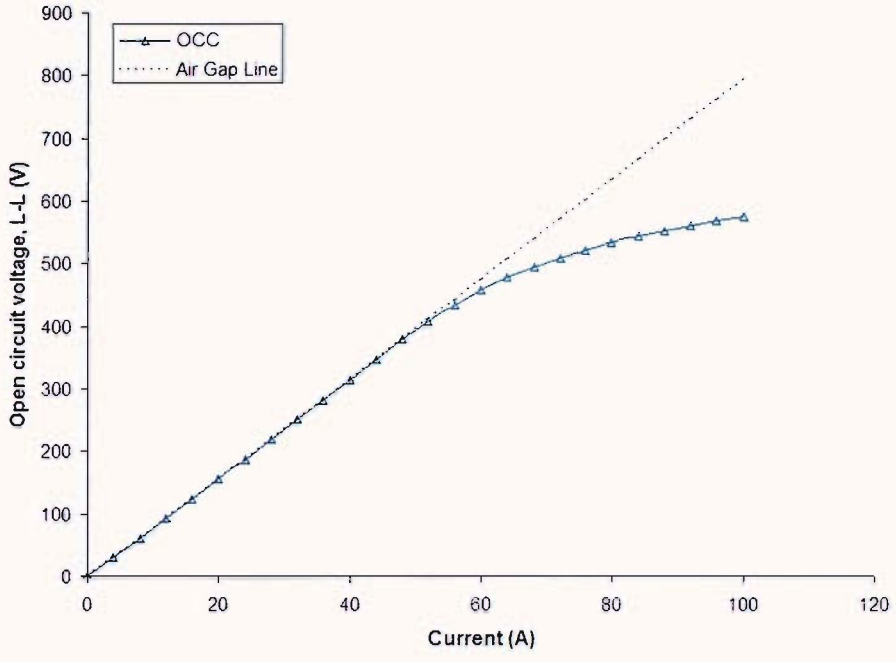

Figure 5.17 Open circuit characteristic of HTS synchronous generator

A low resistance of 10mΩ was also used earlier in the analysis, but for the same number of cycles it only provides limited transient information. This is due to the low resistance of the field circuit in the model, which causes the transient time constant to be very long; the length of the simulation is therefore too short to give any estimate of the synchronous reactance or transient time constant. This is clearly shown in Fig. 5.18, where, for a similar duration, the current decays faster with field circuit of higher resistance. The field current, like armature current, consists of DC and AC components.

Assuming that the field circuit is to poses the 10mΩ resistance, it is expected that during a transient that is caused by a short-circuit, a large positive fault current would be induced into the field. Hence, in order to investigate the voltage required to control this large current, a negative voltage was applied externally to the field winding 5ms after fault initiation. It can be seen from Fig. 5.18 that, with -175 V, the field fault current was successfully reduced. In the next section, the results of the three-phase short-circuit fault simulations are compared and validated with those obtained using standstill frequency response method.

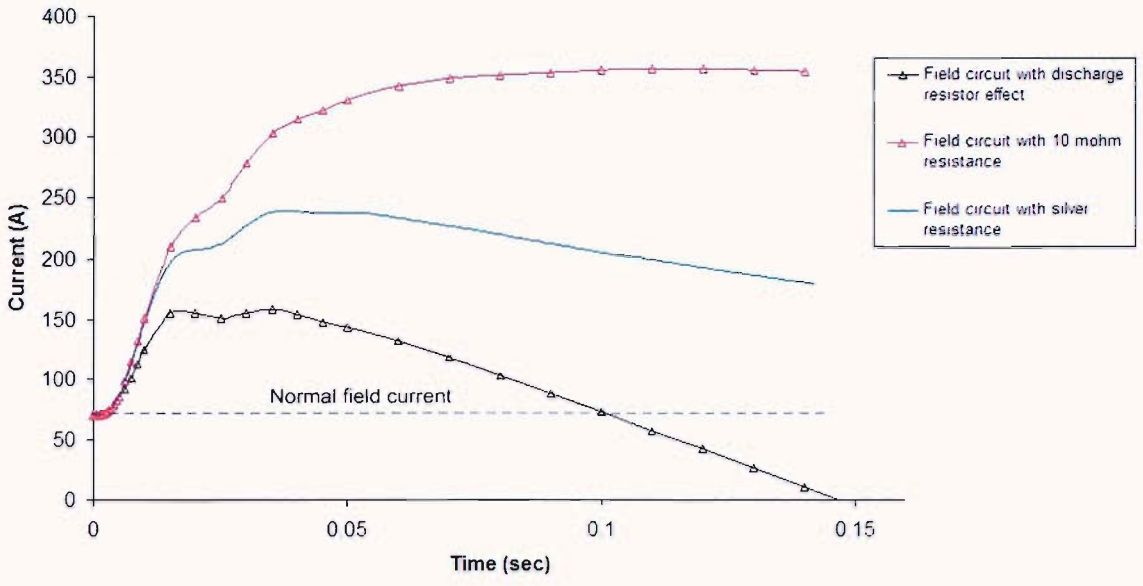

Figure 5.18 The unidirectional component in the field current of the HTS synchronous generator

5.3 Simulated frequency response

Standstill frequency response (SSFR) test has been adopted by many as a standard to evaluate stability parameters for synchronous machines. The standard test procedure for obtaining synchronous machine parameters is described in the IEEE Standard 115 A (1) [106]. Frequency response data describe the response of the machine fluxes to stator current and field voltage changes in both the direct and quadrature axes of synchronous machine. Such responses describe the rates of change of various stator or field quantities over a range of sinusoidal excitations from very low frequencies up to and considerably beyond nominal 50 Hz values. In terms of SSFR test procedures, the advantage over short-circuit testing is that this method can be performed with relatively modest expense, either in factory, or on site. This test also poses a low probability of risk to the machine being tested; data in both direct and quadrature axes are available, with little change in the test setup and without resorting to special short circuit or low voltage tests. Whilst the sudden short circuit test can only provide information on the parameters of second order models in the direct axis, the SSFR tests enable the parameters for higher order models to be determined.

In terms of finite-element modelling, it is apparent that this method has the advantage of less computational effort through the use of AC analysis compared to transient rotating machine model in short-circuit analysis. The reactances of the HTS generator were evaluated based on a modelling technique described by Reece and Preston [94], and Salon [95]; the latter has proved that results obtained from finite-element simulation were in good agreement with the test results. The reactance parameters were obtained by injecting variable-frequency current into one phase of the stator and out through the other two (star connection winding). The direct and quadrature axis data were acquired with the rotor stationary and field axis aligned at the appropriate stator magnetisation direction. These reactances values are usually given in per unit and are related to base quantities which for the stator are usually defined as per phase rated values.

5.3.1 Synchronous reactances

When a machine with salient poles is investigated, two reactances representing the stator reaction must be calculated: in direct axis x_d and in quadrature axis x_q. While the air gap in synchronous machines of the round rotor construction is practically of uniform length, that of the salient pole machine is much longer in the quadrature axis. Since the air gap is of minimum length in the direct axis, a given armature MMF directed along that axis produces a maximum value of flux, and the same armature MMF directed along the quadrature axis where the air gap has its greatest length produces a minimum value of flux. Generally, the pole axis is known as direct axis and the interpolar axis as quadrature axis; the angle between the two axes being 90 electrical degrees. The quadrature axis is located 90 electrical degrees ahead of the direct axis in the direction of the rotor rotation. Figure 5.19 shows a typical schematic diagram of phase windings and field winding along with the notations adopted for voltages and currents, as well as the location of the direct and quadrature axes.

The synchronous reactance associated with direct axis is therefore a maximum and is known as the direct-axis synchronous reactance, x_d. The armature currents produce the same fundamental MMF wave, regardless of angular position of the rotor, but the fundamental flux wave varies greatly with the rotor position. If the rotor is so rotated

that the direct axis stays in line with the crest of the rotating MMF wave, a path of high permeance is offered. Therefore, the fundamental flux wave has its greatest possible magnitude for a given armature current. Accordingly, the total flux linkage of each phase winding of the armature has the greatest possible value for a given current in the winding, and the armature inductance and inductive reactance are greater than they would be for any other position of the rotor. The flux linkage of an armature phase per ampere of armature current under these conditions is the direct-axis synchronous inductance, L_d, whereby $x_d = \omega L_d$.

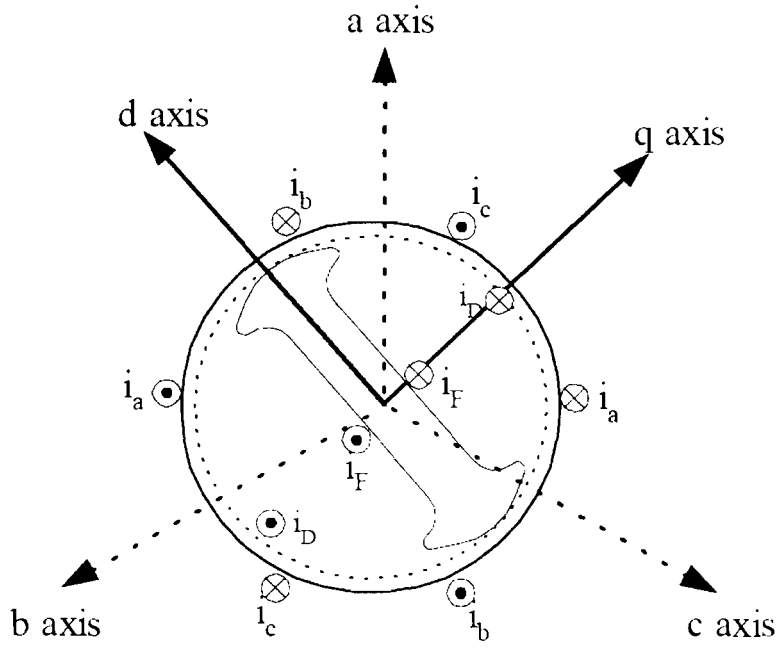

Figure 5.19 The schematic diagram of phase windings and field winding of a synchronous generator

The direct axis reactance was determined by using 2D magnetostatic analysis. In finite-element modelling, field current and armature current were used as the input. The end winding flux linkage, which adds several percent to the reactance value, was included in the model. The symmetry of the machine is exploited to halve the area that needs to be modelled. The finite-element solution is iterative in order to account for nonlinear BH characteristics of the generator magnetic circuits. Linear finite-element computations using the permeabilities from the previous solution were then used for calculation of the

saturated reactances. In these models, the field winding is unexcited and a current of 1A is applied to the main phase winding with -0.5 A in the other two phases. The applied current was chosen arbitrarily for simplicity, since it will be eliminated when calculating the ratio of flux linkage to current. Since the stator is excited with equivalent ampere-turns, care must be taken to include the proper number of turns. Figure 5.20 shows the flux lines distribution in the direct axis. A synchronous generator under consideration exhibits an interesting symmetry condition. Even though the geometry of the generator is symmetric about direct and quadrature axes, the magnetic field is not symmetric about these axes but does retain rotational symmetry about the centre of the generator, with a period of 180° for a two pole generator.

Based on the finite-element vector potential solution, the flux passing through a coil can be obtained. In a model with XY symmetry, there will be X and Y components of flux density and Z directed currents. The flux linking a rectangular loop with two sides parallel to the Z direction is simply given by the product of the length of these sides and the difference in the vector potential, A_z, between the points in the XY plane. The flux linkage λ is given by

$$\lambda = \frac{N}{a_1}\int_{a_A} A_z da - \frac{N}{a_2}\int_{a_{A'}} A_z da \tag{5.18}$$

where a_A is the region occupied by outward half of the coils in phase A, $a_{A'}$ is the return half of the coils, a_1 is the area of each outward coil, a_2 is the area of the return coil and N is the number of turns in each coil. By applying equation 5.18 using the evaluated integrals from finite-element analysis, and including the unaccounted effect of the end winding leakage inductance value (0.125 mH), the direct axis reactance, x_d was found to be 0.22 per unit.

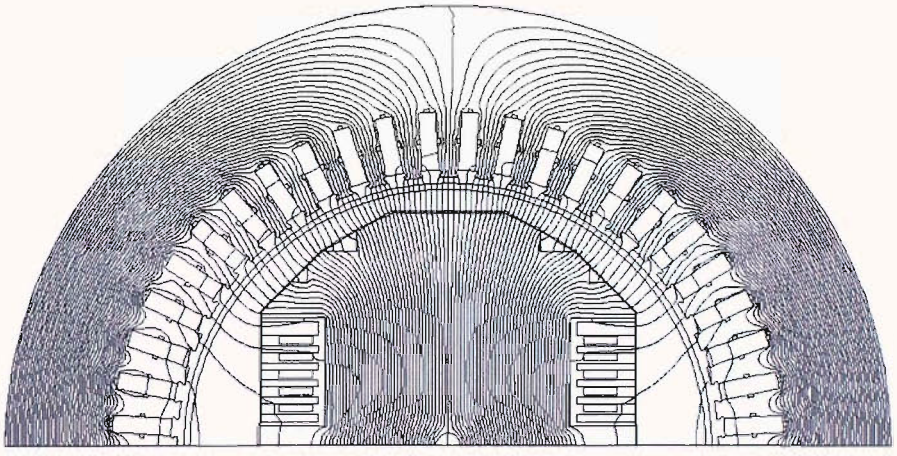

Figure 5.20: Distribution of flux lines for direct axis investigations

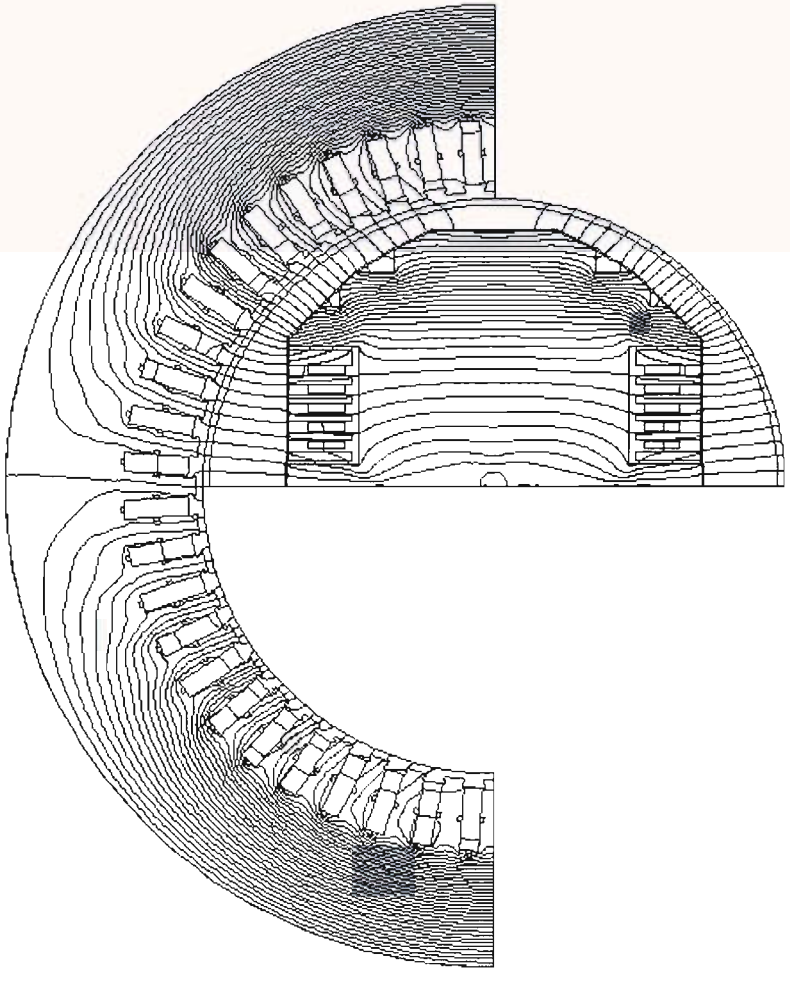

Figure 5.21 Distribution of flux lines for quadrature axis investigations

The same method described above was applied to evaluate the quadrature axis synchronous reactance. The only difference is that the rotor is locked at 90° with respect to the stator. Figure 5.21 shows the flux distribution in quadrature axis FE analysis. With the field winding open, the quadrature axis winding was excited with the same current as in the previous model. The quadrature-axis synchronous reactance was found to be 0.156 per unit. In cylindrical rotor structure, both the direct and quadrature axis reactance are almost similar. However, this is not the case in salient pole rotor because of the larger gap in the quadrature axis. It can be seen that the synchronous reactance, x_s ($= x_d + x_q$) of the superconducting generator is lower than for a conventional machine. This is mainly due to the large air gap that is needed to accommodate the thermal insulation.

5.3.2 Transient reactances

During transient conditions, the synchronous machine exhibits further parameters that need to be considered, namely direct-axis and quadrature-axis transient reactances due to abrupt application of armature currents caused by the sudden appearance of MMF opposite each field pole. The definition of transient reactance is based on the three phase sudden short circuit test. It is the equivalent reactance of the direct axis which applies after first few cycles. In typical synchronous machines, the rotor component of the reactance is dominated by the field winding response to a change in current in the stator. The response of the damper (copper layer) and rotor core are not negligible, but the field winding is the most important rotor circuit.

The term transient reactance was used to describe the reactance that the machine exhibited during transient conditions, which is following a short circuit or following a switched load change. In both cases the rotor is rotated forward at synchronous speed, with its direct axis in line with crest of the armature MMF wave and with the field winding closed but not excited. Abrupt application of the armature currents causes the sudden appearance of a MMF opposite each field pole, tending to establish flux through pole core. Such flux would link the field winding and is opposed by induced field current, tending to maintain the flux linkage of the field winding constant at zero value.

By the theorem of constant flux linkage, at the instant immediately after application of the armature currents, the field linkage is still zero. Therefore the only flux that can be established immediately is that which does not link the field winding but rather passes through low permeance leakage paths (largely in air). Under these conditions the flux per ampere is small and is defined as the direct axis transient inductance, L_d'. The direct axis reactance is $x_d' = \omega L_d'$. In a machine having salient poles, the changing flux can pass sideways through the field coils without linking them and inducing field current, consequently for salient pole machines, x_q' is equal to x_q.

The direct axis transient reactance was evaluated using the same method as described in the previous section; the stator was excited with direct axis current. However, the field windings were short circuited. The short-circuit simulation was carried out using external circuit with the field coils assumed to have silver resistance during fault. Using Steady State AC analysis, the magnitude of the transient reactance was evaluated at low frequency. A value of 1 Hz was chosen because this is a typical power system swing. Hence, the reactance value obtained can be used for transient stability study. The value of the direct axis transient reactance was found to be 0.058 per unit. The response of the generator to 1 Hz excitations is shown in Fig. 5.22.

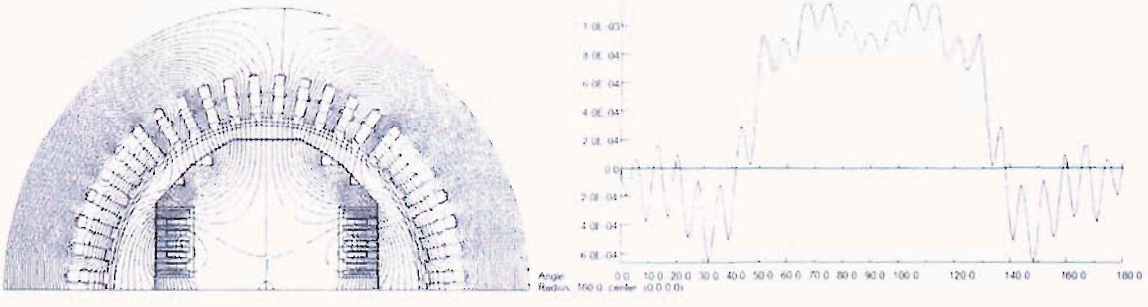

Figure 5.22 Flux lines distribution and air-gap flux densities at 1Hz with field shorted.

5.3.3 Subtransient reactances

In defining x_d', it was assumed that there were no rotor circuits except the main field winding. However, in salient pole machines, as in the case of this superconducting generator, additional rotor circuits are present and known as a damper winding (in HTS

generator the damper winding is the copper layer). If a positive sequence armature currents are suddenly applied in such time phase that the crest of the rotating MMF is in line with the direct axis of the rotor, transients are induced in the additional rotor circuits as well as in the main field winding. These transient currents oppose the armature MMF, and initially they are strong enough to keep the flux linkage of every rotor circuit constant at zero value. The additional rotor circuits are situated nearer to the air-gap compared to the field windings. Consequently, the flux set up by the armature current is initially forced into leakage paths of smaller cross-sectional area and lower permeance than would be the case if the rotor circuit were the field winding. Under these conditions the armature flux linkage per armature ampere is the direct axis subtransient inductance, L_d''. The direct axis subtransient reactance is $x_d'' = \omega L_d''$. The quadrature axis subtransient reactance, x_q'' definition is similar to x_d'' except that the suddenly applied positive sequence armature current is in such time phase that the crest of the space fundamental MMF wave is in line with the quadrature axis of the rotor instead of the direct axis. The subtransient inductance and reactance are always smaller than the corresponding transient quantities due to the effect of saturation [107].

In order to model the direct and quadrature axis subtransient reactances, the stator windings were excited with balanced load as in Section 5.3.1. Various frequencies from 0.01 Hz to 100 Hz were analysed using steady-state AC analysis with the field open circuited. Figure 5.23 shows the frequency response curve for direct and quadrature subtransient analysis at various frequencies. Figure 5.24 shows the flux lines and air gap flux density at 50 Hz where the corresponding curves in Figure 5.19 are obtained, and thus the x_d'' and x_q'' values. At higher frequency (subtransient state) the two curves almost converge, thus x_d'' is 0.038 per unit and x_q'' is 0.036 per unit (with the inclusion of end winding leakage reactance). The damper layer restricts the flux to low permeance paths, as shown in Fig. 5.24, thus making the subtransient reactances much less than the transient values. Furthermore, at higher frequency the damper layer and solid rotor body dominate the situation. Therefore, very little flux penetrates to the depth of the field winding.

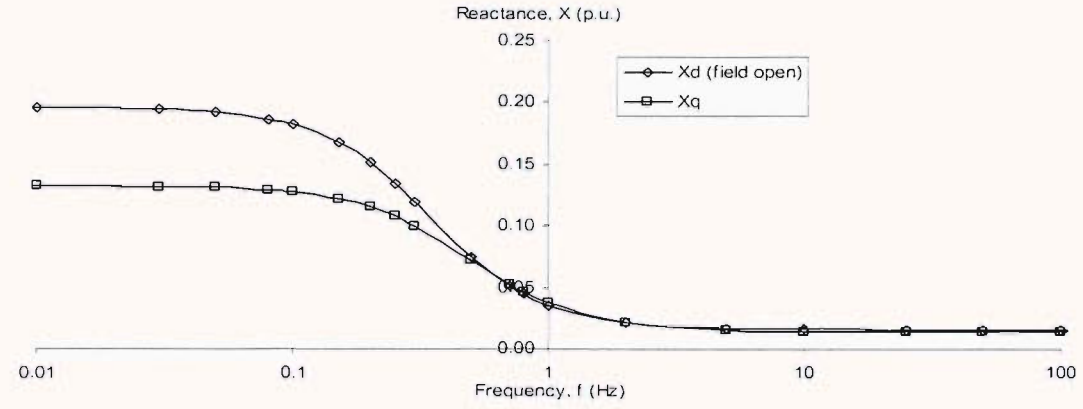

Figure 5.23 Open circuit reactances at various frequencies.

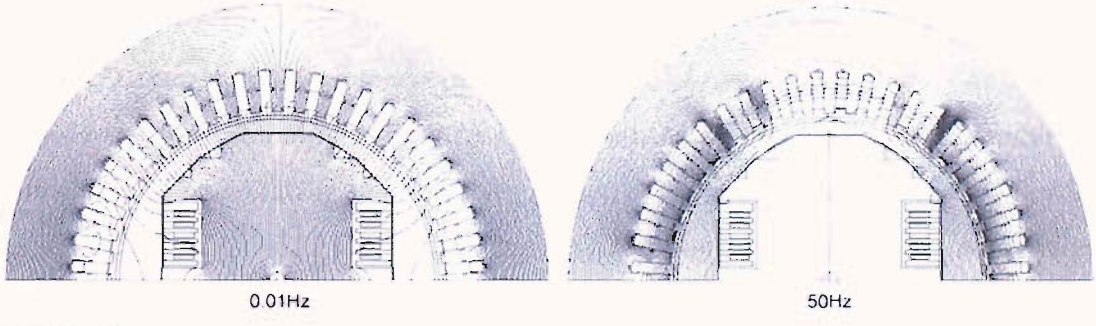

(a) Direct

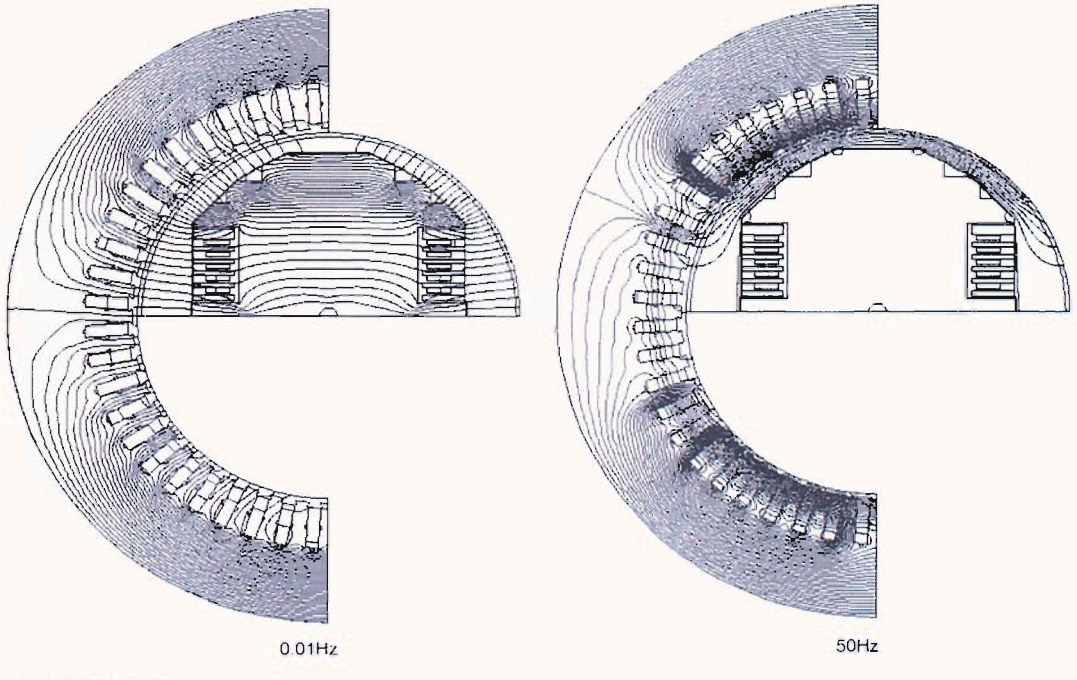

(b) Quadrature

Figure 5.24 Flux lines for subtransient direct and quadrature reactances analysis.

PRELIMINARY DESIGN AND MODELLING OF A SUPERCONDUCTING GENERATOR WITH A HTS CORELESS ROTOR

The presence of the magnetic core was unavoidable in the previous design simply because the properties of the available tape at the time were insufficient to even consider a coreless solution while maintaining the cooling at 57–77 K (rather than 25–30 K) and still achieving reasonable air-gap flux density. The recent advancements in the readily available refrigeration systems have helped significantly in reducing the overall costs, thus making the technology more attractive. Moreover, the availability of high quality BSCCO-2223 tapes with improved strength and critical currents makes the design of the next generation of HTS generator technologically viable. The HTS coils are inherently more stable than low temperature superconducting coils (which require liquid helium cooling), especially when operated in a liquid nitrogen environment. In this chapter, the configuration of the HTS synchronous generator with a coreless rotor will be outlined. Preliminary modelling studies have been undertaken and the results are discussed in Section 6.3.

6.1 Introduction

In the last few years superconducting rotating machines with HTS field windings have been demonstrated and several projects are currently nearing completion. Some of these projects were briefly discussed in Chapter 2. In the proposed generator design with coreless rotor, some of the existing components could be used (that is those used in the previous generator) such as the stator, supporting structure for rotor and the entire refrigeration system built specifically for the previous project. This will have the advantage of not only reducing the cost of the new project but will also allow more direct comparison of performance between the coreless design and the version with 9% nickel steel core. Such comparison would be particularly valuable as it has not been done by any other group in the world.

As indicated already, it is important first to conduct a thorough modelling and simulation study to arrive at the best configuration of the coils with the view of maximising the air-gap flux density while reducing the weight as well as minimising the total length of the tape. There are also other constraints, like avoiding having each coil of different shape and size, fitting the rotor into existing overall space inside the stator and ease of assembling the whole structure.

6.2 Design and structure considerations

In a typical superconducting rotating machine the conventional magnetic iron core is usually not employed. This is because to the high magnetic field in the air-gap would easily saturate the iron core, and thus produce undesirable excessive heat and noise. Only the stator back iron employs magnetic iron to provide shielding and carry flux between adjacent poles. Moreover, the absence of iron in most of the magnetic circuit causes these machines to have a very low synchronous reactance, which provides among other benefits a much larger dynamic stability limit within its MVA rating.

Preliminary design considerations of the coreless HTS generator reveal that it will be possible to use a ribbed fibreglass shell (in two halves) encapsulated in an external

stainless steel cylinder as the main supporting structure so that the space inside the windings – filled with 9% nickel in the current design – may be void. The flux diverters no longer form part of the structure and therefore the choice of materials becomes much easier. Figure 6.1 shows the layout of a possible HTS synchronous generator with coreless rotor. The cold stainless steel shell is designed to support the radiation shield (copper or aluminium) together with the support structure possibly made of fibre glass material, which holds the HTS coils. The field winding should be ducted to allow passage for the coolant. The stainless steel retaining shell design must ensure that it is vacuum isolated to avoid possible heat leak.

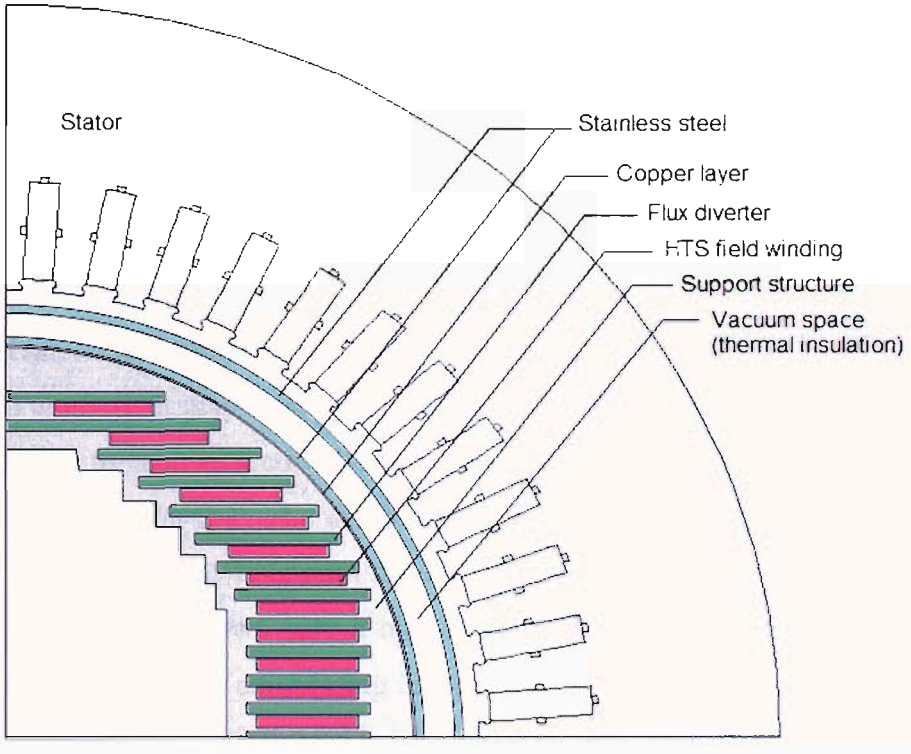

Figure 6.1 Proposed structure of a HTS synchronous generator with coreless rotor

6.3 Modelling and evaluations

In order to achieve a successful design, it is imperative to first conduct computational and simulation studies to predict the performance and identify critical issues. In particular, the severe non-linearity and anisotropy of the BSCCO tapes necessitates very

careful shaping of local distribution of magnetic field in the area of the HTS winding so that the undesirable field components are reduced and maintained at an acceptable level; this is a crucial requirement which may decide about the success or failure of the whole design as HTS tapes will simply not work if the normal component of field is too high. Hence, the geometry and placement of the necessary flux diverters is of paramount importance. This chapter reports on the 2D and 3D studies undertaken to arrive at an optimal magnetic design for further perusal. The modelling evaluations described here have been reported at Fifth International Conference on Computation in Electromagnetics, April 2004 [108]. It should be noted that the main objective of this modelling study is to establish that a coreless rotor configuration is possible electromagnetically. Known critical factors that will affect the machine performance are accounted for, and improvements over the previous model design are expected in particular in weight reduction.

6.3.1 Preliminary model

As explained earlier, the machine will utilise an existing stator, which is similar to the HTS generator that has been built. It has 48 slots and a balanced 2-pole, 3-phase star-connected winding. It may then be preferable to modify the stator as well to remove the teeth and slots to achieve a completely coreless design which might allow air-gap flux density to reach 1.5 to 2 T. The use of an existing stator lowers the costs significantly but restricts the flexibility to control the voltage waveform. Furthermore, a HTS rotor in a conventional stator allows only a modest upgrade in the capabilities of an existing machine. However, when considering this configuration the positioning and shaping of the flux diverters and HTS field winding become very important. These requirements are very different from the usual design criteria for a conventional generator as mentioned earlier.

The target air-gap density of the coreless rotor design is around 0.5 T, similar to the recently built HTS generator while the flux density normal to the broad face of the tape must be kept below 0.1 T or as low as possible. The machine will probably operate using sub cooled liquid nitrogen at 64 K (rather than 77 K); at this temperature – and by

using the currently best available material properties – it is possible for the HTS tape to transport 130 A provided that the normal field is below 0.1 T. The amount of iron used for the flux diverters must be kept to minimum so that the total weight reduction compared with the existing cored design will be significant.

A preliminary model of the machine was based on our previous experience and the following constraints:

- The distance from the HTS tape to the flux diverters is 0.5mm and 1.5mm respectively (top and bottom).
- The flux diverters are longer than the coils by 4mm on both sides.
- The assembly of the HTS coils and flux diverters has to fit within the 140mm radius.

The 0.5 mm and 1.5 mm gaps are there to avoid short circuit contact and at the same time provide space (larger gap) for connecting conductors from one HTS coil to another. The need to reduce the magnetic field component normal to the broad face of the tape, especially in the corner region, has already been explained. Finally, the large air-gap was needed to accommodate the supporting structure and thermal insulation. Moreover, for ease of manufacture, it was decided later that the inner diameters of some HTS coils (and flux diverters) should be the same; thus the bottom five sets of coils and diverters were aligned to each other. Figure 6.2 shows the preliminary model with details of the applied constraints, as well as the distribution of the normal field in the HTS coils. This shape was obtained by fitting as many HTS coils as possible within the 140 mm radius. Each coil consisted of 70 turns with each turn being of 0.5 mm width. Figure 6.3 shows the severity of the normal field in the superconducting coils in the absence of flux diverters; its effect is particularly apparent in the top region as shown in Fig. 6.4.

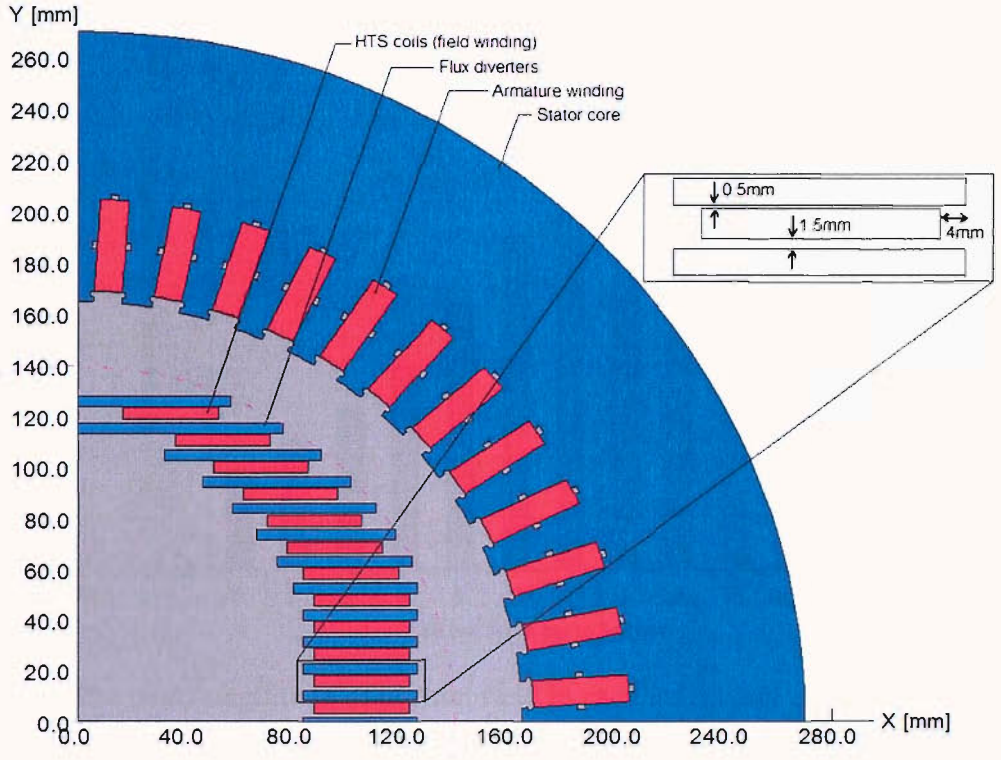

Figure 6.2 Preliminary design of the proposed coreless generator.

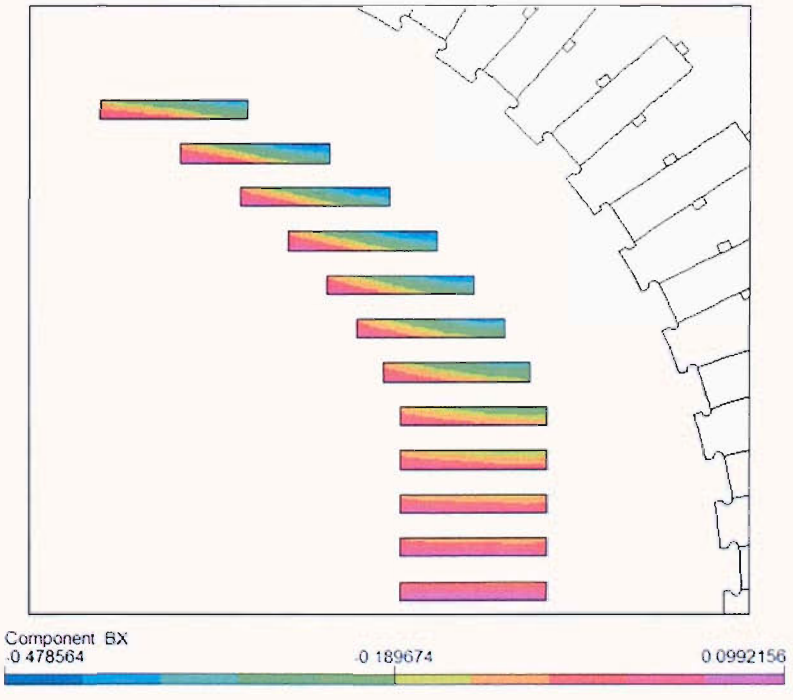

Figure 6.3 The flux density distribution of the normal field component in the superconducting coils in the design without flux diverter

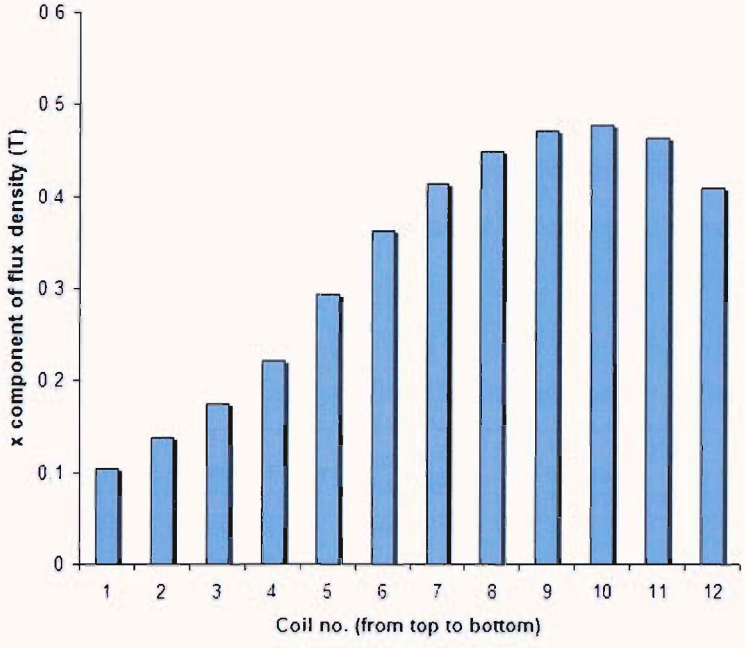

Figure 6.4 The peak magnitude of normal field in each individual coil

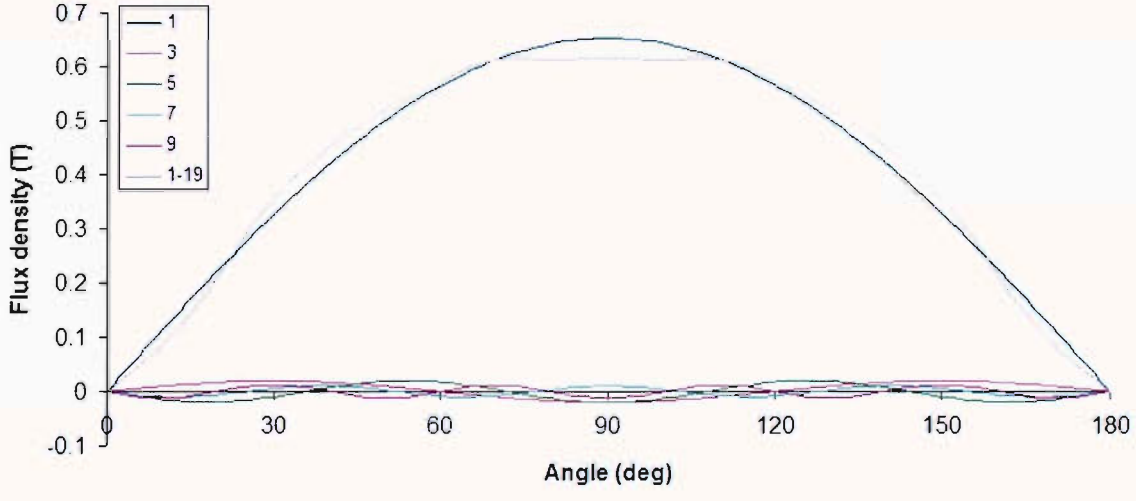

Figure 6.5 The gap field of the preliminary model

A non-linear analysis was performed throughout to include the saturation effects. Natural symmetries of the machine were exploited to reduce the size of the model since only one half-pole pitch of the generator needs to be considered for no-load calculations. Therefore, the regions are bounded by the rotor polar axis, the inter-polar axis and the back of the stator core: the rotor polar axis and back of the stator core were

taken as flux lines with $A = 0$ and the rotor inter-polar axis had a zero normal derivative. The magnitudes of the sine components of odd harmonic order were extracted along the air-gap at radius 160 mm using Fourier series as described in Section 5.2.2.2. These data was used to construct the voltage waveforms in Figure 6.5 and the resultant *rms* values in Table 6.1. It should be noted that due to symmetry the air-gap flux-density waveform contains no even harmonics.

Table 6.1 Harmonic components of air-gap flux density and phase voltage

Space Harmonic Order	Sine Harmonic Magnitude	Winding Factor	Actual Harmonic	% Harmonic Voltage Contribution
1	0.653222	0.758138	100%	100
3	0.019463	0.245196	0.96%	0.12
5	-0.019798	0.192774	0.77%	3.48
7	-0.010120	0.018445	0.04%	0.16
9	-0.011982	0.207867	0.50%	0.46
11	-0.001474	0.057705	0.02%	0.23
13	0.000697	0.050606	0.01%	0.04
15	-0.000124	0.138893	0.00%	0.26
17	0.002121	0.009096	0.00%	0.01
19	-0.000261	0.065438	0.00%	0.04

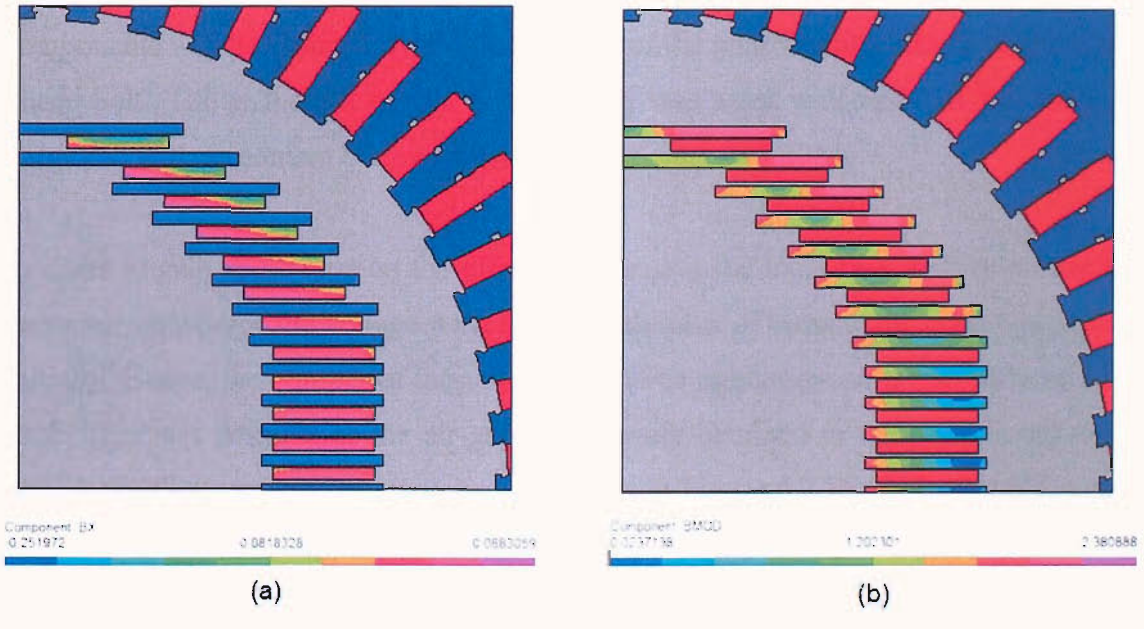

(a) (b)

Figure 6.6 The flux density distribution in the rotor (a) normal field in HTS coils and (b) the magnitude of flux density in the flux diverters.

In the preliminary model, it was found that the total *rms* harmonic voltage content was 1.33% and the air-gap flux density estimated at 0.65 T. Figure 6.6 (a) and (b) show the distribution of the normal field in the HTS and the saturation levels in the flux diverters coil, respectively. The component of the magnetic field normal to the broad face tape was unfortunately found to peak at 0.252 T (as shown in Figure 6.6 (b)). This undesirable high normal field would significantly reduce the critical current and could cause the coils to loose superconducting properties.

6.3.2 2D optimisation

The preliminary investigation revealed that the main problem in the design is due to the normal component of magnetic field in the HTS coils. Through careful examination it was found that the high normal field was caused by the saturation of flux diverters. In order to minimise this effect, the amount of iron could be increased in the identified areas. Therefore, one HTS coil was removed leaving 11 coils as shown in Figure 6.7(a). Figure 6.7(a) also shows harmonic content of the voltage waveform and the distribution of the normal field after the thickness of the four upper most flux diverters was increased. The graph shows the gap field up to 19^{th} harmonic, while the higher order components will be reduced by the distribution of the phase conductors throughout each phase belt. The reduction of the normal field was very welcome but the total *rms* harmonic voltage content became worse and increased to 3.898%.

In order to gain some idea on the effect of changing the local flux density on the total harmonic content of the voltage waveform, the number of turns in the coils was reduced initially. Hence, the number of turns in the top three uppermost coils was reduced by 10 each. This was possible as the air-gap flux density obtained in the preliminary design was above the target value. However, as shown in Figure 6.7 (b), reducing the number of turns in the three upper most coils to 60 gave only a slight improvement to the normal field and caused significant deterioration of the voltage waveform. Therefore, it was suggested that the air-gap flux density should be optimised at an angle where the higher harmonic voltage waveform diverges away from the fundamental. Hence, to deal with the problem, two particular regions of the waveform were identified. First, at the

angle between 70° and 90°, a block of iron with width and height of 10mm was placed on top of the upper flux diverter and the results shown in Figure 6.7 (c) proved very encouraging. The dimension of the block was chosen arbitrarily to show the effectiveness by targeting specific area for improvement. Furthermore, the overall weight was considered important. A wider block, by making full use of the limiting 140 mm radius from the upper most flux diverter, will almost certainly produce even better voltage waveform in that region as this will be shown later.

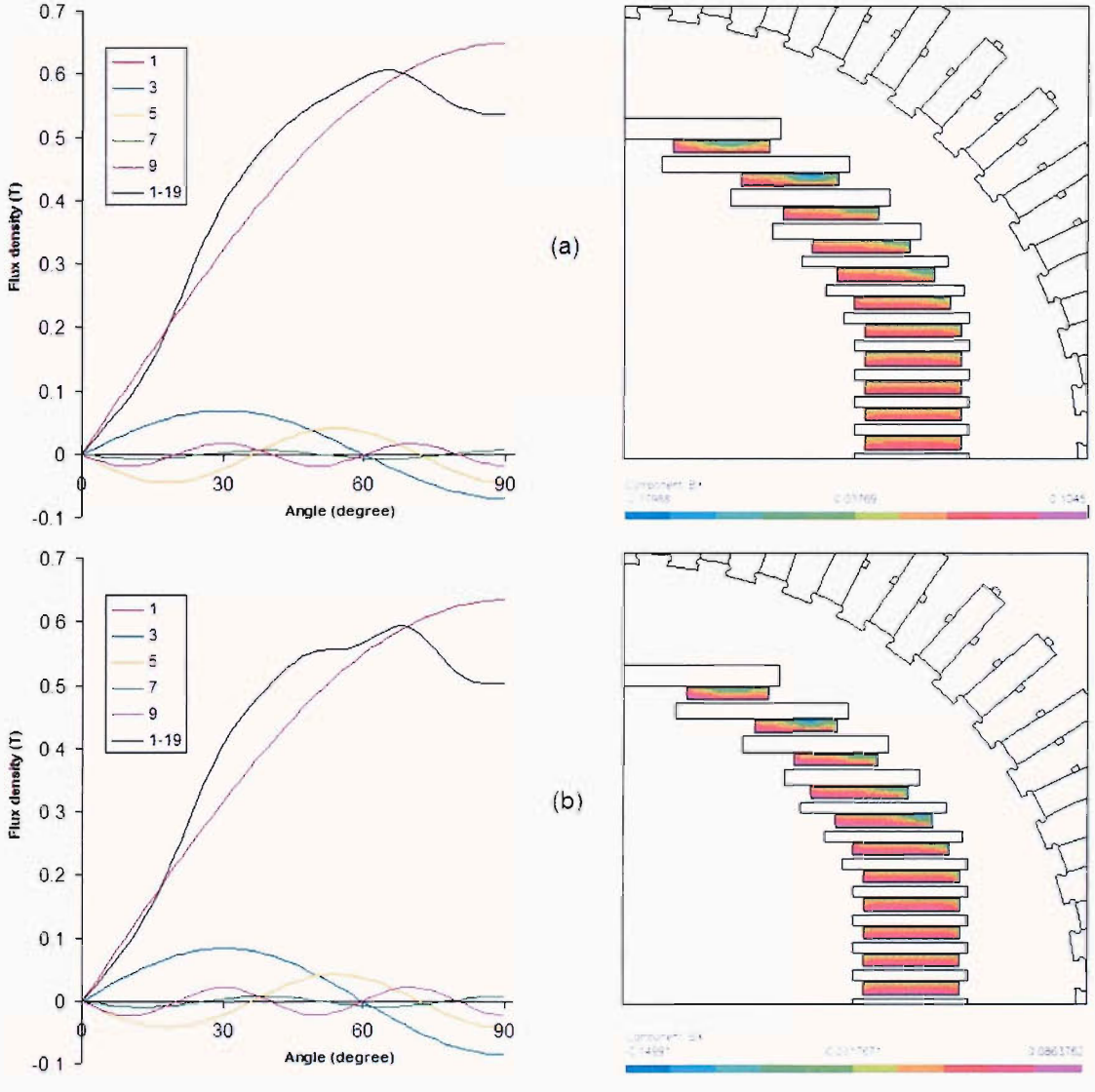

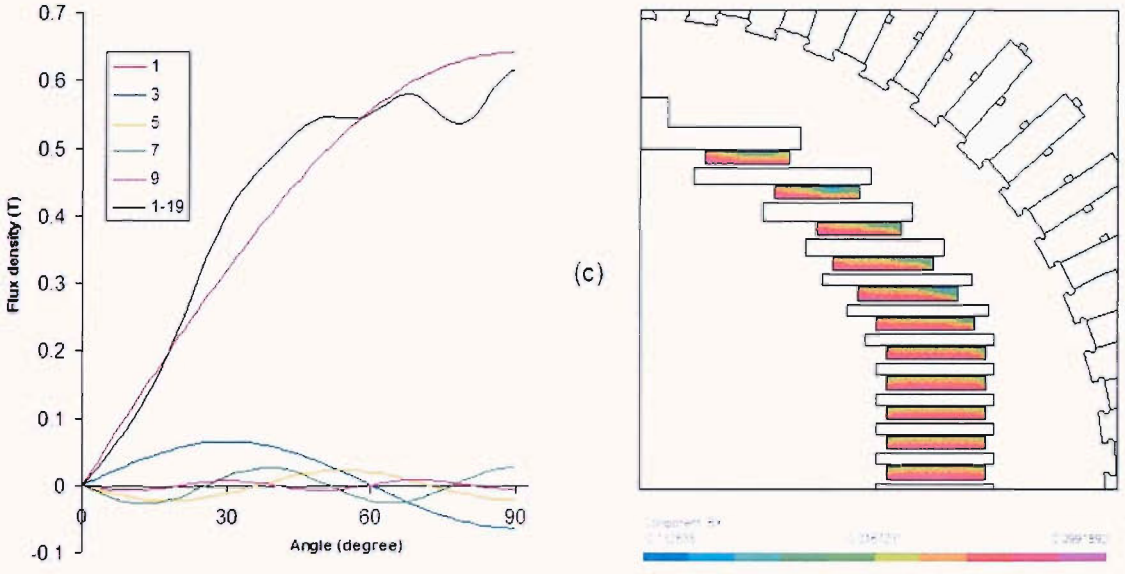

Figure 6.7 The air-gap field and the distribution of the normal field in the HTS coils for three different designs of flux diverters

At this stage, in order to obtain voltage waveform with minimum content of undesirable harmonics, it was obvious that the flux diverters should be moved further away from the stator teeth in the region between 20° to 60° (based on waveform in Figure 6.7 (c)). Since more than one harmonic is dominant, the expression described in section 5.4.4 was used to target the specific area for optimisation. This expression had been evaluated for angles between 0° to 90° and is plotted in Figure 6.8.

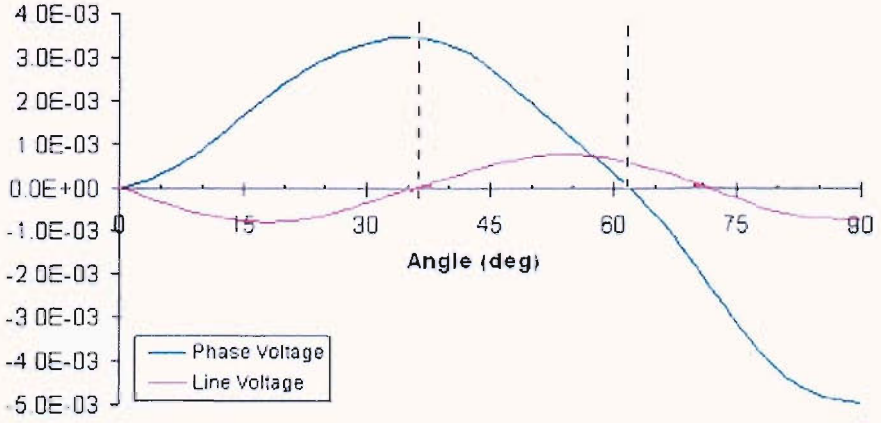

Figure 6.8 Weighted errors in the air-gap flux density

Based on the weighted errors, the flux diverters and coils were moved further away from the stator at the angle between 36° to 62° (between dotted lines) and – when possible – the number of turns in selected coils was further reduced without compromising the earlier constraints. The results, after the final modifications, are shown in Fig. 6.9 and its resultant *rms* values are shown in Table 6.2. The normal field in the coils was reduced from 0.133 T to 0.086 T and the total *rms* harmonic voltage content improved from 3.39% to 1.34%, whereas the air-gap flux density maintained at 0.58 T, thus within the specified target value.

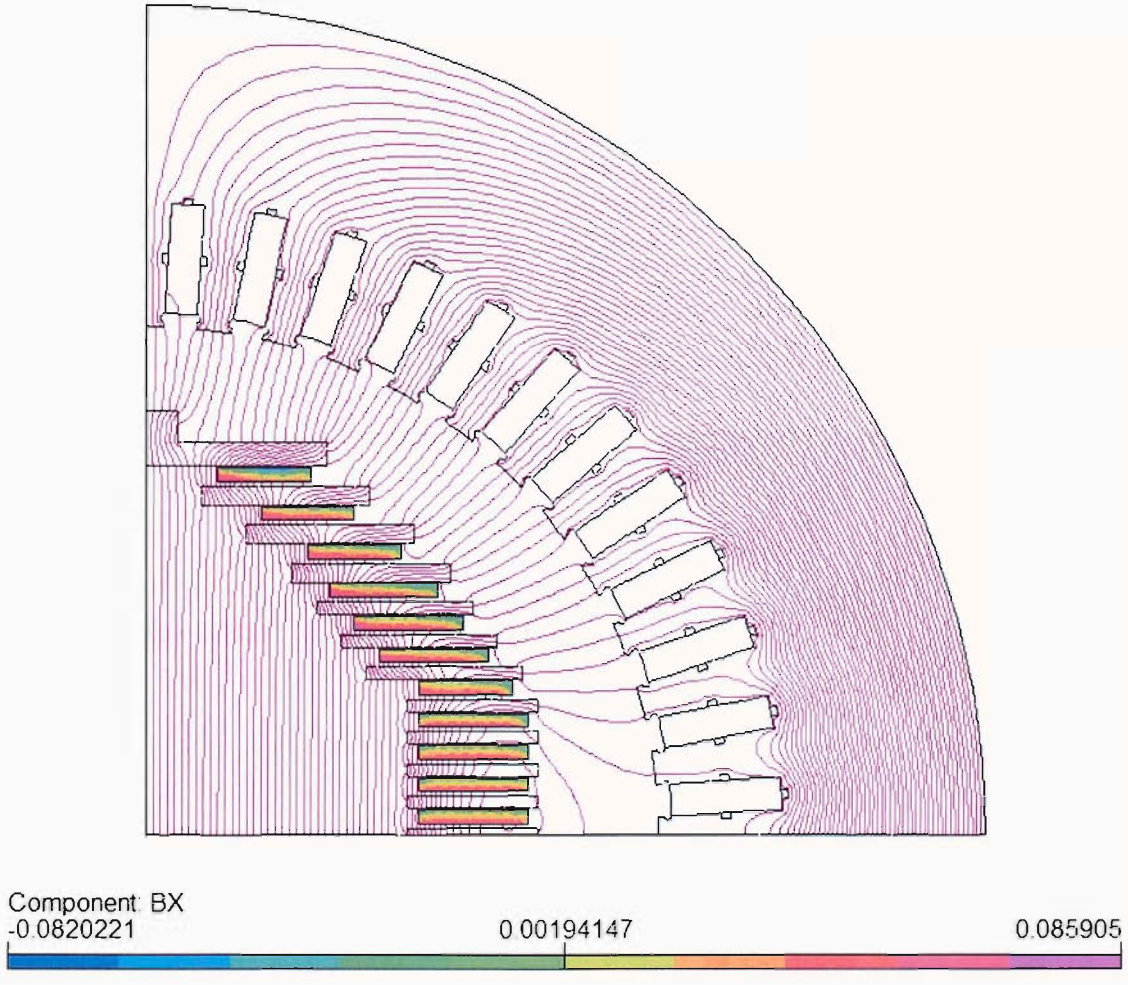

Figure 6.9 The flux lines and normal field distribution in the superconducting coils of the final model.

The straightforward and effective optimisation process described above based on the voltage waveform and the field distribution has proven to be successful in reducing the magnetic field normal to the broad face of the HTS tape below acceptable maximum levels while maintaining the necessary air-gap flux density and at the same time controlling the harmonic content of the voltage waveform. Such modelling studies have therefore been shown to be essential before the actual design could commence.

Table 6.2 Harmonic components of air-gap flux density and phase voltage

Space Harmonic Order	Sine Harmonic Magnitude	Winding Factor	Actual Harmonic	% Harmonic Voltage Contribution
1	0.583994	0.758138	0.442748	100%
3	0.022603	0.245196	0.005542	1.25%
5	0.004744	0.192774	0.000915	0.21%
7	0.006407	0.018445	0.000118	0.03%
9	-0.004368	0.207867	0.000908	0.21%
11	-0.006590	0.057705	0.000380	0.09%
13	0.006919	0.050606	0.000350	0.08%
15	-0.010914	0.138893	0.001516	0.34%
17	0.006024	0.009096	0.000055	0.01%
19	-0.002061	0.065438	0.000135	0.03%

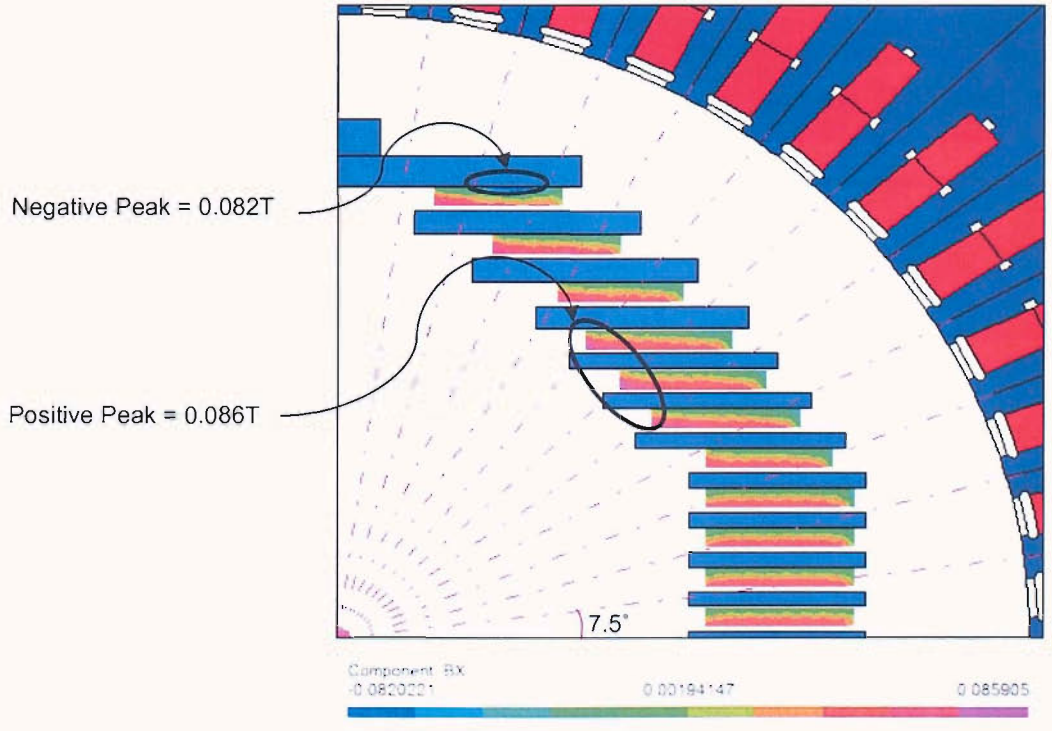

Figure 6.10 The maximum peak of the normal field distribution in the HTS coils

The normal field on the HTS coils can still be further reduced by extending the flux diverter's length of the 'positive peak' region and at the same time increasing the thickness of the uppermost flux diverters as shown in Figure 6.10. Moreover, based on Figure 6.9 further improvement is possible in the region between 70° and 90° by placing a larger iron in the uppermost flux diverter as shown in Figure 6.11. The total *rms* harmonic voltage content was reduced to 0.87%. It can be seen that the overall voltage waveform has improved significantly which is mainly due to the upper most 'block' of flux diverter. The modification not only improves the waveform, but also minimises the normal field in the negative peak region. However, the overall weight of the machine increases, thus reducing one of the advantages of a coreless design.

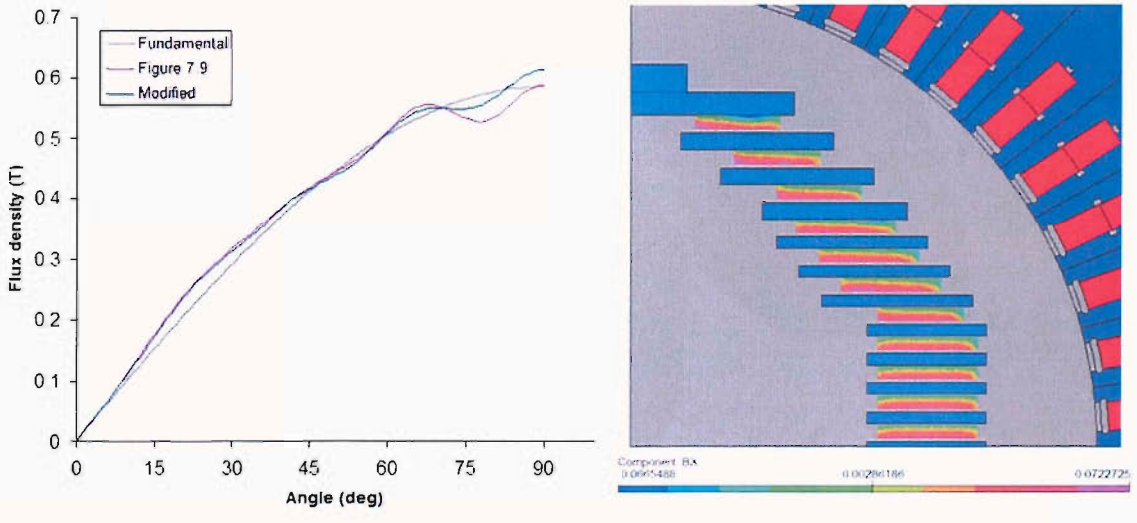

Figure 6.11 The modified and improved HTS generator

6.3.3 3D Modelling

The 3D model was constructed using available software known as Modeller [4]. The package allows a model to be built by creating a set of bodies and then assembling these bodies using Boolean operations. Figure 6.12 shows the basic features of the model used. Since the generator is simulated under no-load condition, by exploiting symmetry using appropriate boundary condition, only one eighth of the complete machine needs to be modelled. This allowed a better control of the mesh with the view to minimise the error, thus resulting in a total of 512951 quadratic tetrahedral elements.

Initially, the length of the rotor was set to 325 mm, which is the same as for the stator core. The distribution of B_y component of magnetic field along the straight line across the stator core at x = 250 mm and in the z direction up to 162.5 mm was considered as shown in Fig. 6.12. The resultant distribution is shown in Fig. 6.13. Ideally, the y component of the magnetic flux density should be uniform, but unfortunately this cannot be achieved due to different saturation levels in the stator core. Nevertheless, an attempt was made to achieve a better uniformity of the field.

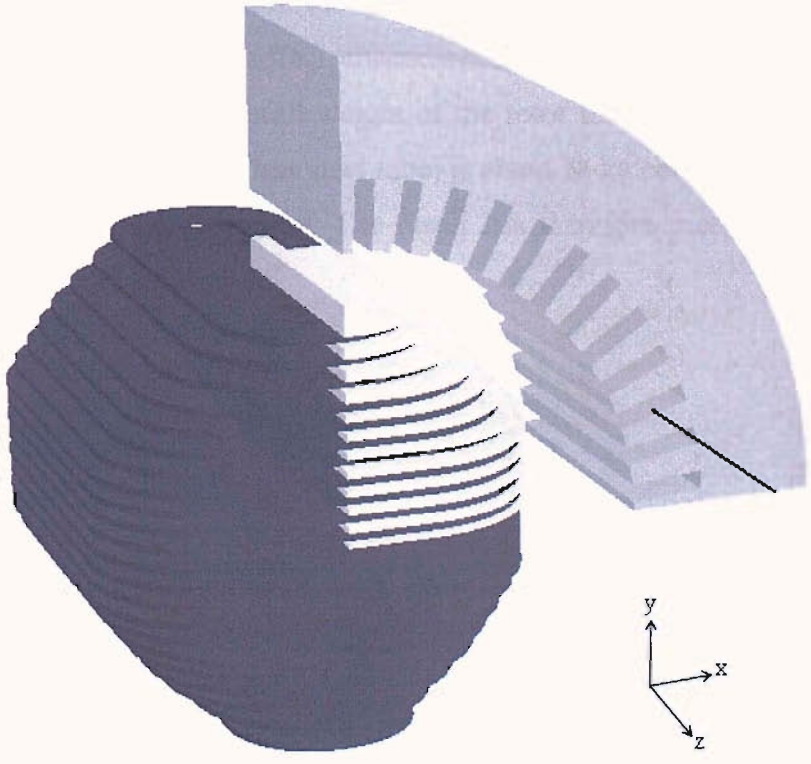

Figure 6.12 Construction of the 3D model of HTS synchronous generator with coreless rotor

Initially, as a reasonable simplification, it was assumed that the field at z = 0 would not be affected by changes of core length and that an increase of the area under the graph might be related to an increase in rotor length multiplied by the field at z = 0. Hence values of the integral of the B_y component divided by the flux density in the middle were examined and compared with the actual length; the difference of 3.7 mm resulted. However, further simulations had shown that this assumption was not entirely correct

because the variation of the y component of flux density at $z = 0$ turned out to be more significant then expected as the axial length of the rotor was increased (with respect to the stator core). The results of the simulations are shown in Figure 6.13; it can be clearly seen that the rotor length of approximately 172.5 mm yields the best field uniformity. Hence, the rotor was made longer by 10 mm and the radial field over a patch of 90° arc and 200 mm length at 160 mm radius was evaluated from the modified model to extract the harmonics of the air-gap flux density. The total *rms* harmonic voltage content was found to be 0.54% and the air-gap flux density was 0.51 T, which – as expected – was lower than the value obtained from 2D analysis due to saturation by leakage flux at the ends of the rotor, which is an effect unaccounted for in the 2D model. Furthermore, based on this 3D model the overall weight of the rotor including (diverter rings, HTS coils, packing material and stainless steel tube) is about 75 kg compared to 180 kg of the previous model with magnetic core. The result has therefore met the original design target to achieve weight reduction.

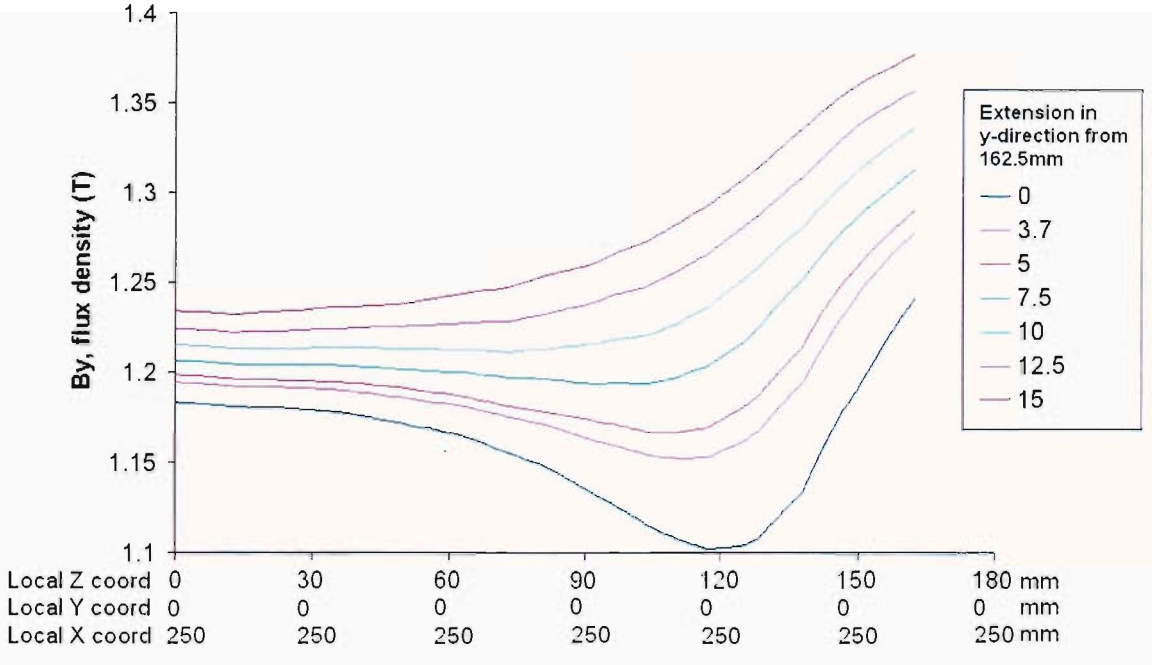

Figure 6.13 Variation of the y component of magnetic flux density for different rotor lengths

CONCLUSIONS

7.1 Summary

The contents of this thesis should be placed in the context of field modelling and simulation of a synchronous generator with a HTS superconducting rotor. The work presented covers a spectrum of topics from fundamentals of superconductivity to applications of the technology in power devices, in particular magnetic field modelling in a synchronous generator. The commercialisation of low temperature superconductors (multifilamentary niobium titanium) since 1960 has initiated many projects, the most noticeable being the Japanese Super-GM project. However, economic considerations with respect to competitive cost combined with the requirement for liquid helium cooling did not make the machines commercially attractive. The discovery of high temperature superconductors in 1986 reignited interest in superconducting power applications, largely because their higher operating temperature translates into lower cooling costs. Significant progress has been made in recent years in overcoming technological and manufacturing challenges. New fabrications techniques have successfully developed the second generation HTS wires with improved properties and significantly lower cost. Manufacturers around the world are in the process of taking the technology to the pilot scale to produce commercially viable 100 m lengths. Furthermore, advancements in the refrigeration systems have helped in reducing the overall costs. All these factors have initiated many research and development projects incorporating HTS in power devices.

The Southampton's University superconducting generator is based around an existing conventional stator core with its three-phase winding and frame, and retrofitted with a magnetic metallic rotor core made of 9% nickel steel equipped with HTS field windings. The field winding is made of silver sheathed BSCCO tape with nominal critical current 115 A at 77 K. A series of measurements have been carried out to confirm the tape characteristics. The use of other materials was also considered for the

rotor core, but ultimate decision to use 9% nickel steel is due to cost, the availability of the material and its suitability working under low temperature environment. An important feature of the design is the use of magnetic rings (flux diverters) placed between the superconducting coils to control flux direction within the coils. The behaviour of these flux diverters was modelled and the results have proven their effectiveness in reducing the normal component of the magnetic field in the HTS coils.

Finite element modelling has been undertaken to minimise the problems caused by air-gap flux harmonics, subject to the restrictions imposed by the choice of the stator. These harmonics, if not controlled, would cause additional losses due to harmonic currents circulating in the stator winding and external circuits. Nonlinear analysis was used throughout to include saturation effect, and the actual BH data of the material was obtained from measurements. A simple formula was devised to target specific area for voltage waveform improvements. The magnetic field normal to the broad face of the HTS tape was successfully reduced below acceptable maximum levels while maintaining the necessary air-gap flux density and at the same time controlling the harmonic content of the voltage waveform. The initial analysis was done using 2D finite-element models, since this allowed a large number of designs to be considered. Finally, 3D models were developed to predict the gap density waveform accurately. Such design details as the through bolts and flanges (made from the same material as the rotor core), connected to both ends of the rotor, were also modelled. The results obtained from 2D and 3D models were compared and found to be consistent. Measurements were also carried out, and the total *rms* harmonic voltage content of the output voltage was found to be in good agreement with those obtained from finite element evaluations.

Substantial computational and simulation studies have also been conducted to evaluate and identify critical performance. The design requirements for the superconducting machine are very unique and differ from the usual criteria for a conventional generator. The use of a superconducting field winding, hence operation in a low temperature environment, makes the machine more vulnerable to system instability. Therefore,

losses in the cold region have been evaluated. Any losses in the rotor will contribute to the load on the cooling system, thus increasing the cooling power required and reducing overall efficiency. Such losses were greatly reduced by introducing a thin layer of copper placed over the rotor surface to provide a low resistance path for the eddy currents. It was found that the losses in the model with Invar rotor are higher than the losses with 9% nickel rotor due to the proximity of the copper screen from stator teeth. Moreover, the largest eddy current loss component is due to the 6^{th} time harmonic eddy currents. The no-load losses, which are caused by the stator slots modulating the synchronous field, are significantly smaller than the full-load 6^{th} harmonic loss. Losses due to the 11^{th} and higher order harmonics of the stator MMF were found to be negligible.

The machine's response to a symmetrical three-phase short-circuit fault was also modelled. The non-linear transient modelling was simulated taking into account the relative movement between the stator and rotor. The high temperature superconducting field windings were analysed using external circuit equations as the equivalent supply voltage and resistance. As expected, the reactances were found to be of very low value compared to conventional generators. This is due to the large air gap needed to accommodate the thermal insulation. The field current during the fault condition was also analysed due to the anticipated large values that could cause damage to the superconducting field windings. It was confirmed that during fault the current in the HTS field winding is large and it peaks at four times larger than the normal DC excited field current of 63 A. This is based on the assumption that the field winding possesses resistance equivalent to silver at 77 K. Further analysis has demonstrated that the fault current could have been even larger with a lower resistance. The machine reactances were also estimated based on the symmetrical three-phase short circuit curve. The reactances were found to be lower compared to conventional generators of similar capacity. This is due to the large air-gap needed to accommodate the thermal insulation. Further analysis using standstill frequency response has been performed to evaluate the reactances; the reactances values are consistent with those obtained using three-phase short-circuit simulations.

The availability of high quality BSCCO-2223 tapes with improved strength and critical currents makes the design of the next generation of HTS generator technologically viable. Currently, the best available tape has nominal critical current of 145 A at 77 K in self-field, and it is expected to increase up 165 A in the next two to three years. Hence, this will enable the consideration of the next phase HTS generator with coreless rotor structure (air-core). Preliminary modelling has shown that with this design it is possible to achieve the required performance using the best available HTS tape. It will also meet the design goal to reduce the overall weight of the generator.

FE modelling has become a standard tool for most who work with electric and magnetic fields. Many different types of finite-element software are available and they are now routinely used in every branch of electromagnetics including the analysis of electrical machines. The well known finite-element simulation software, OPERA, was used to model the generator [67]. The software consists of many different electromagnetic analysis modules with user friendly graphical environment and semi-automatic or automatic mesh generation, which reduces the time needed to create and analyse the model. It has been improved significantly compared to earlier versions with many features added, for example the capability of checking for multi-valued total magnetic scalar potential regions, and automatically introducing potential "cuts" where appropriate in order to rectify the problem. Considerable time and effort has been invested to master the knowledge of finite-element simulation, and to build and analyse the complicated geometries. In all the cases, the models built strictly follow the actual dimensions of the machine. The adaptive refinement of the mesh was implemented where possible to reduce the error in the solution by improving mesh discretisation.

The unique modelling requirement of a generator containing superconducting tapes has been identified, namely that the normal component of the magnetic field in the HTS coils has to be kept within the operational region. This is a prerequisite for the success of this project. Comprehensive studies of field distributions and loss calculations have also been undertaken for the two different rotor topologies. The overall accuracy of 2D field distributions modelling is satisfactory compared to test results. On some occasions

a full 3D treatment was introduced for comparison and to analyse the effect on the overall performance. The losses in the cold region were evaluated using a full transient non-linear rotating machine model to simulate the no-load case and the much less computationally expensive static and steady-state AC models to model the loaded case. Since the inception of the project, hundreds of 2D and 3D models had to be built to model the generator and accommodate changes made during the design and manufacturing stages. The overall modelling and simulation work done proved to be very successful. In many aspects of the design, the mechanical considerations were often given priority over electromagnetic considerations. This inevitably led to many compromises which had to be adopted to meet the overall objectives of the project, and meant that not always the 'best' electromagnetically solution was selected. The project has been a considerable challenge and required thorough understanding of many technologies and methods: superconductivity, machine design, modelling and finite-element techniques. The work was closely linked with the EPSRC grant and supported the design efforts directly. It is believed that all the objectives formulated in section 1.1 have been achieved.

7.2 Future considerations

This project has demonstrated the value and importance of detailed modelling of magnetic field distributions to assist the design and optimisation of superconducting machines. The high temperature superconducting tapes have extremely non-linear and anisotropic properties and thus the performance of the machine is very sensitive to the position, shape and dimensions of various magnetically active parts, much more than would be the case in a conventional design. As the EPSRC project demonstrated, the design of a HTS generator is a very complex process involving electromagnetic, mechanical and thermal aspects and requiring continuous monitoring – through simulation – of the expected performance following changes and modifications, sometimes even fairly minor. As expected, the 2D modelling gave quite good initial results and was very helpful during the initial stages of the design process. However, in order to achieve reliable performance prediction taking account of complicated end

connections and details such as through bolts, full 3D models were essential with all their unwelcome complexity. Three particular electromagnetic issues were identified as of particular importance in this design: shaping of the magnetic field in the region of the HTS tapes to reduce the field perpendicular to the broad face of the tape, harmonic content in the voltage waveform and reduction of losses released in the cold region. Similar issues are likely to be faced by designers of other types of power devices based on superconducting technology, hence the findings of this thesis should be directly applicable to future designs. The actual configuration and dimensions will of course be different, but the proposed methodology should be similar. The area where further improvements could be made might include an attempt to model the whole machine as a multiphysics problem, with the electromagnetic solution coupled to the driving circuitry and/or thermal field and mechanical stress. Further investigation could also be conducted regarding the performance of the machine under transient conditions.

REFERENCES

[1] J. K. Sykulski et al., "High Temperature Superconducting Demonstrator Transformer," National Grid Report PES. TECH.218, University of Southampton, UK, 1999.

[2] Y. D. Chun, H. W. Lee, J. Lee, Y. K. Kwon, K. S. Ryu and J. P. Hong, "Transient analysis of a AC superconducting generator using the compensated 2-D model," *IEEE Trans. Magnetics*, vol. 35, no. 5, pp. 4085-4087, 1999.

[3] Y. D. Chun, Y. H. Kim, S. Kim and J Lee, "Transient analysis of superconducting generator under the three phases of sudden grounding fault condition," *Physica C*, vol. 372-376, pp. 1546-1550, 2002.

[4] Yoshihiro Imai, Hidehiro Nagamura, Hiroshi Kusafuka, Masatoyo Shibuya, Hiroshi Hasegawa, Kiyoshi Miyaike, and Ryoichi Shiobara, "Development of a 70 MW class quick response excitation superconducting generator," *Electrical Engineering in Japan*, vol. 140, no. 1, pp. 1017-1022, 2002.

[5] John Bardeen, Leon N. Cooper, J. Robert Schrieffer. "Theory of Superconductivity," *Physical Review*, vol. 108, pp. 1175-1204, 1957.

[6] A.C. Rose-Innes and E.H. Rhoderick, *Introduction to Superconductivity*. Oxford: Pergamon Press, 1978, pp. 168-170.

[7] Oleg D. Jefimenko, *Electricity and Magnetism: An Introduction to the Theory of Electric and Magnetic Fields*. Star City: Electret Scientific Co., 1989, chapter 1.

[8] M. Tinkham, *Introduction to Superconductivity*. New York: MacGraw-Hill, 1996, pp. 12-14.

[9] W. J. Carr, Jr., *AC Loss and Macroscopic Theory of Superconductors*. New York: Gordon & Breach, 1983.

[10] T. P. Sheahan, *Introduction to High-Temperature Superconductivity*. New York: Plenum Press, 1994.

[11] J.G. Bednorz and K.A. Müller, "Possible high-Tc superconductivity in the Ba-La-Cu-O system," *Physical B*, vol. 64, pp. 189, 1986.

[12] G. Elert, Superconductivity: The Physics Hypertextbook. Available: http://hypertextbook.com/physics/modern/superconductivity/

[13] *Handbook of Applied Superconductivity*, Institute of Physics Publishing, Bristol, UK, 1998, pp.128-131.

[14] B. Lehndorff, M. Hortig and H. Piel, "Temperature-dependent critical current anisotropy in Bi-2223 tapes," *Supercond. Sci. Technol.*, vol. 11, pp. 1261-1265, 1998.

[15] P. Usak, L. Jansak and F. Chovanec, "Anisotropy of E(I) characteristics of Ag-sheathed BSCCO tapes with respect to external magnetic field," *Applied Superconductivity*, vol. 4, no. 12, pp. 577-581, 1998.

[16] M. R. Koblischka, T. H. Johansen, H. Bratsberg and P. Vase, "Study of flux entry and exit into Bi-2223 multifilamentary," *Supercond. Sci. Technol.* Vol. 11, pp. 479–484, 1998.

[17] J. Ilsted, "Manufacturing of Superconductors," PhD dissertation, Department of Manufacturing Engineering and Management, Technical University of Denmark, Denmark, 2001.

[18] J. A. Parrell, "The materials processing, connectivity, flux pinning, and critical current density of ag-clad $(Bi,Pb)_2Sr_2Ca_2Cu_3Ox$ superconducting tapes," PhD dissertation, University of Wisconsin-Madison, 1996.

[19] A. P. Malozemoff et al., "Low-cost YBCO coated conductor technology," *Superconductor Science and Technology*, vol. 13, pp. 473-476, 2000.

[20] A. P. Malozemoff, "2G HTS Wire Technology: An Assessment," American Superconductor, Westborough, 2004. Available: http://www.amsuper.com/products/htsWire/documents/4122GWhitePaper_v5.pdf

[21] P.N. Arendt, J.R. Groves, S.R. Foltyn, Q.X. Jia, E.J. Peterson, R.F. DePaula, P.C. Dowden, J.Y. Coulter, and M. Ma, "Fabrication of High-Quality Ion-Beam Deposited Cubic Oxide Template Films on Meter-Length Substrates," *Materials Research Society Symposium Proceedings*, vol. 585, pp. 67-73, 2000.

[22] A. P. Malozemoff, "Second generation HTS wire: an assessment," AMSC Technical Report, July 2004.

[23] Alicia Ayala, "Aspects of the SrO-CuO-TiO2 ternary system related to the deposition of SrTiO3 and copper doped srtio3 thin film buffer layers," PhD dissertation, The University of New Mexico, 2004.

[24] M. P. Paranthaman and T. Izumi, "High-Performance YBCO-Coated Superconductor Wires," *MRS Bulletin*, vol. 29, no. 8, 2004.

[25] S. P. Ashworth, M. Ciszek., A. M. Campbell, W. Y. Liang, and B. A. Glowacki, "AC Losses in Silver Clad High Temperature Superconducting Tapes," *Chinese Journal Of Physics*, vol. 34, no. 2-11, pp. 232-242, 1996.

[26] G. E. Marsh and A.M. Wolsky, "AC losses in high-temperature superconductors and the importance of these losses to the future use of HTS in the power sector," *IEA Implementing Agreement for a Co-Operative Programme for Assessing the Impacts of High-Temperature Superconductivity on the Electric Power Sector*, Argonne National Laboratory, Illinois, May 2000.

[27] U.S. Department of Energy report "At the Frontiers of Science: Superconductivity and its Electric Power Applications", DOE/GO-10098-434, July 1998.

[28] A.P. Malozemoff et al., "Power applications of high-temperature superconductors: status and perspectives," *IEEE Transactions on Applied Superconductivity*, vol. 12, no. 1, pp. 778-781, March 2002.

[29] J. R. Hull, "Superconductors: An emerging power technology", NIST Boulder Lab., Colorado, gdx2004

[30] Tsutomu Hoshino, Itsuya Muta and Taketsune Nakamura, "Applied high-Tc superconducting electrical machines," *Proceedings of 2000 KIASC Conference*, Taejeon, Korea, 2000, pp. 73-76.

[31] S. S. Kalsi, "Development status of superconducting machines," presented at *IEEE PES Meeting 2002*, New York, January 2002.

[32] S. S. Kalsi, "Advances in synchronous machines employing high temperature superconductors (HTS)," in *Electric Machines and Drives Conference*, 2003, vol. 1, pp. 24 - 28.

[33] U.S. Department of Energy, "Motor," an SPI Project Fact Sheet, DOE Annual Peer Review, July 1999.

[34] B. B. Gamble et al., "Status of HTS motor", IEEE Power Engineering Society Summer Meeting, 2002, vol. 1 , pp. 270 - 274

[35] M. Frank et al., "Large-term operational experience with first siemens 400 kW HTS machines in diverse configurations," *IEEE Trans. Appl. Supercond.*, vol. 13, no. 2, pp. 2120-2123, June 2003.

[36] E. A. Bretz, "Superconductors on the high seas," *IEEE Spectrum*, January 2004.

[37] Jim Bray, "Design and development of a 100 MVA generator for commercial entry," DOE Peer Review, Washington, 24 July 2003. Available: http://www.energetics.com/meetings/supercon/pdfs/presentations/d3_pres_1.pdf

[38] K. Yamaguchi et al., "70 MW class superconducting generator test," *IEEE Transactions on Applied Superconductivity*, vol. 9, no. 2, pp. 1209-1212, 2000.

[39] K. Yamaguchi et al., "Development of a 70 MW class superconducting generator," *IEEE Transactions on Applied Superconductivity*, vol. 7, no. 2, pp. 527-530, 1997.

[40] K. Inoue et al., "Recent progress of 70 MW class superconducting generators," *IEEE Transactions on Applied Superconductivity*, vol. 7, no. 2, pp. 654-659, 1997.

[41] N. Maki et al., "Design Study of Small-Scale to Large-Scale Superconducting Generators," *IEEE Transactions on Applied Superconductivity*, vol. 14, no. 2, pp. 887-891, 2004.

[42] P. Kummeth, R. Schlosser, P. Massek, H. Schmidt, C. Albrecht, D. Breitfelder and H. W. Neumuller, "Development and test of a 100 kVA superconducting transformer operated at 77 K," *Supercond. Sci. Technol.*, vol. 13, pp. 503–505, 2000.

[43] ABB Press Release, "ABB first to connect superconducting transformer to a utility power network," ABB, March 1997. Available at www.abb.com

[44] M. Leghissa et al., "Development and application of superconducting transformers," EUCAS2001, Copenhagen, August 2001, paper no. B4-01.

[45] P. Mehta et al., "Transforming Transformers," *IEEE Spectrum,* July 1997.

[46] S. Kalsi and A.P. Malozemoff, "HTS fault current limiter concept," presented at IEEE Power Engineering Society Meeting, Colorado, June 2004.

[47] W. Paul et al., "Test of 1.2 MVA high-Tcsuperconducting fault current limiter," *Supercond. Sci. Technol.*, vol. 10, pp. 914-918, 1997.

[48] M. Chen et al. 2004. *Fault Current Limiter based on High Temperature Superconductors*. Available: http://www.manep.ch/pdf/research_teams/sciabb.pdf

[49] US Department of Energy Press Release, "Matrix fault current limiter". Office of Electric Transmission and Distribution, 2003. Available: http://www.electricity.doe.gov/documents/matrix_fault_current_limiter.pdf

[50] D. Larbalestier et al., "Power applications of superconductivity in Japan and Germany", World Technology Evaluation Center Report, September 1997.

[51] Diego Politano et al., "Technical and Economical Assessment of HTS Cables," *IEEE Transactions on Applied Superconductivity*, vol. 11, no. 1, pp. 2477-2480, March 2001.

[52] David Linsay and Dag Willén, "Superconductivity for Power Transmission and Distribution Cables," Ultera, Carrollton, October 2003 Available: http://www.ultera.net/documents/Ultera%20-%20HTS%20white%20paper.pdf

[53] US Department of Energy Project Fact Sheet, "Power Cable," US Department of Energy Superconductivity Partnership with Industry, March 2000. Available: http://www.electricity.doe.gov/documents/power_cable2.pdf

[54] Lawrence L. R. Jr. et al., "High temperature superconductivity: The product and their benefits," Bob Lawrence & Associates Inc. report for US DOE, Contract DE-AC05-00OR22725, July 2002.

[55] Annual Peer Review, "Superconductivity Program for Electric System: High Temperature Superconducting Cable," 2004. Available:

http://www.energetics.com/meetings/supercon04/pdfs/presentations/g_cable_peer_review_2004_r6.pdf

[56] Richard Silberglitt, Emile Ettedgui, Anders Hove, "Strengthening the Grid: Effect of High-Temperature Superconducting Power Technologies on Reliability, Power Transfer Capacity, and Energy Use," *RANDS Corp Monograph*, pp. 89-101, 2002.

[57] S. O. Siems and W. R. Canders, "Advances in the design of superconducting magnetic bearings for static and dynamic applications," *Supercond. Sci. Technol.*, vol. 18, pp. s86–s89, 2005.

[58] R. Kreutz, et al., "Design of a 150 kJ high-Tc SMES (HSMES) for a 20 kVA uninterruptible power supply system," *IEEE Transactions on Applied Superconductivity*, vol. 13, no. 2, pp. 1860-1862, June 2003.

[59] A. C. Day et al. "Design and testing of the HTS bearing for a 10 kWh flywheel system," *Supercond. Sci. Technol.*, vol. 15, pp. 838-841, 2002.

[60] Wolsky, A. M., "The Status of Progress Toward Flywheel Energy Storage Systems Incorporating High- Temperature Superconductors," IEA Technical Report, 2000, pp. III 9-12

[61] Conectus Roadmap, "Market survey," 2004, Consortium of European Companies Determined to use Superconductivity. Available: www.conectus.org

[62] J. Mullholland, T. P. Sheahen and B. Mcconnell, "Analysis of Future Prices and Markets for High Temperature Superconductors," Oak Ridge National Laboratory, Reports and Roadmaps, June 2003. Available: http://www.ornl.gov/sci/htsc/documents/pdf/Mulholland%20Report%20063003.pdf

[63] J. Mullholland, T. P. Sheahen and B. Mcconnell, "Method for estimating future markets for high-temperature superconducting power devices," *IEEE Transactions on Applied Superconductivity*, vol. 1, no. 2, pp. 1784-1789, June 2002.

[64] J. Dadin, "High temperature superconducting electric power products," Energetics, Columbia, Tech. report 62X-5V815C, January 2000.

[65] Y. Yang et al., "Reduction of AC Loss in Ag Sheathed PbBi2223 Tapes with Twisted Filaments in External and Self-fields," presented at Applied Superconductivity Cenference, California, 1998, Paper LUA-04.

[66] P. B. Bailey et al., "High performance flight cryocooler compressor," in *proceedings of the Eleventh International Cryocooler Conference*, Colorado, July 2000, pp. 45-49.

[67] D. Larbalestier et al., "Power Applications of Superconductivity in Japan and Germany," World Technology Evaluation Commission, Loyola College, Tech. Report, Maryland, 1997. Available: http://www.wtec.org/loyola/scpa/

[68] N. S. Nasar, *Handbook of electric machines*. New York: McGraw-Hill, 1987, chapter 3.

[69] Mario Rabinowitz, "Superconducting Power Generation", *IEEE Power Engineering Review*, vol. 20, no.5, pp.8 – 11, 2000.

[70] Richard M. Bozorth, "Ferromagnetism," *D. Van Nostrand Company, Inc.*, New York, pp. 55, 1951.

[71] W. V. Hassenzahl, "Applications of superconductivity to electric power systems," *IEEE Power Engineering Review*, vol. 20, no. 5, pp. 4-7, May 2000.

[72] T. Nitta, "Progress of technology for superconducting generator," *Cyrogenics*, 2002, vol. 42, pp. 151-155, 2002.

[73] R. Ackermann et al., "Testing of a 1.8 MVA high temperature superconducting generator," presented at the IEEE 2003 Power Engineering Soc. Annual Meeting, Toronto, 2003, Emerging Technologies Panel Session.

[74] S. Kalsi et al., "Development status of rotating machines employing superconducting field windings," *IEEE Transactions on Applied Superconductivity*, vol. 92, no. 10, pp. 1688-1704, October 2004.

[75] B. Gamble et al., "The status of HTS motors," presented at the IEEE Power Engineering Soc. Meeting, Chicago, 2002.

[76] L. Masur et al., "Long length manufacturing of Bi-2223 wire for motor and cable applications," *Adv. Cryogenic Eng.*, vol. 46, pp.871–877, 2000.

[77] O. A. Chevtchenko, "On The Application Of High-Tc Superconductors In Power Coils and Transformers," PhD dissertation, University of Twente, The Netherlands, 2002.

[78] P. Vase, R. Flükiger, M. Leghissa and B. Glowacki, "Current status of high-Tc wire", *Superconductor Science and Technology*, vol. 13, pp. R71-R84, 2000.

[79] B. Seeber, *Handbook of Applied Superconductivity*. Bristol: Institute of Physics Publishing, 1998, pp. 12-13.

[80] R. P. Aloysius, A. Sobha, P. Guruswamy and U. Syamaprasad, "Bend strain and tensile stress characteristics of (Bi, Pb)-2223/Ag–Cu alloy sheathed tapes", *Supercond. Sci. Technol.*, vol. 14, pp. 85–89, 2001.

[81] M. K. Al-Mosawi et al., "Design of a 100 kVA high temperature superconducting demonstration synchronous generator," *Physica C*, vol. **372-376**, pp. 1539-1542, 2002.

[82] '2D & 3D OPERA', Vector Fields Ltd, 24 Bankside, Kidlington, Oxford, UK. Available: http://www.vectorfields.co.uk/

[83] 'Flux2D and Flux3D', Cedrat & Cedrat Technologies, 15 Chemin de Malacher, 38246 Meylan, France. Available: http://www.cedrat.com

[84] 'Maxwell', Ansoft Corporation, Four Station Square, Suite 200, Pittsburgh, PA 15219-1119, US. Available: http://www.ansoft.com/

[85] J. Nielsen, and R. Molich, "Heuristic evaluation of user interfaces," in *Proc. ACM CHI'90 Conference*. Seattle, 1990 pp. 249-256.

[86] R. L. Stoll and K. Zakrzewski, "Finite-difference method," in *Computational electromagnetics*, London: Chapman & Hall, 1995, pp. 35.

[87] G. Beer and J. O. Watson, Introduction to Finite and Boundary Element Methods for Engineers. New York: J. Wiley & Sons, 1992, pp. 36.

[88] R. F. Harrington, Field Computation by Moment Methods. New York: The Macmillan Co., 1968.

[89] M. J. Turner et al., "Stiffness and deflection analysis of complex structures," *Journal Aero Sci.*, vol. 23, no. 9, pp. 805-823, 1956.

[90] A. Winslow, "Numerical solution of the quasilinear Poisson equation in a nonuniform triangle mesh," *Journal of Computational Physics*, vol. 2, pp. 149-172, 1967.

[91] P. P. Silvester and R. L. Ferrari, "Finite Elements for Electrical Engineers," *Cambridge University Press*, New York, 1996.

[92] S. Ratnajeevan and H. Hoole, *Computer Aided Analysis and Design of Electromagnetic Devices*. New York: Elsevier Science Publishing, 1989, pp. 238.

[93] K. Hameyer and R. Belmans, Numerical Modelling and Design of Electrical Machines and Devices. Southampton: WIT Press, 1999.

[94] A. B. J. Reece and T. W. Preston, Finite element methods in Electrical Power Engineering. Oxford: Oxford University Press, 2000.

[95] S. J. Salon, Finite element analysis of electrical machines. Massachusetts: Kluwer Academic Publishers, 1995.

[96] J. R. Shewchuk, "Delaunay Refinement Mesh Generation," PhD dissertation, Computer Science Department, Carnegie Mellon University, Pittsburgh, 1997.

[97] S. McFee and D. Giannacopoulos, "Introduction to Adaptive Finite Element Analysis for Electromagnetic Simulations," *ICS Newsletter*, vol. 2, no. 2, July 2002.

[98] J. K. Sykulski, K. F. Goddard, and K. S. Ship, "Modelling and evaluations of eddy-current loss in high temperature superconducting synchronous generator," in *Studies in Applied Electromagnetics and Mechanics*, 2002, pp. 142-147.

[99] J. K. Sykulski et al., "Design, build, and test a high temperature superconducting demonstration synchronous generator," University of Southampton, Southampton, Review Report, GR/N21253/01, 2004.

[100] C. B. Gray, Electrical Machines and Drive Systems. New York: John Wiley & Son, 1989, pp. 142.

[101] M. S. Sarma, Electric Machines: Steady State Theory and Dynamic Performance. St. Paul: West Publishing Company, 1985, pp. 502.

[102] P. Hammond and J. K. Sykulski, Engineering Electromagnetism: Physical Processes and Computation. Oxford: Oxford University Press, 1994, pp. 109-117.

[103] P. J. Turner, "Finite-element simulation of turbine generator terminal faults and application to machine parameter prediction," IEEE Trans. on Energy Conversion, vol. EC-2, no. 1, pp. 122-131, March 1987.

[104] *Copper and Copper Alloys*, ASM International, Ohio, 2001.

[105] D. R. Smith and F. R. Fickett, "Low temperature properties of silver," *J. Res. Natl. Inst. Stand. Technol.*, vol. 100, no. 2, pp. 119-171, March 1995.

[106] IEEE Standard Procedure for Obtaining Synchronous Machine Parameters by Standstill Frequency Response Testing, IEEE Standard 115A, 1987.

[107] E. W. Kimbark, Power system stability: Synchronous machines. New York: Dover Publications, 1968, pp. 1-52.

[108] K. S. Ship, and J. K. Sykulski, "Field modelling and optimisation of a high temperature superconducting synchronous generator with a coreless rotor," in *Fifth IEE International Conference on Computation in Electromagnetics*, Stratford-upon-Avon, 2004, pp. 109-110.

PUBLICATIONS

Refereed Papers:

- K. S. Ship and J. K. Sykulski, "Field Modelling And Optimisation of a High Temperature Superconducting Synchronous Generator With a Coreless Rotor," *IEE Proceedings Science Measurement and Technology*, vol. 151, no. 6, pp. 414-418, 2004.
- D. H. Kim, K. S. Ship and J. K. Sykulski, "Applying Continuum Design Sensitivity Analysis combined with standard EM software to Shape Optimisation in Magnetostatic Problems," *IEEE Transactions on Magnetics*, vol. 40, no. 2, pp. 1156-1159, 2004.
- K. S. Ship, K. F. Goddard and J. K. Sykulski, "Field optimisation in a synchronous generator with high temperature superconducting field winding and magnetic core," *IEE Proceedings Science Measurement and Technology*, vol. 149, no. 5, pp. 194-198, 2002.
- M. K. Mosawi, C. Beduz, K. F. Goddard, J. K. Sykulski, Y. Yang, B. Xu, K. S. Ship, R. Stoll and N. G. Stephen, "Design of a 100 kVA high temperature superconducting demonstration synchronous generator," *Physica C*, vol. 372-6, no. P3, pp. 1539-1542, 2002.

Compiled volumes:

- K. S. Ship, K. F. Goddard and J. K. Sykulski, "Two dimensional finite-element simulation of a high temperature superconducting synchronous generator during three-phase short-circuit fault condition using full transient non-linear rotating machine model," in *Computer Engineering in Applied Electromagnetism*, Springer, 2005, pp. 355-358.
- K. S. Ship, J. K. Sykulski and K. F. Goddard, "Load characteristics analysis of a 100kVA synchronous generator with high temperature superconducting field winding

using finite element modelling," in *Recent Advances in Computational Science and Engineering*, Cambridge: Imperial College Press, 2002, pp. 295-298.

- J. K. Sykulski, K. F. Goddard and K. S. Ship. "Modelling and Evaluation of Eddy-Current Loss in High Temperature Superconducting Synchronous Generator," in *Studies in Applied Electromagnetics and Mechanics*, Amsterdam: IOS, 2002, pp. 142-147.

Contributions to Symposia:

- K. S. Ship, K. F. Goddard and J. K. Sykulski, "Field Modelling And Optimisation of a High Temperature Superconducting Synchronous Generator With a Coreless Rotor," in *Proceedings The Fifth International Conference on Computation in Electromagnetics*, Stratford-upon-Avon, UK, 2004, pp. 109-110.
- K. S. Ship, K. F. Goddard and J. K. Sykulski, "Two dimensional finite-element simulation of a high temperature superconducting synchronous generator during three-phase short-circuit fault condition using full transient non-linear rotating machine model," in *Proceedings ISEF 2003 XI International Symposium on Electromagnetic Fields in Electrical Engineering*, Maribor, Slovenia, 2003, pp. 285-288.
- K. S. Ship, J. K. Sykulski and K. F. Goddard, "Design and Performance Evaluations of a Synchronous Generator with High Temperature Superconducting Field Winding and Magnetic Core Using Finite Element Modelling," in *Proceedings EMF 2003 Sixth International Symposium on Electric and Magnetic Fields*, Aachen, Germany, 2003, pp. 183-186.
- D. H. Kim, K. S. Ship and J. K. Sykulski, "Applying Continuum Design Sensitivity Analysis combined with standard EM software to shape optimisation in magnetostatic problems," in *Proceedings COMPUMAG 2003*, Saratoga Springs, US, 2003, pp. 112-113.